

**University of Alberta**

**Experimental and Theoretical Study on Biaxial Normal-Shear Bonding  
Strength at Interface between Elastic/Elastic, Elastic/Viscoelastic and  
Viscoelastic/Viscoelastic Materials**

by

**Mohammad Al Amin Khan Chowdhuri**

A thesis submitted to the Faculty of Graduate Studies and Research  
in partial fulfillment of the requirements for the degree of

**Doctor of Philosophy**

Department of Mechanical Engineering

© Mohammad Al Amin Khan Chowdhuri

Fall 2012  
Edmonton, Alberta

Permission is hereby granted to the University of Alberta Libraries to reproduce single copies of this thesis and to lend or sell such copies for private, scholarly or scientific research purposes only. Where the thesis is converted to, or otherwise made available in digital form, the University of Alberta will advise potential users of the thesis of these terms.

The author reserves all other publication and other rights in association with the copyright in the thesis and, except as herein before provided, neither the thesis nor any substantial portion thereof may be printed or otherwise reproduced in any material form whatsoever without the author's prior written permission.

*Dedicated to .....*

My Father, who wished to see the completion of my PhD degree.

“Though I have lost you during my program, I believe you are watching this  
endeavor”.

## **ABSTRACT**

Bi-material interface is often observed in many advanced materials and structures. Measurement of the interface bonding strength is more challenging than the measurement of pure tensile or shear strength of a homogeneous material because of the presence of the stress singularity at the interface corner, non-uniform stress distribution along the interface and the co-existence of normal and shear stress components. In this PhD research project, a new innovative test method including specimen design, test procedure and an iterative calculation algorithm, is developed for more accurate determination of the interface bonding strength.

Three different types of bi-material interface are considered in this study; interface between elastic and elastic materials, between elastic and viscoelastic materials, and between viscoelastic and viscoelastic materials. Analytical solutions are developed to determine the stress singularity and conditions for its elimination for all the above three types of interface. The analytical solution for the elastic/elastic bi-material interface is derived based on the axi-symmetric asymptotic analysis. For the elastic/viscoelastic and viscoelastic/viscoelastic bi-material interfaces, the analytical solutions are obtained from the solution of elastic/elastic interface through the elastic-viscoelastic correspondence principle. The developed analytical solutions are further verified by FEM numerical analyses.

Three different materials; Aluminum, Epoxy and Polyvinylchloride (PVC) are considered. The elastic material properties of the selected materials are

determined by uni-axial tensile tests. To determine the viscoelastic properties, relaxation tests are carried out on the viscoelastic materials. It is found that the order of the stress singularity changes with time due to the viscoelasticity of materials. If any stress singularity exists at the interface corner, with time the order of singularity increases. For a non-singular stress case at the interface corner, the order of the stress singularity may increase or decrease with time, depends on the bonding angle (specimen geometry).

With the proposed design that can eliminate the stress singularity at the bi-material interface corner, the loading capacity of the specimen is also increased. For example, the tensile load carrying capacity of such designed aluminum/epoxy bonded joint is increased by 2.65 times than that of the ASTM (American Society for Testing and Materials) butt joint design. Finally, as a practical application of this research, the optimal ranges of bonding angles at the interface corners of porcelain fused to metal (PFM) dental crowns with precious or non-precious metal alloys are suggested.

## **PREFACE**

This thesis is based on the work I have done in the Advanced Composite Materials Engineering Group of University of Alberta from January 2009 to April 2012 on the bi-material interface bonding strength. The idea of conducting the study on this topic came forward in order to study the debonding failure or damage mechanism of composite materials, as the reliable interface bonding strength data are not available. This thesis is written in mixed format. It consists of eight different chapters. In Chapter 1, a brief review on the interface of bi-materials is presented. At the end of this chapter, the disadvantages or shortcomings of current methods for the interface bonding strength measurement are summarized and the objectives of this study to overcome those disadvantages/shortcomings are given. In Chapter 2, the developed new method to determine the bi-material interface bonding strength is explained. In Chapter 3, the experimental facilities and characterization of materials are presented. Experimental determination of elastic and viscoelastic properties of three materials (aluminum, epoxy and PVC) is described. In Chapters 4, 5 and 6, the interface bonding strength determination of elastic/elastic, elastic/viscoelastic and viscoelastic/viscoelastic interfaces are presented by the developed method respectively including the analytical solutions to determine the stress singularity at the interface corner. In Chapter 7, an optimal design of a PFM dental crown is developed based on this study. Finally, in Chapter 8, the summary of the thesis and further recommendations are presented.

## **ACKNOWLEDGEMENT**

I would like to express my unfeigned gratitude to my supervisor, Dr. Zihui Xia, for his stupendous supervision, superior guidance and considerable patience throughout this work. I greatly appreciate his continuous encouragement to enrich my innovation capabilities and helping me to develop professional attitude. His vast experiences and enthusiasm in research inspired and motivated me for doing this research work.

I wish to thank Dr. Tian Tang, Dr. Pierre Mertiny, Dr. Donald Yu and Dr. Hao Zhang for being part of my supervisory committee and their constructive comments on this thesis. I am indebted to Mr. Bernie Faulkner for his cordial behaviour and considerable assistance for completing the experimental works of this study. I would also like to thank Mr. Gabriel Shi for his cooperation and all of my research group mates for providing me a friendly research environment.

It's my pleasure to pay tribute to the funding sources, NSERC, Sadler Graduate Scholarship foundation and Ivy A Thomson and William A Thomson Graduate Scholarship foundation for supporting me to do this research. I am also grateful to Universal Dental Lab and MITAC Accelerate for funding me for two internship projects. Special thanks to Dr. Donald Yu for his valuable suggestions as one of my academic supervisors for these two internship projects.

Finally and most importantly, my deepest gratitude goes to my wife, Rifat Hossain, for her dedication, encouragement and patience. I would like to thank my mother and other family members for keeping their faith on me and providing unselfish support throughout my life.

# TABLE OF CONTENTS

<b>CHAPTER 1</b>	<b>INTRODUCTION</b>	<b>1</b>
1.1	Bi-Material Interfaces .....	1
1.2	Stress Singularity at Bi-Material Interface.....	3
1.3	Elimination of the Stress Singularity from Bi-Material Interface.....	8
1.4	Measurement of Interface Bonding Strength.....	18
1.5	Objectives.....	23
	Bibliography.....	25
<b>CHAPTER 2</b>	<b>NEW METHOD TO DETERMINE BONDING STRENGTH OF BI-MATERIAL INTERFACE</b>	<b>39</b>
2.1	Design of the Specimen.....	39
2.2	Test Procedure .....	45
2.3	Iteration Calculation Method to Determine the Interface Strength Envelope .....	46
	Bibliography.....	49
<b>CHAPTER 3</b>	<b>MATERIAL CHARACTERIZATION AND TEST SET UP</b>	<b>50</b>
3.1	Experimental Set Up.....	50
	3.1.1 Tensile and viscoelastic testing system.....	50
	3.1.2 Mold design.....	53
	3.1.3 Multi axial testing machine.....	54
	3.1.4 Grip design.....	55
3.2	Material Testing.....	60
	3.2.1 Materials selection.....	60

3.2.2	Determination of the elastic properties of materials.....	62
3.2.3	Determination of the viscoelastic properties of materials.....	68
3.2.3.1	<i>Linear viscoelastic stress-strain relation</i> .....	69
3.2.3.2	<i>Experimental procedures</i> .....	70
	Bibliography .....	76
<b>CHAPTER 4 ELASTIC/ELASTIC BI-MATERIAL INTERFACE</b>		<b>78</b>
4.1	Specimen Design.....	78
4.2	Determination of the Stress Singularity and Critical Bonding Angle.....	79
4.2.1	Determination of the critical bonding angle by analytical method.....	79
4.2.2	Verification of the critical bonding angle by finite element analysis.....	91
4.2.3	Experimental verification of the critical bonding angle .....	94
4.3	Specimen and Experiments.....	95
4.4	Experimental Results and Finite Element Analysis to Obtain the Stress Distribution along the Interface.....	96
4.5	Obtaining Biaxial Normal-Shear Interface Bonding Strength Criterion (Envelope) through Iteration.....	98
4.6	Further Observation and Remarks.....	101
	Bibliography .....	104

<b>CHAPTER 5</b>	<b>ELASTIC/VISCOELASTIC BI-MATERIAL INTERFACE</b>	<b>106</b>
5.1	Viscoelasticity.....	106
5.2	Background Study.....	108
5.3	Material Modeling.....	110
5.3.1	Case -1: the viscoelastic shear modulus is modeled as the standard linear solid model and Poisson's ratio is considered as constant.....	111
5.3.2	Case -2: both the viscoelastic shear modulus and Poisson's ratio are modeled as the standard linear solid model.....	113
5.3.3	Case -3: both the viscoelastic shear modulus and Poisson's ratio are modeled as the Wiechert model.....	115
5.4	Viscoelastic Properties of Epoxy.....	116
5.5	Analytical Solution for an Elastic/Viscoelastic Bonded Joint.....	119
5.5.1	Case-1: the shear modulus is time dependent but Poisson's ratio is time independent.....	119
5.5.2	Case-2: both the shear modulus and Poisson's ratio are time dependent.....	123
5.5.3	Case-3: Both the shear modulus and Poisson's ratios are time dependent and more accurately represent the behavior of the material .....	125
5.6	Stress Singularity and Critical Bonding Angle for an Aluminum/ Epoxy Bonded Joint.....	128
5.7	Determination of the Critical Bonding Angle by Finite Element Analysis.....	136
5.8	Determination of the Interface Bonding Strength between Elastic/Viscoelastic Materials.....	140

5.8.1	Iterative method for determining the interface bonding strength envelope.....	141
	Bibliography .....	151
<b>CHAPTER 6</b>	<b>VISCOELASTIC/VISCOELASTIC BI-MATERIAL INTERFACE</b>	<b>154</b>
6.1	Scope of the Study.....	154
6.2	Viscoelastic Properties of PVC.....	155
6.3	Analytical Solution for Viscoelastic/Viscoelastic Bonded Joints.....	158
6.3.1	Case-1: the shear modulus is time dependent but Poisson's ratio is time independent.....	158
6.3.2	Case-2: both the shear modulus and Poisson's ratio are time dependent.....	162
6.3.3	Case -3: Both the shear modulus and Poisson's ratios are time dependent and more accurately represent the behavior of the material.....	164
6.4	Stress Singularity and Critical Bonding Angle for a PVC/Epoxy Bonded Joint.....	166
6.5	Determination of Critical Bonding Angle by Finite Element Analysis.....	175
6.6	Determination of Interface Bonding Strength Between Viscoelastic/Viscoelastic Materials.....	178
	Bibliography .....	185
<b>CHAPTER 7</b>	<b>APPLICATION IN DENTAL RESTORATIONS</b>	<b>186</b>
7.1	Background Study.....	186
7.2	Materials.....	189

7.3	Development of the Model.....	192
7.4	Stress Singularity Analysis using Finite Element Modeling.....	194
7.5	Stress Singularity Analysis by an Analytical Method.....	202
7.6	Optimal Off-Vertical Angle of the Metal Layer.....	207
7.7	Further Observation and Remarks.....	210
	Bibliography.....	212
<b>CHAPTER 8 CONCLUSIONS</b>		<b>217</b>
8.1	Summary of the Research.....	217
8.2	Further Recommendations.....	224

## LIST OF TABLES

Table 4.1	Material properties of aluminum and epoxy.....	78
Table 4.2	Values of $\lambda$ in the range $0 < \lambda < 1$ for different bonding angles.....	90
Table 4.3	Maximum failure loads of the aluminum/epoxy specimen.....	96
Table 5.1	Experimental viscoelastic properties of epoxy.....	117
Table 5.2	Maximum failure loads and time required to reach failure.....	140
Table 6.1	Experimental viscoelastic properties of PVC.....	155
Table 6.2	Maximum failure loads and time required to reach failure.....	178
Table 7.1	Poisson's ratio calculation for Wirobond-280.....	191
Table 7.2	Elastic properties of dental materials.....	192
Table 7.3	Value of $\lambda$ corresponding to different bonding angles for precious alloy crown.....	204
Table 7.4	Value of $\lambda$ corresponding to different bonding angles for non-precious alloy crown.....	205

## LIST OF FIGURES

Figure 1.1	Schematic of initial shape of a single-lap joint as presented in Hu et al. (1998).....	9
Figure 1.2	Scarf joint geometries as presented in Qian and Akisanya (1999) (a) A scarf joint consisting of two long elastic materials (b) A scarf joint consisting of a thin layer of elastic solid sandwiched between two substrates.....	10
Figure 1.3	Rectangular plate with a skewed interface as presented in Ding et al. (1996).....	11
Figure 1.4	Specimen with convex interface (Plane strain) as presented in Xu et al. (2004).....	13
Figure 1.5	Specimen with curve interface (Planar Specimen) as presented in Lauke (2007).....	15
Figure 1.6	Specimen with convex interface (Planar Specimen) showing singularity as presented in Wang and Xu (2006).....	16
Figure 1.7	Specimen with axi-symmetric convex interface as presented in Wang and Xu (2006).....	17
Figure 2.1	Conceptual design of the invented cylindrical specimen with spherical interface.....	40
Figure 2.2	General axi-symmetric finite element model for checking the stress singularity.....	42
Figure 3.1	Testing machine for tensile and viscoelastic experiment..	51
Figure 3.2	Axial and diametrical extensometers.....	52
Figure 3.3	Mold for making interface testing specimen.....	54
Figure 3.4	Multi axial testing machine.....	55
Figure 3.5	Grip to hold the interface testing specimen in multi-axial machine.....	56
Figure 3.6	Grip dimension to calculate glue length.....	57

Figure 3.7	Modified grip to hold the interface testing specimen.....	59
Figure 3.8	Stress- strain curve for aluminum.....	63
Figure 3.9	Determination of Poisson’s ratio for aluminum.....	63
Figure 3.10	Tension test specimen for epoxy and PVC.....	64
Figure 3.11	Stress- strain curve for epoxy.....	65
Figure 3.12	Determination of Poisson’s ratio for epoxy.....	66
Figure 3.13	Stress- strain curve for PVC.....	67
Figure 3.14	Determination of Poisson’s ratio for PVC.....	67
Figure 3.15	Applied axial strain in relaxation test of epoxy.....	71
Figure 3.16	Measured axial stress in relaxation test of epoxy.....	72
Figure 3.17	Relaxation modulus of epoxy.....	72
Figure 3.18	Viscoelastic Poisson’s ratio of epoxy.....	73
Figure 3.19	Applied axial strain in relaxation test of PVC.....	74
Figure 3.20	Measured axial stress in relaxation test of PVC.....	74
Figure 3.21	Relaxation modulus of PVC.....	75
Figure 3.22	Viscoelastic Poisson’s ratio of PVC.....	75
Figure 4.1	(a) Two materials are joined along curved interface (b) Detail geometry of the interface (c) Axi-symmetric model of bi-material interface.....	79
Figure 4.2	Normal, shear and effective stress distributions along the interface for bonding angles of 40° and 60° with pure tensile load.....	91
Figure 4.3	Effective stress distributions at the interface corner for bonding angles of 49° and 50° with pure tensile load.....	92
Figure 4.4	Shear stress distribution along the interface under pure torsional load (bonding angle of 50°).....	93
Figure 4.5	Variation of failure loads with bonding angle under pure tensile loading.....	94
Figure 4.6	Aluminum-epoxy specimen for interface strength test....	95
Figure 4.7	Stress distribution along the interface of epoxy and aluminum of specimen No. 6.....	97

Figure 4.8	Shear stress distribution along the interface for pure torsional load.....	98
Figure 4.9	(a) Interface strength envelope of epoxy and aluminum based on maximum effective stresses (b) Interface strength envelope of epoxy and aluminum after 1 <sup>st</sup> iteration (c) Final interface strength envelope of epoxy and aluminum interface.....	100
Figure 4.10	Interface of the failed specimen under pure tensile load...	103
Figure 5.1	Standard linear solid model.....	112
Figure 5.2	Wiechert model consisting of two Maxwell elements with a spring in parallel.....	115
Figure 5.3	Experimental and modeled viscoelastic shear modulus of epoxy.....	118
Figure 5.4	Experimental and modeled viscoelastic Poisson's ratio of epoxy.....	119
Figure 5.5	Variation of Dundurs' parameter $\alpha(t)$ with time.....	128
Figure 5.6	Variation of Dundurs' parameter $\beta(t)$ with time.....	129
Figure 5.7	Variation of $\lambda$ with time for a bonding angle of 40° .....	131
Figure 5.8	Variation of $\lambda$ with time for a bonding angle of 60°.....	132
Figure 5.9	Variation of $\lambda$ with time for bonding angles 49° and 50° for Case-1.....	133
Figure 5.10	Variation of $\lambda$ with time for a bonding angle of 49° .....	134
Figure 5.11	Variation of $\lambda$ with time for a bonding angle of 48°.....	135
Figure 5.12	Effective stress along the interface for bonding angles of 40° and 60° (Case-3).....	138
Figure 5.13	Effective stress along the interface for bonding angles of 48° and 49° (Case-3).....	139
Figure 5.14	Stress-strain curves of epoxy for different loading rates...	141
Figure 5.15	3D finite element model for the bi-material interface bonding strength specimen.....	142
Figure 5.16	Effect of finite element model length on the analysis.....	143

Figure 5.17	Stress distribution along the interface for combined loading.....	144
Figure 5.18	Stress distribution along the interface for pure torsional loading case.....	145
Figure 5.19	Interface bonding strength envelope based on effective stress criterion.....	147
Figure 5.20	Interface bonding strength envelope after 1 <sup>st</sup> iteration.....	148
Figure 5.21	Bonding strength envelope for the tested aluminum/epoxy interface.....	149
Figure 6.1	Experimental and modeled viscoelastic shear modulus of PVC.....	157
Figure 6.2	Experimental and modeled viscoelastic Poisson's ratio of PVC.....	158
Figure 6.3	Variation of Dundurs' parameter $\alpha(t)$ with time.....	167
Figure 6.4	Variation of Dundurs' parameter $\beta(t)$ with time.....	168
Figure 6.5	Variation of $\lambda$ with time for the bonding angle 40° .....	170
Figure 6.6	Variation of $\lambda$ with time for the bonding angle 60°.....	171
Figure 6.7	Variation of $\lambda$ with time for the bonding angle 49°.....	172
Figure 6.8	Variation of $\lambda$ with time for the bonding angle 48°.....	173
Figure 6.9	Variation of $\lambda$ with time for the bonding angle 47°.....	174
Figure 6.10	Effective stress along the interface for bonding angles of 40° and 60° (Case-3) .....	176
Figure 6.11	Effective stress along the interface for the bonding angles of 47°, 48° and 49° (Case-3).....	177
Figure 6.12	Stress distribution along the interface for pure tensile loading.....	179
Figure 6.13	Stress distribution along the interface for pure torsional loading case.....	180
Figure 6.14	Interface bonding strength envelope based on effective stress criterion.....	182

Figure 6.15	Interface bonding strength envelope in different iterations.....	183
Figure 7.1	Sectional view of a PFM crown and local model near the free edge corner of the interface.....	193
Figure 7.2	Finite element models: (a) single interface and (b) two interfaces.....	195
Figure 7.3	Effective stress distribution along porcelain-metal interface for different bonding angles: (a) precious-metal-based crown and (b) non-precious-metal based crown.....	197
Figure 7.4	Effective stress distribution along metal-cement interface for different bonding angles: (a) precious-metal-based crown and (b) non-precious-metal based crown.....	199
Figure 7.5	Variation of effective stress of precious-metal-based crown along both interfaces for bonding angles of: (a) 5°; (b) 20°; and (c) 50°.....	200
Figure 7.6	Variation of effective stress of non-precious-metal-based crown along both interfaces for bonding angles of: (a) 5°; (b) 32°; and (c) 50°.....	201
Figure 7.7	Variation of $\lambda$ with the bonding angle $\theta$ for (a) precious-metal-based crown and (b) non-precious-metal-based crown.....	206
Figure 7.8	(a) Global axisymmetric model of PFM crown and (b) FEM mesh and applied boundary.....	207
Figure 7.9	Contour plot of nodal effective stresses of (a) precious-metal based crown for (i) $\varphi=5^\circ$ , (ii) $\varphi=10^\circ$ , (iii) $\varphi=20^\circ$ ; and (b) non-precious-metal based crown for (i) $\varphi=5^\circ$ , (ii) $\varphi=10^\circ$ , (iii) $\varphi=12^\circ$ .....	209
Figure 7.10	Different types of margin for tooth crown: (a) feather; (b) chamfer; (c) shoulder; (d) bevel; and (e) bevel-shoulder...	210

## NOMENCLATURE

$A, B, S, C$	Constants
$[A]$	Eigen vectors
$[C]$	Co-efficient matrix
$D$	Specimen diameter
$E$	Elastic modulus
$G(t)$	Relaxation modulus
$H$	Stress intensity factor
$L$	Specimen length
$M_{grip}^{ult}$	Maximum torque at the grip
$M_{int}^{ult}$	Maximum torque at the interface
$N$	Number of stress data points
$P$	Applied load
$R$	Specimen radius
$R_l$	Ratio of radial distance to specimen radius
$U$	Displacement fields
$V$	Volume fraction
$W$	Weight fraction
$a$	Radius of the spherical interface
$b$	Variable
$d$	Grip diameter to hold specimen
$f$	Function
$i, j$	Index
$k$	Bulk modulus
$l$	Glue length
$m$	Material index
$r, r_l$	Radial distance from interface corner
$s$	Laplace transform parameter
$t$	Time; Thickness

$t_0$	Viscoelastic relaxation time
$x$	Distance from interface corner
$(r_1, \varphi)$	Polar coordinates
$(r, \theta)$	Polar coordinates
$(\rho, \psi, z)$	Cylindrical coordinates
$\alpha, \beta$	Dundurs' parameters
$\theta_0$	Bonding angle
$\theta_c$	Critical bonding angle
$\theta_s$	Skew angle
$\rho$	Density; Radial direction
$\lambda$	Eigenvalue
$\mu$	Shear modulus
$\sigma$	Stress
$\sigma_l$	Axial Stress
$\sigma_n$	Interface normal stress
$\sigma_{eff}$	Effective stress
$\tau$	Interface shear stress
$\tau_s$	Interface shear strength
$\tau_{glue}^{ult}$	Glue's shear strength
$\nu$	Poisson's ratio
$\varepsilon_0$	Unit step axial strain
$\varepsilon_1$	Axial strain
$\varepsilon_2$	Lateral strain
$\varphi$	Off-vertical angle; Inverse of relaxation time
$\varphi_1, \varphi_2$	Harmonic stress functions
$\gamma$	An adjacent complementary angle of the bonding angle
$\gamma_1$	An arbitrary positive constant
$\delta$	Kronecker delta
$L\{f(t)\}$	Laplace transform of function $f(t)$
$L^{-1}\{F(s)\}$	Inverse Laplace transform of function $F(s)$
$\tau_1, \dots, \tau_6$	Coefficients

ER	Extended range
FEM	Finite Element Method
PFM	Porcelain Fused to metal
RSC	Remote Station Control
MTS	Material Testing System
PVC	Polyvinyl Chloride
CNC	Computer Numerical Controlled

## **CHAPTER 1: INTRODUCTION**

Part of this chapter has been published as

**Chowdhuri, M. A. K.,** Xia, Z., 2010. Elimination of Stress Singularity from Interface Corner and Measurement of Interface Bonding Strength: A review. *International Review of Mechanical Engineering*, 4(7), 908-916.

# CHAPTER 1

## INTRODUCTION

---

Bi-material interfaces exist in many advanced materials and engineering structures. It has been established that because of the presence of the stress concentration/singularity at the interface corner, failure may initiate from the interface corner. In order to characterize the interface properties, it is necessary to determine the bonding strength of interface accurately by eliminating the stress singularity. This chapter presents a brief review on the studies available in open literature covering the stress singularity analysis at bi-material interface, determination of the order of the stress singularity, stress singularity elimination techniques, and measurement of the interface strength. Finally, the objectives of the current research are presented.

### 1.1 BI-MATERIAL INTERFACES

Interfaces between reinforcement and matrix in composite materials; metal and ceramic in electronic packaging and metal coating; ceramic and polymer in biomaterials; sensor and structural components in smart structures; and solder joints in electronics are some of the typical examples of bi-material interface. As one kind of composite material structure, bi-material lap joints have been widely used in aircraft, spacecraft, helicopters and automotive industries (Chaudhuri and

---

Chiu, 2009). Usually, these joints can satisfy some special requirements of engineering structures that cannot be fulfilled by using single material components. For example, ceramics/metal joints can make full use of the superiority of both materials, such as the resistance to high temperature and corrosion and unique electronic functions in ceramics, and the ductility and good machinability of metals (Hu et al., 1998). Other advantages of adhesive bonding of dissimilar parts in the aerospace, automotive and electronic industries are high strength to weight ratio, improved appearance, improved corrosion resistance and cost effectiveness (Kinloch, 1993).

Adhesive bonding has been increasingly used in joining and repairing load-carrying structural components (Adams and Wake, 1984; Baker and Jones, 1988; Kinloch, 1993). Compared to the mechanical fastening, e.g. riveting or bolting, adhesive bonding may provide more uniform and efficient load transfer into the patch and can reduce the risk of high stress concentrations. This leads to the wide use of bonded repairs instead of using riveted repairs in aircraft structures (Vlot et al., 2000). One of the common examples of bonded joint is the single-lap joint. Existing single lap joints are made of two substrates joined by using the mechanical connection method, chemical connection method or solid-phase bonding process.

However, bi-material joint is sensitive to the changes in the geometrical parameters. These geometrical parameters affect the performances of a bonded joint. It is well known that there are discontinuities of material and geometry at the bonding edges in these joints. These discontinuities may cause singularities in

the stress fields or very high stress concentration near the vertex of the bonding edges. This stress concentration/singularity may lead to the delamination initiation in the local area, and subsequently to the global failure of the joint structures (Hu et al., 1998; De Chen and Chue, 2003).

That is why most researches on bi-material interfaces deal with the stress singularity. In fact, to characterize the interface properties, sound knowledge on the stress singularity is required.

## **1.2 STRESS SINGULARITY AT BI-MATERIAL INTERFACE**

The singularity in the stress fields near the free edges of dissimilar material components is one of the main factors responsible for debonding under the mechanical and/or thermal loading (Stenger et al., 2000; Wu, 2004). Numerous studies have shown that the failure often occurs along the interface/joint between two materials with high property mismatch (e.g., free-edge delamination in composite laminates and debonding between thin film/substrate) and improving the interfacial properties (especially reducing the interfacial stress level) can enhance the overall material/structural behaviors (Kerans et al., 1989; Hutchinson and Suo, 1992; Kallas et al., 1992; Liechti and Liang, 1992; Gundel et al., 1995; Krawczak and Pabiot, 1995; Xu et al., 2003). Stress singularity at the interface between the adhesive and adherend is reported by many researchers (Williams, 1952; Hein and Erdogan, 1971; Groth, 1988; Akisanya and Fleck, 1997). The existence of bi-material interfaces is an intrinsic characteristic of

adhesive joints which results in asymptotic singular stress fields at the bi-material interface corners. This type of stress singularity is the major driving force for the failure of adhesive joints (Gradin, 1982; Reedy, 1990; Ding and Kumosa, 1994; Ding et al., 1994). Ding et al., (1994) reported that the corner stress singularity at an adhesive interface is a major problem for the joint design. Of the many factors affecting the strength of a bonded joint, the magnitude and distribution of stresses in both the adhesive layer and substrates are most crucial to the design of bonded joints. For elastic adhesive layer and the substrates, a complex stress singularity exists at the termination of the adhesive layer (Bogy, 1971; Hein and Erdogan, 1971). Many researchers considered the case of interface with singularity as a crack problem in fracture mechanics. The interface corner is identified as a potential fracture initiation site because of the stress singularity at the interface corner (Liu and Fleck, 1999; Akisanya and Meng, 2003). Many researchers reported that fracture always starts at the stress concentration points, which are often the stress singularities at the corners of elastic/elastic bi-material interfaces (Williams, 1952; Kondrat'ev, 1967; Stern and Soni, 1976; Grisvard, 1989), or at joints consisting of anisotropic layers (Leguillon and Sanchez-Palencia, 1987; Desmorat, 1996; Desmorat and Leckie, 1998; Liu and Fleck, 1999).

To find the analytical solutions of stress distribution near the interface corners, extensive research has been conducted by many researchers (Bogy, 1968, 1971; Hein and Erdogan, 1971; Theocaris, 1974). Since Tranter (1948) used the Mellin transforms to obtain an analytical stress solution for an infinite wedge, the stress singularities in a single-material wedge under different boundary conditions

---

has been investigated extensively. For example, Williams (1952) employed the Airy stress function and the separation of variables to study the single-material wedge under various boundary conditions. A  $r^{-\lambda}$  ( $0 < \lambda < 1$ ) type singular stress field was found near the apex of an isotropic elastic material. The value of ' $-\lambda$ ' can be real or complex. Bogy (1968) employed the Mellin transform to treat the wedge problems of two bonded materials subjected to the surface traction at the boundaries. The singular stress problems have been studied for the angular corners of isotropic materials by Williams (1952); Bogy (1968); England (1971); Stern and Soni (1976); Reedy (1990) and for the multilayered media by Schmauder (1989); Kelly et al. (1992); Reedy (1993). This study has been extended to the anisotropic layers by Leguillon and Sanchez-Palencia (1987) using a numerical method and then by Desmorat (1996) who derived a closed-form solution. Theocaris (1974) studied a multi-material wedge by a series solution using the Kolosov-Muskhelishvili (Muskhelishvili, 1953) complex stress functions. Ma and Wu (1990); Munz et al. (1993); Munz and Yang (1994); Yang and Munz (1994,1997); Chen (1995); Ma (1995); Yang (1998, 1999), all devoted themselves to the formulation of an angular function for a single or two material wedges. Sinclair (1999) carried out a detailed investigation on the logarithmic stress singularities resulting from various boundary conditions in a single-material wedge. Many other investigators (Cook and Erdogan, 1972; Fenner, 1976; Barsoum, 1988; Yang and Munz, 1994; Pageau and Biggers, 1995) examined the behavior of the stress singularity around the wedge, edge crack and the interface crack.

Bogy (1968, 1970, 1971); Bogy and Wang (1971); Hein and Erdogan (1971); Theocaris (1974); and Dempsey and Sinclair (1979, 1981) established the dependence of the order of the stress singularity on the elastic constants of materials and local geometry of the multi-material wedges or junctions. Dundurs (1969) developed two composite elastic parameters to relate the order of the stress singularity in a two-material wedge. Lazzarin et al. (2002) presented a method for the evaluation of the singular stress fields in the bonded joints of different geometries. The stress distributions are represented by a two-term stress expansion, under the hypothesis that both the first and second terms are in the variable separable form.

Singular solutions are also used to solve the linear elastic fracture mechanics problems and the procedures are illustrated in the standard texts (Liebowitz, 1968; and Kanninen and Popelar, 1985). The singular crack solutions for the power-law hardening plasticity were studied by Hutchinson (1968); Rice and Rosengren (1968). Desmorat and Leckie (1998) provided a fast calculation technique for the 2D-elastic singular strains, stresses and displacements close to the corners, edges or interface ends of joints constituted of anisotropic layers. Isotropic results are also derived as a limiting case of the general anisotropic study. Akisanya and Meng (2003) characterized the stresses near the interface corner of bonded joints by the interface corner stress intensity factor and the order of the elastic singularity. Based on the theoretical solution for the order of the stress singularity, De Chen and Chue (2003) determined the corresponding stress

intensity factors for a one or two-bonded wedge, under the mechanical or thermal loadings by using the finite element approach.

Ding et al. (1994) addressed that in evaluating the asymptotic field for the corner stress singularity, it is essential to consider various joint geometries, adhesive and adherend elastic properties, and the non-linear material effects. Marsavina and Craciun (2009) considered the non-linear elasto-plastic material with Ramberg-Osgood power hardening law bonded to a rigid elastic substrate to derive asymptotic plane-strain solution near the interface free edge with small-scale yielding. Desmorat and Lemaitre (1998) studied the singularity of the elastic stress field close to a sharp notch with any angle in a multi-material joint by means of the complex potential method. The order of the singularity is obtained as a closed-form solution depending upon the angle of the sharp notch. Studies have also shown that for the joints bonded with brittle adhesives, the intensity of the stress singularity at the interface corner could be used to predict the failure of the bonded joints (Groth, 1988; Reedy, 1990).

The stress behavior at the interface corner of three materials has been investigated by Qian and Akisanya (2001). It was found that the stresses near such interface corner are significantly higher than those at a free-edge corner of two materials under the same thermal loading conditions. Qian (2001) considered the stresses near the wedge corner consisted of a singular stress term and a regular constant stress term. The influence of adhesive joint design parameters such as the type of joint, geometry and material properties on the generalized stress intensity factors are presented by Lazzarin et al. (2002).

### **1.3 ELIMINATION OF THE STRESS SINGULARITY FROM BI-MATERIAL INTERFACE**

There have been a lot of studies on the characterization of the stresses at the interface corners of various joint geometries and on the minimization of the stress singularity. Cherry and Harrison (1970); and Groth and Nordlund (1991) suggested an iterative procedure for optimizing the geometry of the adherend to obtain a uniform stress distribution in the adhesive layer, while Adams et al. (1973) proposed the use of varying adhesive layer thickness to reduce the stress singularity. Akisanya and Meng (2003) reported that the geometry profile of the adherend needed to eliminate the stress singularity is complex and it is often difficult to machine the adherend to the required shape. The type of singularity depends on the choice of joint geometry, and the elastic and thermal properties of the materials (Williams, 1952; Bogy, 1968, 1971). Goglio and Rossetto (2010) confirmed that the most influencing parameter on the stress singularity is the edge angle.

Sawa et al. (2009) conducted a two-dimensional stress analysis of adhesive butt joints with elastic circular fillers in the adhesive subjected to the external tensile loadings and reported that as the amount of filler particles increased, the stiffness of filler increased and more filler particles approached to the edges of the interfaces. Thus, the joint strengths were increased. However,

though joint strengths were increased, the singularity cannot be avoided in this process.

The shape optimization of bi-material single-lap joints was performed by Hu et al. (1998). They investigated the free-edge stress singularity and condition for its disappearance near the vertex of bonding edges in a single-lap joint. On the basis of sequential linear programming, they proposed a shape-optimization approach for the single-lap joint. They also reported that the strength of a single-lap joint can be improved significantly by using their optimum technique because of the stress concentration at the interface can be reduced significantly by using their proposed optimum approach. According to their recommendation, the general characteristic of the optimum shapes is that those parts of the two substrates near the bonding edges should be cut appropriately to make the joint into a tapered form as shown in Figure 1.1.

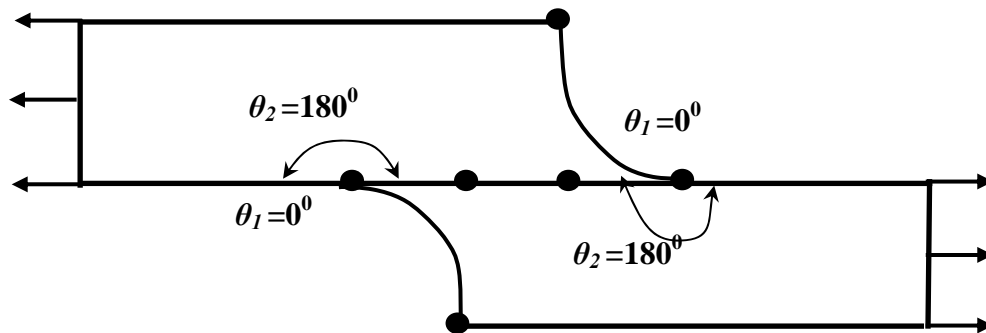


Figure 1.1: Schematic of initial shape of a single-lap joint as presented in Hu et al. (1998)

They did the analysis for some ranges of shear modulus and reported that the efficiency of the shape optimization becomes lower with increasing ratio of shear moduli,  $\mu_2/\mu_1$ . It is also proved later that this design is not enough for complete removal of the stress singularity. Qian and Akisanya (1999) proposed a scarf joint of two materials and a scarf joint consisting of a thin layer of elastic solid sandwiched between two substrates, as shown in Figure 1.2, to remove the stress singularity at the interface corner.

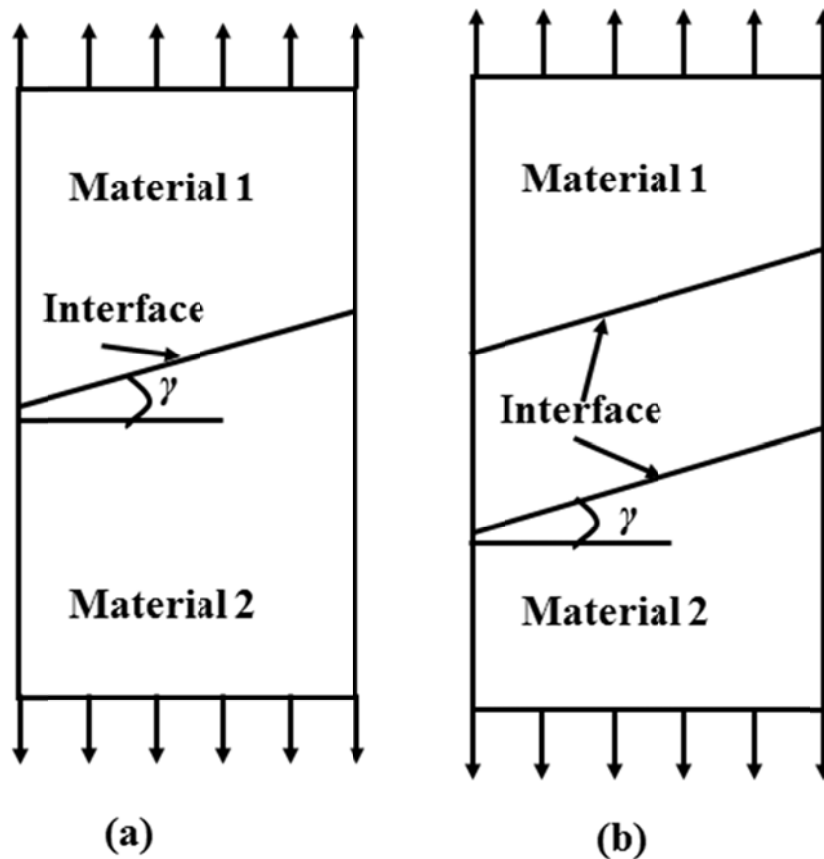


Figure 1.2: Scarf joint geometries as presented in Qian and Akisanya (1999) (a) A scarf joint consisting of two long elastic materials (b) A scarf joint consisting of a thin layer of elastic solid sandwiched between two substrates

They concluded that it is impossible to completely eliminate the singularity in many practical joint problems but the free edge singularity can be minimized by an appropriate selection of materials and joint geometry characterized by the scarf angle,  $\gamma$ . However, they also mentioned that for some specific material properties, their design can eliminate the stress singularity from the interface corner considering as a plane strain problem.

An optimized Iosipescu specimen (Figure 1.3) for the shear testing of adhesive joints to avoid (or reduce) the bi-material stress singularity was proposed by Ding et al. (1996).

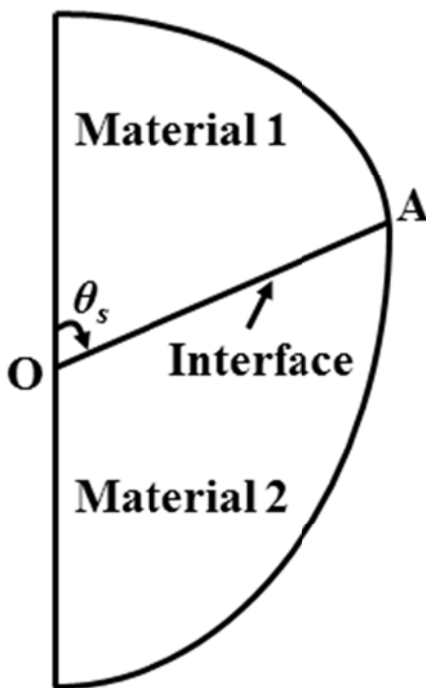


Figure 1.3: Rectangular plate with a skewed interface as presented in Ding et al. (1996)

They determined a critical skewed interface angle of  $\theta_s = 126^\circ$  (see Figure 1.3) and reported that if the skewed interface angle is greater than this value, the singularity of asymptotic stress field at the bi-material wedge will totally disappear irrespective of the mechanical properties of the two materials making up the wedge. Liu and Fleck (1999) mentioned that the scarf joints are preferable over butt joints as the adhesive is loaded by a combination of shear and tension rather than in a tensile peel mode, resulting higher joint strengths.

It should be pointed out that all the above cases of scarf joint may eliminate the stress singularity in the width direction only but could not eliminate the singularity in the thickness direction. In fact, any 2D geometry with a straight edge cannot eliminate the stress singularity completely. Any scarf joint as shown in Figure 1.2 may remove the singularity from one corner of the interface, but there will be stress singularity at other corner of the interface.

A three-dimensional eigen function expansion approach for the prediction of the singular stress field in the neighborhood of the interfacial front of an adhesively bonded scarf joint is presented by Chaudhuri and Chiu (2009). They provided two solutions for the elimination of the stress singularity at scarf joints. One is by changing the materials and another one is by designing the joint with the wedge angle that satisfies certain conditions. Their specimen was made from two pieces of rectangular plates (same dimensions), which were adhesively bonded by means of a scarf joint. However, their proposed design has the same limitation as described earlier for the 2D scarf joint given in Figure 1.2.

A specimen design as shown in Figure 1.4 is proposed in Xu et al. (2004) to remove the stress singularity at the free edge of the interface. They also claimed that it can provide reasonable interfacial strength measurement and suppress edge debonding of dissimilar material joints.

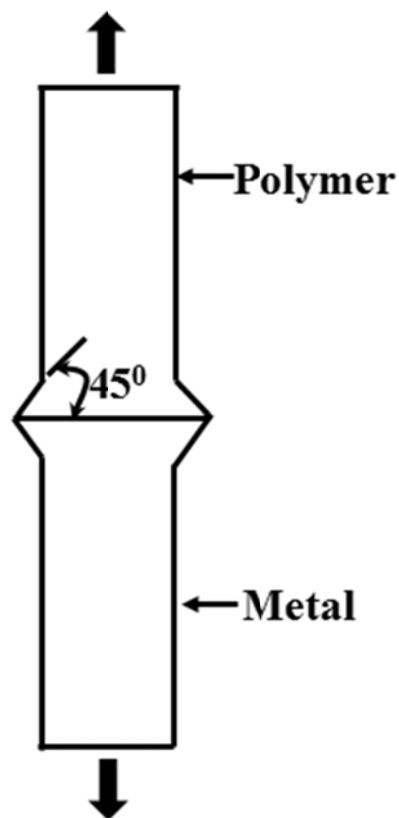


Figure 1.4: Specimen with convex interface (Plane strain) as presented in Xu et al. (2004)

They selected typical polycarbonate/aluminum joints for the demonstration of their proposed design through an in-situ photo elasticity

---

experiment. They reported that the stress intensity (indicates the existence of singularity) has decreased by several orders in their proposed joint. They also mentioned that the higher fringe orders signifying larger stress intensity move away from the interface towards the polycarbonate curved edge. In fact, this design also cannot eliminate the stress singularity in the thickness direction since the plane strain condition cannot be realized near the two boundary surfaces in thickness direction. In addition, the cross-sectional area of the specimen close to the interface is notably reduced and, as a result, the material may fail before the interface failure.

Addressing the above problems, Lauke et al. (2003); Schneider et al. (2003) and Lauke (2007) proposed a new type of specimen configurations by introducing a curved interface between two materials in the flat coupon specimen as shown in Figure 1.5.

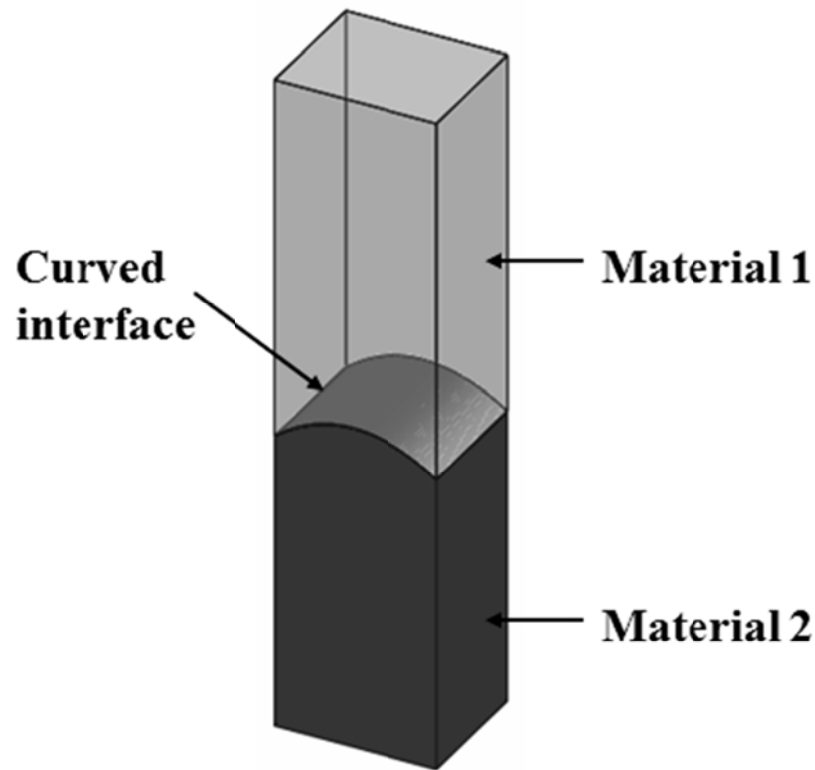


Figure 1.5: Specimen with curve interface (Planar Specimen) as presented in Lauke (2007)

This method successfully eliminates the stress singularity along the width direction but not along the thickness direction. The similarity and difference between an axi-symmetric joint and a plane strain joint were pointed out by Li et al. (2000). The similarity is that the stresses near the bond edges of the joints have the same singularity. The difference is that the stresses in an axi-symmetric joint cannot be determined as a plane strain deformation joint under prescribed traction. Therefore, asymptotic descriptions for the stress fields near the bond edges of the joints must be different under axi-symmetric deformation and under plane strain deformation, even though the stress singularities are same (Koguchi, 1997; Li et al., 2000). That's why all the proposed designs presented above based on the 2D

plane strain analysis cannot eliminate the stress singularity completely. To clearly understand the stress singularity in all directions, 3-D analysis is needed. The fact is clearly described by Wang and Xu (2006) in Figure 1.6. At one edge there exists no singularity but in the other edge there exists the stress singularity. The 2D plane strain analysis only deals with the edge that has no singularity. Also, the stress concentration in the axi-symmetric joints could be reduced by varying suitably the edge angle and then the strength of joints could be improved (Wang and Xu, 2006).

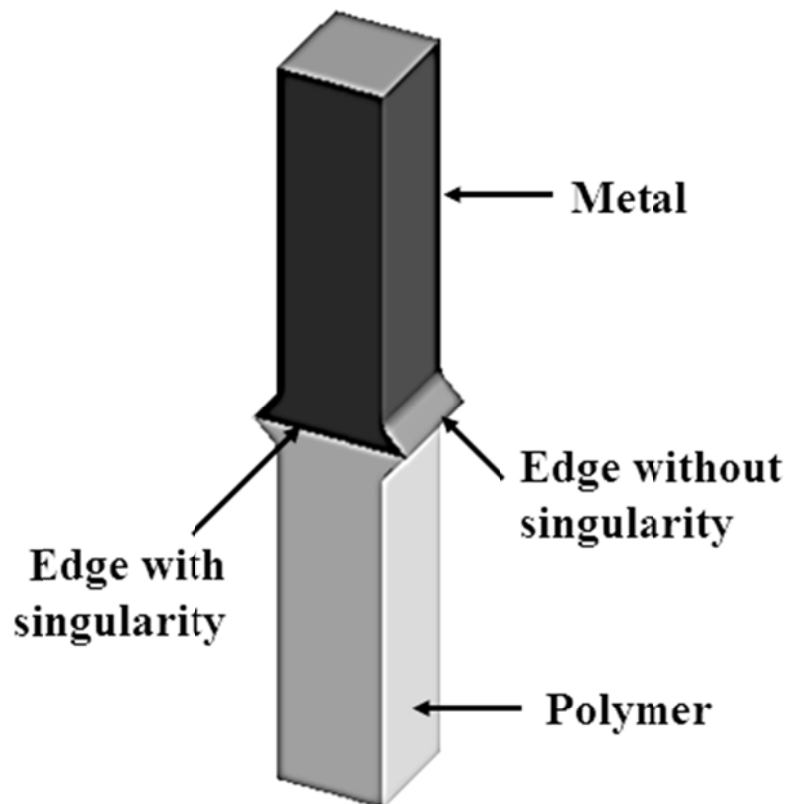


Figure 1.6: Specimen with convex interface (Planar Specimen) showing singularity as presented in Wang and Xu (2006)

Wang and Xu (2006) proposed a new axi-symmetric convex joint for the least free-edge stress singularity shown in Figure 1.7. They conducted quasi-static tension and dynamic tension experiments of both straight and convex bi-material joints. They showed that the convex joint yields an increase in the final failure strength (up to 22%) compared to the traditional straight-edged joint.

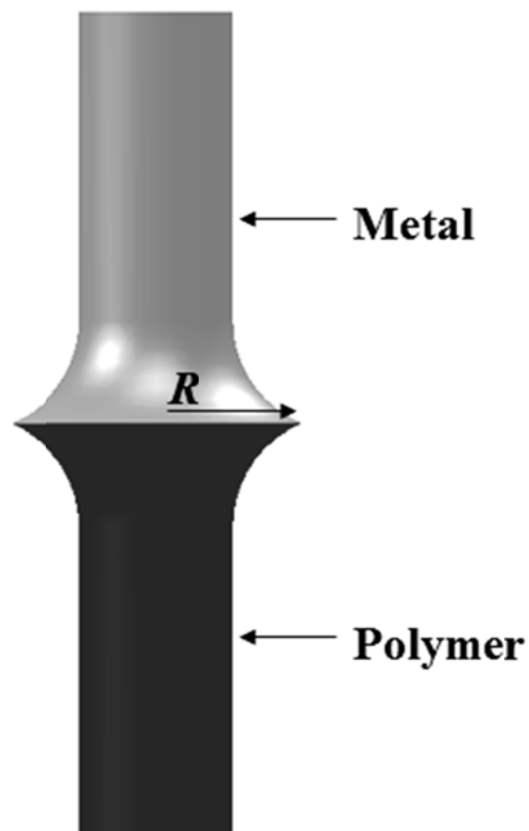


Figure 1.7: Specimen with axi-symmetric convex interface as presented in Wang and Xu (2006)

Xu (2006) also proposed a similar design for determining the interface strength between epoxy and E-glass by creating a proper bonding angle through machining a circumferential fillet between two materials. With that design the stress singularity is avoided but the cross-sectional area of the specimen in the epoxy segment is reduced and the stress concentration is produced in the epoxy material at the area near the interface, as a result, the epoxy may fail before the interface failure.

As the complexity of stress singularity at the vertex of a general 3-D joint can be avoided for an axi-symmetric joint (Zhixue, 2006), Wu (2008) performed finite element analysis of a curved interface using axi-symmetric model for the elimination of the stress singularity. However, they admitted that the practical applications of their results may be very limited. They also mentioned that a suitable failure criterion for a bi-material joint is very important in the situation without any stress singularity since the influence of material mismatch parameters and interface geometry on the different stress components is not the same.

#### **1.4 MEASUREMENT OF INTERFACE BONDING STRENGTH**

The measurement of the interface bonding strength of bi-materials is more complicated than the measurement of tensile or shear strength of a homogeneous material. The current practices for the measurement of interface strength of bi-materials can be classified into two separate test methods: tensile test and shear test. These two test methods are with different specimen designs and test

procedures, or in other words, the specimen design and test setup for testing tensile strength cannot be used for shear strength testing, and vice versa.

For the shear strength test, most commonly used methods are in the category of lap joint tests, such as these specified in ASTM D3165 (2007) and ASTM D3528 (2008). In these standard test setups, shear stress is generated by the tensile load at the two ends of the specimen. The interface shear strength is obtained through dividing the maximum tensile load by the area of the bonding interface. Ideally, the pure shear stress should be parallel to the bonding plane in the test to obtain the correct interface shear strength. The current test setups, however, generate a multi-axial stress status at the bond termini areas, and as a result, the specimen could be failed in shear, tensile, or cleavage crack mode (Pizzi, 1994). Tensile bonding strength tests are based on the butt joint specimen as described in ASTM D897 (2008) and ASTM D2095 (2008), where tensile loadings are applied to the two ends of the specimen. The interface tensile strength is obtained through dividing the maximum tensile load by the cross-sectional area of the bonding interface. The disadvantage of this test setup is the existence of the stress singularity at the interface free edge. Theoretically, the stress will be infinite at the free edge of the interface due to the singularity. Therefore, it is not accurate or doesn't make sense to calculate the interface strength by the ratio of the failure load to the entire bonding area. It should be noted that the above ASTM standards are mainly for measuring the bonding strength between two materials by using a third adhesive medium, and in this

way, it may not be an exact bi-material interface unless the two materials are directly bonded without the third adhesive medium.

For fiber reinforced composites, the interface failure has been the main concern in design and applications. Many experimental methods have been suggested to determine the interface strength between fiber and matrix in composite materials, such as single fiber pull-out, push-out tests (Chua et al., 1992; Drzal, 2000; Xu et al., 2005), droplet test (Miller et al., 1987), single-fiber fragmentation test (Zhou et al., 2001) and peel-off test (Alimuddin and Piggott, 1999). Except for the peel-off test, which mainly concerns the tensile strength, other methods quoted above are to measure the shear bonding strength.

Many investigations have been carried out on butt, scarf and lap adhesive joints using finite element method (Gradin, 1982; Reedy, 1990), photo elastic experiments (Ding and Kumosa, 1994) and the theory of elasticity (Weissberg, 1988; Ding et al., 1994). All those approaches encounter difficulties to accurately determine the value of the bonding strength. Because, all of them have the same disadvantages as ASTM standard methods: the non-uniform multi-axial stress distribution over the interface area and/or the presence of singularities of the interfacial stress components.

Another important consideration in determining the interface bonding strength of bi-materials is the size effect. There are two different terms used for size effect; the material size effect and the mechanics size effect. Material size effect is due to the initial material defects. Even for a simple tensile test of homogeneous material, specimens with different sizes may yield different results.

---

Of course, the obtained results depend on the degree of defects. However, by making specimens from the same material carefully, more consistent results might be obtained. However, for a butt tensile specimen fabricated from two dissimilar materials (singularity exist), the normal stress distribution across the flat interface is not uniform according to the previous discussion. Obviously, this type of specimen will provide data with a stronger size effect in the context of mechanical behavior. Moreover, the mechanics size effect (related to the free-edge stress singularity) will be coupled with the material size effect, and thus lead to complexities in the measurement data because they cannot be treated as the intrinsic material properties. Therefore, the measured nominal interfacial strengths based on the current test standards cannot be used in mechanics predictions, because the interfacial properties obtained from the laboratory tests are quite different from the real values of structures in service (Xu et al., 2004). Any data obtained from specimen containing singularity need careful consideration of the size effect.

For the failure criterion of bi-material interface, the concept of stress is very useful if there is no stress singularity at the interface. However, as a basis for the prediction of failure, the concept of stress becomes meaningless when the structure encompasses singularities as a result of discrete stiffness steps or geometric anomalies such as cracks (Van Tooren and Krakkers, 2006).

So, in order to measure the interface bonding strength more reasonably and accurately, the singularity elimination is a must. If there is no stress singularity at the interface, even if the stress distribution are not uniform along

interface, the interface debonding should initiate from certain critical point where the interface stress state reaches certain limit value. Such limit value represents the actual interface strength property for a given bi-material interface. Also, in that case the mechanics size effect may be reduced to minimum if the specimens are carefully manufactured and tested. Moreover, in practical applications, the bi-material interface can be in multi-axial stress status with various combinations of normal and shear stresses depending on the loading conditions. Therefore, besides the pure tensile strength and the pure shear strength, a general biaxial normal-shear bonding strength criterion, for example, in the form of a strength envelope in normal-shear stress plane, is needed to realistically and adequately characterize the strength of bi-material interface.

From the above review, it can be concluded that:

- i) The current test standards for interface shear and tensile strength measurements may merely give the loading capacity of the specimen, instead of accurate values of the bi-material interface strength as intended although they can still be useful as a relative comparison of bonding strengths of different combinations of bi-materials.
- ii) Current test standards can only give separate nominal interface shear and tensile strength while, in reality, multi-axial stress status and stress singularity exist at the edge of the bonding interfaces of these specimens even though the bonding structure is subjected to the simple tensile or shear load.

- iii) Improved test methods are therefore needed to avoid the stress singularity and to obtain reasonable results of bi-material interface bonding strength. To adequately characterize the bi-material bonding strength for practical applications, a biaxial normal-shear interface bonding strength criterion (strength envelope) is also needed.

The measurement of the interface bonding strength is crucial for the design and applications of structures with two or more materials. With the increasing applications of bi-material, a branch of solid mechanics, the mechanics of interface has been rapidly developing in the past two decades. It studies mechanical behavior, strength, life and optimal design of material interfaces. Theoretical and experimental characterization/evaluation of bonding strength of interface is the most important topic for the mechanics of interface.

## **1.5 OBJECTIVES**

The overall objective of this research is to develop a new test method for the determination of biaxial bonding strength of bi-material interfaces based on, theoretical solutions for the new designed interface geometry, and applications of the new knowledge to the design and manufacture of stronger bi-material interfaces. The main objectives of the proposed research are:

- i) Development of a new test method to characterize the interface bonding strength of bi-materials more accurately and realistically.

- ii) Development of analytical models for the elastic/elastic, elastic/viscoelastic and viscoelastic/viscoelastic bi-material interfaces, obtaining solutions for the critical bonding angle, which delineates the finite and singular stress fields.
- iii) Determination of the biaxial shear-normal bonding strength of bi-material interface according to the proposed method.
- iv) Application of the new test method and theories to optimize the design of bi-material interfaces, such as in the area of dental restorations.

---

**BIBLIOGRAPHY**

Adams, R. D., Chambers, S. H., Del Strother, P. J. A., Peppiatt, N. A., 1973.

Rubber model for adhesive lap joints. *Journal of Strain Analysis*. 8, 52-57.

Adams, R. D., Wake, W. C., 1984. *Structural Adhesive Joints in Engineering*.

Elsevier Applied Science, Oxford.

Akisanya, A. R., Fleck, N. A., 1997. Interfacial cracking from the free-edge of a

long bi-material strip. *International Journal of Solids and Structures*. 34,

1645-1665.

Akisanya, A. R., Meng, C. S., 2003. Initiation of fracture at the interface corner of

bi-material joints. *Journal of the Mechanics and Physics of Solids*. 51, 27-

46.

Alimuddin, M. A., Piggott, M. R., 1999. Fracture toughness of fiber-polymer

interfaces estimated from single fiber peel tests. *Polymer Composites*. 20,

655-663.

ASTM-D897, 2008. *Test Method for Tensile Properties of Adhesive Bonds*.

ASTM International, West Conshohocken, PA.

ASTM-D2095, 2008. *Standard Test Method for Tensile Strength of Adhesives by*

*Means of Bar and Rod Specimens*. ASTM International. ASTM

International, West Conshohocken, PA.

---

ASTM-D3165, 2007. Standard Test Method for Strength Properties of Adhesives in Shear by Tension Loading of Single-Lap-Joint Laminated Assemblies.

ASTM International, West Conshohocken, PA.

ASTM-D3528, 2008. Standard Test Method for Strength Properties of Double Lap Shear Adhesive Joints by Tension Loading. ASTM International,

West Conshohocken, PA.

Baker, A. A., Jones, R., 1988. Bonded Repairs of Aircraft Structures. Martinus Nijhoff, The Hague.

Barsoum, R. S., 1988. Theoretical basis of the finite-element iterative method for the eigenvalue problem in stationary cracks. *International Journal for Numerical Methods in Engineering*. 26, 531-539.

Bogy, D. B., 1968. Edge-bonded dissimilar orthogonal elastic wedges under normal and shear loading. *Journal of Applied Mechanics*. 35, 460-466.

Bogy, D. B., 1970. On the problem of edge-bonded elastic quarter-planes at the boundary. *Int J Solids Struct*. 6, 1287-1313.

Bogy, D. B., 1971. Two edge-bonded elastic wedges of different materials and wedge angles under surface tractions. *Journal of Applied Mechanics*. 38, 377-386.

- 
- Bogy, D. B., Wang, K. C., 1971. Stress singularities at interface corners in bonded dissimilar isotropic elastic materials. *International Journal of Solids and Structures*. 7, 993-1005.
- Chaudhuri, R. A., Chiu, S. H. J., 2009. Three-dimensional asymptotic stress field in the vicinity of an adhesively bonded scarf joint interface. *Composite Structures*. 89, 475-483.
- Chen, D. H., 1995. Stress intensity factors for v-notched strip under tension or inplane bending. *International Journal of Fracture*. 70, 81-97.
- Cherry, B. W., Harrison, N. L., 1970. Optimum profile for a lap joint. *Journal of Adhesion*. 2, 125-128.
- Chua, P. S., Dai, S. R., Piggott, M. R., 1992. Mechanical-properties of the glass-fiber polyester interphase .1. Effects due to silanes. *Journal of Materials Science*. 27, 913-918.
- Cook, T. S., Erdogan, F., 1972. Stresses in bonded materials with a crack perpendicular to interface. *International Journal of Engineering Science*. 10, 677-697.
- De Chen, C., Chue, C. H., 2003. Singular stresses near apex of wedge by finite element analysis. *Journal of the Chinese Institute of Engineers*. 26, 423-434.

- 
- Dempsey, J. P., Sinclair, G.B., 1979. On the stress singularities in the plane elasticity of the composite wedge. *Journal of Elasticity*. 9, 373-391.
- Dempsey, J. P., Sinclair, G.B., 1981. On the singular behavior at the vertex of a bi-material wedge. *Journal of Elasticity*. 11, 317-327.
- Desmorat, R., 1996. Singular fields for a bi-material in anisotropic plane elasticity. *Comptes Rendus De L Academie Des Sciences Serie Ii Fascicule B-Mecanique Physique Chimie Astronomie*. 322, 355-361.
- Desmorat, R., Leckie, F. A., 1998. Singularities in bi-materials: parametric study of an isotropic/anisotropic joint. *European Journal of Mechanics a-Solids*. 17, 33-52.
- Desmorat, R., Lemaitre, J., 1998. Stress singularities applied to crack initiation by damage of multimaterial joints. *Mechanics of Materials*. 29, 153-160.
- Ding, S., Erdinc, I., Buchholz, F. G., Kumosa, M., 1996. Optimization of the adhesive joint Iosipescu specimen for pure shear test. *International Journal of Fracture*. 76, 1-20.
- Ding, S. L., Kumosa, M., 1994. Singular stress behavior at an adhesive interface corner. *Engineering Fracture Mechanics*. 47, 503-519.
- Ding, S. L., Meekisho, L., Kumosa, M., 1994. Analysis of stress singular fields at a bimaterial wedge corner. *Engineering Fracture Mechanics*. 49, 569-585.

- 
- Drzal, L. T., Herrera-Franco, Ho, P., 2000. Fiber-Matrix Interface Tests. *Comprehensive Composite Materials*. 5, 71-111.
- Dundurs, J., 1969. Discussion of edge-bonded dissimilar orthogonal elastic wedges under normal and shear loading. *Journal of Applied Mechanics*. 36, 650-652.
- England, A. H., 1971. On Stress Singularities in Linear Elasticity. *International Journal of Engineering Science*. 9, 571-585.
- Fenner, D. N., 1976. Stress singularities in composite-materials with an arbitrarily oriented crack meeting an interface. *International Journal of Fracture*. 12, 705-721.
- Goglio, L., Rossetto, M., 2010. Stress intensity factor in bonded joints: Influence of the geometry. *International Journal of Adhesion and Adhesives*. 30, 313-321.
- Gradin, P. A., 1982. A fracture criterion for edge-bonded bimaterial bodies. *Journal of Composite Materials*. 16, 448-456.
- Grisvard, P., 1989. Singularities en elasticite. *Archive for Rational Mechanics and Analysis*. 107, 157-180.
- Groth, H. L., 1988. Stress singularities and fracture at interface corners in bonded joints. *International Journal of Adhesion and Adhesives*. 8, 107-113.

- 
- Groth, H. L., Nordlund, P., 1991. Shape optimization of bonded joints. *International Journal of Adhesion and Adhesives*. 11, 204-212.
- Gundel, D. B., Majumdar, B. S., Miracle, D. B., 1995. Evaluation of the transverse response of fiber-reinforced composites using a cross-shaped sample geometry. *Scripta Metallurgica Et Materialia*. 33, 2057-2065.
- Hein, V. L., Erdogan, F., 1971. Stress singularities in a two-material wedge. *International Journal of Fracture Mechanics*. 7, 317-330.
- Hu, N., Wang, B., Sekine, H., Yao, Z. H., Tan, G. W., 1998. Shape-optimum design of a bi-material single-lap joint. *Composite Structures*. 41, 315-330.
- Hutchinson, J. W., 1968. Singular Behavior at the End of a Tensile Crack in a Hardening Material. *Journal of Mechanics and Physics of Solids*. 16, 13-31.
- Hutchinson, J. W., Suo, Z., 1992. Mixed-mode cracking in layered materials. *Advances in Applied Mechanics*, Vol 29, vol.29, pp. 63-191.
- Kallas, M. N., Koss, D. A., Hahn, H. T., Hellmann, J. R., 1992. Interfacial stress state present in a thin-slice fiber push-out test. *Journal of Materials Science*. 27, 3821-3826.
- Kanninen, M. F., Popelar, C. H., 1985. *Advanced Fracture Mechanics*, New York.

- 
- Kelly, P. A., Hills, D. A., Nowell, D., 1992. The design of joints between elastically dissimilar components (with special reference to ceramic metal joints). *Journal of Strain Analysis for Engineering Design*. 27, 15-20.
- Kerans, R. J., Hay, R. S., Pagano, N. J., Parthasarathy, T. A., 1989. The role of the fiber matrix interface in ceramic composites. *American Ceramic Society Bulletin*. 68, 429-442.
- Kinloch, A. J., 1993. *Adhesive and Adhesives*. Chapman and Hall, London.
- Koguchi, H., 1997. Stress singularity analysis in three-dimensional bonded structure. *International Journal of Solids and Structures*. 34, 461-480.
- Kondrat'ev, V. A., 1967. Boundary-value problems for elliptic equations in domains with conical or angular points. *Transactions of the Moscow Mathematical Society*. 16, 227-313.
- Krawczak, P., Pabiot, J., 1995. Fracture Mechanics Applied to Glass Fiber/Epoxy Matrix Interface Characterization. *Journal of Composite Materials*. 29, 2230–2253.
- Lauke, B., 2007. Stress concentration along curved interfaces as basis for adhesion tests. *Composite Interfaces*. 14, 307-320.
- Lauke, B., Schuller, T., Schneider, K., 2003. Determination of interface strength between two polymer materials by a new curved interface tensile test. *Composite Interfaces*. 10, 1-15.

- 
- Lazzarin, P., Quaresimin, M., Ferro, P., 2002. A two-term stress function approach to evaluate stress distributions in bonded joints of different geometries. *Journal of Strain Analysis for Engineering Design*. 37, 385-398.
- Leguillon, D., Sanchez-Palencia, E., 1987. *Computation of Singular Solutions in Elliptic Problems and Elasticity*. Masson, Paris.
- Li, Y. L., Hua, S. Y., Yang, Y. Y., 2000. Stresses around the bond edges of axisymmetric deformation joints. *Engineering Fracture Mechanics*. 66, 153-170.
- Liebowitz, H., 1968. *Fracture*. Academic Press, New York.
- Liechti, K. M., Liang, Y. M., 1992. The interfacial fracture characteristics of bimaterial and sandwich blister specimens. *International Journal of Fracture*. 55, 95-114.
- Liu, D., Fleck, N. A., 1999. Scale effects in the initiation of cracking of a scarf joint. *International Journal of Fracture*. 95, 67-88.
- Ma, C. C., 1995. Plane solution of thermal-stresses for anisotropic bimaterial elastic wedges. *Journal of Thermal Stresses*. 18, 219-245.
- Ma, C. C., Wu, H. W., 1990. Analysis of inplane composite wedges under traction-displacement or displacement-displacement boundary-conditions. *Acta Mechanica*. 85, 149-167.

- 
- Marsavina, L., Craciun, M., 2009. The asymptotic stress field for free edge joints under small-scale yielding conditions. *Analele Stiintifice Ale Universitatii Ovidius Constanta-Seria Matematica*. 17, 171-181.
- Miller, B., Muri, P., Rebenfeld, L., 1987. A microbond method for determination of the shear-strength of a fiber-resin interface. *Composites Science and Technology*. 28, 17-32.
- Munz, D., Fett, T., Yang, Y. Y., 1993. The regular stress term in bonded dissimilar materials after a change in temperature. *Engineering Fracture Mechanics*. 44, 185-194.
- Munz, D., Yang, Y. Y., 1994. Stresses near the free-edge of the interface in ceramic-to-metal joints. *Journal of the European Ceramic Society*. 13, 453-460.
- Muskhelishvili, N. I., 1953. *Some Basic Problems of the Mathematical Theory of Elasticity*. Noordhoff, Netherlands.
- Pageau, S. S., Biggers, S. B., 1995. Finite-element evaluation of free-edge singular stress-fields in anisotropic materials. *International Journal for Numerical Methods in Engineering*. 38, 2225-2239.
- Pizzi, A., Mittal, K. L., 1994. *Handbook of Adhesive Technology*. Marcel Dekker Inc, New York.

- 
- Qian, Z. Q., 2001. On the evaluation of wedge corner stress intensity factors of bi-material joints with surface tractions. *Computers & Structures*. 79, 53-64.
- Qian, Z. Q., Akisanya, A. R., 1999. An investigation of the stress singularity near the free edge of scarf joints. *European Journal of Mechanics A-Solids*. 18, 443-463.
- Qian, Z. Q., Akisanya, A. R., 2001. Stress distribution at the interface corner of a tri-material structure. *Journal of Engineering Mechanics*. 127, 747-753.
- Reedy, E. D., 1990. Intensity of the stress singularity at the interface corner between a bonded elastic and rigid layer. *Engineering Fracture Mechanics*. 36, 575-583.
- Reedy, E. D., 1993. Asymptotic interface corner solutions for butt tensile joints. *International Journal of Solids and Structures*. 30, 767-777.
- Rice, J. R., Rosengren, G. F., 1968. Plane strain deformation near a crack tip in a power-law hardening material. *Journal of the Mechanics and Physics of Solids*. 16, 1-12.
- Sawa, T., Akita, Y., Iwamoto, T., 2009. Two-Dimensional Stress Analysis of Adhesive Butt Joints Filled With Elastic Circular Fillers in the Adhesive Subjected to Static Tensile Loadings. *Journal of Adhesion Science and Technology*. 23, 195-214.

- 
- Schmauder, S., 1989. Influence of Elastic Anisotropy on the Edge Problem. *Metal-Ceramic Interfaces*. 4, 413-419.
- Schneider, K., Lauke, B., Schuller, T., 2003. Determination of the interface strength between two polymer materials by a new curved interface tensile test: Preliminary experimental results. *Composite Interfaces*. 10, 581-591.
- Sinclair, G. B., 1999. Logarithmic stress singularities resulting from various boundary conditions in angular corners of plates in extension. *Journal of Applied Mechanics*. 66, 556-560.
- Stenger, F., Chaudhuri, R., Chiu, J., 2000. A novel sinc solution of the boundary integral form for two-dimensional bi-material elasticity problems. *Composites Science and Technology*. 60, 2197-2211.
- Stern, M., Soni, M. L., 1976. On the computation of stress intensities at fixed-free corners. *International Journal of Solids and Structures*. 12, 331-337.
- Theocaris, P. S., 1974. The Order of Singularity at a Multi-wedge Corner of a Composite Plate. *International Journal of Engineering Science*. 12, 107-120.
- Tranter, C. J., 1948. The use of the mellin transform in finding the stress distribution in an infinite wedge. *Quarterly Journal of Mechanics and Applied Mathematics*. 1, 125-130.

- 
- Van Tooren, M. J. L., Krakkers, L. A., 2006. A generalized stress singularity approach for material failure prediction and its application to adhesive joint strength analysis. *Journal of Adhesion Science and Technology*. 20, 981-985.
- Vlot, A., Verhoeven, S., Ipenburg, G., Siwipersad, D. R. C., Woerden, H. J. M., 2000. Stress concentrations around bonded repairs. *Fatigue & Fracture of Engineering Materials & Structures*. 23, 263-276.
- Wang, P., Xu, L. R., 2006. Convex interfacial joints with least stress singularities in dissimilar materials. *Mechanics of Materials*. 38, 1001-1011
- Weissberg, V., Arcan, M., 1988. *Adhesively Bonded Joints, Analysis and Design*, ASTM STP 981. W S Johnson (ed), Philadelphia.
- Williams, M. L., 1952. Stress singularities resulting from various boundary conditions in angular corners of plates in extension. *Journal of Applied Mechanics*. 19, 526-528.
- Wu, Z. X., 2004. Design free of stress singularities for bi-material components. *Composite Structures*. 65, 339-345.
- Wu, Z. X., 2008. Stress concentration analyses of bi-material bonded joints without in-plane stress singularities. *International Journal of Mechanical Sciences*. 50, 641-648.

- 
- Xu, K., 2006. Experimental Study on Biaxial Normal-Shear interface Bonding Strength between E-glass and Epoxy Polymer. M.Sc Thesis, University of Alberta, Canada.
- Xu, L. R., Huang, Y. G. Y., Rosakis, A. J., 2003. Dynamic crack deflection and penetration at interfaces in homogeneous materials: experimental studies and model predictions. *Journal of the Mechanics and Physics of Solids*. 51, 461-486.
- Xu, L. R., Kuai, H., Sengupta, S., 2004. Dissimilar material joints with and without free-edge stress singularities: Part I. A biologically inspired design. *Experimental Mechanics*. 44, 608-615.
- Xu, L. R., Kuai, H., Sengupta, S., 2005. Free-edge stress singularities and edge modifications for fiber pushout experiments. *Journal of Composite Materials*. 39, 1103-1125.
- Yang, Y. Y., 1998. Asymptotic Description of the Logarithmic Singular Stress Field and Its Application. *International Journal of Solids and Structures*. 35, 3917-3933.
- Yang, Y. Y., 1999. The Type of  $r^{-\omega} \ln(r)$  Stress Singularities in a Two-dissimilar-materials Joint under Thermal Loading. *Journal of Thermal Stresses*. 22, 101-121.

- Yang, Y. Y., Munz, D., 1994. Determination of the regular stress term in a dissimilar materials joint under thermal loading by the mellin transform. *Journal of Thermal Stresses*. 17, 321-336.
- Yang, Y. Y., Munz, D., 1997. Stress singularities in a dissimilar materials joint with edge tractions under mechanical and thermal loadings. *International Journal of Solids and Structures*. 34, 1199-1216.
- Zhixue, W., 2006. A method for eliminating the effect of 3-D bimaterial interface corner geometries on stress singularity. *Engineering Fracture Mechanics*. 73, 953-962.
- Zhou, X. F., Wagner, H. D., Nutt, S. R., 2001. Interfacial properties of polymer composites measured by push-out and fragmentation tests. *Composites Part A-Applied Science and Manufacturing*. 32, 1543-1551.

## **CHAPTER 2: NEW METHOD TO DETERMINE BONDING STRENGTH OF BI-MATERIAL INTERFACE**

Part of this chapter has been accepted as

Xia, Z., **Chowdhuri, M. A. K.**, Ju, F., 2012. A New Test Method for Measurement of Biaxial Normal-Shear Bonding Strength at Bi-material Interface. *Mechanics of Advanced Materials and Structures*, DOI: 10.1080/15376494.2011.643278 (In press)

## CHAPTER 2

# NEW METHOD TO DETERMINE BONDING STRENGTH OF BI-MATERIAL INTERFACE

---

An innovative method to determine the bonding strength of bi-material interface is developed and presented in this Chapter. The developed method includes a new design of the specimen with special interface geometry to eliminate the stress singularity, test methodology and an iterative calculation technique integrated with FEM analysis to determine the interface biaxial normal-shear bonding strength envelope.

### 2.1 DESIGN OF THE SPECIMEN

A cylindrical specimen of two bulk materials with a spherical interface as shown in Figure 2.1 is developed to measure the interface bonding strength between the two materials. In this design, the soft material is at the convex side of the interface, while the hard material is at the concave side of the interface. The bonding angle,  $\theta_0$ , is defined as the angle between the tangent of the spherical interface at the free edge to the generator of the cylindrical surface as shown in Figure 2.1.

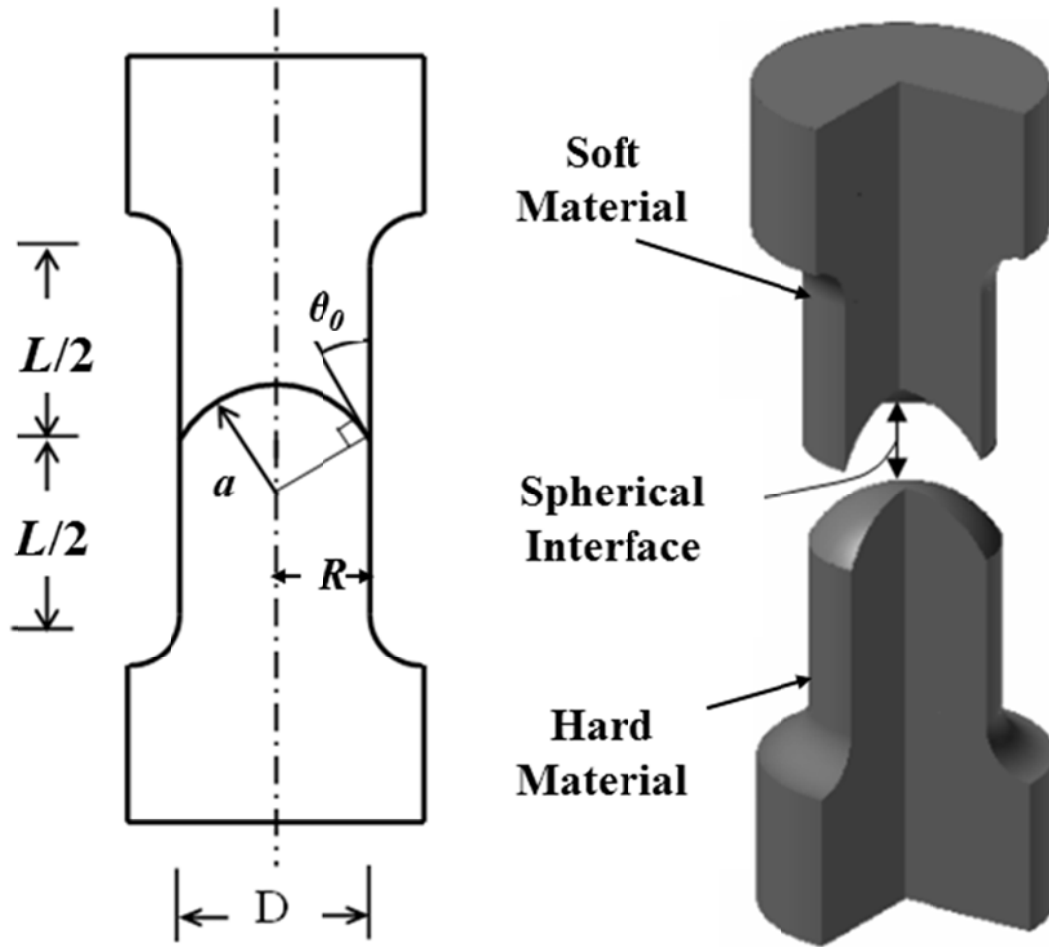


Figure 2.1: Conceptual design of the invented cylindrical specimen with spherical interface

It can be seen that the bonding angle is geometrically dependent on the ratio of the specimen radius,  $R$ , to the radius of the spherical interface,  $a$ :

$$\cos \theta_0 = \frac{R}{a} = \frac{D}{2a} \quad (2.1)$$

For a given pair of materials, there exists a critical value of the bonding angle,  $\theta_c$ , which delineates the singular and non-singular stress field near the free edge of the interface. When  $\theta_0 < \theta_c$ , the stress singularity at the free edge can be avoided and a finite stress field along the spherical bi-material interface can be obtained. The stress distribution along the interface would not be uniform; however, it can be accurately determined by either the analytical or numerical analysis methods.

It should be noticed that the critical bonding angle,  $\theta_c$ , is dependent on the mechanical properties of the two materials. The critical bonding angle,  $\theta_c$ , is essentially an upper bound of the bonding angle  $\theta_0$  to avoid the stress singularity. Actual selection of the specimen geometry, i.e. the  $\theta_0$  can be accommodate according to the test equipment and specimen fabrication requirements as soon as the condition  $\theta_0 < \theta_c$  is satisfied.

Finite element stress analysis has been performed on the specimen geometry with an extreme case of material combination by assuming a rigid hard material bonded with a soft material (in the FEM analysis assuming the hard material stiffness several order larger than that of the soft material). It is found that the critical bonding angle is  $45^\circ$  for this combination of materials. Thus, this design of geometry of  $\theta_0 = 45^\circ$  can be universally applied to any combination of two elastic materials.

The axi-symmetric finite element model of the specimen shown in Figure 2.2 is used for the FEM analysis.

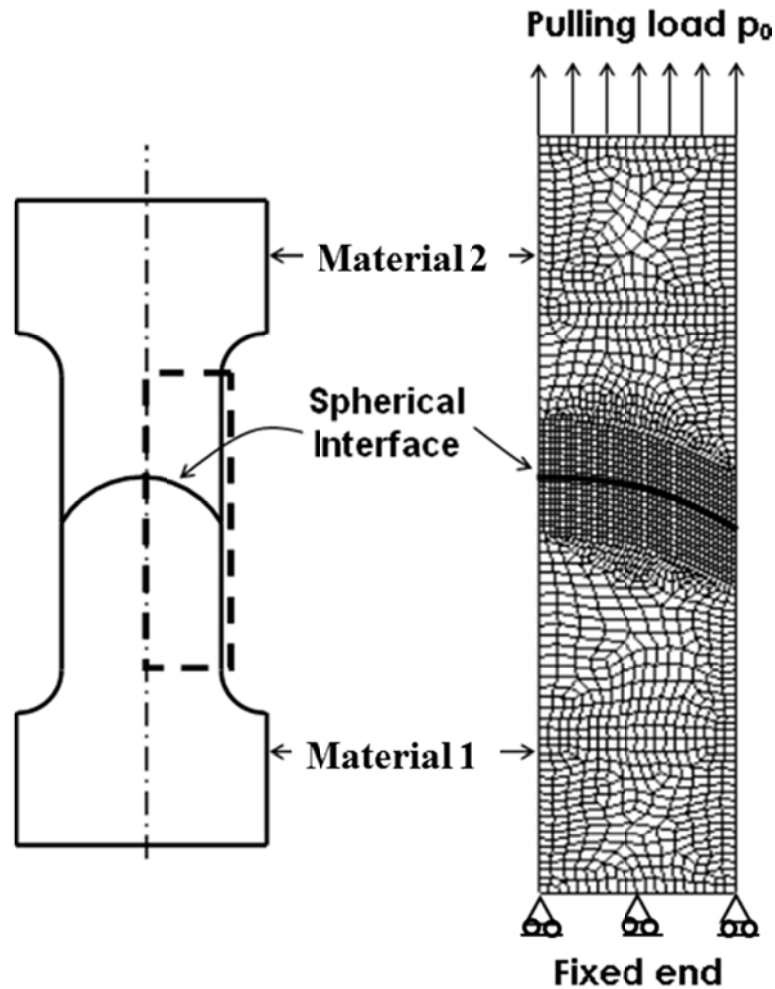


Figure 2.2: General axi-symmetric finite element model for checking the stress singularity

A uniform tensile stress is applied at top end of the specimen, while the bottom end is fixed in vertical direction. The distributions of the interface normal stress,  $\sigma_n$ , interface shear stress,  $\tau$  and effective stress,  $\sigma_{eff} = \sqrt{\sigma_n^2 + 3\tau^2}$  along the interface can be determined by the FEM analysis. If for a specific bonding angle,

excessive stresses exist near the free edge of the interface and these stress values increase without convergent limits with the increase of mesh density, this indicates that the stress singularity occurs at the free edge of the interface for that bonding angle. However, if finite values of the interface stresses are exhibited and the stress convergence is confirmed by the increase of FEM mesh density, this indicates a non-singular stress case. Another fact should be mentioned that there is no interface stress singularity for the application of pure torsional load on the new designed specimen.

To accurately determine the range of bonding angles with or without the stress singularity, the use of an analytical solution could be convenient. The stress field near the free edge of an interface can be deduced into the following asymptotic form (Qian and Akisanya, 1999).

$$\sigma_{ij} = Hr^{\lambda-1} f_{ij}(\theta, \alpha, \beta, \lambda) \quad (i, j = 1, 2) \quad (2.2)$$

In the above expression,  $r, \theta$  are the polar coordinate,  $H$  is the generalized stress intensity factor,  $\alpha, \beta$  are the Dundurs' (1969) parameters which depend on the combinations of elastic constants of the two materials,

$$\alpha = \frac{\mu_1(k_2 + 1) - (k_1 + 1)\mu_2}{\mu_1(k_2 + 1) + (k_1 + 1)\mu_2}, \quad \beta = \frac{\mu_1(k_2 - 1) - (k_1 - 1)\mu_2}{\mu_1(k_2 + 1) + (k_1 + 1)\mu_2} \quad (2.3)$$

where,  $\mu_m = \frac{E_j}{2(\nu_m + 1)}$ ,  $k_m = 3 - 4\nu_m$ ,  $\mu$  is the shear modulus,  $E$  is the elastic modulus,  $\nu$  is the Poisson's ratio and subscript  $m$  is the material index. The  $\lambda$  is eigenvalue obtained from the solution of analytical model.

From Equation (2.2) it is clear that the order of the stress singularity at the edge of the bonded joint is  $\lambda-1$ . If  $0 < \lambda < 1$ , the stress component goes to infinite when  $r \rightarrow 0$ , i.e. there exists the stress singularity. Any angle less than the critical bonding angle will lead  $\lambda > 1$ , thereby eliminates the stress singularity. It can be verified that, for the lap joint as specified in ASTM D3165 (2007) and ASTM D3528 (2008) and the butt joint specimen as described in ASTM D897 (2008) and ASTM D2095 (2008), the stress singularities always exist at the free edge of the interfaces, i.e.  $\lambda - 1 < 0$ .

Our interest is now on the other phase of the stress field solution: for  $\lambda > 1$ , the stress singularity will be eliminated. If the specimen geometry is designed as the present method to avoid the stress singularity under the global tensile or torsional or combined loadings, a finite interface stress field could be accurately obtained for each global loading case. Although the interface stress field is generally not uniform and the normal and shear interface stress components can co-exist, the interface failure (debonding) will be physically initiated at a certain point of the interface with a certain limit stress state. Such limit of stress states represents the bonding strength of the interface. For general combined interface normal and shear stress states, such limit of stress states can be mathematically formulated as a certain interface bonding strength criterion. Note that, the interface bonding strength criterion is physically an inherent mechanical property of each particular bi-material interface. The procedure for obtaining the bonding strength criterion (envelope) through an appropriate

experimental procedure with the specially designed specimen geometry (as described earlier) will be described in the following sections.

## 2.2 TEST PROCEDURE

Test procedures to determine the biaxial normal-shear bonding strength criterion (envelope) for a bi-material interface can be summarized as:

- a) For a given bi-material combination the critical bonding angle for the designed specimen geometry, Fig. 2.1 can be determined through analytical stress analysis method (asymptotic stress analysis near the free edge of the interface, for details, see later chapters). The critical bonding angle result can be further verified by the FEM numerical analysis.

The appropriate geometry of the specimen, more specifically, the bonding angle,  $\theta_0 < \theta_c$  thus can be determined.

- b) Tests on the designed specimens with pure torsional, pure normal and different ratios of the combined normal and torsional loadings are performed. For each test case, the maximum failure load is recorded.

- c) FEM analysis for each test loading case is carried out and the interface normal and shear stress distributions for the maximum failure load obtained through experiments are determined.

It should be pointed out that the FEM analysis may not be limited to an elastic analysis only. Depending on the types of the bi-material and the maximum strength range of the bi-material interface, more accurate nonlinear analyses, such as elastoplastic or viscoelastic analyses may be necessary. There is no principal difficulty to perform the nonlinear FEM analysis as long as the material properties can be accurately calibrated.

- d) The biaxial normal-shear interface bonding strength criterion (envelope) is determined by an iterative calculation method and will be described in the following section.

### **2.3 ITERATION CALCULATION METHOD TO DETERMINE THE INTERFACE STRENGTH ENVELOPE**

It is noted that the interface normal and shear stress distributions are not uniform along the interface even though there is no stress singularity. For the pure torsional loading case, there is no normal interface stress component; therefore, the maximum interface shear stress, denoting as  $\tau_s$ , can be taken as the shear

strength of the bi-material interface. For the pure global normal loading and other combined normal-shear loading cases, both the normal and shear interface stress components exist. Therefore, a biaxial bonding strength criterion (envelope) is required to define the interface bonding strength. The criterion can be expressed as,

$$f(\sigma_n, \tau) = C \quad (2.4)$$

where  $\sigma_n$  and  $\tau$  are the interface normal and shear stress components, respectively, and  $C$  is a constant. The function  $f$  and the constant  $C$  can be determined through the following iteration procedure:

(i) The effective stress is taken as the first trial criterion, i.e.

$$f^{(1)}(\sigma_n, \tau) = \sqrt{\sigma_n^2 + 3\tau^2} = \sqrt{3}\tau_s \quad (2.5)$$

The constant  $C = \sqrt{3}\tau_s$  is obtained by applying the pure torsional loading case in which  $\sigma_n = 0$ .

From the interface normal and shear stress curves, the location of the maximum value of  $\sqrt{\sigma_n^2 + 3\tau^2}$  along the interface is identified and the corresponding pair of normal and shear stress values which contributes for the effective stress is recorded for each test case. These pairs of stresses are denoted as  $[\sigma_{n,j}, \tau_j]^{(1)}$ ,  $j = 1, \dots, N$ , with  $N$  being the number of tests. Note that except the point  $[0, \tau_s]$  obtained from the pure shear test, other  $N-1$  points generally would not be on the curve expressed by Eq. (2.5).

(ii) The second trial criterion is obtained by the best fitting of the above data points,  $[\sigma_{n,j}, \tau_j]^{(1)}, j = 1, \dots, N$ , and denoted as

$$f^{(2)}(\sigma_n, \tau) = C^{(2)} \quad (2.6)$$

From the interface normal and shear stress curves, the location of the maximum value of  $f^{(2)}(\sigma_n, \tau)$  along the interface are found and the corresponding pair of normal and shear stress values are recorded for each test case. These pairs of stresses are denoted as  $[\sigma_{n,j}, \tau_j]^{(2)}, j = 1, \dots, N$ , with  $N$  being the number of tests.

(iii) The third trial criterion are obtained  $f^{(3)}(\sigma_n, \tau) = C^{(3)}$  by the best fitting of the above data points,  $[\sigma_j, \tau_j]^{(2)}, j = 1, \dots, N$ .

(iv) The steps (ii) and (iii) are repeated until converged results are obtained.

The present developed method will be illustrated in details through the application examples in Chapters 4, 5 and 6 for the elastic/elastic, elastic/viscoelastic and viscoelastic/viscoelastic bonded joints respectively.

**BIBLIOGRAPHY**

ASTM-D897, 2008. Test Method for Tensile Properties of Adhesive Bonds.

ASTM International, West Conshohocken, PA.

ASTM-D2095, 2008. Standard Test Method for Tensile Strength of Adhesives by

Means of Bar and Rod Specimens. ASTM International. ASTM

International, West Conshohocken, PA.

ASTM-D3165, 2007. Standard Test Method for Strength Properties of Adhesives

in Shear by Tension Loading of Single-Lap-Joint Laminated Assemblies.

ASTM International, West Conshohocken, PA.

ASTM-D3528, 2008. Standard Test Method for Strength Properties of Double

Lap Shear Adhesive Joints by Tension Loading. ASTM International,

West Conshohocken, PA.

Dundurs, J., 1969. Discussion of edge-bonded dissimilar orthogonal elastic

wedges under normal and shear loading. *Journal of Applied Mechanics*.

36, 650-652.

Qian, Z. Q., Akisanya, A. R., 1999. An investigation of the stress singularity near

the free edge of scarf joints. *European Journal of Mechanics A-Solids*. 18,

443-463.

## **CHAPTER 3: MATERIAL CHARACTERIZATION AND TEST SET UP**

Part of this chapter has been published as

**Chowdhuri, M. A. K.,** Xia, Z., 2010. Experimental determination of aluminum/epoxy interface bonding strength. *CSME Forum-2010*, June 7-9, Victoria, British Columbia, Canada, paper No: 13.

## CHAPTER 3

### MATERIAL CHARACTERIZATION AND TEST SET UP

---

The current Ph.D. research project involves a considerable amount of experimental work. Tensile tests are conducted to determine materials' elastic properties. To determine the viscoelastic properties, relaxation tests are carried out on the viscoelastic materials. Finally, tensile, torsional and combined tension-torsional loading tests are carried out to determine the interface bonding strength envelope. This chapter discusses about the experimental facilities and set up preparation for conducting the above experiments. The results for characterizing basic elastic or viscoelastic properties of three tested materials: aluminum, epoxy and polyvinylchloride (PVC) are presented in this chapter.

#### 3.1 EXPERIMENTAL SET UP

##### 3.1.1 Tensile and Viscoelastic Testing System

The 810 Material Testing System (MTS Systems Corporation, USA) is used for the tensile and relaxation tests. The system is shown in Figure 3.1. This system has the testing capabilities for low or high force, static or dynamic testing of materials ranging from plastics, composites to metals and alloys. By selecting from a variety of force capacities, servo valve flow ratings, pump capacities,

---

software, and accessories, the floor-standing 810 system can easily be configured to meet many specific material or component testing needs. The optional Remote Station Control (RSC) provides a convenient, portable control interface for the specimen handling and test setup. The RSC simplifies the operation of hydraulic controls. In addition to the hydraulic controls and an interlock indicator, it provides run, stop, and hold controls, a display screen and function keys, and an actuator positioning control for the specimen loading.

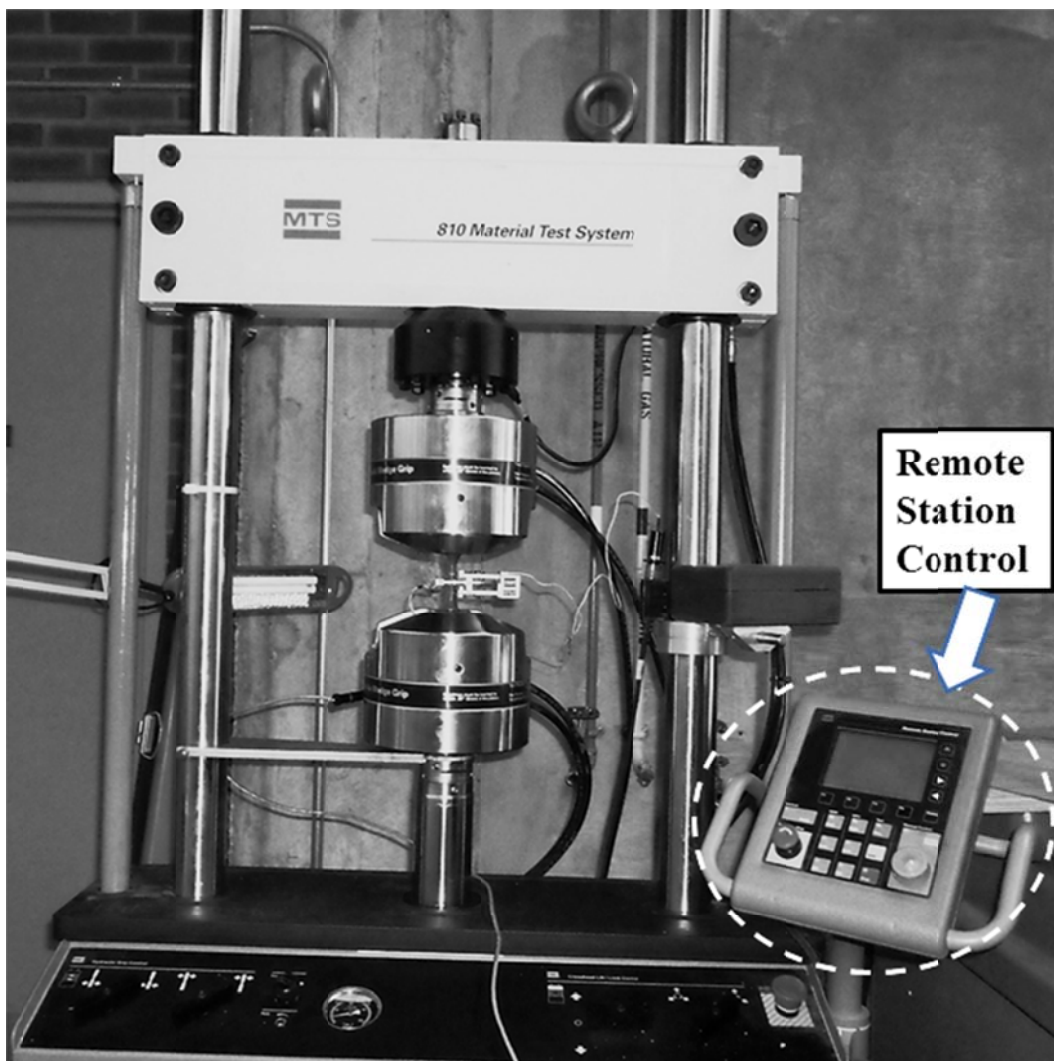


Figure 3.1: Testing machine for tensile and viscoelastic experiment

The test set up is connected to a computer loaded with MTS 793 software. Once a specimen is loaded, the transducers can be zeroed from the computer. All the required tests data are stored in a text file in the computer. Two extensometers are used to measure the displacement in the axial and transverse directions. The extensometers are shown in Figure 3.2.

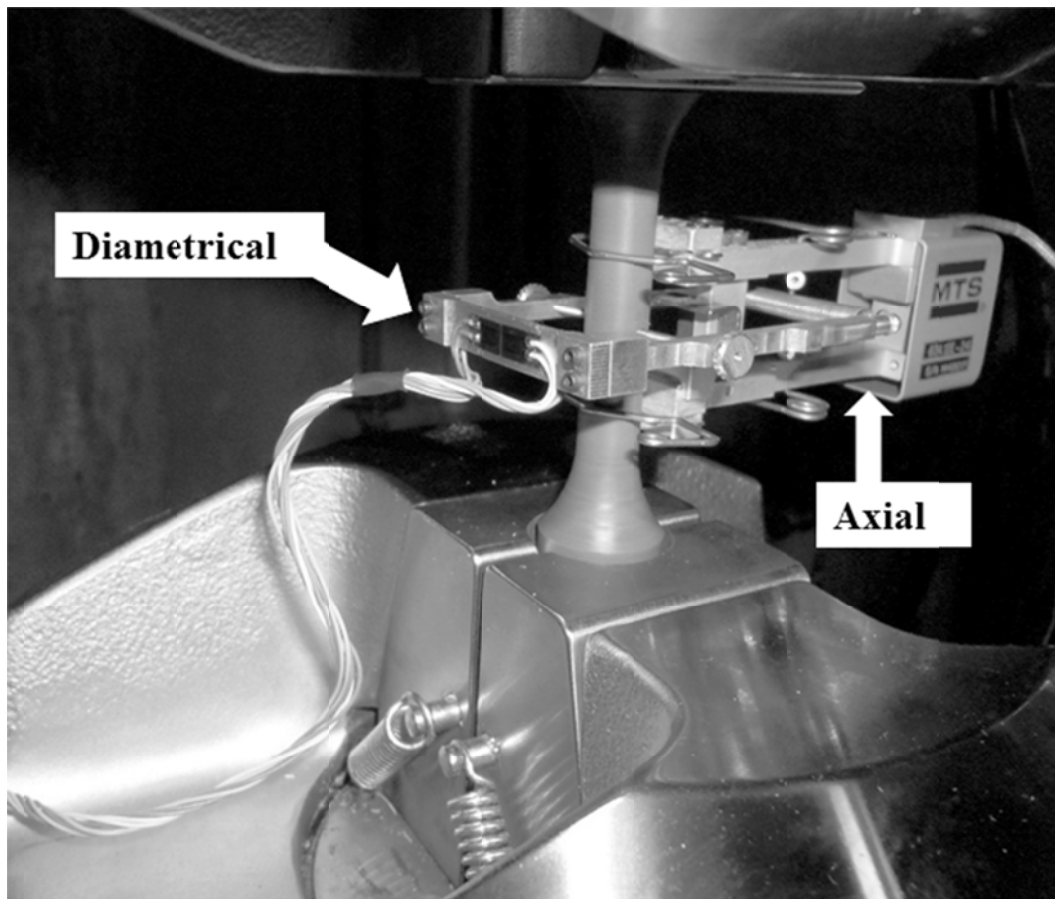


Figure 3.2: Axial and diametrical extensometers

634.11/31 Axial Extensometer, which is good for both the tensile and fatigue testing of materials, are used to record the axial displacement of the gauge length of specimen. This extensometer provides the superior performance in linearity, repeatability, hysteresis, low activation force, and ease of use. MTS' cross-flexure system ensures that the strain gages are always subjected to true center point bending, and stable clamping force. Zero set pin or zero stop provides a quick, accurate setup that is repeatable. For displacement in transverse direction another diametrical extensometer is used. Both the extensometers can acquire data with very high precision and accuracy.

### **3.1.2 Mold Design**

A new mold shown in Figure 3.3 is designed and manufactured to make the interface testing specimen. The proposed specimen is cylindrical shape with spherical interface as described in Chapter 2. The mold has two sections with different diameters. The lower portion is for the hard material part of the specimen whereas the upper portion is for the soft material. The diameter of the mold for the hard material is chosen as equal to the specimen diameter. In order to ensure a perfect bonding between these two materials, the soft material is allowed to flow over the hard material by 4mm. That's why the diameter of the mold for the soft material is also maintained 4 mm larger than that for the hard material. Later the extra portion of the soft material on the specimen is removed by machining before conducting the interface bonding strength test.

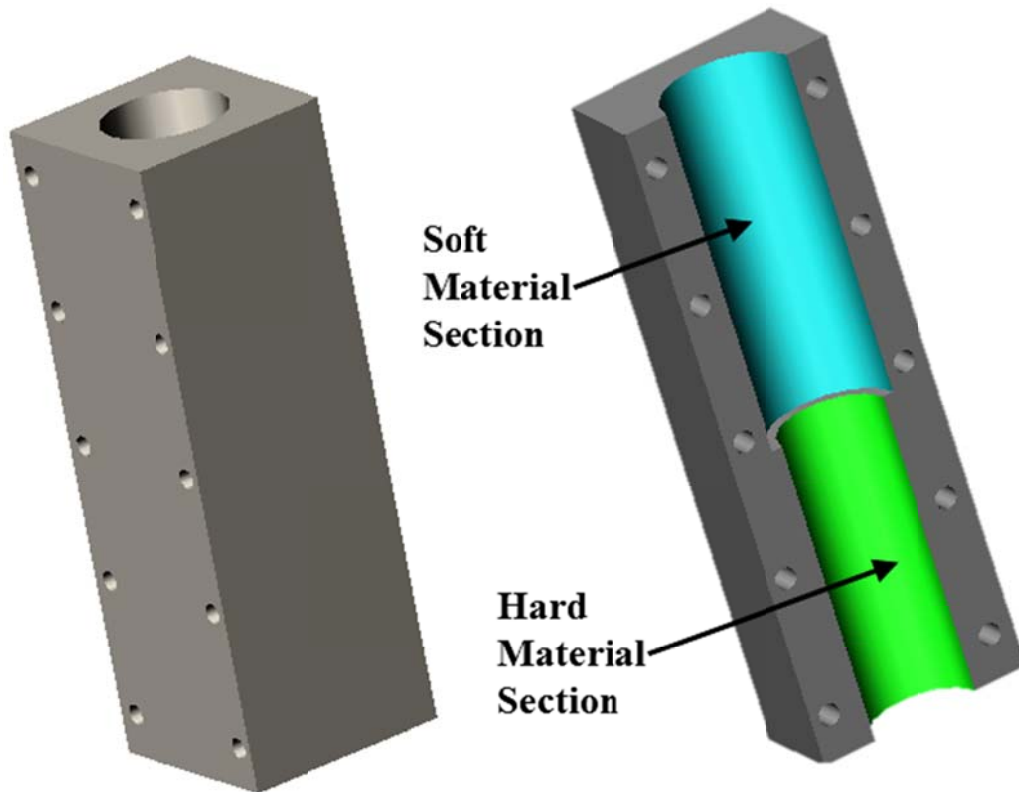


Figure 3.3: Mold for making interface testing specimen

### 3.1.3 Multi Axial Testing Machine

The multi axial testing machine shown in Figure 3.4 is used to conduct the interface strength tests. It has the capability to apply tensile, torsional and combined loads (torsion and tension). Details of the multi-axial test machine can be found in Ellyin and Wolodko (1997) and Xu (2006).

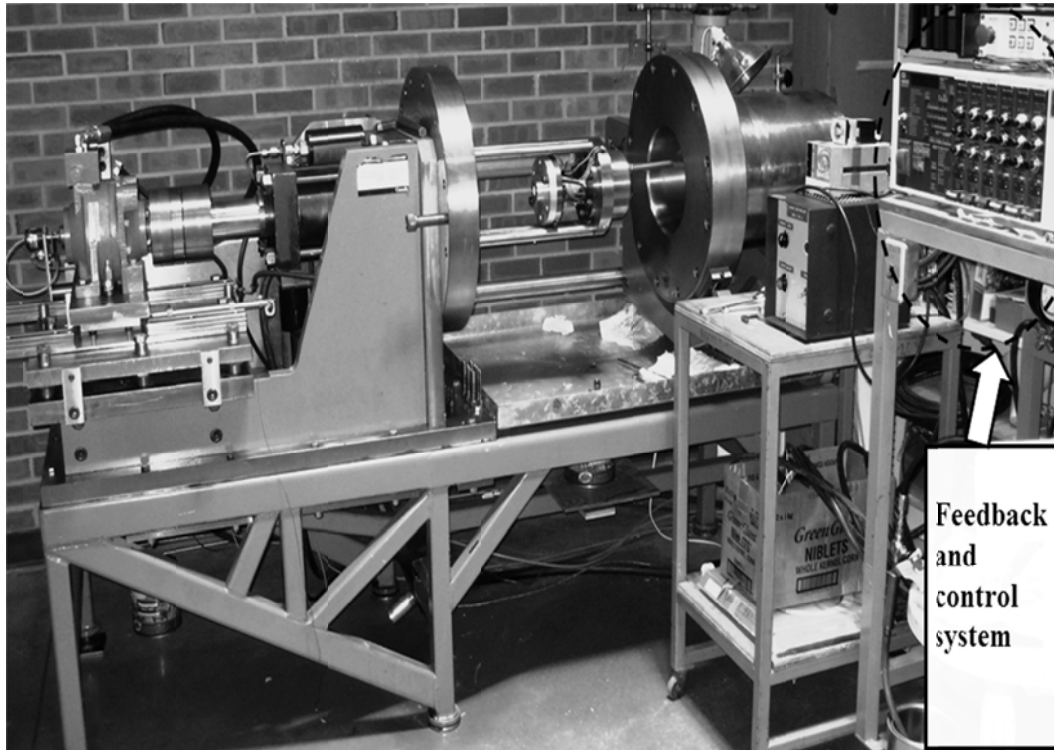


Figure 3.4: Multi axial testing machine

### 3.1.4 Grip Design

The original grips of the multi axial testing machine are too heavy for the present specimen. A new gripping system is thus designed. Figure 3.5 shows the grip design. The 3M<sup>TM</sup> Scotch-Weld<sup>TM</sup> Epoxy Adhesive DP460, which is cured in 24 hours at room temperature, is used to glue the specimen to the flange grip. The

two flanges are bolted to the machine and then the adhesive is applied to both the specimen and flanges' center holes.

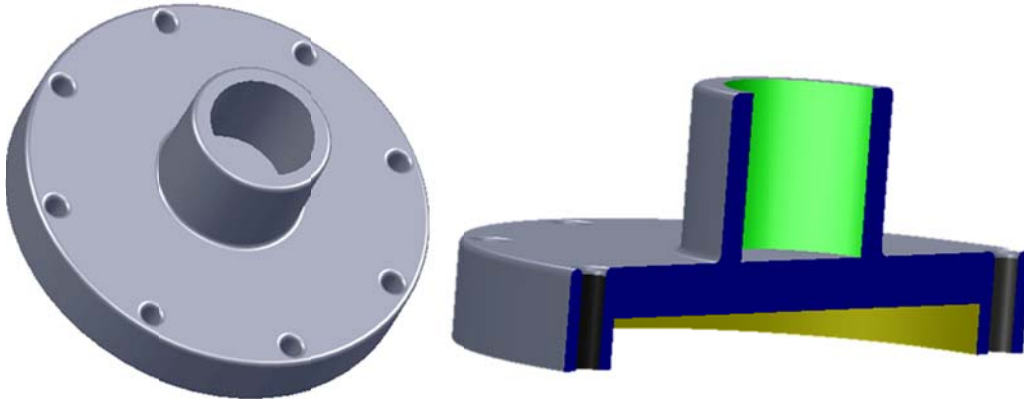


Figure 3.5: Grip to hold the interface testing specimen in multi-axial machine

The length of the adhesive area is one of the key factors to be considered in designing the grip system. For fixed dimensions ' $D$ ' and ' $d$ ' in Figure 3.6, glue length ' $l$ ' can be calculated to ensure that the strength of the adhesion between the grips and the specimen is much greater than the strength of the interface.

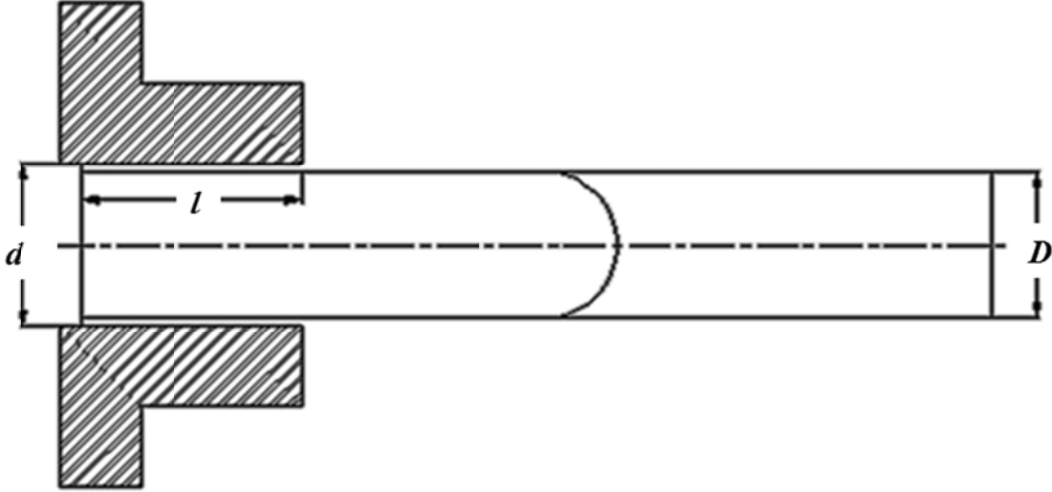


Figure 3.6: Grip dimension to calculate glue length

For torsional load, the maximum torque the grip can transfer is

$$M_{grip}^{ult} = \tau_{glue}^{ult} \pi d l \cdot \frac{d}{2} = \frac{\pi}{2} \tau_{glue}^{ult} d^2 l \quad , \quad \text{where } \tau_{glue}^{ult} \text{ is the glue's maximum shear}$$

strength.

The torque at the interface

$$M_{int}^{ult} = \frac{\pi \tau_{bond}^{ult} D^3}{16}$$

So the condition to be satisfied is,

$$M_{grip}^{ult} > M_{int}^{ult}$$

$$\text{Or, } \frac{\pi}{2} \tau_{glue}^{ult} d^2 l > \frac{\pi \tau_{int}^{ult} D^3}{16}$$

Epoxy is used as the soft material in this research. The adhesive's shear strength is higher than that of the epoxy material. Considering epoxy's shear strength in both sides, the above condition becomes

$$l > \frac{D^3}{8d^2}$$

By conducting a similar analysis for tensile loading, the condition becomes

$$l > \frac{D^2}{2.8d}$$

So, the glue length should be

$$l > \max\left(\frac{D^3}{8d^2}, \frac{D^2}{2.8d}\right)$$

Considering  $d = 20.5$  mm and  $D = 20$  mm, the glue length is obtained as  $l \approx 7$  mm

Considering the factor of safety the glue length is designed as 30 mm.

The grip design described above is excellent for maintaining perfect alignment of the specimen in the testing machine. However, the main disadvantage of the grip is the amount of time required for conducting the test, as the adhesive/glue takes 24 hours to be completely cured. To overcome this limitation a modified grip ER 32 system shown in Figure 3.7 is designed. The base of the grip is a large plate with 6 bolt holes, which is used to mount the grip securely to the test machine. The back of the plate has a 0.08 inch flat circular indentation concentric with the base plate. The extended cylindrical portion of the base plate is for an ER 32 collet. The internal wall of the collet mount is tapered at  $8^\circ$  to facilitate collet closure. Furthermore, the outer surface of the collet mount is

threaded with M40x1.5 to accommodate an ER 32 collet nut. During operation, an ER 32 collet is inserted into the cavity of the collet mount, followed by the test specimen into the collet. An ER 32 collet nut is then screwed over top of the original collet, which is then tightened using a matching collet wrench to tighten the collet around the specimen.



Figure 3.7: Modified grip to hold the interface testing specimen

However, this modified grip system served well for the specimen made from elastic materials. This grip cannot hold the viscoelastic materials for a long time because of the creep/relaxation properties of the viscoelastic materials. This problem has been overcome by attaching a tapered aluminum end cap at the viscoelastic end/ends of the specimen.

## 3.2 MATERIAL TESTING

### 3.2.1 Materials Selection

Three different materials are used in this research. These materials are selected based on their applicability, availability, machinability and low cost. The selected materials are aluminum, epoxy and polyvinylchloride (PVC). Aluminum and epoxy are used for the determination of the interface bonding strength between two elastic materials. Epoxy is a viscoelastic polymer and its properties are time and loading-rate dependent. It is assumed that the properties of a viscoelastic material obtained with a very fast loading rate can be considered as the elastic properties of the material. To find the effect of material's viscoelasticity on the interface bonding strength, the same materials combination (Aluminum/Epoxy) is used to determine the interface bonding strength between elastic and viscoelastic materials. For the viscoelastic/viscoelastic interface, PVC and epoxy are used as the hard and soft materials. Short descriptions on the selected materials are given below.

#### **Aluminum**

Aluminum is frequently observed in many engineering applications. They are used in transportation, automobiles, airplanes, household objects, including a varied assortment of utensils etc. They are commercially available in different sizes and shapes. The advantages of aluminum are light weight, corrosion

resistant, good machinability, ductility, and good electrical and thermal conductivity.

### **Epoxy**

Among the various types of polymers, the use of epoxy is extensive. Epoxy is a thermosetting copolymer; generally formed from two different chemicals: resin and hardener. Epoxies have excellent adhesion, chemical and heat resistance, good mechanical and electrical insulating properties. Another advantage of the epoxy material is that the properties of epoxy can be modified. The applications of epoxy-based materials include coatings, adhesives and composite materials. Epoxy adhesives are used in the construction of aircraft, automobiles, bicycles, boats, golf clubs, skis, snowboards and the rotor blades of wind turbines etc.

### **PVC**

The use of PVC (polyvinylchloride) is also very common. PVC is a thermoplastic vinyl polymer. The structure of PVC is  $(-\text{CH}_2-\text{CHCl}-)_n$ , which is similar to the polyethylene, except that, on every other carbon in the backbone chain, one hydrogen atom is replaced by a chlorine atom. PVC is a very popular polymer because of its excellent corrosion resistance, weather resistance, low moisture absorption, good dimensional strength and low cost as well. It also has a high strength-to-weight ratio and good electrical and thermal insulating properties. Specific applications of PVC include nuts, filters, signs, tanks, pipes,

bolts, valves, bushings, tank, ducts, sprinkler systems, pump parts and fittings, etc.

### **3.2.2 Determination of the Elastic Properties of Materials**

All the materials used in this research are considered to be isotropic and homogeneous. Thus, in order to characterize the elastic materials, only two properties; elastic modulus and Poisson's ratio are necessary. Elastic modulus is the ratio of the stress to the strain up to the proportional limit and elastic Poisson's ratio is defined as the negative ratio of the transverse strain to the axial strain in the above limit. These properties are determined by the uni-axial tensile tests with very fast loading rate in the MTS testing machine shown in Figure 3.1.

The elastic properties of aluminum are determined according to the ASTM B557 (2010) standard method. The cylindrical specimens are prepared from a commercial Al6061-T6 aluminum rod by machining on a computer numerical controlled (CNC) lathe. Tensile loading is applied on the test specimen and the axial and radial displacements are measured by the axial and diametrical extensometer as shown in Figure 3.2. The stress-strain and the transverse strain-axial strain relations of aluminum are shown in Figures 3.8 and 3.9, respectively. From the proportional portion of these two curves, the elastic modulus and Poisson's ratio of aluminum are determined as 71 GPa and 0.3 respectively.

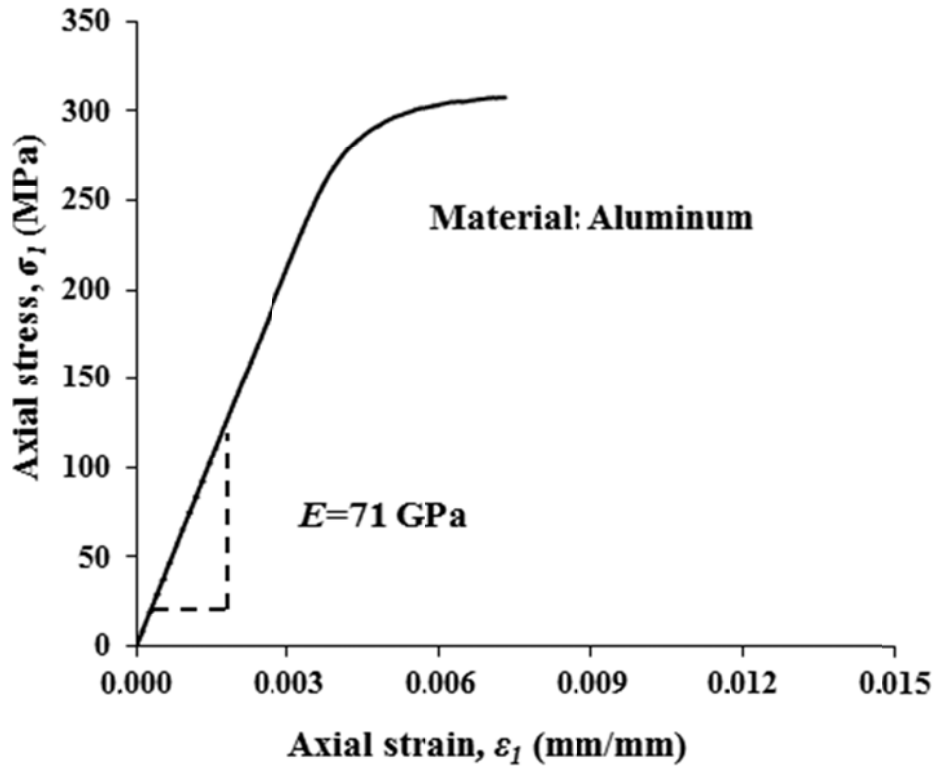


Figure 3.8: Stress- strain curve for aluminum

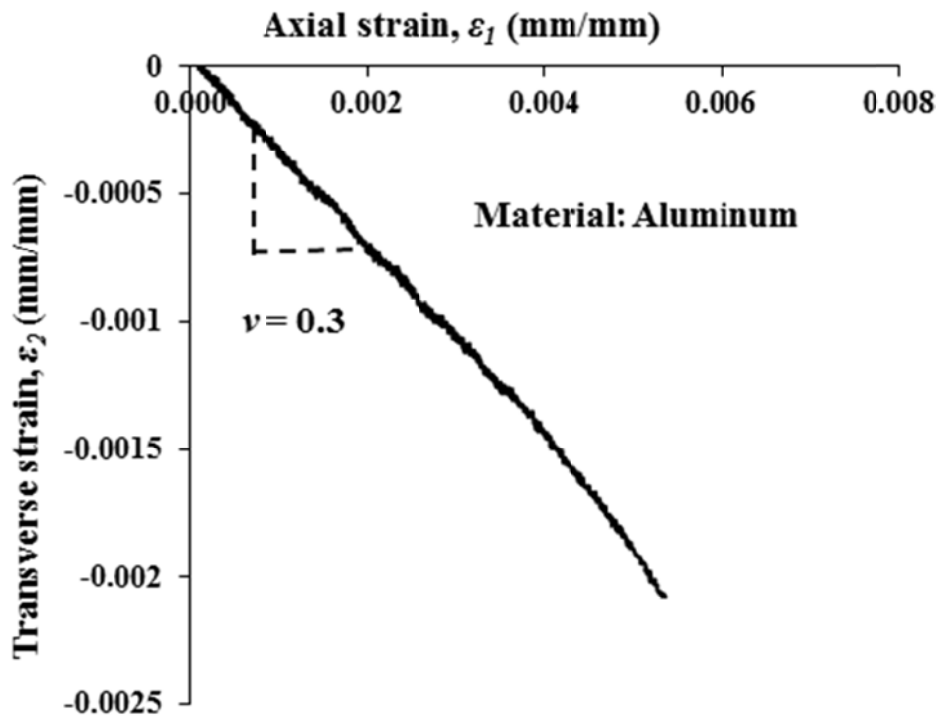


Figure 3.9: Determination of Poisson's ratio for aluminum

The specimens for the determination of elastic properties of epoxy and PVC are designed according to Shen (2004). The specimen design is shown in Figure 3.10.

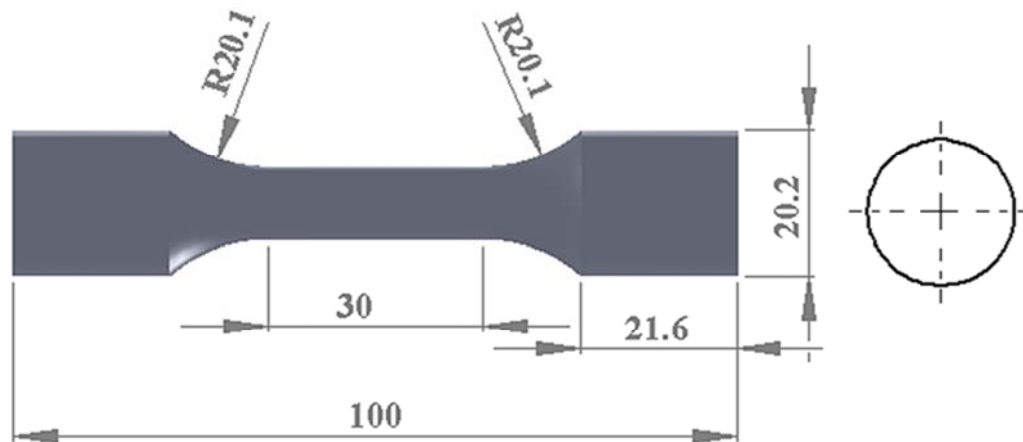


Figure 3.10: Tension test specimen for epoxy and PVC

Epoxy specimens are prepared from EPON 8131 resin and EPI-CURE 3072 hardener. EPON 8131 and EPI-CURE 3072 have less shrinkage rate and greatly reduce the residual stress building up in the specimen. In addition, the EPON 8131 is a flexibilized, 100 percent reactive, low viscosity epoxy resin and widely used in various applications such as concrete patching/resurfacing, reinforced plastics, adhesive and encapsulation. Both the resin and hardener are purchased from Momentive Specialty Chemicals Inc. (Formerly known as Hexion Specialty Chemicals Inc.) ([www.momentive.com](http://www.momentive.com)). The resin and hardener are mixed at 79 to 21 proportions by weight. According to the product data sheet, the

mixture has been left two weeks for complete curing at room temperature. The cured specimens are machined to make the desired size for the experiment on a computer numerical controlled (CNC) lathe that provides the precise machining of any transition profile geometry. The stress-strain and the transverse strain-axial strain curves of the epoxy are shown in Figures 3.11 and 3.12, respectively. From the proportional limit portion of the two curves, the elastic modulus and Poisson's ratio of epoxy are determined as 1271 MPa and 0.415 respectively.

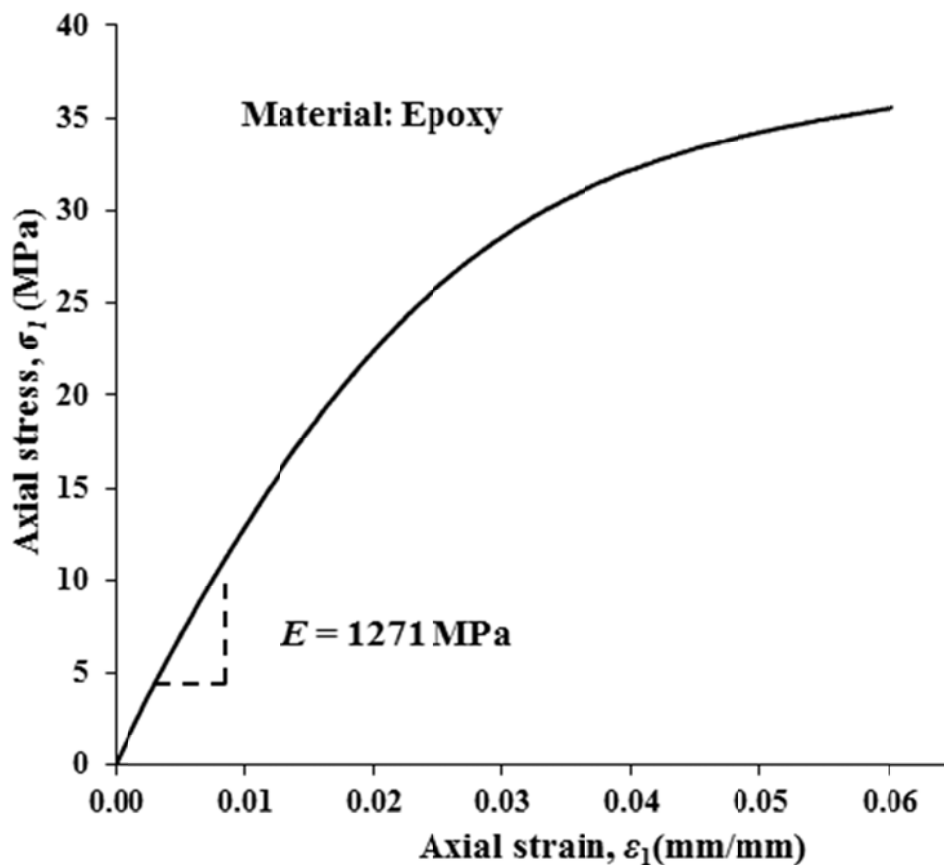


Figure 3.11: Stress- strain curve for epoxy

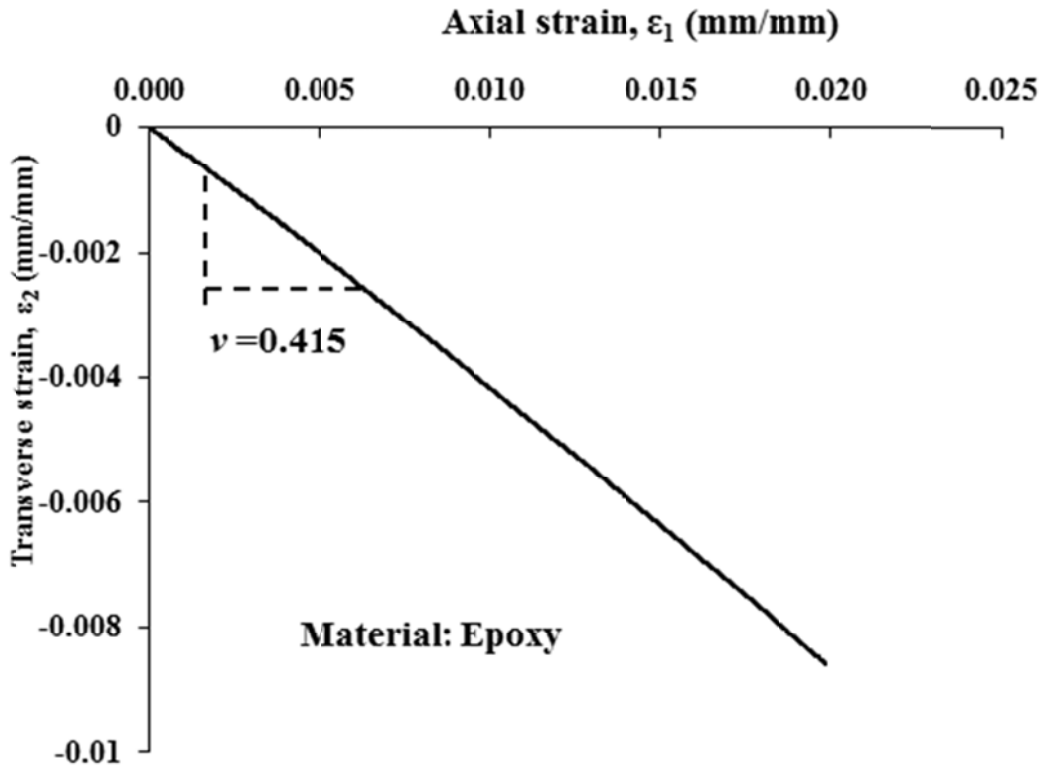


Figure 3.12: Determination of Poisson's ratio for epoxy

PVC is available as sheets, rods, and tubing of many sizes. The specimens for the properties determination of PVC are manufactured on a computer numerical controlled (CNC) lathe from commercial PVC rod (rigid) of diameter 22.22 mm purchased from Johnston Industrial Plastics Ltd ([www.johnstonplastics.com](http://www.johnstonplastics.com)). The specimen and its detail dimensions are shown in Figure 3.10.

The stress-strain and the transverse strain-axial strain curves of the PVC are shown in Figures 3.13 and 3.14 respectively. From the proportional limit portion of the two curves the elastic modulus and Poisson's ratio are determined as 3.38 GPa and 0.362, respectively.

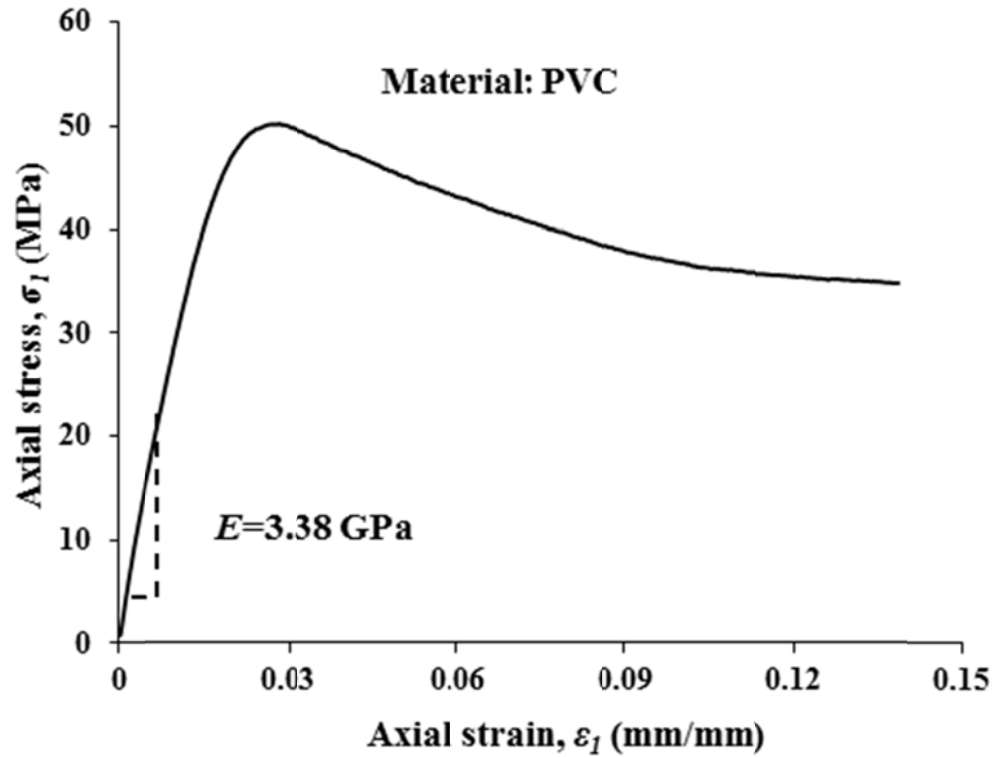


Figure 3.13: Stress- Strain curve for PVC

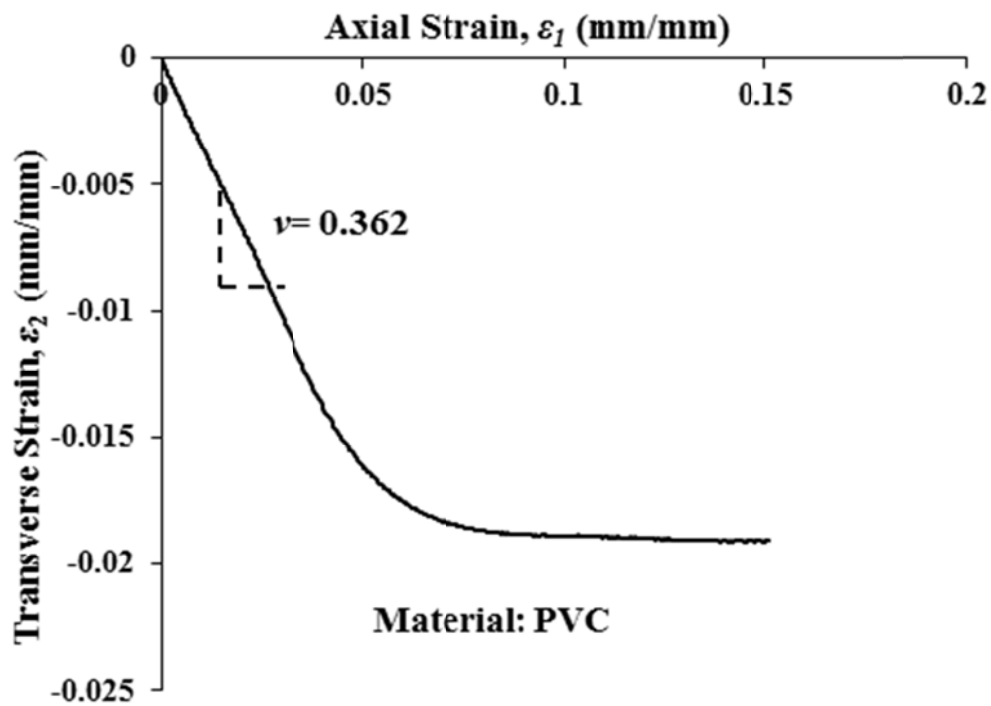


Figure 3.14: Determination of Poisson's ratio for PVC

### 3.2.3 Determination of the Viscoelastic Properties of Materials

Owing to the wide use of polymeric materials, there is a growing need of predicting the mechanical behavior of polymers under general loading conditions (Hu et al., 2003). Viscoelasticity has been primarily focused due to the large scale development and utilization of polymeric materials. Most of the polymeric materials have viscoelastic properties. They possess the capacity of both storing and dissipation of mechanical energy. In many applications, polymers are reinforced with harder material phases such as fibers, ceramic particles, etc. Thus viscoelastic characterization of polymeric materials is extremely important. The time and rate dependent material properties of viscoelastic materials are not readily available in material data handbooks. It is, therefore, necessary to perform one or more of the experimental tests to determine the fundamental properties of these materials (Kim et al., 2010).

To describe the stress and strain states of any linear viscoelastic material, four basic material functions—Poisson's ratio, uniaxial relaxation modulus, shear modulus and bulk modulus are necessary. Similar to the case of an isotropic elastic material, if only two of the above properties can be determined, the remaining two can be calculated. This is referred to as the inter conversion of material functions. Hence, two material functions are often enough for the complete description of the mechanical behavior of linear viscoelastic materials (Tscharnuter et al. 2011). In theory, the choice of the two material functions is arbitrary, but in practice there are limitations that must be considered.

Tschoegl et al. (2002) indicated that in order to avoid excessive errors caused by specimen-to-specimen or environmental variations, the measurement of a pair of viscoelastic material functions must be performed simultaneously on the same specimen. The simultaneous measurement of two material functions is possible in a confined compression setup (Qvale and Ravi-Chandar, 2004; Jerabek et al., 2010a) or a uniaxial relaxation test when the axial and lateral strains are measured (Jerabek et al., 2010b). The former yields the bulk and the shear relaxation moduli, whereas, the latter provides the uniaxial relaxation modulus and Poisson's ratio. Tscharnuter et al. (2011) further suggest that the uniaxial stress relaxation test is a standard method to characterize the viscoelastic materials over the elaborate confined compression test. During the relaxation test, axial and hoop strains can be determined directly using two strain gauges along with the axial stress. In that case, the viscoelastic relaxation modulus and Poisson's ratio can be determined easily and simultaneously.

### 3.2.3.1 *Linear viscoelastic stress-strain relation*

According to the theory of liner viscoelasticity (Christensen, 1982), the time dependent stress,  $\sigma(t)$  of any viscoelastic material can be expressed as,

$$\sigma_{ij}(t) = \delta_{ij} \int_{-\infty}^t \lambda(t-\tau) \frac{\partial \varepsilon_{kk}(\tau)}{\partial \tau} d\tau + 2 \int_{-\infty}^t \mu(t-\tau) \frac{\partial \varepsilon_{ij}(\tau)}{\partial \tau} d\tau \quad (3.1)$$

where,  $\lambda(t) = \frac{2\mu(t) \times \nu(t)}{1 - 2\nu(t)}$  ;  $\mu(t)$  and  $\nu(t)$  are the viscoelastic shear modulus and

Poisson's ratio respectively.

For simple uniaxial extension, the above equation can be deduced to

$$\sigma(t) = \frac{\varepsilon}{2} \left[ \mu(t) + \int_{-\infty}^t \mu(t-\tau) \nu(\tau) d\tau \right]$$

or, 
$$\sigma(t) = \varepsilon(t) * G(t) \quad (3.2)$$

The time dependent stress,  $\sigma(t)$  of a viscoelastic material subjected to the unit step constant strain,  $\varepsilon_0$  can be expressed as

$$\sigma(t) = G(t) \times \varepsilon_0 \quad (3.3)$$

where,  $G(t)$  is the relaxation modulus, which is also a function of the loading time.

The time-dependent Poisson's ratio,  $\nu(t)$  of a linearly isotropic viscoelastic material can be defined as the time-dependent ratio of the transverse/lateral strain,  $\varepsilon_2(t)$ , to the axial step constant strain  $\varepsilon_0$  (Tschoegl et al. 2002).

$$\nu(t) = -\frac{\varepsilon_2(t)}{\varepsilon_0} \quad (3.4)$$

From Equation (3.4) it is quite clear that the viscoelastic Poisson's ratio should be determined by a uniaxial relaxation test in which the strain in the axial direction is maintained as constant.

### 3.2.3.2 *Experimental Procedures*

For the relaxation test of epoxy 4% axial strain is attained within a very short time and then the strain is held for about one and half hour. During this period, time, load, axial strain and transverse strain are recorded in every second. From the measured data, the relaxation modulus and viscoelastic Poisson's ratio

of the epoxy are determined using Equations (3.3) and (3.4). The axial strain, axial stress, relaxation modulus and Poisson's ratio of epoxy obtained from the relaxation test are shown in Figures 3.15 to 3.18. The properties equal to the elastic properties of epoxy are considered as the viscoelastic properties of the epoxy at time  $t = 0$ .

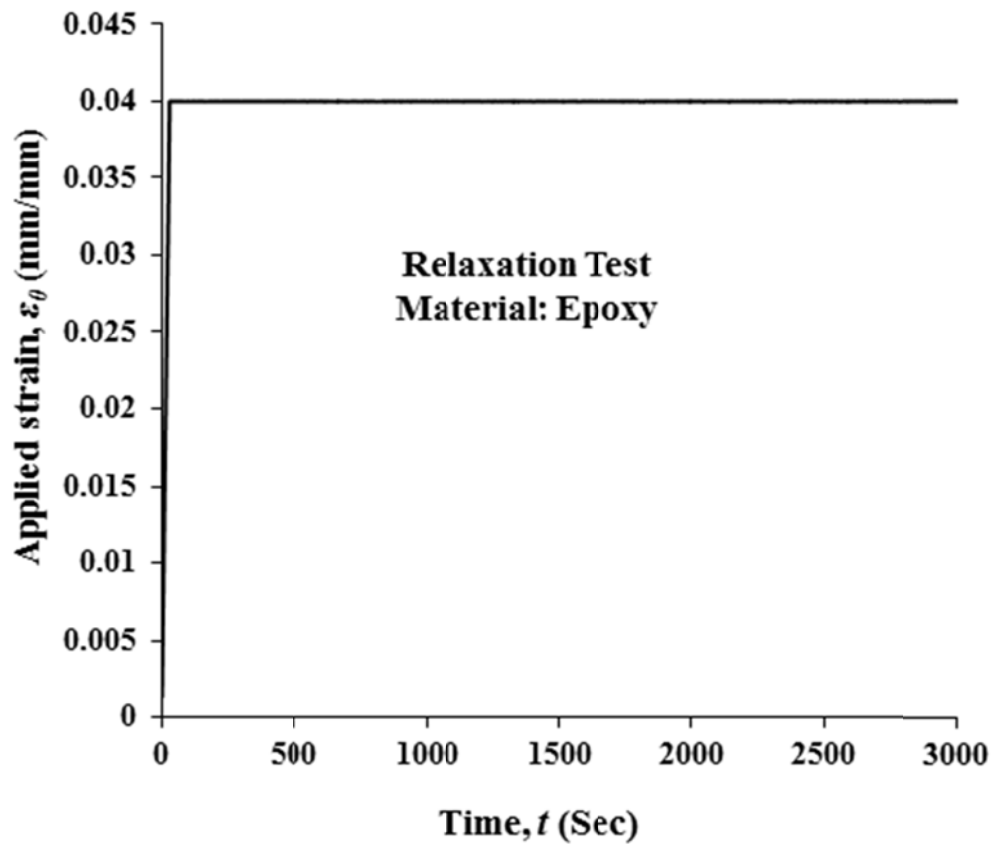


Figure 3.15: Applied axial strain in relaxation test of epoxy

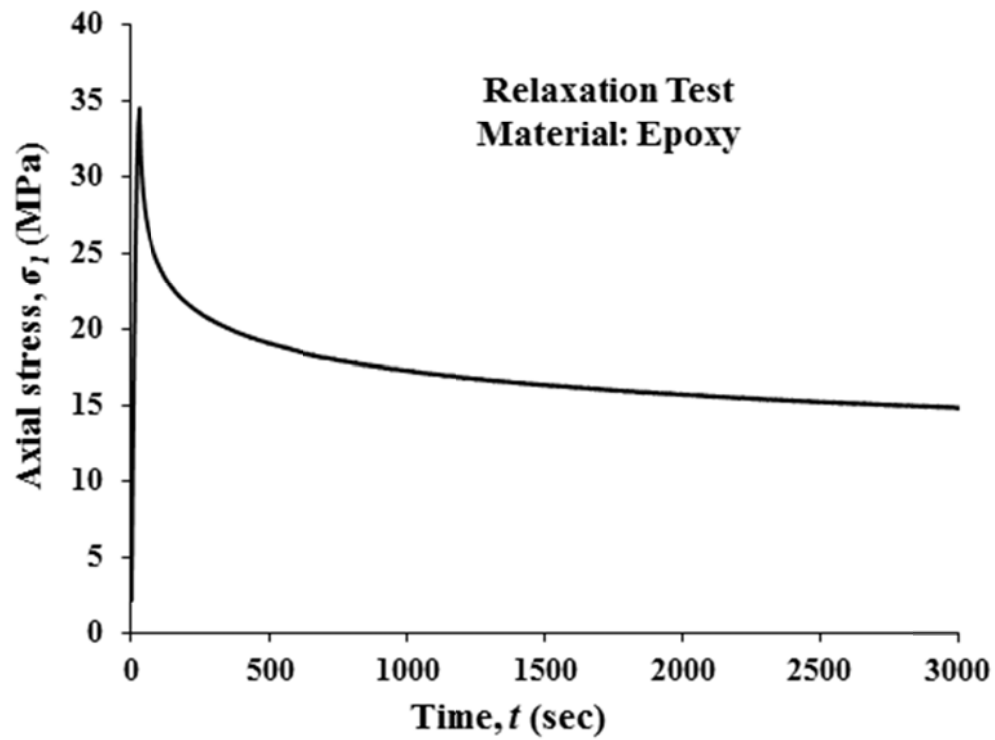


Figure 3.16: Measured axial stress in relaxation test of epoxy

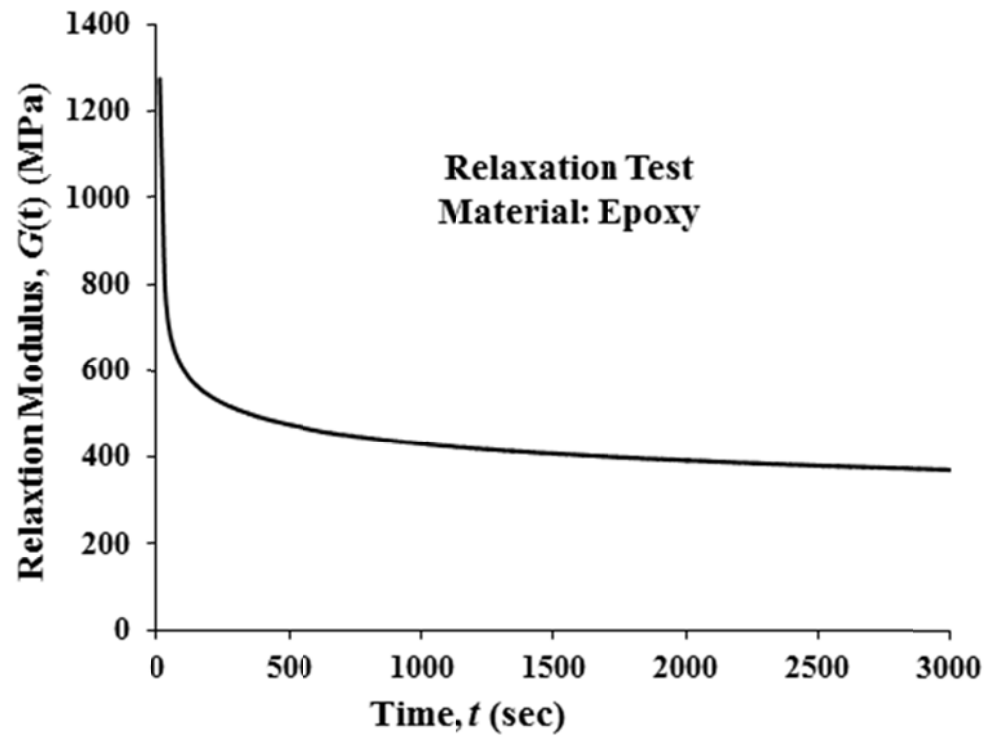


Figure 3.17: Relaxation modulus of epoxy

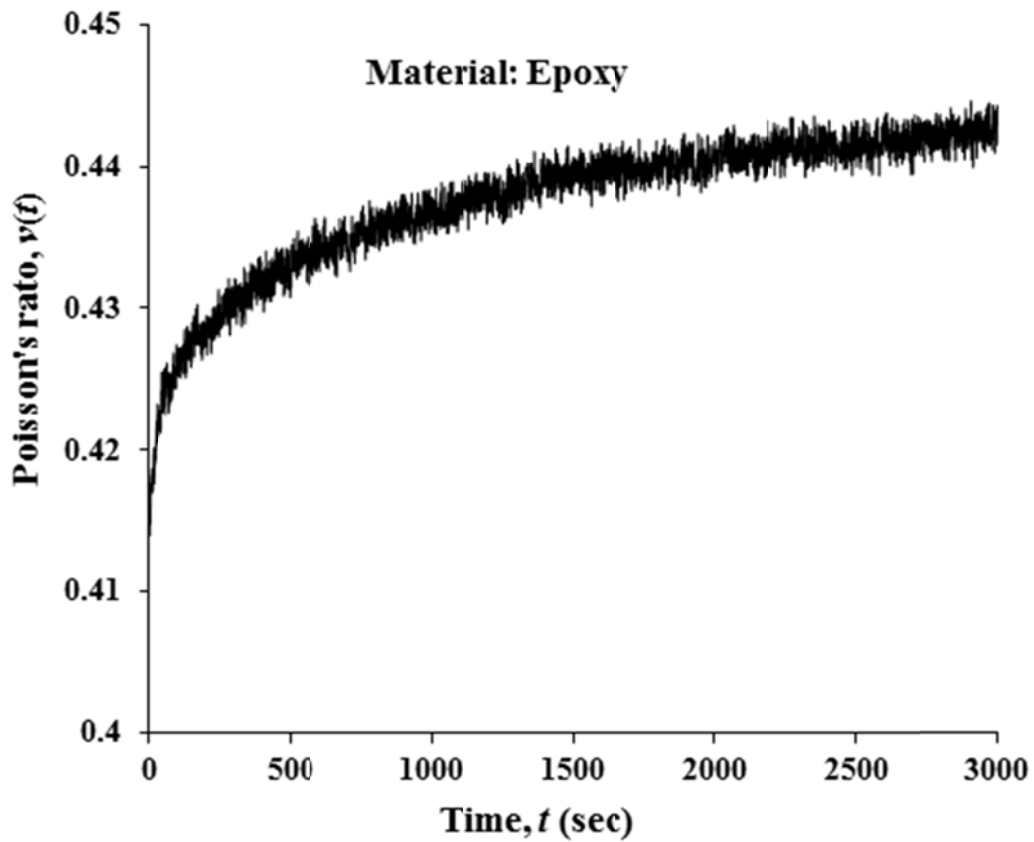


Figure 3.18: Viscoelastic Poisson's ratio of epoxy

Similarly, for the relaxation test of PVC, 1.04% axial strain is attended within a very short time and then it is hold for about one and half hour. During this period time, load, axial strain and transverse strain are recorded in every second. The axial strain, axial stress, relaxation modulus and Poisson's ratio of PVC obtained from the relaxation test are shown in Figures 3.19 to 3.22.

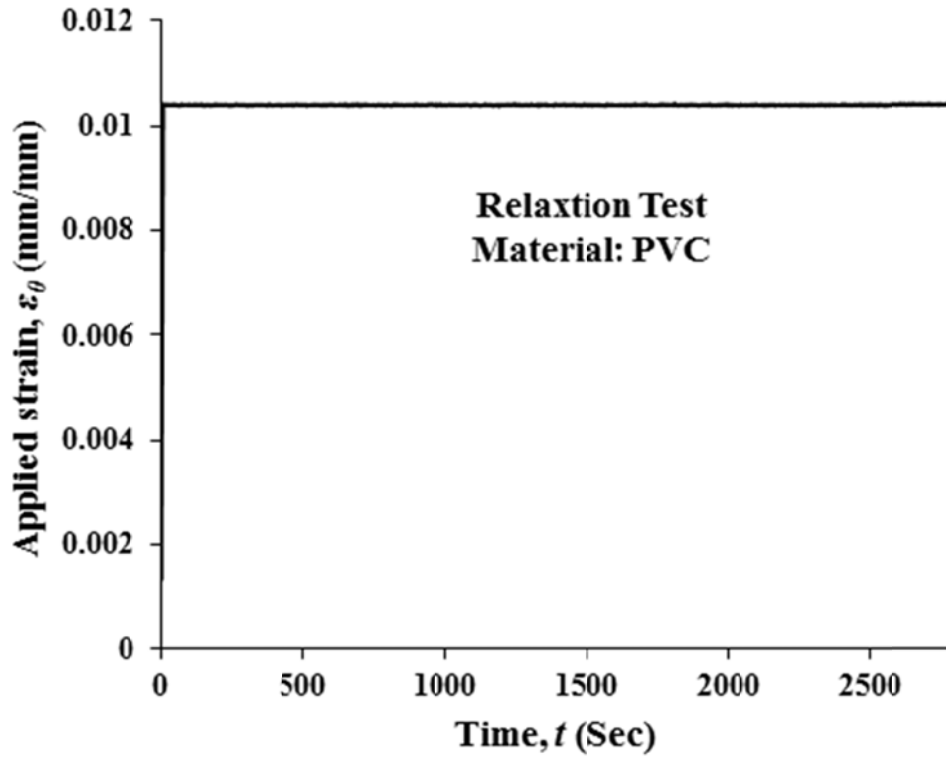


Figure 3.19: Applied axial strain in relaxation test of PVC

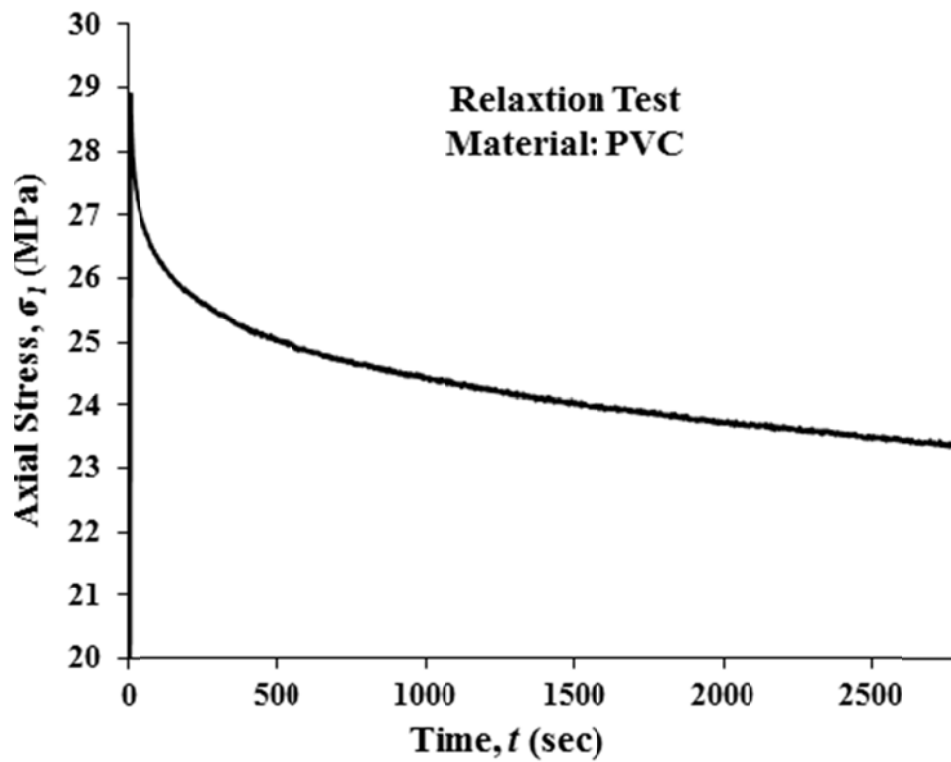


Figure 3.20: Measured axial stress in the relaxation test of PVC

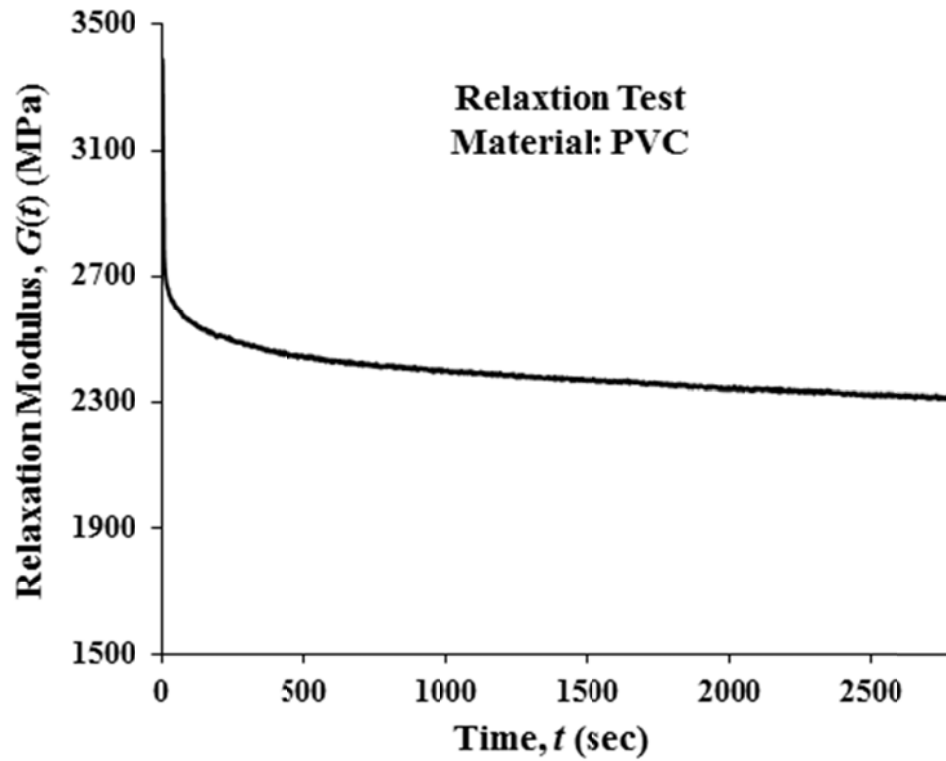


Figure 3.21: Relaxation modulus of PVC

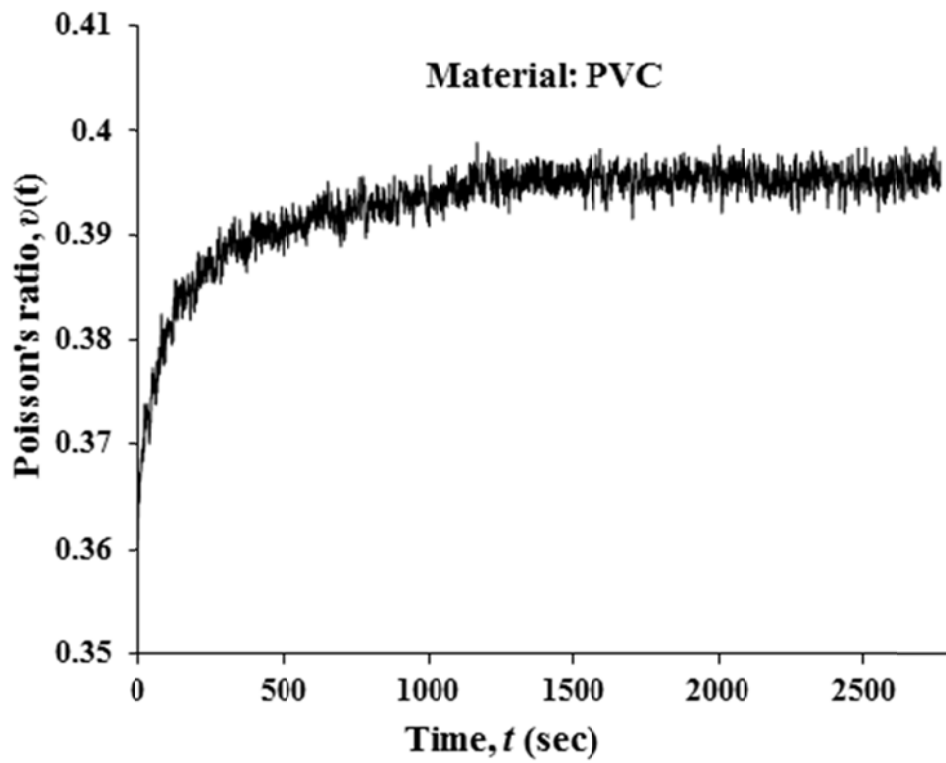


Figure 3.22: Viscoelastic Poisson's ratio of PVC

**BIBLIOGRAPHY**

ASTM-B557, 2010. Standard Test Methods for Tension Testing Wrought and Cast Aluminum and Magnesium-Alloy Products. ASTM International, West Conshohocken, PA.

Christensen, R. M., 1982. Theory of viscoelasticity: An introduction. second edition, Academic press, New York.

Ellyin, F., Wolodko, J. D., 1997. Testing facilities for multi-axial loading of tubular specimen. ASTM STP 1280, 7-24.

Hu, Y., Xia, Z., Ellyin, F., 2003. Deformation behavior of an epoxy resin subject to multiaxial Loadings. Part I: Experimental investigations. Polymer Engineering and Science. 43(3), 721-733.

Jerabek, M., Tscharnuter, D., Major, Z., Ravi-Chandar, K., Lang, R.W., 2010a. Relaxation behavior of neat and particulate filled polypropylene in uniaxial and multiaxial compression. Mechanics of Time-Dependent Materials. 14(1), 47-68.

Jerabek, M., Major, Z., Lang, R. W., 2010b. Strain determination of polymeric materials using digital image correlation. Polymer Testing. 29(3), 407-416.

- Kim, J., Lee, H. S., Kim, N., 2010. Determination of shear and bulk moduli of viscoelastic solids from the indirect tension creep test. *Journal of Engineering Mechanics*. 136(9), 1067-1075.
- MTS Systems Corporation, 14000 Technology Drive, Eden Prairie, MN 55344-2290 USA, [www.mts.com](http://www.mts.com)
- Qvale, D., Ravi-Chandar, K. 2004. Viscoelastic characterization of polymers under multiaxial compression. *Mechanics of Time-Dependent Materials*. 8(3), 193–214.
- Shen, X., Xia, Z., Ellyin, F., 2004. Cyclic deformation behavior of an Epoxy Polymer. Part 1: Experimental Investigation. *Polymer Engineering and Science*, 44 (12), 2240-2246.
- Tscharnutter, D., Jerabek, M., Major, Z., Lang, RW, 2011. Time-dependent poisson's ratio of polypropylene compounds for various strain histories. *Mechanics of Time-Dependent Materials*. 15(1), 15-28.
- Tschoegl, NW, Knauss, W., Emri, I., 2002. Poisson's ratio in linear viscoelasticity - a critical review. *Mechanics of Time-Dependent Materials*. 6(1), 3–51.
- Xu, K., 2006. Experimental Study on Biaxial Normal-Shear interface Bonding Strength between E-glass and Epoxy Polymer. M.Sc Thesis, University of Alberta, Canada.

## CHAPTER 4: ELASTIC/ELASTIC BI-MATERIAL INTERFACE

Part of this chapter has been accepted / published as

1. **Chowdhuri, M. A. K.,** Xia, Z., 2011. An Innovative Method to Determine Bonding Strength Envelope Based on Theory of Bi-Material Interface Mechanics. *Procedia Engineering*, 10, 118-123
2. Xia, Z., **Chowdhuri, M. A. K.,** Ju, F., 2012. A New Test Method for Measurement of Biaxial Normal-Shear Bonding Strength at Bi-material Interface. *Mechanics of Advanced Materials and Structures* DOI: 10.1080/15376494.2011.643278 (In press).
3. **Chowdhuri, M. A. K.,** Xia, Z., 2012. Theory and Experimental Method to Determine Bi-Material Interface Bonding Strength. *International Journal of Structural Integrity* (Accepted).

## CHAPTER 4

### ELASTIC/ELASTIC BI-MATERIAL INTERFACE

---

This chapter discusses about the determination of the interface bonding strength of an elastic/elastic bonded joint by the developed method. Aluminum and epoxy are chosen for the interface constituent materials. Both materials are assumed to be elastic and isotropic.

#### 4.1 SPECIMEN DESIGN

A cylindrical specimen of aluminum and epoxy with a spherical interface is designed as shown in Figure 2.1 (in Chapter 2). The epoxy (material 2) is at the convex side of the interface, while the aluminum (material 1) is at the concave side of the interface. The elastic material properties of aluminum and epoxy are determined in Chapter 3 and given below in Table 4.1.

Table 4.1: Material properties of aluminum and epoxy

	<b>Aluminum</b>	<b>Epoxy</b>
Elastic Modulus	71 GPa	1271 MPa
Poisson's Ratio	0.3	0.415

---

## 4.2 DETERMINATION OF THE STRESS SINGULARITY AND CRITICAL BONDING ANGLE

### 4.2.1 Determination of the critical bonding angle by analytical method

The axi-symmetric model of the developed specimen shown in Chapter 2 (Fig 2.1) is shown in Figure 4.1. The radius of the spherical interface is “ $a$ ”, the radius of the specimen is  $R$  and the bonding angle is  $\theta_0$ .

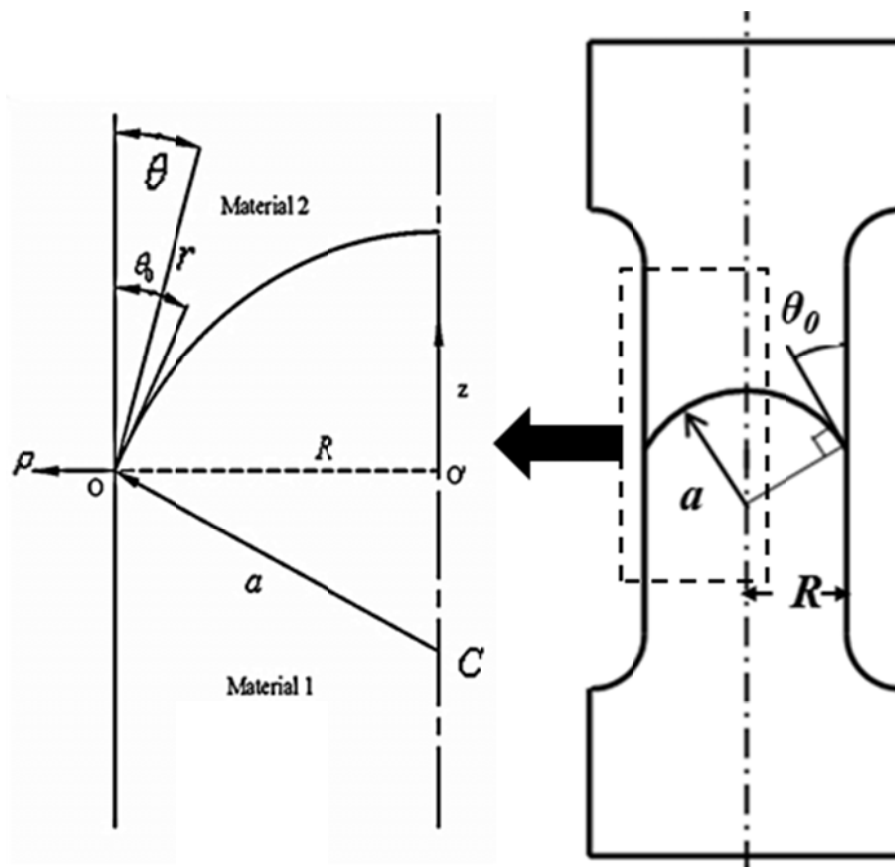


Figure 4.1: Axi-symmetric model of the developed bi-material interface

Bogy(1971); Akisanya and Fleck (1997) and Lauke et al. (2003) represented the stress and displacement fields for a straight interface edge near the singular point as follows;

$$\sigma(r, \lambda, \theta) = Hr^{\lambda-1} f(\lambda, \theta) \quad (4.1)$$

$$U(r, \lambda, \theta) = Hr^{\lambda} f(\lambda, \theta) \quad (4.2)$$

where  $(r, \theta)$  are the polar coordinates from the edge point of the interface.

For the curved interface the above representation of the stress and displacement fields can still be used. By using Taylor series expansion, the stress functions near the edge point can be expressed as,

$$\sigma(r, \lambda, \phi) = \sigma(r, \lambda, \theta_0) + (r/a)\sigma'(r, \lambda, \theta_0) + \frac{1}{2}(r/a)^2\sigma''(r, \lambda, \theta_0) + \dots \quad (4.3a)$$

$$U(r, \lambda, \phi) = U(r, \lambda, \theta_0) + (r/a)U'(r, \lambda, \theta_0) + \frac{1}{2}(r/a)^2U''(r, \lambda, \theta_0) + \dots \quad (4.3b)$$

Perlman and Sih (1967); and Aksentain (1967) have shown that the order of the singularity in the vicinity of the curved edge is to be the same as that in the two-dimensional plane wedge problem. Later, Ting (1985) repeated the same comment while studying the stress distribution at the apex of a two-dimensional curved wedge using axi-symmetric analysis. He concluded that the additional terms from the curved interface changes the form of the eigen functions only.

From the above discussion, it is clear that though additional terms are present in Equation (4.3a) due to the curved interface, to find the order of the stress singularity, consideration of the first term in Equation (4.3a) is quite enough. Thus, the problem leads to finding of the dependence of order of the

singularity on the edge angle  $\theta_0$ , which is defined as the bonding angle for the spherical bi-material interface studied.

Let consider the  $z$ -axis as the axi-symmetric axis,  $\rho$  is the radial direction and  $R$  is the radius of the cylindrical specimen (Fig. 4.1). Using the elasticity theory (Timoshenko and Goodier, 1951), the displacement and stress components in cylindrical coordinates  $(\rho, \psi, z)$  can be represented in terms of two harmonic functions  $\phi_1(\rho, z)$  and  $\phi_2(\rho, z)$ . At the same time the following compatibility equation (Equation 4.4) should be satisfied.

$$\left( \frac{\partial^2}{\partial \rho^2} + \frac{1}{\rho} \frac{\partial}{\partial \rho} + \frac{\partial^2}{\partial z^2} \right) \phi_i = 0, \text{ where } i = 1, 2 \quad (4.4)$$

The displacement and stress fields are given by

$$U_\rho = (1/2\mu) \frac{\partial}{\partial \rho} (\phi_1 + z\phi_2) \quad (4.5a)$$

$$U_z = (1/2\mu) \frac{\partial}{\partial z} (\phi_1 + z\phi_2) - 4(1-\nu)\phi_2 \quad (4.5b)$$

$$\sigma_\rho = \frac{\partial^2}{\partial \rho^2} (\phi_1 + z\phi_2) - 2\nu \frac{\partial}{\partial z} (\phi_2) \quad (4.5c)$$

$$\sigma_z = \frac{\partial^2}{\partial z^2} (\phi_1 + z\phi_2) - 2(2-\nu) \frac{\partial}{\partial z} (\phi_2) \quad (4.5d)$$

$$\tau_{\rho z} = \frac{\partial}{\partial \rho} \left[ \frac{\partial}{\partial z} (\phi_1 + z\phi_2) - 2(1-\nu)\phi_2 \right] \quad (4.5e)$$

where,  $\mu$  is the shear modulus and  $\nu$  is the Poisson's ratio.

From Figure 4.1, with the following geometric relations:

$$\rho = R - r \sin \theta \text{ and } z = r \cos \theta$$

$$\text{So, } r^2 = (\rho - R)^2 + z^2 \text{ and } \tan \theta = \frac{R - \rho}{z}$$

Using the above relations, the differential operators are defined as follows:

$$\frac{\partial}{\partial \rho} = -\sin \theta \frac{\partial}{\partial r} - \frac{\cos \theta}{r} \frac{\partial}{\partial \theta}$$

$$\frac{\partial^2}{\partial \rho^2} = \sin^2 \theta \frac{\partial^2}{\partial r^2} + \frac{\cos^2 \theta}{r^2} \frac{\partial^2}{\partial \theta^2} + \frac{\cos^2 \theta}{r} \frac{\partial}{\partial r} - \frac{\sin 2\theta}{r^2} \frac{\partial}{\partial \theta}$$

$$\frac{\partial}{\partial z} = \cos \theta \frac{\partial}{\partial r} - \frac{\sin \theta}{r} \frac{\partial}{\partial \theta}$$

$$\frac{\partial^2}{\partial z^2} = \cos^2 \theta \frac{\partial^2}{\partial r^2} + \frac{\sin^2 \theta}{r^2} \frac{\partial^2}{\partial \theta^2} + \frac{\sin^2 \theta}{r} \frac{\partial}{\partial r} + \frac{\sin 2\theta}{r^2} \frac{\partial}{\partial \theta}$$

Substituting these into Equations (4.4 and 4.5) and doing some algebraic manipulations, the transformed equations into the  $(r, \theta)$  coordinate system are obtained as,

$$\left( \frac{\partial^2}{\partial r^2} + \frac{1}{r} \frac{\partial}{\partial r} + \frac{1}{r^2} \frac{\partial^2}{\partial \theta^2} + \frac{1}{-R + r \sin \theta} \left( \sin \theta \frac{\partial}{\partial r} + \frac{\cos \theta}{r} \frac{\partial}{\partial \theta} \right) \right) \phi_i = 0, \text{ where } i = 1, 2 \quad (4.6)$$

$$\begin{aligned} U_r &= -U_\rho \sin \theta + U_z \cos \theta \\ &= (1/2\mu) \left[ \frac{\partial}{\partial r} (\phi_1 + \phi_2 \cdot r \cos \theta) - 4 \cos \theta (1 - \nu) \phi_2 \right] \end{aligned} \quad (4.7a)$$

$$\begin{aligned} U_\theta &= U_\rho \cos \theta + U_z \sin \theta \\ &= (1/2\mu) \left[ \left( -\frac{1}{r} \right) \frac{\partial}{\partial \theta} (\phi_1 + \phi_2 \cdot r \cos \theta) - 4 \sin \theta (1 - \nu) \phi_2 \right] \end{aligned} \quad (4.7b)$$

$$\begin{aligned} \sigma_r &= \sigma_\rho \sin^2 \theta + \sigma_z \cos^2 \theta - 2\tau_{\rho z} \sin \theta \cos \theta \\ &= \frac{\partial^2}{\partial r^2} (\phi_1 + \phi_2 \cdot r \cos \theta) - 2[(2 - \nu) \cos \theta \frac{\partial}{\partial r} - \frac{\nu \sin \theta}{r} \frac{\partial}{\partial \theta}] \phi_2 \end{aligned} \quad (4.7c)$$

$$\begin{aligned}\sigma_\theta &= \sigma_\rho \cos^2 \theta + \sigma_z \sin^2 \theta + 2\tau_{\rho z} \sin \theta \cos \theta \\ &= \left( \frac{1}{r} \frac{\partial}{\partial r} + \frac{1}{r^2} \frac{\partial^2}{\partial \theta^2} \right) (\phi_1 + \phi_2 \cdot r \cos \theta) - 2 \left[ \nu \cos \theta \frac{\partial}{\partial r} - \frac{(2-\nu) \sin \theta}{r} \frac{\partial}{\partial \theta} \right] \phi_2\end{aligned}\quad (4.7d)$$

$$\begin{aligned}\tau_{r\theta} &= (\sigma_z - \sigma_\rho) \sin \theta \cos \theta - \tau_{\rho z} (\sin^2 \theta - \cos^2 \theta) \\ &= -\frac{\partial}{\partial r} \left( \frac{1}{r} \frac{\partial}{\partial \theta} \right) (\phi_1 + \phi_2 \cdot r \cos \theta) - 2(1-\nu) \left[ \sin \theta \frac{\partial}{\partial r} - \frac{\cos \theta}{r} \frac{\partial}{\partial \theta} \right] \phi_2\end{aligned}\quad (4.7e)$$

Further, with the following expansion

$$\begin{aligned}\frac{1}{-R + r \sin \theta} &= -\frac{1}{R} \left( 1 - \frac{r}{R} \sin \theta \right)^{-1} \\ &= -\frac{1}{R} \sum_{k=0}^{\infty} \left( \frac{r}{R} \sin \theta \right)^k\end{aligned}$$

Equation (4.6) becomes,

$$\left( \frac{\partial^2}{\partial r^2} + \frac{1}{r} \frac{\partial}{\partial r} + \frac{1}{r^2} \frac{\partial^2}{\partial \theta^2} - \frac{1}{R} \sum_{k=0}^{\infty} \left( \frac{r}{R} \sin \theta \right)^k \left( \sin \theta \frac{\partial}{\partial r} + \frac{\cos \theta}{r} \frac{\partial}{\partial \theta} \right) \right) \phi_i = 0 \quad (4.8)$$

Assuming the following asymptotic solutions of the harmonic functions  $\phi_1(r, \theta)$

and  $\phi_2(r, \theta)$ ,

$$\phi_1(r, \theta) = \sum_{k=0}^{\infty} (r/R)^{\lambda+1+k} f_{1k}(\theta)$$

$$\phi_2(r, \theta) = \sum_{k=0}^{\infty} (r/R)^{\lambda+k} f_{2k}(\theta)$$

In general

$$\phi_i(r, \theta) = \sum_{k=0}^{\infty} (r/R)^{\lambda+2-i+k} f_{ik}(\theta); \quad i=1, 2 \quad (4.9)$$

Substituting Equation (4.9) into Equation (4.8)

$$\sum_{k=0}^{\infty} [(r/R)^{\lambda-i+k} (\lambda+2-i+k)(\lambda+1-i+k) f_{ik}(\theta) + (r/R)^{\lambda-i+k} (\lambda+2-i+k) f_{ik}(\theta) + (r/R)^{\lambda-i+k} f_{ik}''(\theta) - \sum_{n=0}^{\infty} (r/R)^n \sin^n \theta \{ \sin \theta (\lambda+2-i+k)(r/R)^{\lambda+1-i+k} f_{ik}(\theta) + \cos \theta (r/R)^{\lambda+1-i+k} f_{ik}'(\theta) \}] = 0$$

or,

$$\sum_{k=0}^{\infty} [(r/R)^{\lambda-i+k} (\lambda+2-i+k)^2 f_{ik}(\theta) + (r/R)^{\lambda-i+k} f_{ik}''(\theta) - \sum_{n=0}^{\infty} \sin^n \theta \{ \sin \theta (\lambda+2-i+k)(r/R)^{\lambda+1-i+k+n} f_{ik}(\theta) + \cos \theta (r/R)^{\lambda+1-i+k+n} f_{ik}'(\theta) \}] = 0$$

By equating the co-efficients of  $r^{\lambda-i}$  and  $r^{\lambda+1-i}$  from both sides of the equation, the following two equations can be obtained

$$(\lambda+2-i)^2 f_{i0}(\theta) + f_{i0}''(\theta) = 0 \quad (4.10a)$$

and

$$(\lambda+3-i)^2 f_{i1}(\theta) + f_{i1}''(\theta) = (\sin \theta)(\lambda+2-i) f_{i0}(\theta) + \cos(\theta) f_{i0}'(\theta) \quad (4.10b)$$

Solution of Equation (4.10 a) is determined as,

$$f_{i0}(\theta) = A_{i0} \sin(\lambda+2-i)\theta + B_{i0} \cos(\lambda+2-i)\theta \quad (4.11a)$$

Using Equation (4.10 a), the solution of Equation (4.10 b) is obtained as

$$f_{i1}(\theta) = A_{i1} \sin(\lambda+3-i)\theta + B_{i1} \cos(\lambda+3-i)\theta + \frac{A_{i0}}{4} \cos(\lambda+1-i)\theta - \frac{B_{i0}}{4} \sin(\lambda+1-i)\theta \quad (4.11b)$$

Based on Liu et al. (1999), the above two terms are the main dominating terms for the stress state to be singular.

To identify the materials, a new index 'm' is introduced here.

Let,  $m = 1$  for material 1

$$A_{11} = \frac{A_{10}(\lambda + 1)}{R^2}, \quad A_{21} = \frac{A_{20}}{2R}, \quad B_{11} = \frac{B_{10}(\lambda + 1)}{R^2}, \quad B_{21} = \frac{B_{20}}{2R}$$

and  $m = 2$  for material 2

$$A_{12} = \frac{A_{10}(\lambda + 1)}{R^2}, \quad A_{22} = \frac{A_{20}}{2R}, \quad B_{12} = \frac{B_{10}(\lambda + 1)}{R^2}, \quad B_{22} = \frac{B_{20}}{2R}$$

Also,  $R_1 = r/R$  and using  $k_m = 3 - 4\nu_m$ , Equation (4.7) could be rewritten as

$$2\mu U_r = R_1^\lambda \frac{1}{R} [(\lambda + 1)f_{10}(\theta) + R(\lambda - 3 + 4\nu) \cos(\theta)f_{20}(\theta)]$$

$$U_r = \frac{R_1^\lambda}{\mu_m} \frac{R}{2} \left[ A_{1m} \sin(\lambda + 1)\theta + B_{1m} \cos(\lambda + 1)\theta + (\lambda - k_m)(\sin(\lambda + 1)\theta + \sin(\lambda - 1)\theta)A_{2m} \right. \\ \left. + (\lambda - k_m)(\cos(\lambda + 1)\theta + \cos(\lambda - 1)\theta)B_{2m} \right]$$

$$(U_r)_1 = \frac{R_1^\lambda}{\mu_1} \frac{R}{2} \left[ A_{11} \sin(\lambda + 1)\theta + B_{11} \cos(\lambda + 1)\theta + (\lambda - k_1)(\sin(\lambda + 1)\theta + \sin(\lambda - 1)\theta)A_{21} \right. \\ \left. + (\lambda - k_1)(\cos(\lambda + 1)\theta + \cos(\lambda - 1)\theta)B_{21} \right] \quad (4.12a)$$

$$(U_r)_2 = \frac{R_1^\lambda}{\mu_2} \frac{R}{2} \left[ A_{12} \sin(\lambda + 1)\theta + B_{12} \cos(\lambda + 1)\theta + (\lambda - k_2)(\sin(\lambda + 1)\theta + \sin(\lambda - 1)\theta)A_{22} \right. \\ \left. + (\lambda - k_2)(\cos(\lambda + 1)\theta + \cos(\lambda - 1)\theta)B_{22} \right] \quad (4.12b)$$

$$2\mu U_\theta = - \left[ R_1^\lambda \frac{1}{R} \{ f'_{10}(\theta) + R \cos(\theta)f'_{20}(\theta) + R(3 - 4\nu) \sin(\theta)f_{20}(\theta) \} \right]$$

$$U_\theta = - \frac{R_1^\lambda}{\mu_m} \frac{R}{2} \left[ A_{1m} \cos(\lambda + 1)\theta - B_{1m} \sin(\lambda + 1)\theta + A_{2m} \{ (\lambda - k_m) \cos(\lambda + 1)\theta + (\lambda + k_m) \cos(\lambda - 1)\theta \} \right. \\ \left. - B_{2m} \{ (\lambda - k_m) \sin(\lambda + 1)\theta + (\lambda + k_m) \sin(\lambda - 1)\theta \} \right]$$

$$(U_\theta)_1 = - \frac{R_1^\lambda}{\mu_1} \frac{R}{2} \left[ A_{11} \cos(\lambda + 1)\theta - B_{11} \sin(\lambda + 1)\theta + A_{21} \{ (\lambda - k_1) \cos(\lambda + 1)\theta + (\lambda + k_1) \cos(\lambda - 1)\theta \} \right. \\ \left. - B_{21} \{ (\lambda - k_1) \sin(\lambda + 1)\theta + (\lambda + k_1) \sin(\lambda - 1)\theta \} \right] \quad (4.13a)$$

$$(U_\theta)_2 = - \frac{R_1^\lambda}{\mu_2} \frac{R}{2} \left[ A_{12} \cos(\lambda + 1)\theta - B_{12} \sin(\lambda + 1)\theta + A_{22} \{ (\lambda - k_2) \cos(\lambda + 1)\theta + (\lambda + k_2) \cos(\lambda - 1)\theta \} \right. \\ \left. - B_{22} \{ (\lambda - k_2) \sin(\lambda + 1)\theta + (\lambda + k_2) \sin(\lambda - 1)\theta \} \right] \quad (4.13b)$$

$$\begin{aligned}
\sigma_\theta &= R_1^{\lambda-1} \frac{1}{R^2} \left[ \begin{aligned} &f_{10}''(\theta) + (\lambda+1)f_{10}(\theta) + R \cos(\theta)f_{20}''(\theta) + 2(1-\nu)R \sin(\theta)f_{20}'(\theta) \\ &+ R \cos(\theta)f_{20}(\theta)(1-2\nu)(\lambda+k) \end{aligned} \right] \\
&= R_1^{\lambda-1} \frac{1}{R^2} \left[ \begin{aligned} &-(\lambda+1)^2 A_{10} \sin(\lambda+1)\theta - (\lambda+1)^2 B_{10} \cos(\lambda+1)\theta + (\lambda+1)\{A_{10} \sin(\lambda+1)\theta + B_{10} \cos(\lambda+1)\theta\} \\ &+ 2(1-\nu) \sin \theta R \{\lambda A_{20} \cos(\lambda\theta) - \lambda B_{20} \sin(\lambda\theta)\} + R \cos \theta \{-\lambda^2 A_{20} \sin(\lambda\theta) - \lambda^2 B_{20} \cos(\lambda\theta)\} \\ &+ \lambda(1-2\nu)R \cos \theta \{A_{20} \sin(\lambda\theta) + B_{20} \cos(\lambda\theta)\} \end{aligned} \right] \\
&= R_1^{\lambda-1} \left[ \begin{aligned} &-\lambda A_{1m} \sin(\lambda+1)\theta - \lambda B_{1m} \cos(\lambda+1)\theta + A_{2m} \{2\lambda(1-\nu).2 \sin \theta \cos(\lambda\theta) + (\lambda(1-2\nu) - \lambda^2) 2 \cos \theta \sin(\lambda\theta)\} \\ &+ B_{2m} \{-2\lambda(1-\nu).2 \sin \theta \sin(\lambda\theta) + (\lambda(1-2\nu) - \lambda^2) 2 \cos \theta \cos(\lambda\theta)\} \end{aligned} \right] \\
&= -\lambda R_1^{\lambda-1} \left[ \begin{aligned} &A_{1m} \sin(\lambda+1)\theta + B_{1m} \cos(\lambda+1)\theta + A_{2m} \{(\lambda - k_m) \sin(\lambda+1)\theta + (\lambda+1) \sin(\lambda-1)\theta\} + \\ &B_{2m} \{(\lambda - k_m) \cos(\lambda+1)\theta + (\lambda+1) \cos(\lambda-1)\theta\} \end{aligned} \right]
\end{aligned}$$

$$(\sigma_\theta)_1 = -\lambda R_1^{\lambda-1} \left[ \begin{aligned} &A_{11} \sin(\lambda+1)\theta + B_{11} \cos(\lambda+1)\theta + A_{21} \{(\lambda - k_1) \sin(\lambda+1)\theta + (\lambda+1) \sin(\lambda-1)\theta\} + \\ &B_{21} \{(\lambda - k_1) \cos(\lambda+1)\theta + (\lambda+1) \cos(\lambda-1)\theta\} \end{aligned} \right] \quad (4.14a)$$

$$(\sigma_\theta)_2 = -\lambda R_1^{\lambda-1} \left[ \begin{aligned} &A_{12} \sin(\lambda+1)\theta + B_{12} \cos(\lambda+1)\theta + A_{22} \{(\lambda - k_m) \sin(\lambda+1)\theta + (\lambda+1) \sin(\lambda-1)\theta\} + \\ &B_{22} \{(\lambda - k_2) \cos(\lambda+1)\theta + (\lambda+1) \cos(\lambda-1)\theta\} \end{aligned} \right] \quad (4.14b)$$

$$\begin{aligned}
\tau_{r\theta} &= -R_1^{\lambda-1} \frac{1}{R^2} \left[ \lambda f_{10}'(\theta) + (\lambda-2+2\nu)R \cos(\theta)f_{20}'(\theta) + R \sin(\theta)f_{20}(\theta)(1-2\nu)\lambda \right] \\
&= \frac{-R_1^{\lambda-1}}{R^2} \left[ \begin{aligned} &\lambda(\lambda+1)A_{10} \cos(\lambda+1)\theta - \lambda(\lambda+1)B_{10} \sin(\lambda+1)\theta + A_{20}(\lambda-2+2\nu)R \lambda \cos \theta \cos(\lambda\theta) \\ &- B_{20}(\lambda-2+2\nu)R \lambda \cos \theta \sin(\lambda\theta) + A_{20}(1-2\nu)R \lambda \sin \theta \sin(\lambda\theta) + B_{20}(1-2\nu)R \lambda \sin \theta \cos(\lambda\theta) \end{aligned} \right] \\
&= -R_1^{\lambda-1} \left[ \begin{aligned} &A_{1m} \cos(\lambda+1)\theta - B_{1m} \sin(\lambda+1)\theta + A_{2m} \{(\lambda - k_m) \cos(\lambda+1)\theta + (\lambda-1) \cos(\lambda-1)\theta\} \\ &- B_{2m} \{(\lambda - k_m) \sin(\lambda+1)\theta + (\lambda-1) \sin(\lambda-1)\theta\} \end{aligned} \right]
\end{aligned}$$

$$(\tau_{r\theta})_1 = -R_1^{\lambda-1} \left[ \begin{aligned} &A_{11} \cos(\lambda+1)\theta - B_{11} \sin(\lambda+1)\theta + A_{21} \{(\lambda - k_1) \cos(\lambda+1)\theta + (\lambda-1) \cos(\lambda-1)\theta\} \\ &- B_{21} \{(\lambda - k_1) \sin(\lambda+1)\theta + (\lambda-1) \sin(\lambda-1)\theta\} \end{aligned} \right] \quad (4.15a)$$

$$(\tau_{r\theta})_2 = -R_1^{\lambda-1} \left[ \begin{aligned} &A_{12} \cos(\lambda+1)\theta - B_{12} \sin(\lambda+1)\theta + A_{22} \{(\lambda - k_2) \cos(\lambda+1)\theta + (\lambda-1) \cos(\lambda-1)\theta\} \\ &- B_{22} \{(\lambda - k_2) \sin(\lambda+1)\theta + (\lambda-1) \sin(\lambda-1)\theta\} \end{aligned} \right] \quad (4.15b)$$

Continuity and boundary conditions for the problem are:

At  $\theta = \theta_0$  (continuity condition)

$$(U_r)_1 = (U_r)_2, \quad (U_\theta)_1 = (U_\theta)_2, \quad (\sigma_\theta)_1 = (\sigma_\theta)_2, \quad (\tau_{r\theta})_1 = (\tau_{r\theta})_2$$

At  $\theta = 0$  (free surface)

$$(\sigma_\theta)_2 = 0, \quad (\tau_{r\theta})_2 = 0$$

At  $\theta = \pi$  (free surface)

$$(\sigma_\theta)_1 = 0, \quad (\tau_{r\theta})_1 = 0$$

$$\text{Let, } \mu = \frac{\mu_1}{\mu_2},$$

$$\sin(\lambda + 1)\theta_0 = S_1, \quad \sin(\lambda - 1)\theta_0 = S_2, \quad \sin(\lambda + 1)\pi = S_3, \quad \sin(\lambda - 1)\pi = S_4$$

$$\cos(\lambda + 1)\theta_0 = C_1, \quad \cos(\lambda - 1)\theta_0 = C_2, \quad \cos(\lambda + 1)\pi = C_3, \quad \cos(\lambda - 1)\pi = C_4$$

Using these expressions along with the boundary conditions to Equation (4.12)-(4.15), the following system of homogeneous linear equations of the eight constants  $A_{1m}, B_{1m}, A_{2m}, B_{2m}, m = 1, 2$  is obtained.

$$A_{11}S_1 - \mu A_{12}S_1 + (\lambda - k_1)A_{21}(S_1 + S_2) - \mu(\lambda - k_2)A_{22}(S_1 + S_2) + B_{11}C_1 - \mu B_{12}C_1 + (\lambda - k_1)B_{21}(C_1 + C_2) - \mu(\lambda - k_2)B_{22}(C_1 + C_2) = 0$$

$$A_{11}C_1 - \mu A_{12}C_1 + A_{21}\{(\lambda - k_1)C_1 + (\lambda + k_1)C_2\} - \mu A_{22}\{(\lambda - k_2)C_1 + (\lambda + k_2)C_2\} - B_{11}S_1 + \mu B_{12}S_1 - B_{21}\{(\lambda - k_1)S_1 + (\lambda + k_1)S_2\} + \mu B_{22}\{(\lambda - k_2)S_1 + (\lambda + k_2)S_2\} = 0$$

$$A_{11}S_1 - A_{12}S_1 + A_{21}[(\lambda - k_1)S_1 + (\lambda + 1)S_2] - A_{22}[(\lambda - k_2)S_1 + (\lambda + 1)S_2] + B_{11}C_1 - B_{12}C_1 + B_{21}[(\lambda - k_1)C_1 + (\lambda + 1)C_2] - B_{22}[(\lambda - k_2)C_1 + (\lambda + 1)C_2] = 0$$

$$A_{11}C_1 - A_{12}C_1 + A_{21}\{(\lambda - k_1)C_1 + (\lambda - 1)C_2\} - A_{22}\{(\lambda - k_2)C_1 + (\lambda - 1)C_2\} - B_{11}S_1 + B_{12}S_1 - B_{21}\{(\lambda - k_1)S_1 + (\lambda - 1)S_2\} + B_{22}\{(\lambda - k_2)S_1 + (\lambda - 1)S_2\} = 0$$

$$A_{11} \cdot 0 + A_{12} \cdot 0 + A_{21} \cdot 0 + A_{22} \cdot 0 + B_{11} \cdot 0 + B_{12} - B_{21} \cdot 0 + B_{22}(2\lambda + 1 - k_2) = 0$$

$$A_{11}.0 + A_{12} + A_{21}.0 + A_{22}.(2\lambda - 1 - k_2) + B_{11}.0 + B_{12}.0 - B_{21}.0 + B_{22}.0 = 0$$

$$A_{11}S_3 + A_{12}.0 + A_{21}[(\lambda - k_1)S_3 + (\lambda + 1)S_4] + A_{22}.0 + B_{11}C_3 + B_{12}.0 + B_{21}[(\lambda - k_1)C_3 + (\lambda + 1)C_4] + B_{22}.0 = 0$$

$$A_{11}C_3 + A_{12}.0 + A_{21}\{(\lambda - k_1)C_3 + (\lambda - 1)C_4\} + A_{22}.0 - B_{11}S_3 + B_{12}.0 - B_{21}\{(\lambda - k_1)C_3 + (\lambda - 1)C_4\} + B_{22}.0 = 0$$

The above equations in the matrix form

$$\begin{bmatrix} S_1 & -\mu S_1 & (\lambda - k_1)(S_1 + S_2) & -\mu(\lambda - k_2)(S_1 + S_2) & C_1 & -\mu C_1 & (\lambda - k_1)(C_1 + C_2) \\ C_1 & -\mu C_1 & (\lambda - k_1)C_1 + (\lambda + k_1)C_2 & -\mu[(\lambda - k_2)C_1 + (\lambda + k_2)C_2] & -S_1 & \mu S_1 & -(\lambda - k_1)S_1 - (\lambda + k_1)S_2 \\ S_1 & -S_1 & (\lambda - k_1)S_1 + (\lambda + 1)S_2 & -[(\lambda - k_2)S_1 + (\lambda + 1)S_2] & C_1 & -C_1 & (\lambda - k_1)C_1 + (\lambda + 1)C_2 \\ C_1 & -C_1 & (\lambda - k_1)C_1 + (\lambda - 1)C_2 & -[(\lambda - k_2)C_1 + (\lambda - 1)C_2] & -S_1 & S_1 & -[(\lambda - k_1)S_1 + (\lambda - 1)S_2] \\ 0 & 0 & 0 & 0 & 0 & 1 & 0 \\ 0 & 1 & 0 & 2\lambda - 1 - k_2 & 0 & 0 & 0 \\ S_3 & 0 & (\lambda - k_1)S_3 + (\lambda + 1)S_4 & 0 & C_3 & 0 & (\lambda - k_1)C_3 + (\lambda + 1)C_4 \\ C_3 & 0 & (\lambda - k_1)C_3 + (\lambda - 1)C_4 & 0 & -S_3 & 0 & -[(\lambda - k_1)S_3 + (\lambda - 1)S_4] \end{bmatrix} \begin{bmatrix} A_{11} \\ A_{12} \\ A_{21} \\ A_{22} \\ B_{11} \\ B_{12} \\ B_{21} \\ B_{22} \end{bmatrix} = 0$$

Or,

$$[C][A] = 0 \quad (4.16)$$

where,  $[C]$  is the coefficient matrix.

The condition for the existence of the non-trivial solution of Equation (4.16) is,

$$Det[C] = 0 \quad (4.17)$$

For any angle,  $\gamma = 90 - \theta_0$ , where,  $\theta_0$  is the bonding angle, Equation (4.17) is equivalent to

$$\begin{aligned} & \sin^2 \lambda \pi + 2(2\lambda^2 \cos^2 \gamma - 1)\alpha \sin \lambda \pi \sin 2\lambda \gamma - 4\lambda^2 \beta \sin \lambda \pi \sin 2\lambda \gamma \cos^2 \theta + 4\lambda^2 \cos^2 \gamma \\ & (1 - \cos \lambda \pi \cos 2\lambda \gamma - 2\lambda^2 \cos^2 \gamma) \cdot \alpha \beta + [\sin^2 2\lambda \gamma + 4\lambda^2 (\lambda^2 - 1) \cos^2 \gamma - \lambda^4 \sin^2 2\gamma] \cdot \alpha^2 + \\ & [4\lambda^2 \cos^2 \gamma (\lambda^2 \cos^2 \gamma - 1 + \cos \lambda \pi \cos 2\lambda \gamma) + (\cos \lambda \pi - \cos 2\lambda \gamma)^2] \cdot \beta^2 = 0 \end{aligned} \quad (4.18)$$

where,  $\alpha, \beta$  are the Dundurs' (1969) parameters, defined in Chapter 2 as follows

$$\alpha = \frac{\mu_1(k_2 + 1) - (k_1 + 1)\mu_2}{\mu_1(k_2 + 1) + (k_1 + 1)\mu_2}; \quad \beta = \frac{\mu_1(k_2 - 1) - (k_1 - 1)\mu_2}{\mu_1(k_2 + 1) + (k_1 + 1)\mu_2};$$

Thus, an eigenvalue equation (4.18) for  $\lambda$  is obtained. Since the lowest order of the stress at the edge of the bonded joint is  $\lambda - 1$ , for  $0 < \text{Re}(\lambda) < 1$ , the stress component goes to infinite when  $r \rightarrow 0$ , i.e. there exists a stress singularity. For any combination of materials the critical bonding angle  $\theta_c$  is determined by using Equation (4.18) for which the value of  $\lambda$  equals one. Any angle less than the critical angle will lead  $\lambda > 1$ , i.e. the stress singularity can be eliminated. Thus the condition for the elimination of the stress singularity from the interface corner is,  $\theta_0 < \theta_c$ .

Substituting the properties of materials given in Table 4.1 into Equation (4.18), the real roots of “ $\lambda$ ” in the range  $0 < \lambda < 1$  are determined for different bonding angles. The results are tabulated in Table 4.2.

Table 4.2: Values of  $\lambda$  in the range  $0 < \lambda < 1$  for different bonding angles

Bonding Angle, $\theta_0$	$\lambda$
90	0.6624
75	0.7338
60	0.8604
55	0.9215
54	0.9353
53	0.9496
52	0.9645
51	0.9801
50	0.9964
49	1.013

From the analytical result, it is quite clear that the critical bonding angle for the considered aluminum and epoxy interface is in between  $49^\circ$  and  $50^\circ$ . In order to eliminate the stress singularity from the interface corner, the bonding angle at the interface corner must be less than  $49^\circ$ .

### 4.2.2 Verification of the critical bonding angle by finite element analysis

The axi-symmetric finite element model of the suggested specimen has been shown earlier in Figure 2.2 (Chapter 2), where aluminum and epoxy are the hard and soft materials, respectively. The radius of the cylindrical specimen,  $R$ , is 10 mm and a uniform tensile stress of 10 MPa is applied at the top end of the specimen while the bottom end is kept as fixed in the axial direction. The distributions of the interface normal stress, interface shear stress and effective stress along the interface are shown in Figure 4.2 for two different bonding angles of  $40^\circ$  and  $60^\circ$ , respectively.

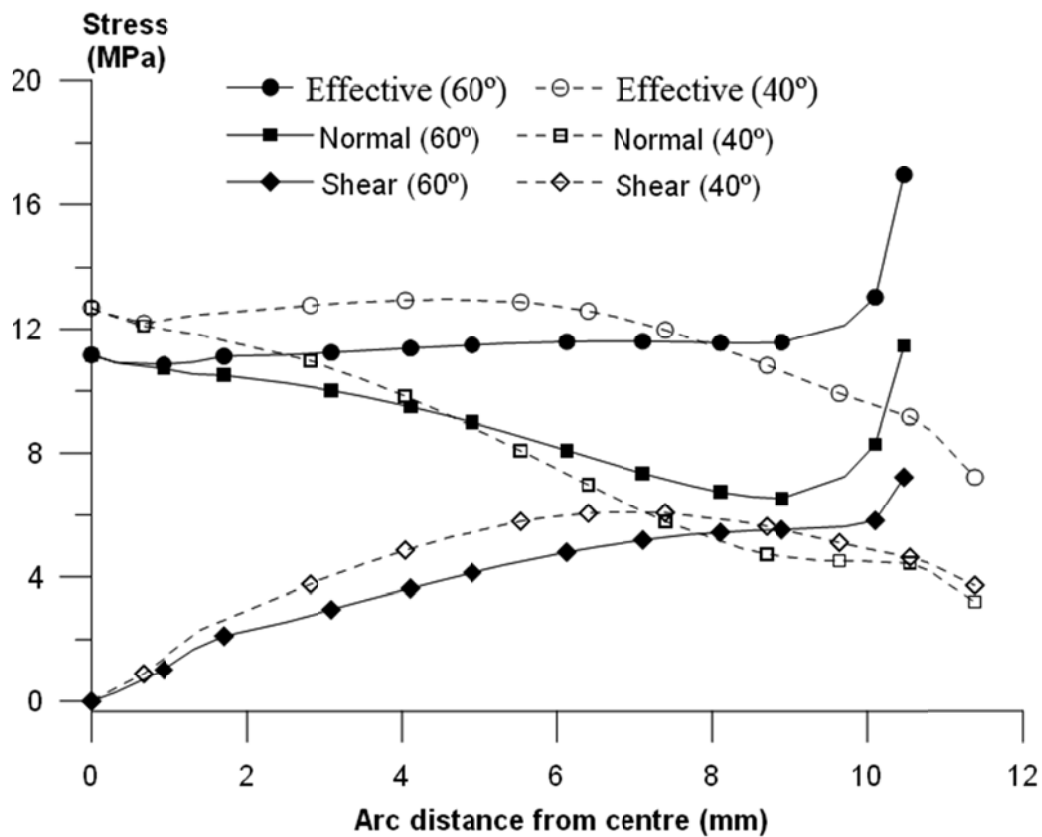


Figure 4.2: Normal, shear and effective stress distributions along the interface for bonding angles of  $40^\circ$  and  $60^\circ$  with pure tensile load

It is seen that excessive stresses exist near the free edge of the interface, when the bonding angle is  $60^\circ$ . These stress values increase without convergent limits with increasing mesh density, indicating that the stress singularity occurs at the free edge of the interface. However, for the case of  $40^\circ$  bonding angle, finite values of the interface stresses are exhibited and the stress convergence is confirmed by increasing the FEM mesh density. Then the similar analysis is carried out for other bonding angles from  $40^\circ$  to  $60^\circ$  by the increment of  $1^\circ$  each time. It is found that the shape of the effective stress curve near the free edge starts to change from the downward to the upward direction, when the bonding angle changes from  $49^\circ$  to  $50^\circ$  as shown in Figure 4.3.

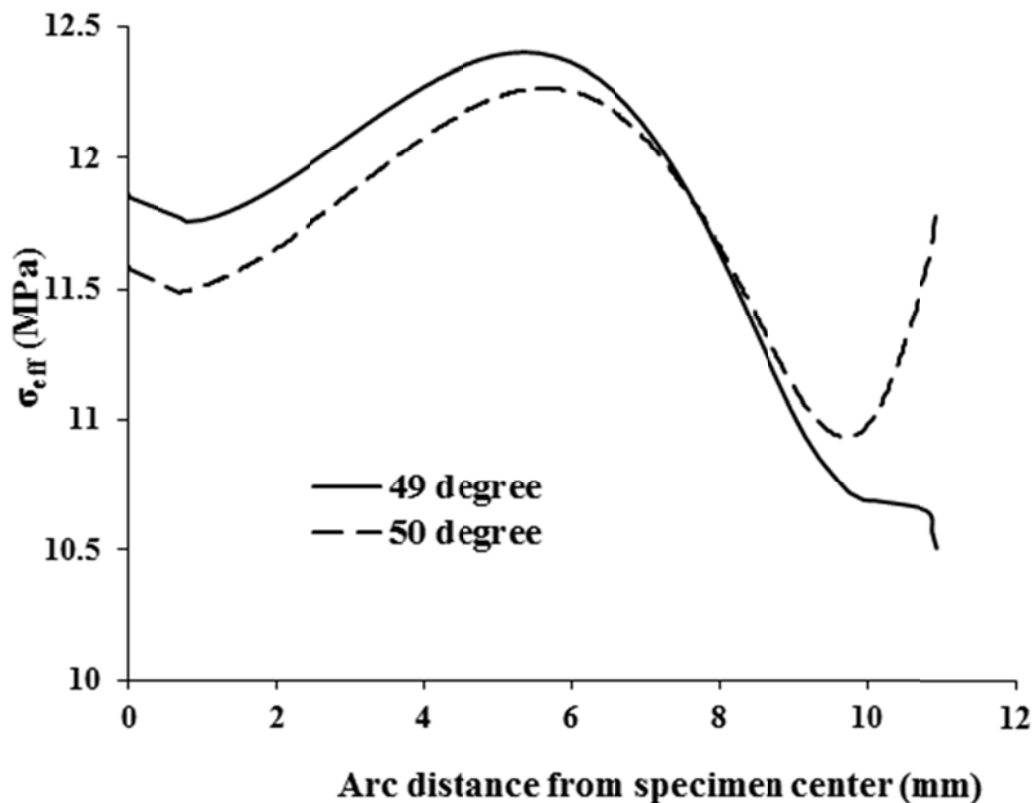


Figure 4.3: Effective stress distributions at the interface corner for bonding angles of  $49^\circ$  and  $50^\circ$  with pure tensile load

This indicates that the value of the critical bonding angle for the present aluminum/epoxy elastic bi-materials interface is between  $49^\circ$  and  $50^\circ$ . Thus, the finite element analysis results have verified the accuracy of the analytical method. For any combined normal-shear loading on the specimen with bonding angle less than  $49^\circ$ , finite interface normal/shear stress field can be obtained.

Another fact should be mentioned is that there is no interface stress singularity for the application of pure torsional load on the specimen designed according to the developed method. Figure 4.4 shows the interface shear stress distribution along the spherical interface by applying a torque of 21 N-m at the ends of the specimen, where the bonding angle is  $50^\circ$ . Note that in this case, only interface shear stress (along the circumferential direction) is developed and there is no interface normal stress.

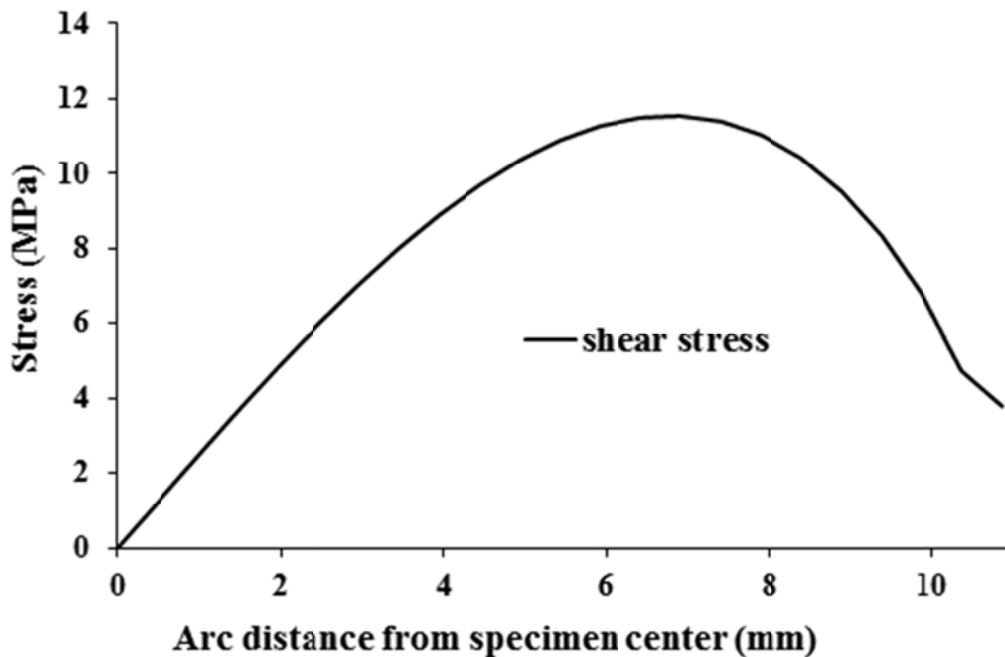


Figure 4.4: Shear stress distribution along the interface under pure torsional load (bonding angle of  $50^\circ$ )

### 4.2.3 Experimental verification of the critical bonding angle

The above analytical and FEM results are verified by the following experimental results. In order to determine the critical bonding angle by experiment, specimens are made from aluminum and epoxy with different edge bonding angles. Each specimen is tested under the pure tensile loading until final failure at the interface and the failure loads are recorded. The variation of failure loads with bonding angle is shown in Figure 4.5.

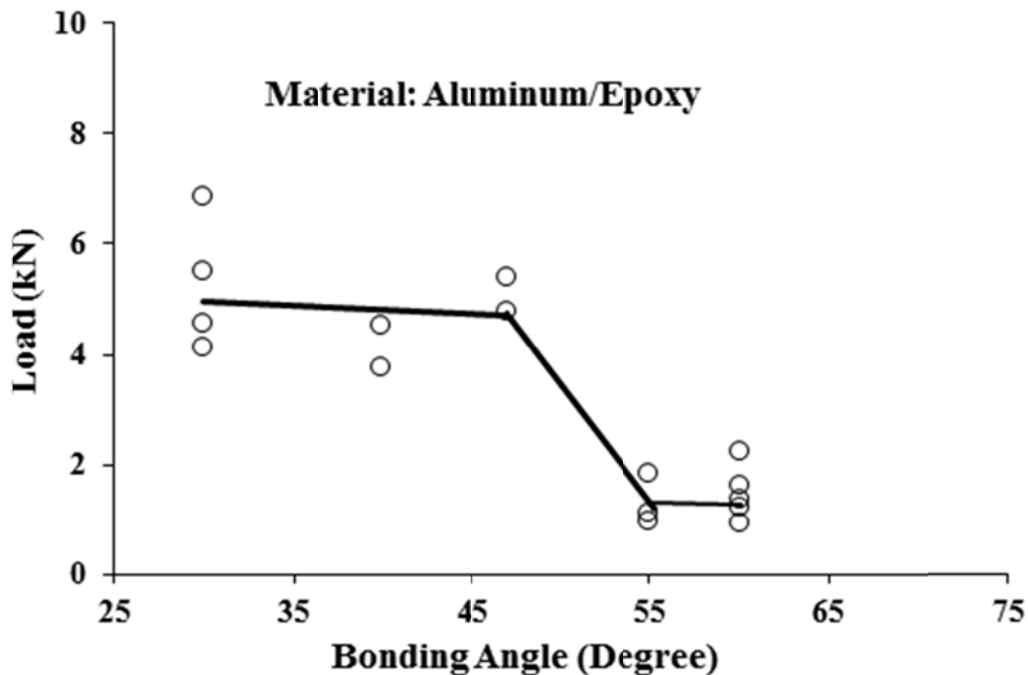


Figure 4.5: Variation of failure loads with bonding angle under pure tensile loading

It can be seen from Figure 4.5 that the failure loads at the bonding angles of  $\theta_0 \leq 47^\circ$  are much higher than those at the bonding angles  $\theta_0 \geq 55^\circ$ . There is an abrupt drop of the failure load from  $\theta_0 = 47^\circ$  to  $\theta_0 = 55^\circ$  indicating a transition from a finite interface stress field to a singular interface stress field. Therefore, the

experimental results have also verified that the critical bonding angle for the current aluminum/epoxy interface is in the range of  $47^\circ < \theta_c < 55^\circ$ .

### 4.3 SPECIMEN AND EXPERIMENTS

The critical bonding angle  $\theta_c$  for the aluminum/epoxy interface is determined as in between  $49^\circ$  and  $50^\circ$ . Therefore, the test specimens are manufactured with a bonding angle of  $47^\circ$ . The detailed geometry of the specimen is shown in Figure 4.6.

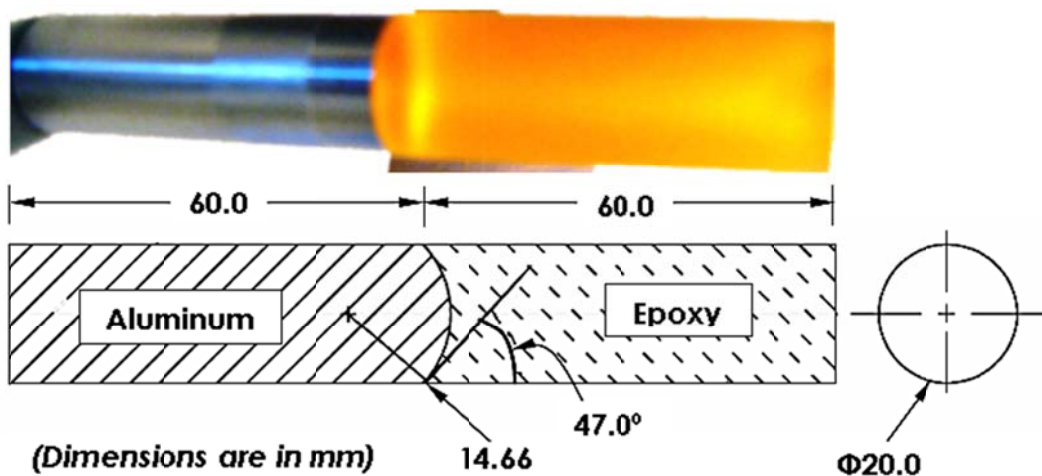


Figure 4.6: Aluminum-epoxy specimen for interface strength test

The aluminum portion of the specimen is first fabricated to the cylindrical shape with a spherical interface by CNC lathe machine. The same interface roughness condition is kept for all the aluminum parts. EPON 8131/EPI-CURE 3072 is used for the epoxy portion of the specimens. EPON 8131 resin and EPI-CURE 3072 hardener are mixed at a proportion of 79 to 21 weight percent. A

special mold described in Chapter 3 is used to make the interface specimen. The multi-axial testing machine is used to conduct the tests. Using the controller of the machine, various combinations of normal and shear loads are applied on the specimens. With the help of an accurate data acquisition system, the failure loads are recorded for each test case.

#### **4.4 EXPERIMENTAL RESULTS AND FINITE ELEMENT ANALYSIS TO OBTAIN THE STRESS DISTRIBUTION ALONG THE INTERFACE**

Tensile load, torsional load and various combinations of tensile and torsional loads are applied on the specimens by the multi axial testing machine. In each case, the maximum failure load is recorded and is given in Table 4.3.

Table 4.3: Maximum failure loads of the aluminum-epoxy specimen

No	Tensile load (N)	Torsional Load (N. m)
1	0	37.53
2	264.4	36.96
3	1691	37.86
4	2358	37.3
5	3000	37.29
6	3250	28.27
7	3540	33.96
8	4639	23.71
9	4702	21.17
10	5727	0

Each of the above failure loads are the average values from two tests with same combined loading conditions. The failure loads in tests given in Table 4.3 are applied in the finite element analysis for each loading case. The normal, shear and effective stress distributions are obtained along the interface. As an example, the stress distributions along the interface of Specimen No. 6 with the maximum tensile and torsional loads of 3250 N and 28.27 N-m, respectively, are shown in Figure 4.7.

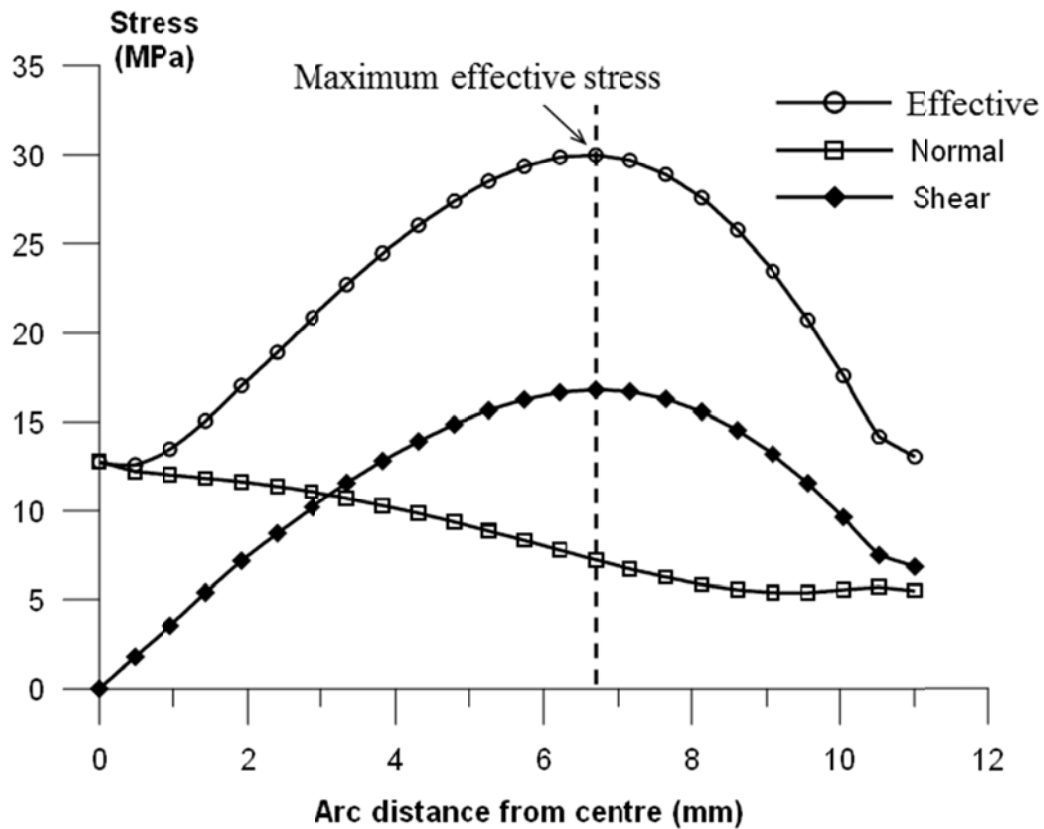


Figure 4.7: Stress distribution along the interface of epoxy and aluminum of specimen No. 6.

#### 4.5 OBTAINING BIAXIAL NORMAL-SHEAR INTERFACE BONDING STRENGTH CRITERION (ENVELOPE) THROUGH ITERATION

The pure torsion test gives the pure shear stress at the interface. Figure 4.8 shows the shear stress distribution along the interface with the specimen subjected to the maximum pure torsional loading. The normal stress along the interface vanishes in this case. The maximum value of the shear stress is  $\tau_s = 20.86$  MPa.

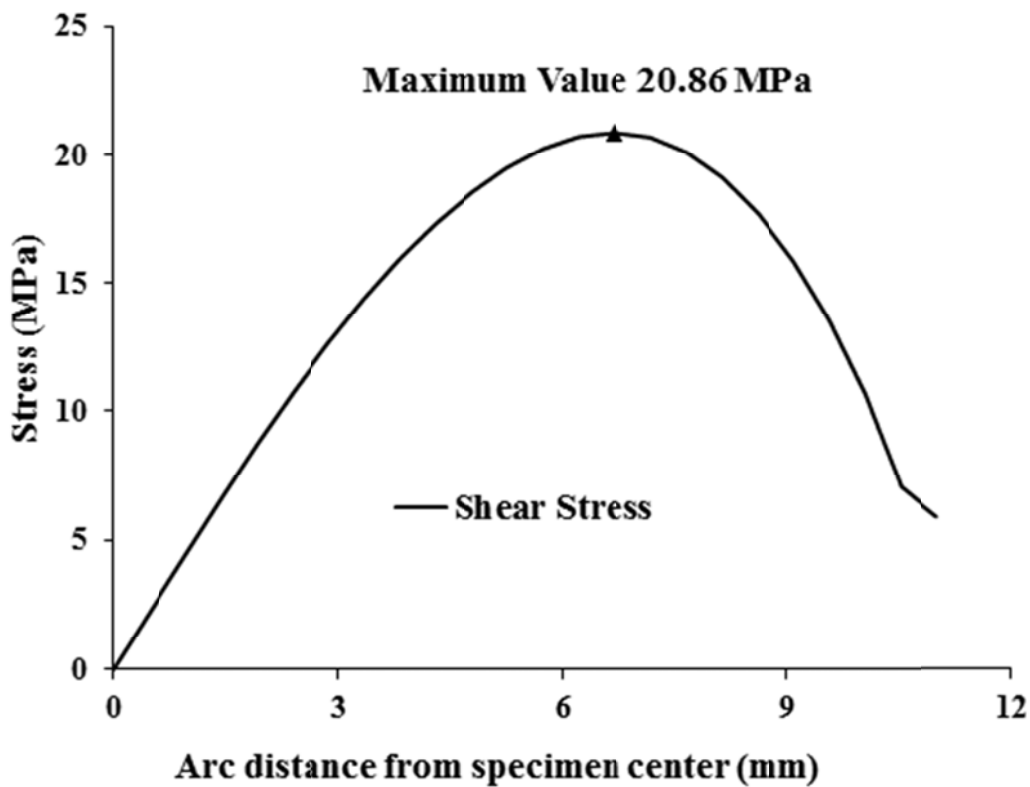


Figure 4.8: Shear stress distribution along the interface for pure torsional load

Therefore, the first trial criterion (effective stress) is

$$f^{(1)} = \sqrt{\sigma_n^2 + 3\tau^2} = \sqrt{0 + 3 \times 20.86^2} = 36.13 \quad (4.19)$$

Or, it can be written as

$$\left(\frac{\sigma_n}{36.13}\right)^2 + \left(\frac{\tau}{20.86}\right)^2 = 1 \quad (4.20)$$

Figure 4.9(a) shows the effective stress envelope, Equation (4.20), and the stress points  $[\sigma_{n,k}, \tau_k]^{(1)}$ ,  $k = 1, \dots, 10$  based on the maximum effective stress value  $\sqrt{\sigma_n^2 + 3\tau^2}$  for each test case.

Next, we try to find best fit curve for the 10 points in Figure 4.9(a). It can be seen that a quadratic expression may still be suitable to fit this set of ten points. By keeping the value  $\tau_s = 20.86$  MPa, the second trial criterion is obtained as

$$\left(\frac{\sigma_n}{16.45}\right)^2 + \left(\frac{\tau}{20.86}\right)^2 = 1 \quad (4.21)$$

Based on the above second trial criterion, a second set of the stress points  $[\sigma_{n,k}, \tau_k]^{(2)}$ ,  $k = 1, \dots, 10$  is obtained based on the maximum values of the left side of Equation (4.21) for each test case. Figure 4.9(b) shows the Equation (4.21) and corresponding stress point set  $[\sigma_{n,k}, \tau_k]^{(2)}$ ,  $k = 1, \dots, 10$ .

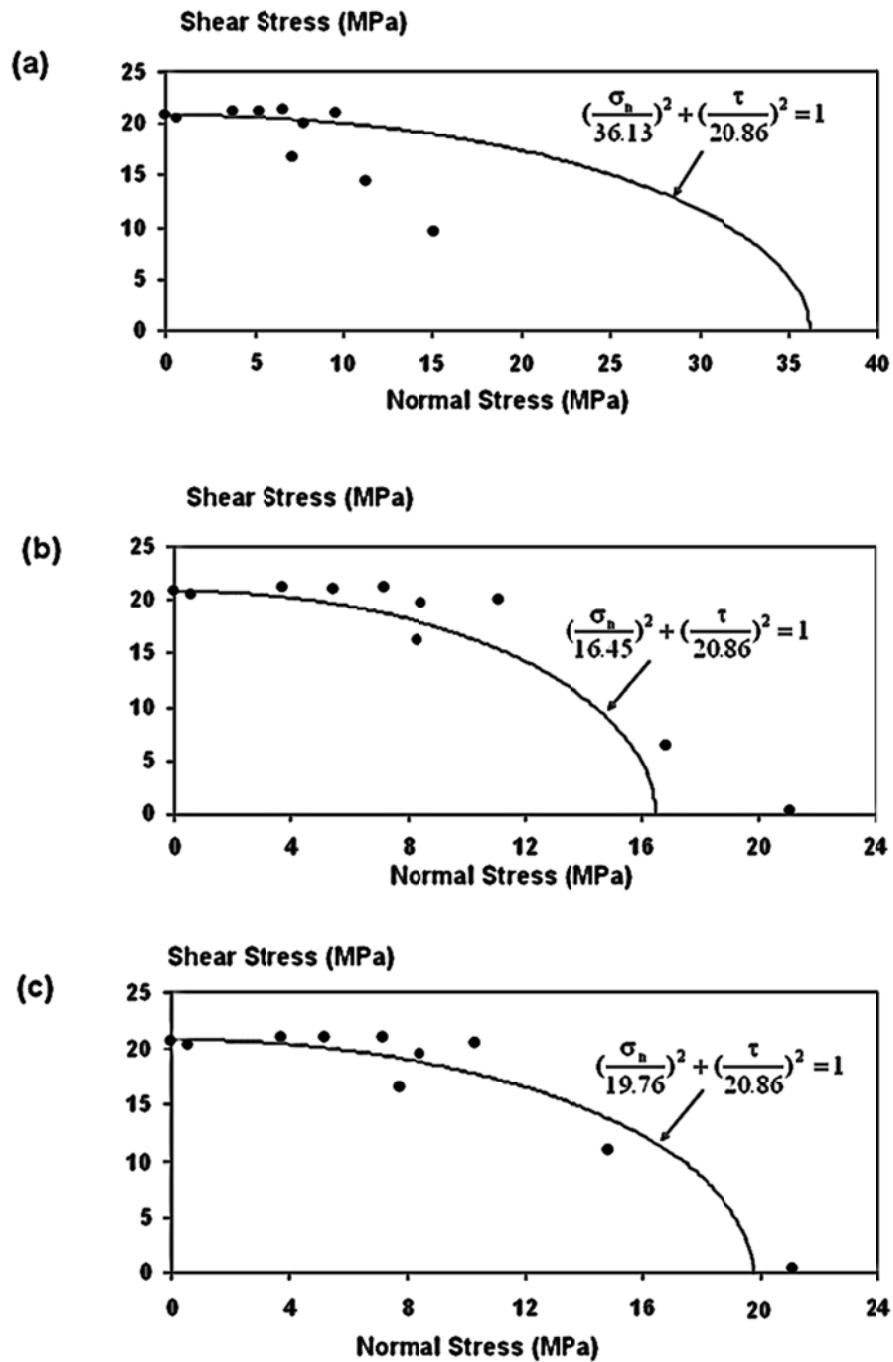


Figure 4.9: (a) Interface strength envelope of epoxy and aluminum based on maximum effective stresses (b) Interface strength envelope of epoxy and aluminum after 1<sup>st</sup> iteration (c) Final interface strength envelope of epoxy and aluminum interface

Continue taking the quadratic form and keeping the value of  $\tau_s = 20.86$  MPa, the third trial criterion is obtained as

$$\left(\frac{\sigma_n}{19.76}\right)^2 + \left(\frac{\tau}{20.86}\right)^2 = 1 \quad (4.22)$$

The further iteration produces the same results as the Equation (4.22). Therefore, for the tested aluminum/epoxy bi-material interface, Equation (4.22), as shown in Figure 4.9(c), represents its normal-shear interface bonding strength criterion (envelope) in the range of the first quarter of the normal-shear stress plane.

#### 4.6 FURTHER OBSERVATION AND REMARKS

It is interesting to compare the current test results with the results obtained by using the butt joint specimens recommended by ASTM D897 (2008) and ASTM D2095 (2008). The butt joint specimens are made with the same dimension as shown in Figure 4.6 except that the interface is flat, or the bonding angle is  $\theta_0 = 90^\circ$ . Both the groups of specimens with  $\theta_0 = 90^\circ$  and  $\theta_0 = 47^\circ$  (each group of 5 specimens) are tested under the pure tensile loading for a comparison. The average maximum failure (debonding) load for the ASTM butt specimens is 2161N with a data scatter band of 13%, while for the proposed designed specimens this value is 5727 N with a scatter band of 12%. It can be seen that the

tensile load carrying capacity of the aluminum/epoxy joints with the proposed design is improved by 2.65 times over the ASTM butt joint design. The large difference in the load carrying capability of the two groups of specimens shows the great potential in the optimal design of bi-material interface for the advanced materials and structures.

For the ASTM butt joint specimen, the tensile interface bonding strength is directly calculated by dividing the failure load by the bonding area and is obtained as 6.88 MPa in this case. This value is obviously much lower than the actual tensile strength of the interface since the stress singularity exists at the free edge, which initiates the failure at a lower applied tensile load.

On the other hand, the tensile strength of 19.76 MPa obtained from the current test method is a more reliable data than that obtained by using ASTM methods. Although both normal and shear stress components exist at the interface, the distributions of the normal and shear stresses from the FEM analysis and the obtained strength envelope, Figure 4.9(c) and Equation (4.22), indicate that the failure should start near the central area of the interface where the normal stress is dominated ( $\sigma_n = 21.07\text{MPa}$ ,  $\tau = 0.36\text{MPa}$ ). Figure 4.10 shows the failed specimen under pure tensile load in the current test.

It can be seen that the interface debonding indeed started near the central area of the interface, not from the edge of the interface as in the case of the ASTM

butt specimens. Therefore, the experimental observation also supports the currently obtained bonding strength data for the aluminum/epoxy interface.



Figure 4.10: Interface of the failed specimen under pure tensile load

**BIBLIOGRAPHY**

- Akisanya, A. R., Fleck, N. A., 1997. Interfacial cracking from the free-edge of a long bi-material strip. *International Journal of Solids and Structures*. 34, 1645-1665.
- Aksentian, O. K., 1967. Singularities of the stress-strain state of a plate in the neighborhood of an edge. *Prikladnaya Matematika i Mekhanika*. 31, 78-186.
- ASTM-D897, 2008. Test Method for Tensile Properties of Adhesive Bonds. ASTM International, West Conshohocken, PA.
- ASTM-D2095, 2008. Standard Test Method for Tensile Strength of Adhesives by Means of Bar and Rod Specimens. ASTM International. ASTM International, West Conshohocken, PA.
- Bogy, D. B., 1971. Two edge-bonded elastic wedges of different materials and wedge angles under surface tractions. *Journal of Applied Mechanics*. 38, 377-386.
- Dundurs, J., 1969. Discussion of edge-bonded dissimilar orthogonal elastic wedges under normal and shear loading. *Journal of Applied Mechanics*. 36, 650-652.

- 
- Lauke, B., Schuller, T., Schneider, K., 2003. Determination of interface strength between two polymer materials by a new curved interface tensile test. *Composite Interfaces*. 10, 1-15.
- Liu, Y. H., Xu, J. Q., Ding, H. J., 1999. Order of singularity and singular stress field about an aximetric interface corner in three dimensional isotropic elasticity. *International Journal of Solids and Structures*. 36, 4425-4445.
- Perlman, A. B., Sih, G. C., 1967. Elastostatic problems of curvilinear cracks in bonded dissimilar materials. *International Journal of Engineering Science*. 5, 845-867.
- Timoshenko, S., Goodier, J. N., 1951. *Theory of Elasticity*. McGraw-Hill Book Company, Inc., NY.
- Ting, T. C. T., 1985. Asymptotic solution near the apex of an elastic wedge with curved boundaries. *Quarterly of Applied Mathematics*. XLII, 467-476.

## **CHAPTER 5: ELASTIC/VISCOELASTIC BI-MATERIAL INTERFACE**

Part of this chapter has been accepted as

1. **Chowdhuri, M. A. K.,** Xia, Z., 2012. An analytical model to determine the stress singularity and critical bonding angle of an Elastic/Viscoelastic bonded joint. *Mechanics of Time Dependent Materials*, DOI: 10.1007/s11043-011-9166-5 (In press).
2. **Chowdhuri, M. A. K.,** Xia, Z., 2012. Interface Bonding Strength Measurement of a Joint between Elastic and Viscoelastic Materials. *Composites-Part B: Engineering*, DOI: 10.1016/j.compositesb.2012.05.027 (In press).

## CHAPTER 5

### ELASTIC/VISCOELASTIC BI-MATERIAL INTERFACE

---

Due to the increasing utilization of polymeric materials in automobile, aerospace, oil and gas, and marine industries, viscoelastic properties of these polymeric materials have received much attention. This chapter presents the determination of bi-material interface bonding strength envelope of an elastic/viscoelastic bonded joint. As an example, the interface between aluminum and epoxy is considered. Aluminum is considered as an elastic isotropic material, whereas epoxy is as a linear viscoelastic material. This chapter is organized as in the following orders: at first, short discussions about the viscoelasticity are presented. Next, literatures related to the elastic/viscoelastic bonded joint are reviewed, three different cases of material modeling are discussed, the analytical solution for the elastic/viscoelastic bonded joint to find the stress singularity and critical bonding angle are presented, and finally, the interface bonding strength of an aluminum (elastic)/epoxy (viscoelastic) are determined.

#### 5.1 VISCOELASTICITY

Most of the polymeric materials exhibit mechanical response characteristics which are outside the scope of elasticity and viscosity; thus a more general theory is needed. The theory of elasticity deals with the materials which

---

have a capacity to store mechanical energy with no dissipation and a newtonian viscous fluid in a non-hydrostatic stress state implies a capacity for dissipating the energy, but none for storing it (Christensen, 1982). The fundamental difference between the polymers and other materials is that the mechanical properties of polymers vary with time.

Under the application of a suddenly applied loading state and held constant after that, an elastic material responds instantly with a state of deformation which remains constant. A Newtonian viscous fluid responds to a suddenly applied state of uniform shear stress by a steady flow process. There are some materials, which possess the capacity to both store and dissipate mechanical energy. For these materials some of the work done to deform them, can be recovered. A suddenly applied and maintained state of uniform stress on these materials induces an instantaneous deformation followed by a flow process which may or may not be limited in magnitude as the time grows. This behavior cannot be clearly described by either the elasticity or viscosity theory but combines feature of each. Thus, viscoelasticity is the study of materials whose mechanical properties have the characteristics of both elastic and viscous materials. All polymers (fluid or solid) have time or temperature domains in which they are viscoelastic (Brinson and Brinson, 2008).

Some other theories of mechanical behavior of materials also have a memory of deformation but they have some fundamental differences with the viscoelasticity. For example, the incremental theory of plasticity has memory effect (final state of deformation depends not only the final state of stress, but also

upon the path in stress space traversed to reached this final state). However, the plasticity theory is independent of time scale involved in loading and unloading, whereas, the viscoelastic theory has a specific time or rate dependences (Christensen, 1982).

## 5.2 BACKGROUND STUDY

In many applications, polymers are reinforced with harder material phases such as fibers, ceramic particles, etc. The interface strength between the polymer and reinforcing agent is therefore critical to the overall performance of these polymeric composite materials. Publications related to analytical solutions for the elastic/viscoelastic bi-material interfaces are relatively limited. Since the stress, strains and displacements of viscoelastic polymers are all time-dependent, the stress analysis of the viscoelastic materials is thus more difficult (Nagaraja and Alwar, 1980). The integral transform technique or the so-called correspondence principal has been commonly used for the viscoelastic analyses: a viscoelastic problem is first converted to an equivalent elastic one by using the Laplace transformation, after solving the equivalent elastic problem, the viscoelastic solution is then obtained through an inverse Laplace transformation of the elastic solution (Lee, 1954, 1955; Schapery, 1962).

Delale and Erdogan (1981) performed the viscoelastic analyses of an adhesively bonded lap joint using the Laplace transform technique, assuming that the adherends are elastic and the adhesive is linearly viscoelastic. Because of the complexity of the problem, the inverse transform can only be obtained

numerically. They reported that at the edge of the interface, the stresses are much higher than the stresses further away from the interface corner. Due to their use of plate theory, the stress singularity cannot be identified. Nagaraja and Alwar (1980) conducted a similar analysis of an adhesive-bonded lap joint using finite element methods. Yadagiri et al. (1987) also used the finite element method to perform the viscoelastic analyses of bonded joints. Lee (1997) presented a solution that was used to find the order of the stress singularity and the free edge stress intensity factor for a two-dimensional, elastic-viscoelastic bonded joint. He used the standard Laplace transform together with the boundary element method. However, the problem was simplified by assuming a time-independent Poisson's ratio for the viscoelastic material. Understanding the importance of the time-dependent viscoelastic properties of the material in stress singularity analysis for bi-material interfaces, Qian et al. (2000) presented the stress and displacement solutions for an elastic-viscoelastic joint whilst considering the time-dependent Poisson's ratio for the viscoelastic material. However, his time-dependent Poisson's ratio was derived from an assumption of a time-independent bulk modulus. Tscharnuter et al. (2011) reported that the time-dependent Poisson's ratio is essential for the accurate simulation results, and cannot be achieved accurately by assuming a constant bulk modulus. In addition, the determination of the time-dependent Poisson's ratio from a constant bulk modulus involves some unnecessary complexity in the analysis of the stress singularity (Qian et al., 2000). It is also difficult to directly determine the bulk modulus from experimentation (Deng and Knauss, 1997). There are only two independent time-dependent

material functions for a standard linear viscoelastic solid. The simultaneous measurements of these two materials are explained clearly in Chapter 3.

Moreover, Qian et. al (2000) used the solutions for the elastic/elastic bonded joints (Eq (3) in Qian et. al 2000) from their previously published paper (Qian and Akisanya, 1999) to obtain the solutions for elastic/viscoelastic joints, but the definition of Dundurs' (1969) parameter,  $\beta$  is not the same in these two papers. The Dundurs' parameter,  $\beta$  in the viscoelastic analysis (Qian et. al 2000) is twice than the Dundurs' parameter,  $\beta$ , they used to obtain the elastic solution (Qian and Akisanya 1999). The material parameter  $\beta$  has a significant effect on the stress singularity.

From the above review it is clear that an accurate and realistic method for determining the order of the stress singularity and thus the interface bonding strength for an elastic/viscoelastic bonded joint needs to be further explored.

### **5.3 MATERIAL MODELING**

In order to determine the stress singularity at the interface corner of a bonded joint with viscoelastic materials, the material properties need to be modeled accurately. However, from the discussions in the earlier section it is easily understandable that the analysis of viscoelastic materials is more difficult than the analysis of elastic materials. There always exists a critical relation between the accuracy and level of difficulty in the analysis. If the materials are tried to model more accurately, the analysis will also become more challenging. That's why, three different cases of material modeling are considered in this study

based on their level of difficulty and accuracy in the analysis to ensure that the desired accuracy level in the stress singularity analysis is attained.

It is mentioned here again that only two properties; shear modulus and Poisson's ratio are needed to determine the stress singularity at the interface corner. In chapter 3, the viscoelastic relaxation modulus and Poisson's ratio are obtained simultaneously and directly from the relaxation tests of viscoelastic materials. The time dependent shear modulus can be obtained from the relaxation modulus and Poisson's ratio using Equation (5.1).

$$\mu(t) = \frac{G(t)}{2[1 + \nu(t)]} \quad (5.1)$$

where,  $G(t)$  is the viscoelastic relaxation modulus, and  $\nu(t)$  is the viscoelastic Poisson's ratio.

The three different cases of material modeling are briefly explained in the following sections.

### **5.3.1 Case -1: The viscoelastic shear modulus is modeled as the standard linear solid model and Poisson's ratio is considered as constant**

This model is the simplest among the three models used in this study for the analysis of the stress singularity at the viscoelastic material bonded joints. Lee (1997) assumed the constant Poisson's ratio in his analysis to determine the stress

singularity for an elastic/viscoelastic bonded joint. Though in section 5.2, it is mentioned that this assumption simplifies the problem very much, it is considered in this study to see the effect of time dependent Poisson's ratio on the stress singularity. Another reason to consider this model is that for a viscoelastic/viscoelastic interface bonded joint (which will be discussed in the next chapter), there is no analytical solution available in open literature. Our intension is to start with this model to develop the analytical solution for the stress singularity at the viscoelastic/viscoelastic interface.

The standard linear solid model is shown in Figure 5.1. It contains a kelvin-voigt solid model with a spring in series.

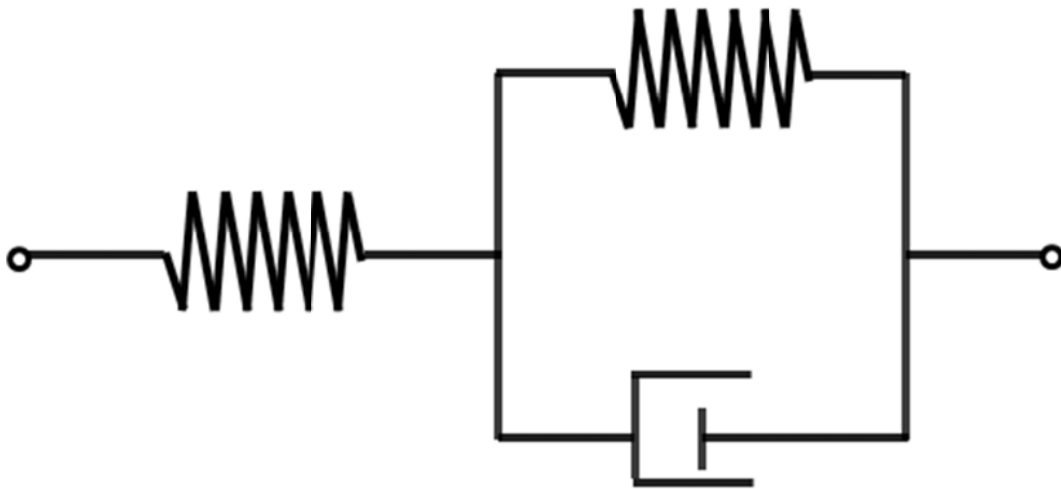


Figure 5.1: Standard linear solid model

Based on the above model, the shear modulus of the viscoelastic material can be expressed as Equation (5.2)

$$\mu(t) = A_1 + A_2 e^{-\phi t} \quad (5.2)$$

where,  $\phi = 1/t_0$  and  $t_0$  is the viscoelastic relaxation time.

The coefficient  $A_1$  and  $A_2$  can be determined easily as follows

$$\text{at } t = 0, \quad \mu(0) = A_1 + A_2$$

$$\text{at } t = \infty, \quad \mu(\infty) = A_1$$

$$\text{Solving, } A_2 = \mu(0) - \mu(\infty)$$

Thus from equation (5.2),

$$\mu(t) = \mu(0) e^{-\phi t} + \mu(\infty) (1 - e^{-\phi t}) \quad (5.3)$$

As described earlier that for case-1, the viscoelastic Poisson's ratio is considered as constant. So,

$$\nu(t) = \nu_0 \quad (5.4)$$

### 5.3.2 Case -2: Both the viscoelastic shear modulus and Poisson's ratio are modeled as the standard linear solid model

It is clear that the difference between case-1 and case-2 lies in the modeling of Poisson's ratio. Case-1 considers the time independent Poisson's ratio, whereas, Case-2 considers the time dependent Poisson's ratio. The

importance of considering the time dependent Poisson's ratio in the singularity analysis is described briefly in section 5.2.

Since in both cases (case-1 and case-2), the shear moduli are modeled as the standard linear solid model, the shear modulus for case-2 is also represented by Equation (5.3). The Poisson's ratio of the viscoelastic material can be determined in the similar way as the procedure followed for the shear modulus determination in case-1.

The time-dependent Poisson's ratio is expressed by Equation (5.5) according to the standard linear solid model

$$\nu(t) = B_1 - B_2 e^{-\phi t} \quad (5.5)$$

where,  $\phi = 1/t_0$  and  $t_0$  is the viscoelastic relaxation time

The coefficient  $B_1$  and  $B_2$  are determined as follows

$$\text{at } t = 0, \quad \nu(0) = B_1 - B_2$$

$$\text{at } t = \infty, \quad \nu(\infty) = B_1$$

$$\text{Solving,} \quad B_2 = \nu(\infty) - \nu(0)$$

Thus, from Equation (5.5), the time-dependent Poisson's ratio is expressed as follows:

$$\nu(t) = \nu(0) e^{-\phi t} + \nu(\infty) (1 - e^{-\phi t}) \quad (5.6)$$

### 5.3.3 Case -3: Both the viscoelastic shear modulus and Poisson's ratio are modeled as the Wiechert Model

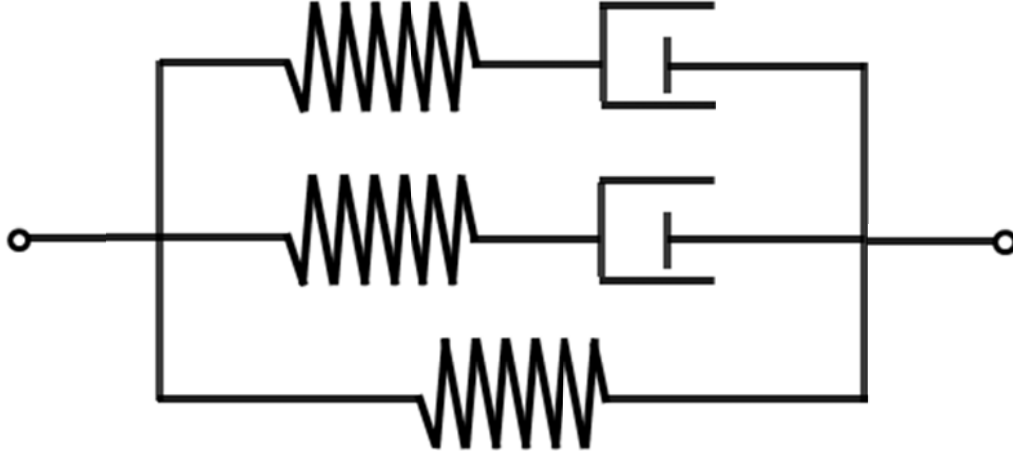


Figure 5.2: Wiechert model consisting of two Maxwell elements with a spring in parallel

This model is most accurate among the three models considered in this study to represent the properties of the viscoelastic materials. This model consists two Maxwell elements with a spring in parallel. Of course, the singularity analysis considering this model becomes more difficult than the previous two cases.

Based on the above model, the shear modulus of the viscoelastic material can be expressed as Equation (5.7)

$$\mu(t) = A_1 + A_2 e^{-\phi_1 t} + A_3 e^{-\phi_2 t} \quad (5.7)$$

Where,  $\phi_1 = 1/t_{10}$  and  $\phi_2 = 1/t_{20}$  depends on the spring and damping constant of the Wiechert model.

The coefficient  $A_2$ , and  $A_3$  cannot be obtained directly as the previous two cases. However, at  $t = \infty$ ,  $\mu(\infty) = A_1$

The other two coefficients are obtained by best fitting the measured data from the relaxation test. Same procedure is followed for the Poisson's ratio.

Let the Poisson's ratio be expressed by Equation (5.8)

$$\nu(t) = B_1 - B_2 e^{-\phi_3 t} - B_3 e^{-\phi_4 t} \quad (5.8)$$

Where,  $\phi_3 = 1/t_{30}$  and  $\phi_4 = 1/t_{40}$  depends on the spring and damping constant of the Wiechert model.

#### 5.4 VISCOELASTIC PROPERTIES OF EPOXY

For the cases 1 and 2, the viscoelastic properties of material depend on its value at time,  $t = 0$  and  $t = \infty$ . The variation of the properties depends on the relaxation time. Using the measured data from the relaxation tests described in section 3.2.3 in Chapter 3, the required properties of epoxy to express as Equations (5.3), (5.4) and (5.6) are given in Table 5.1

Table 5.1: Experimental viscoelastic properties of epoxy

Property	At $t = 0$	At $t = \infty$	Relaxation time
Shear Modulus, $\mu$ (MPa)	$\mu(0) = 449$	$\mu(\infty) = 135$	$t_0 = 90$ sec
Poisson's ratio, $\nu$	$\nu_0 = \nu(0) = 0.415$	$\nu(\infty) = 0.443$	$t_0 = 90$ sec

Thus the viscoelastic properties of epoxy are as follows:

Case-1:

$$\text{The viscoelastic shear modulus, } \mu(t) = 135 + 314 e^{-t/90} \quad (5.8)$$

$$\text{and Poisson's ratio, } \nu(t) = 0.415$$

Case-2:

$$\text{The viscoelastic shear modulus, } \mu(t) = 135 + 314 e^{-t/90} \quad (5.9)$$

$$\text{and Poisson's ratio, } \nu(t) = 0.443 - 0.028 e^{-t/90}$$

Case-3:

As mentioned earlier that the viscoelastic properties for case-3 are determined using the best fit curve technique. Figure 5.3 shows the experimental curve of the viscoelastic shear modulus of epoxy and the fitting curve according to the model described in Case-3. The equation of the best fitting curve is given below (Equation 5.10)

$$\mu(t) = 135 + 237 e^{-t/21.25} + 77 e^{-t/650} \quad (5.10)$$

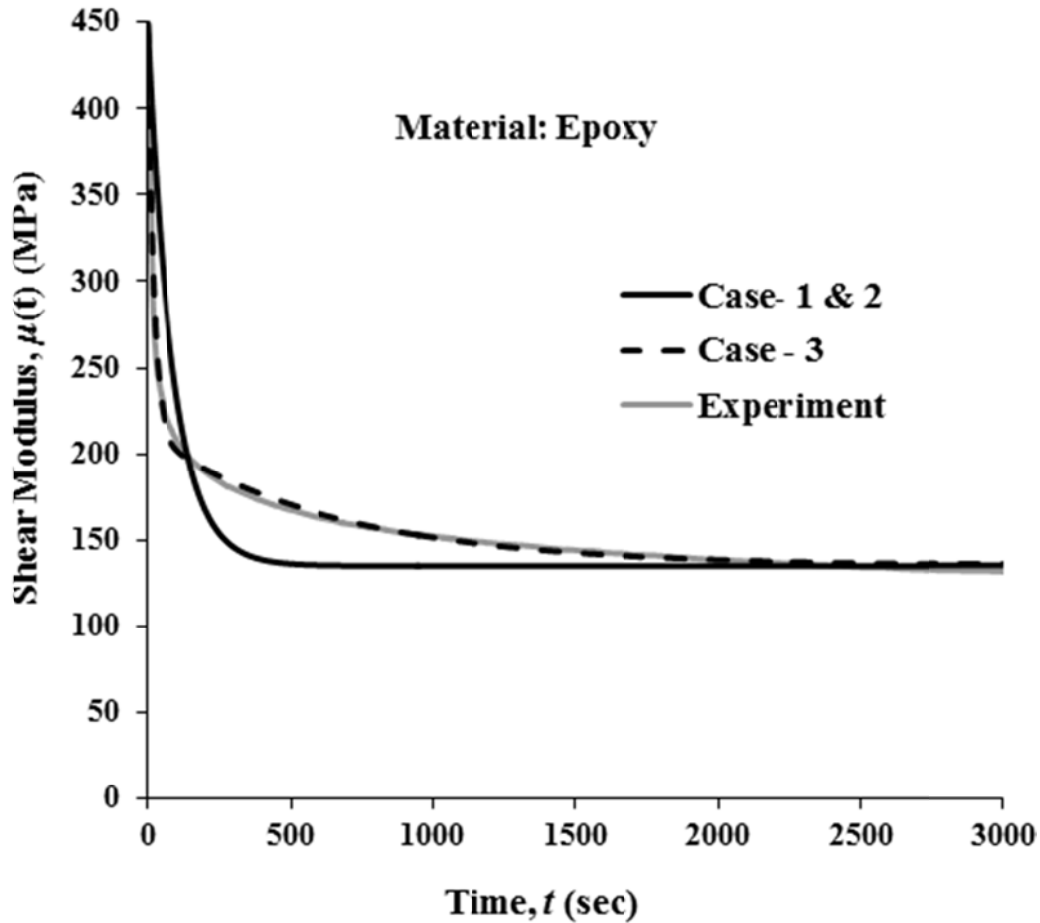


Figure 5.3: Experimental and modeled viscoelastic shear modulus of epoxy

From Figure 5.3, it is quite clear that the case-1 and case-2 can represent the shear modulus accurately only at the beginning and end region. However, case-3 can predict the viscoelastic shear modulus accurately for the whole tested period.

Following the same procedure as the viscoelastic shear modulus, from Figure 5.4, the Poisson's ratio of epoxy for the case-3 is given by Equation (5.11)

$$\nu(t) = 0.443 - 0.017 e^{-t/1055} - 0.011 e^{-t/50} \quad (5.11)$$

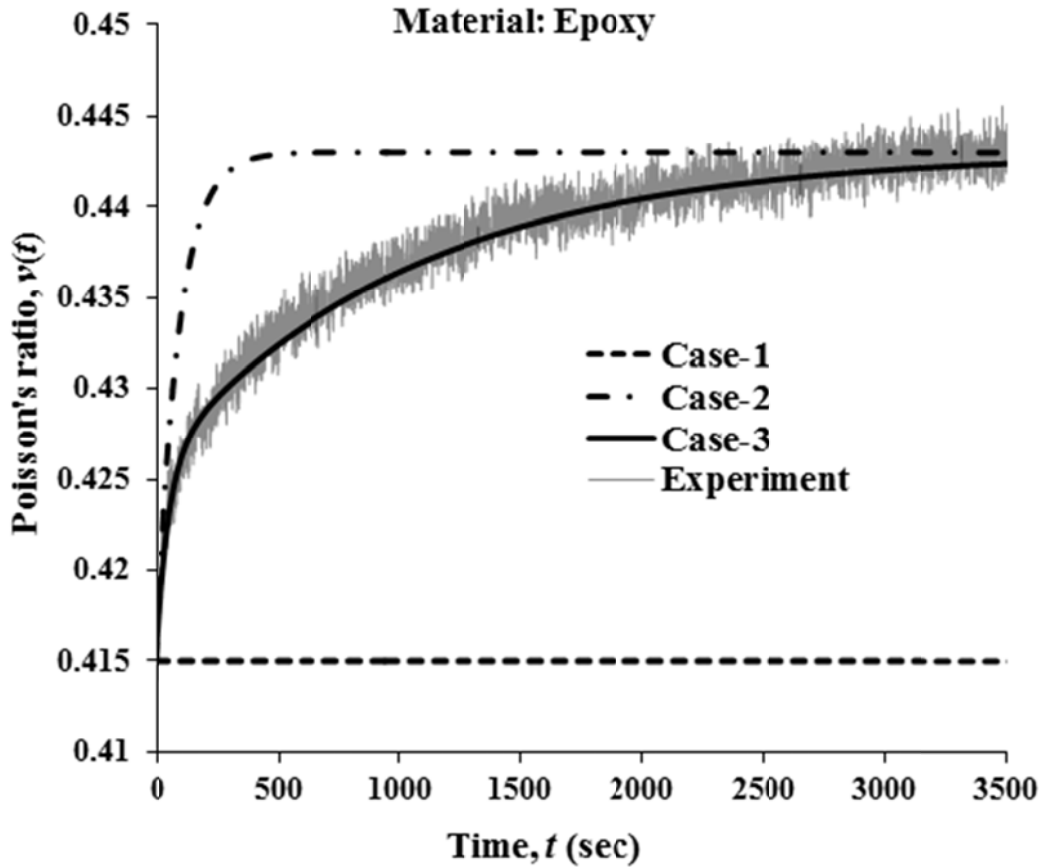


Figure 5.4: Experimental and modeled viscoelastic Poisson's ratio of epoxy

## 5.5 ANALYTICAL SOLUTION FOR AN ELASTIC/VISCOELASTIC BONDED JOINT

### 5.5.1 Case-1: The Shear modulus is time dependent but Poisson's ratio is time independent

The Laplace transform of any function  $f(t)$  can be defined as

$$L\{f(t)\} = \int_0^{\infty} f(t) e^{-st} dt$$

where,  $L\{f(t)\}$  is the Laplace transform of the function  $f(t)$  and  $s$  is the *Laplace transform parameter*.

Conducting Laplace transformation of Equations (5.2 and 5.4)

$$\mu_2^*(s) = \frac{A_1}{s} + \frac{A_2}{s + \phi} \quad \text{and} \quad \nu_2^*(s) = \nu_{20} / s$$

Where, ‘s’ is the *Laplace transform parameter* and the superscript “\*” of any variable indicates that the parameter is in the transformed domain.

The elastic-viscoelastic analogy (Fung, 1965; Christensen, 1982 ) states that elastic solutions can be converted to Laplace transformed viscoelastic solutions through the replacement of elastic moduli and elastic Poisson’s ratio by the transformed viscoelastic moduli and Poisson’s ratio multiplied by the *Laplace transform parameter*  $s$ , respectively. Thus, using the elastic viscoelastic analogy, the Dundurs’ Parameters (Equation 2.3) in the transformed domain for an elastic/viscoelastic bonded joint are obtained as follows:

$$s\alpha^*(s) = \frac{\mu_1(1 - s\nu_2^*(s)) - s\mu_2^*(s)(1 - \nu_1)}{\mu_1(1 - s\nu_2^*(s)) + s\mu_2^*(s)(1 - \nu_1)}$$

or,

$$\alpha^*(s) = \frac{1}{s} \left[ \frac{\mu_1(1 - \nu_{20}) - s\left(\frac{A_1}{s} + \frac{A_2}{s + \phi}\right)(1 - \nu_1)}{\mu_1(1 - \nu_{20}) + s\left(\frac{A_1}{s} + \frac{A_2}{s + \phi}\right)(1 - \nu_1)} \right] \quad (5.12a)$$

and,

$$s\beta^*(s) = \frac{\mu_1(1 - 2s\nu_2^*(s)) - s\mu_2^*(s)(1 - 2\nu_1)}{2[\mu_1(1 - s\nu_2^*(s)) + s\mu_2^*(s)(1 - \nu_1)]}$$

Or,

$$\beta^*(s) = \frac{1}{s} \left[ \frac{\mu_1(1 - 2\nu_{20}) - s\left(\frac{A_1}{s} + \frac{A_2}{s + \phi}\right)(1 - 2\nu_1)}{2[\mu_1(1 - \nu_{20}) + s\left(\frac{A_1}{s} + \frac{A_2}{s + \phi}\right)(1 - \nu_1)]} \right] \quad (5.12b)$$

The inverse Laplace transform of a function  $F(s)$  is defined as:

$$L^{-1}\{F(s)\} = \frac{1}{2\pi i} \int_{\gamma_1 - i\infty}^{\gamma_1 + i\infty} F(s) e^{st} ds$$

where  $\gamma_1$  is an arbitrary positive constant lying to the right of all the singularities of the function  $F(s)$  (Schiff, 1999).

By performing the inverse Laplace transformation on Equation (5.12) the Dundurs' (1969) parameters in time domain are obtained as follows:

$$\alpha(t) = \frac{(e^\varepsilon - 1)(A_1(\nu_1 - 1) - \mu_1(\nu_{20} - 1))}{A_1(\nu_1 - 1) + \mu_1(\nu_{20} - 1)} + \frac{e^\varepsilon ((A_1 + A_2)(1 - \nu_1) + \mu_1(\nu_{20} - 1))}{(A_1 + A_2)(\nu_1 - 1) + \mu_1(\nu_{20} - 1)}$$

Or,

$$\alpha(t) = \frac{(e^\varepsilon - 1)(\mu_2(\infty)(\nu_1 - 1) - \mu_1(\nu_{20} - 1))}{\mu_2(\infty)(\nu_1 - 1) + \mu_1(\nu_{20} - 1)} + \frac{e^\varepsilon (\mu_2(0)(1 - \nu_1) + \mu_1(\nu_{20} - 1))}{\mu_2(0)(\nu_1 - 1) + \mu_1(\nu_{20} - 1)}$$

(5.13 a)

and,

$$\beta(t) = \frac{1}{2} \left[ \frac{(e^\varepsilon - 1)(\mu_1(1 - 2\nu_{20}) + A_1(2\nu_1 - 1))}{A_1(\nu_1 - 1) + \mu_1(\nu_{20} - 1)} + \frac{e^\varepsilon ((A_1 + A_2)(1 - 2\nu_1) + \mu_1(2\nu_{20} - 1))}{\mu_1(\nu_{20} - 1) + (A_1 + A_2)(\nu_1 - 1)} \right]$$

Or,

$$\beta(t) = \frac{1}{2} \left[ \frac{(e^\varepsilon - 1)(\mu_1(1 - 2\nu_{20}) + \mu_2(\infty)(2\nu_1 - 1))}{\mu_2(\infty)(\nu_1 - 1) + \mu_1(\nu_{20} - 1)} + \frac{e^\varepsilon (\mu_2(0)(1 - 2\nu_1) + \mu_1(2\nu_{20} - 1))}{\mu_1(\nu_{20} - 1) + \mu_2(0)(\nu_1 - 1)} \right]$$

(5.13b)

where,

$$\varepsilon = - \frac{\varphi(A_1(\nu_1 - 1) + \mu_1(\nu_{20} - 1))}{(A_1 + A_2)(\nu_1 - 1) + \mu_1(\nu_{20} - 1)} t$$

Or,

$$\varepsilon = - \frac{\varphi(\mu_2(\infty)(\nu_1 - 1) + \mu_1(\nu_{20} - 1))}{\mu_2(0)(\nu_1 - 1) + \mu_1(\nu_{20} - 1)} t$$

Again, following the elastic-viscoelastic analogy and using the Laplace transformation and inverse Laplace transformation, the eigenvalue equation (Equation 4.18) in the time domain is given as follows by Equation (5.14).

$$\begin{aligned} & \tau_1 \sin^2 \lambda \pi - \tau_2 \cdot 2(2\lambda^2 \cos^2 \gamma - 1) \sin \lambda \pi \sin 2\lambda \gamma + \tau_3 \cdot 4\lambda^2 \sin \lambda \pi \sin 2\lambda \gamma \cos^2 \gamma \\ & + \tau_4 \cdot 4\lambda^2 \cos^2 \gamma (1 - \cos \lambda \pi \cos 2\lambda \gamma - 2\lambda^2 \cos^2 \gamma) + \tau_5 \cdot \{\sin^2 2\lambda \gamma + 4\lambda^2 (\lambda^2 - 1) \cos^2 \gamma - \lambda^4 \sin^2 2\gamma\} \\ & + \tau_6 \cdot \{4\lambda^2 \cos^2 \gamma (\lambda^2 \cos^2 \gamma - 1 + \cos \lambda \pi \cos 2\lambda \gamma) + (\cos \lambda \pi - \cos 2\lambda \gamma)^2\} = 0 \end{aligned} \quad (5.14)$$

Where,

$$\begin{aligned} \tau_1 = & [\mu_2(\infty)]^2 (\nu_1 - 1)^2 - e^{-\phi t} \{[\mu_2(0) - \mu_2(\infty)]^2 (\phi t - 1)(\nu_1 - 1)^2 + 2\mu_2(\infty)(\nu_1 - 1)[\mu_2(0) - \mu_2(\infty)](\nu_1 - 1) + e^{\phi t} \mu_4(\nu_{20} - 1) + \\ & 2[\mu_2(0) - \mu_2(\infty)]\mu_4(\nu_1 - 1)(\nu_{20} - 1)\} + \mu_4^2 (\nu_{20} - 1)^2 \end{aligned}$$

$$\begin{aligned} \tau_2 = & \mu_4^2 (\nu_{20} - 1)^2 - [\mu_2(\infty)]^2 (\nu_1 - 1)^2 + e^{-\phi t} [\mu_2(0) - \mu_2(\infty)] \{[\mu_2(0) - \mu_2(\infty)](\phi t - 1) - 2\mu_2(\infty)\} \dots \\ & \dots (\nu_1 - 1)^2 \end{aligned}$$

$$\begin{aligned} \tau_3 = & \frac{1}{2} \{[\mu_2(\infty)]^2 (3\nu_1 - 1 - 2\nu_1^2) + \mu_2(\infty)\mu_4(\nu_1 - \nu_{20}) + \mu_4^2 (1 - 3\nu_2 + 2\nu_{20}^2) + e^{-\phi t} (\mu_2(0) - \mu_2(\infty)) [2\mu_2(\infty)(3\nu_1 - 1 - 2\nu_1^2) + \\ & [\mu_2(0) - \mu_2(\infty)](\phi t - 1)(1 - 3\nu_1 + 2\nu_1^2) + \mu_4(\nu_1 - \nu_{20})]\} \end{aligned}$$

$$\begin{aligned} \tau_4 = & \frac{1}{2} \{[\mu_2(\infty)]^2 (1 - 3\nu_1 + 2\nu_1^2) + \mu_2(\infty)\mu_4(\nu_1(3 - 4\nu_2) + 3\nu_2 - 2) + \mu_4^2 (1 - 3\nu_2 + 2\nu_2^2) - e^{-\phi t} (\mu_2(0) - \mu_2(\infty)) [\mu_2(\infty) \dots \\ & \dots (6\nu_1 - 4\nu_1^2 - 2) + [\mu_2(0) - \mu_2(\infty)](\phi t - 1)(1 - 3\nu_1 + 2\nu_1^2) + \mu_4(2 - 3\nu_2 + \nu_1(4\nu_2 - 3))]\} \end{aligned}$$

$$\begin{aligned} \tau_5 = & (\mu_2(\infty)(\nu_1 - 1) - \mu_4(\nu_{20} - 1))^2 - e^{-\phi t} (\mu_2(0) - \mu_2(\infty))(\nu_1 - 1) \{[\mu_2(0) - \mu_2(\infty)](\phi t - 1)(\nu_1 - 1) - 2\mu_2(\infty)(\nu_1 - 1) \dots \\ & \dots + 2\mu_4(\nu_{20} - 1)\} \end{aligned}$$

$$\begin{aligned} \tau_6 = & \frac{1}{4} \{(\mu_2(\infty)(2\nu_1 - 1) + \mu_4(1 - 2\nu_{20}))^2 - e^{-\phi t} (\mu_2(0) - \mu_2(\infty))(2\nu_1 - 1) \{[\mu_2(0) - \mu_2(\infty)](\phi t - 1)(2\nu_1 - 1) + \\ & 2\mu_2(\infty)(1 - 2\nu_1) + 2\mu_4(2\nu_{20} - 1)\}\} \end{aligned}$$

### 5.5.2 Case-2: Both the shear modulus and Poisson's ratio are time dependent

Using the Laplace transformation, the transformed equations of Equations (5.2 and 5.5) are given by:

$$\mu_2^*(s) = \frac{A_1}{s} + \frac{A_2}{s + \phi} \quad \text{and} \quad \nu_2^*(s) = \frac{B_1}{s} - \frac{B_2}{s + \phi}$$

where, 's' is the *Laplace transform parameter* and the superscript "\*" indicates that the parameter is in the transformed domain.

Thus, using the elastic viscoelastic analogy, the transform Dundurs' Parameters are given by:

$$s\alpha^*(s) = \frac{\mu_1(1 - s\nu_2^*(s)) - s\mu_2^*(s)(1 - \nu_1)}{\mu_1(1 - s\nu_2^*(s)) + s\mu_2^*(s)(1 - \nu_1)}$$

or,

$$\alpha^*(s) = \frac{1}{s} \left[ \frac{\mu_1(1 - s(\frac{B_1}{s} - \frac{B_2}{s + \phi})) - s(\frac{A_1}{s} + \frac{A_2}{s + \phi})(1 - \nu_1)}{\mu_1(1 - s(\frac{B_1}{s} - \frac{B_2}{s + \phi})) + s(\frac{A_1}{s} + \frac{A_2}{s + \phi})(1 - \nu_1)} \right] \quad (5.15a)$$

and,

$$s\beta^*(s) = \frac{\mu_1(1 - 2s\nu_2^*(s)) - s\mu_2^*(s)(1 - 2\nu_1)}{2[\mu_1(1 - s\nu_2^*(s)) + s\mu_2^*(s)(1 - \nu_1)]}$$

Or,

$$\beta^*(s) = \frac{1}{s} \left[ \frac{\mu_1(1 - 2s(\frac{B_1}{s} - \frac{B_2}{s + \phi})) - s(\frac{A_1}{s} + \frac{A_2}{s + \phi})(1 - 2\nu_1)}{2[\mu_1(1 - s(\frac{B_1}{s} - \frac{B_2}{s + \phi})) + s(\frac{A_1}{s} + \frac{A_2}{s + \phi})(1 - \nu_1)]} \right] \quad (5.15b)$$

Using the inverse Laplace transformation of Equation (5.15), the Dundurs' parameter in time domain are given by:

$$\alpha(t) = \frac{(e^\varepsilon - 1)(\mu_2(\infty)(\nu_1 - 1) - \mu_1(\nu_2(\infty) - 1))}{\mu_2(\infty)(\nu_1 - 1) + \mu_1(\nu_2(\infty) - 1)} + \frac{e^\varepsilon (\mu_2(0)(1 - \nu_1) + \mu_1(\nu_2(0) - 1))}{\mu_1(\nu_2(0) - 1) + \mu_2(0)(\nu_1 - 1)} \quad (5.16a)$$

and,

$$\beta(t) = \frac{1}{2} \left[ \frac{(e^\varepsilon - 1)(\mu_1(1 - 2\nu_2(\infty)) + \mu_2(\infty)(2\nu_1 - 1))}{\mu_2(\infty)(\nu_1 - 1) + \mu_1(\nu_2(\infty) - 1)} + \frac{e^\varepsilon (\mu_2(0)(1 - 2\nu_1) + \mu_1(2\nu_2(0) - 1))}{\mu_1(\nu_2(0) - 1) + \mu_2(0)(\nu_1 - 1)} \right] \quad (5.16b)$$

$$\text{where, } \varepsilon = -\frac{\varphi(A_1(\nu_1 - 1) + \mu_1(B_1 - 1))}{(A_1 + A_2)(\nu_1 - 1) + \mu_1(B_1 - B_2 - 1)} t$$

$$\text{Or, } \varepsilon = -\frac{\varphi(\mu_2(\infty)(\nu_1 - 1) + \mu_1(\nu_2(\infty) - 1))}{\mu_2(0)(\nu_1 - 1) + \mu_1(\nu_2(0) - 1)} t$$

Similarly, using the same procedure as described in the earlier section, the eigenvalue equation (Equation 4.18) in the time domain is given by:

$$\begin{aligned} & \tau_1 \sin^2 \lambda \pi - \tau_2 \cdot 2(2\lambda^2 \cos^2 \gamma - 1) \sin \lambda \pi \sin 2\lambda \gamma + \tau_3 \cdot 4\lambda^2 \sin \lambda \pi \sin 2\lambda \gamma \cos^2 \gamma \\ & + \tau_4 \cdot 4\lambda^2 \cos^2 \gamma (1 - \cos \lambda \pi \cos 2\lambda \gamma - 2\lambda^2 \cos^2 \gamma) + \tau_5 \cdot \{\sin^2 2\lambda \gamma + 4\lambda^2 (\lambda^2 - 1) \cos^2 \gamma - \lambda^4 \sin^2 2\gamma\} \\ & + \tau_6 \cdot \{4\lambda^2 \cos^2 \gamma (\lambda^2 \cos^2 \gamma - 1 + \cos \lambda \pi \cos 2\lambda \gamma) + (\cos \lambda \pi - \cos 2\lambda \gamma)^2\} = 0 \end{aligned} \quad (5.17)$$

where,

$$\tau_1 = (\mu_1(\nu_2(\infty) - 1) + \mu_2(\infty)(\nu_1 - 1))^2 - e^{-\phi t} ([\mu_2(0) - \mu_2(\infty)](\nu_1 - 1) - [\nu_2(\infty) - \nu_2(0)]\mu_1) \\ (\mu_1(2 - 2\nu_2(\infty) + [\nu_2(\infty) - \nu_2(0)](1 - \phi)) - 2\mu_2(\infty)(\nu_1 - 1) + [\mu_2(0) - \mu_2(\infty)](\nu_1 - 1)(\phi - 1))$$

$$\tau_2 = \mu_1^2(\nu_2(\infty) - 1)^2 - [\mu_2(\infty)]^2(\nu_1 - 1)^2 + e^{-\phi t} ([\mu_2(0) - \mu_2(\infty)]([\mu_2(0) - \mu_2(\infty)](\phi t - 1) - 2\mu_2(\infty)(\nu_1 - 1)^2 \dots \\ \dots + [\nu_2(\infty) - \nu_2(0)]\mu_1^2(2 - 2\nu_2(\infty) + [\nu_2(\infty) - \nu_2(0)](\phi t - 1))$$

$$\begin{aligned}\tau_3 = & \frac{1}{2} \{ [\mu_2(\infty)]^2 (3\nu_1 - 1 - 2\nu_1^2) + \mu_2(\infty)\mu_1(\nu_1 - \nu_2(\infty)) + \mu_1^2(1 - 3\nu_2(\infty) + 2[\nu_2(\infty)]^2) \dots \\ & \dots + e^{-\phi t} ((\mu_2(0) - \mu_2(\infty))[2\mu_2(\infty)(3\nu_1 - 1 - 2\nu_1^2) + (\mu_2(0) - \mu_2(\infty))(\phi t - 1)(1 - 3\nu_1 + 2\nu_1^2)] \dots \\ & \dots + \mu_1([\mu_2(\infty) - \mu_2(0)](1 - \phi t) + \nu_1 - \nu_2(\infty))] + \mu_2(\infty)[\mu_2(\infty) - \mu_2(0)]\mu_1 \dots \\ & \dots + [\mu_2(\infty) - \mu_2(0)]^2 \mu_1^2 (3 - 4\nu_2(\infty) + 2[\mu_2(\infty) - \mu_2(0)](1 - \phi t)) \}\end{aligned}$$

$$\begin{aligned}\tau_4 = & \frac{1}{2} \{ [\mu_2(\infty)]^2 (1 - 3\nu_1 + 2\nu_1^2) + [\mu_2(\infty)]\mu_1(\nu_1 + 3 + [\nu_2(\infty)](3 - 4\nu_1) - 2) + \mu_1^2(1 - 3[\nu_2(\infty)] + 2[\nu_2(\infty)]^2) - \dots \\ & \dots - e^{-\phi t} [[\nu_2(\infty) - \nu_2(0)]\mu_1^2(3 - 4[\nu_2(\infty)] + 2[\nu_2(\infty) - \nu_2(0)](1 - \phi t)) - [\mu_2(0) - \mu_2(\infty)]^2(\phi t - 1)(1 - 3\nu_1 + 2\nu_1^2)] \dots \\ & \dots + [\mu_2(0) - \mu_2(\infty)]\mu_1(-2 + [\nu_2(\infty)](3 - 4\nu_1) + 3\nu_1 - [\nu_2(\infty) - \nu_2(0)](\phi t - 1)(4\nu_1 - 3)) \dots \\ & \dots + [\mu_2(\infty)]([\nu_2(\infty) - \nu_2(0)]\mu_1(4\nu_1 - 3) + [\mu_2(0) - \mu_2(\infty)](2 - 6\nu_1 + 4\nu_1^2)) \}\end{aligned}$$

$$\begin{aligned}\tau_5 = & (\mu_2(\infty)(\nu_1 - 1) - \mu_1(\nu_2(\infty) - 1))^2 - e^{-\phi t} [(\nu_2(\infty) - \nu_2(0))\mu_1 + (\mu_2(0) - \mu_2(\infty))(\nu_1 - 1)] \dots \\ & \dots (\mu_1(2\nu_2(\infty) - 2 + (\nu_2(\infty) - \nu_2(0))(\phi t - 1)) - 2\mu_2(\infty)(\nu_1 - 1) + (\mu_2(0) - \mu_2(\infty))(\phi t - 1)(\nu_1 - 1))\end{aligned}$$

$$\begin{aligned}\tau_6 = & \frac{1}{4} \{ (\mu_2(\infty)(2\nu_1 - 1) + \mu_1(1 - 2\nu_2(\infty)))^2 - e^{-\phi t} (2(\nu_2(\infty) - \nu_2(0))\mu_1 + A_2(2\nu_1 - 1)) \dots \\ & \dots (2\mu_1(2\nu_2(\infty) - 1 + (\nu_2(\infty) - \nu_2(0))(\phi t - 1)) + (\mu_2(0) - \mu_2(\infty))(\phi t - 1)(2\nu_1 - 1) + 2\mu_2(\infty)(1 - 2\nu_1)) \}\end{aligned}$$

### 5.5.3 Case-3: Both the shear modulus and Poisson's ratios are time dependent and more accurately represent the behavior of the material

Using the Laplace transformation, the transform equations of Equations (5.7 and 5.8) are:

$$\mu_2^*(s) = \frac{A_1}{s} + \frac{A_2}{s + \phi_1} + \frac{A_3}{s + \phi_2} \quad \text{and} \quad \nu_2^*(s) = \frac{B_1}{s} - \frac{B_2}{s + \phi_3} - \frac{B_3}{s + \phi_4}$$

where, 's' is the Laplace transform parameter and the superscript "\*" indicates that the parameter is in the transformed domain.

Using the elastic viscoelastic analogy, the transform Dundurs' Parameter is given by

$$s\alpha^*(s) = \frac{\mu_1(1 - s\nu_2^*(s)) - s\mu_2^*(s)(1 - \nu_1)}{\mu_1(1 - s\nu_2^*(s)) + s\mu_2^*(s)(1 - \nu_1)}$$

$$\text{Or, } \alpha^*(s) = \frac{1}{s} \left[ \frac{\mu_1 \left( 1 - s \left( \frac{B_1}{s} - \frac{B_2}{s + \phi_3} - \frac{B_3}{s + \phi_4} \right) \right) - s \left( \frac{A_1}{s} + \frac{A_2}{s + \phi_1} + \frac{A_3}{s + \phi_2} \right) (1 - \nu_1)}{\mu_1 \left( 1 - s \left( \frac{B_1}{s} - \frac{B_2}{s + \phi_3} - \frac{B_3}{s + \phi_4} \right) \right) + s \left( \frac{A_1}{s} + \frac{A_2}{s + \phi_1} + \frac{A_3}{s + \phi_2} \right) (1 - \nu_1)} \right]$$

(5.18a)

and,

$$s\beta^*(s) = \frac{\mu_1(1 - 2s\nu_2^*(s)) - s\mu_2^*(s)(1 - 2\nu_1)}{2[\mu_1(1 - s\nu_2^*(s)) + s\mu_2^*(s)(1 - \nu_1)]}$$

$$\text{Or, } \beta^*(s) = \frac{1}{s} \left[ \frac{\mu_1 \left( 1 - 2s \left( \frac{B_1}{s} - \frac{B_2}{s + \phi_3} - \frac{B_3}{s + \phi_4} \right) \right) - s \left( \frac{A_1}{s} + \frac{A_2}{s + \phi_1} + \frac{A_3}{s + \phi_2} \right) (1 - 2\nu_1)}{2[\mu_1 \left( 1 - s \left( \frac{B_1}{s} - \frac{B_2}{s + \phi_3} - \frac{B_3}{s + \phi_4} \right) \right) + s \left( \frac{A_1}{s} + \frac{A_2}{s + \phi_1} + \frac{A_3}{s + \phi_2} \right) (1 - \nu_1)]} \right]$$

(5.18b)

Using the properties expressed by Equations (5.10 and 5.11) and carrying out the Laplace transformation of Equation (5.18), the Dundurs' parameters in time domain are given by

$$\alpha(t) = (987.65 - 19.89e^{-2.795t} + 0.08e^{-1.178t} - 6.48e^{-0.092t} + 0.043e^{-0.055t}) \times 10^{-3}$$

(5.19a)

$$\beta(t) = (999.38 - 4.41e^{-2.795t} + 16.3e^{-1.178t} - 14.68e^{-0.092t} + 26.61e^{-0.055t}) \times 10^{-3}$$

(5.19b)

Similarly, the eigenvalue equation (Equation 4.18) in the time domain is obtained as follows:

$$\begin{aligned} & \tau_1 \sin^2 \lambda \pi - \tau_2 2(2\lambda^2 \cos^2 \gamma - 1) \sin \lambda \pi \sin 2\lambda \gamma + \tau_3 4\lambda^2 \sin \lambda \pi \sin 2\lambda \gamma \cos^2 \gamma \\ & + \tau_4 4\lambda^2 \cos^2 \gamma (1 - \cos \lambda \pi \cos 2\lambda \gamma - 2\lambda^2 \cos^2 \gamma) + \tau_5 \{ \sin^2 2\lambda \gamma + 4\lambda^2 (\lambda^2 - 1) \cos^2 \gamma - \lambda^4 \sin^2 2\gamma \} \\ & + \tau_6 \{ 4\lambda^2 \cos^2 \gamma (\lambda^2 \cos^2 \gamma - 1 + \cos \lambda \pi \cos 2\lambda \gamma) + (\cos \lambda \pi - \cos 2\lambda \gamma)^2 \} = 0 \end{aligned} \quad (5.20)$$

where,

$$\tau_1 = e^{-4.173t} \left( \begin{array}{l} 234.28e^{4.173t} + e^{2.97t} (9.54 - 0.108t) + e^{1.35t} (5.46 - 0.078t) + \dots \\ \dots e^{4.12t} (14.33 - 0.0123t) + e^{4.081t} (1.78 - 0.27 \times 10^{-3} t) \end{array} \right)$$

$$\tau_2 = e^{-4.173t} \left( \begin{array}{l} 231.39e^{4.173t} + e^{2.97t} (9.52 - 0.108t) + e^{1.35t} (0.078t - 0.077) + \dots \\ \dots e^{4.12t} (14.33 - 0.0123t) + e^{4.081t} (0.27 \times 10^{-3} t - 0.012) \end{array} \right)$$

$$\tau_3 = e^{-4.173t} \left( \begin{array}{l} 23.41e^{4.173t} + e^{2.97t} (5.43 - 0.108t) + e^{1.35t} (0.022t - 0.367) + \dots \\ \dots e^{4.12t} (7.99 - 0.0123t) + e^{4.081t} (0.08 \times 10^{-3} t - 0.108) \end{array} \right)$$

$$\tau_4 = e^{-4.173t} \left( \begin{array}{l} 23.12e^{4.173t} + e^{2.97t} (5.41 - 0.108t) - e^{1.35t} (0.022t + 1.17) + \dots \\ \dots e^{4.12t} (7.99 - 0.0123t) - e^{4.081t} (0.08 \times 10^{-3} t + 0.397) \end{array} \right)$$

$$\tau_5 = e^{-4.173t} \left( \begin{array}{l} 228.53e^{4.173t} + e^{2.97t} (9.50 - 0.108t) - e^{1.35t} (0.078t + 5.30) + \dots \\ \dots e^{4.12t} (14.32 - 0.0123t) - e^{4.081t} (0.27 \times 10^{-3} t + 1.76) \end{array} \right)$$

$$\tau_6 = e^{-4.173t} \left( \begin{array}{l} 2.34e^{4.173t} + e^{2.97t} (1.31 - 0.108t) - e^{1.35t} (0.063t + 0.236) + \dots \\ \dots e^{4.12t} (1.646 - 0.0123t) - e^{4.081t} (0.22 \times 10^{-3} t + 0.083) \end{array} \right)$$

## 5.6 STRESS SINGULARITY AND CRITICAL BONDING ANGLE FOR AN ALUMINUM/ EPOXY BONDED JOINT

The order of the stress singularity and the critical bonding angle for an aluminum-epoxy bonded joint are determined using the analytical solutions developed. The elastic properties of aluminum are taken from Chapter 4 (Table 4.1) and the viscoelastic properties of epoxy are described in the previous sections for three different cases of material modeling. The time dependent Dundurs' parameters are determined by using Equations (5.13), (5.16) and (5.19) for the above three cases respectively. The variation in Dundurs' parameters ( $\alpha$ ,  $\beta$ ) with time is shown in Figures 5.5 and 5.6.

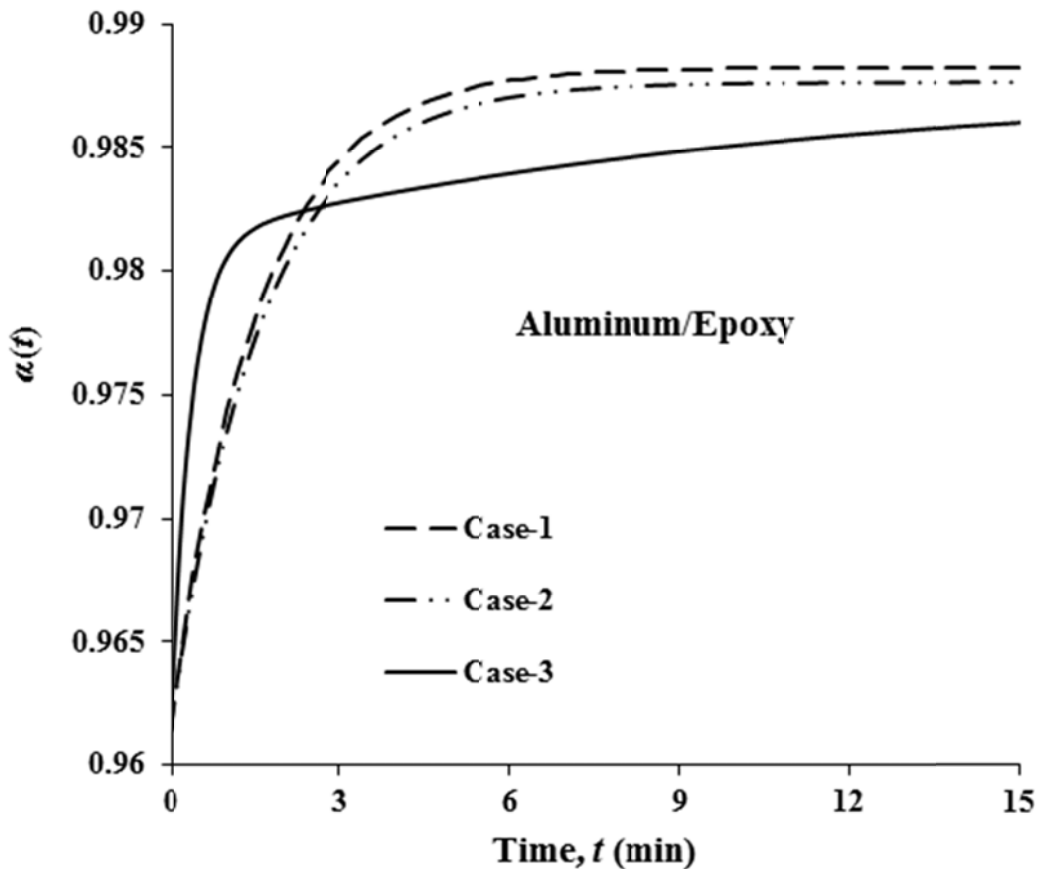


Figure 5.5: Variation of Dundurs' parameter  $\alpha(t)$  with time

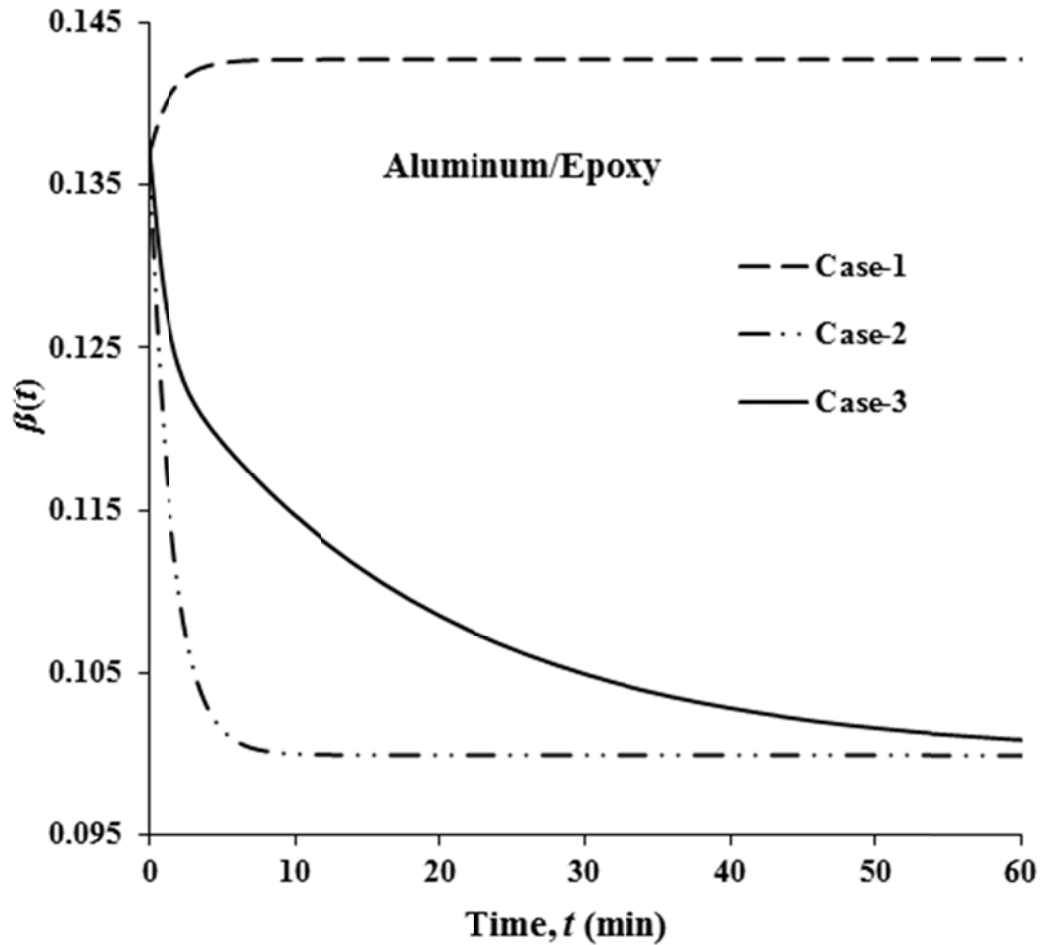


Figure 5.6: Variation of Dundurs' parameter  $\beta(t)$  with time

From Figure 5.5, it can be seen that the time dependency of Poisson's ratio has no significant influence on  $\alpha$ . For the same viscoelastic shear modulus, the value of  $\alpha$  is almost the same for either the constant or time-dependent Poisson's ratio (Case-1 and Case- 2) of epoxy. However,  $\alpha$  is influenced by the viscoelastic shear modulus. Thus, the value of  $\alpha$  for case-3 is different from those for the

cases-1&2. However, Figure 5.6 shows that the time dependency of Poisson's ratio has a more significant influence on parameter  $\beta$ . In addition, for the same viscoelastic shear modulus the value of  $\beta$  increases with time for a constant Poisson's ratio, whereas it decreases with a time-dependent Poisson's ratio. For case-3, the variation in  $\beta$  with time follows the same trend as that of case-2 but at a slower rate. After sufficient time, the Dundurs' parameter  $\beta$  is expected to be the same for these two cases (Case-2 and Case-3). Since, for any specific bonding angle, the eigenvalue  $\lambda$  or the order of the stress singularity depends on both the Dundurs' parameters ( $\alpha, \beta$ ), assuming a constant Poisson's ratio, the true behavior of the stress singularity cannot be predicted accurately.

Next, the eigenvalue  $\lambda$  is determined for different bonding angles from Equations (5.14), (5.17) and (5.20) for the three different material models, respectively. It is noted that the order of the stress singularity is  $(\lambda-1)$  and the condition for the elimination of the stress singularity is  $\lambda > 1$ . Higher values of  $\lambda$  (when  $\lambda < 1$ ) indicates a lower order of the stress singularity at the interface corner. Figure 5.7 shows the variation of  $\lambda$  with time for a 40 degree bonding angle.

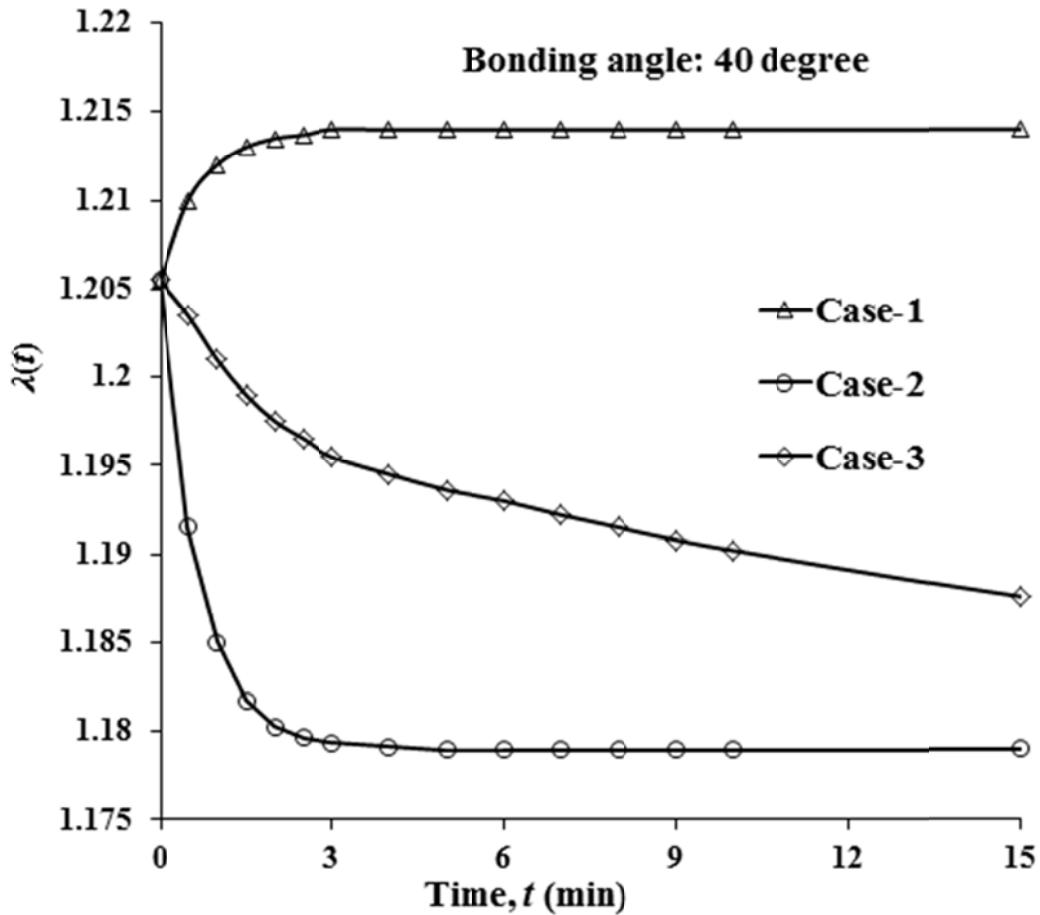


Figure 5.7: Variation of  $\lambda$  with time for a bonding angle of  $40^\circ$

At this bonding angle the value of  $\lambda$  is always greater than 1 for all three cases. This indicates that there is no stress singularity at the interface corner for the  $40^\circ$  bonding angle. For case-1, the value of  $\lambda$  increases with time; indicates the order of the stress singularity decreases with time. However, for the other two cases, the trend is just opposite. Therefore, prediction based on case-1 is a more conservative one for this bonding angle. In Figure 5.8, the results are shown for a bonding angle of  $60^\circ$ . It is seen that for the bonding angle of  $60^\circ$ , a stress singularity always exists ( $\lambda < 1$ ) at the interface corner. The

time effects on the change in value of  $\lambda$  for the three different cases are clearly noticeable here.

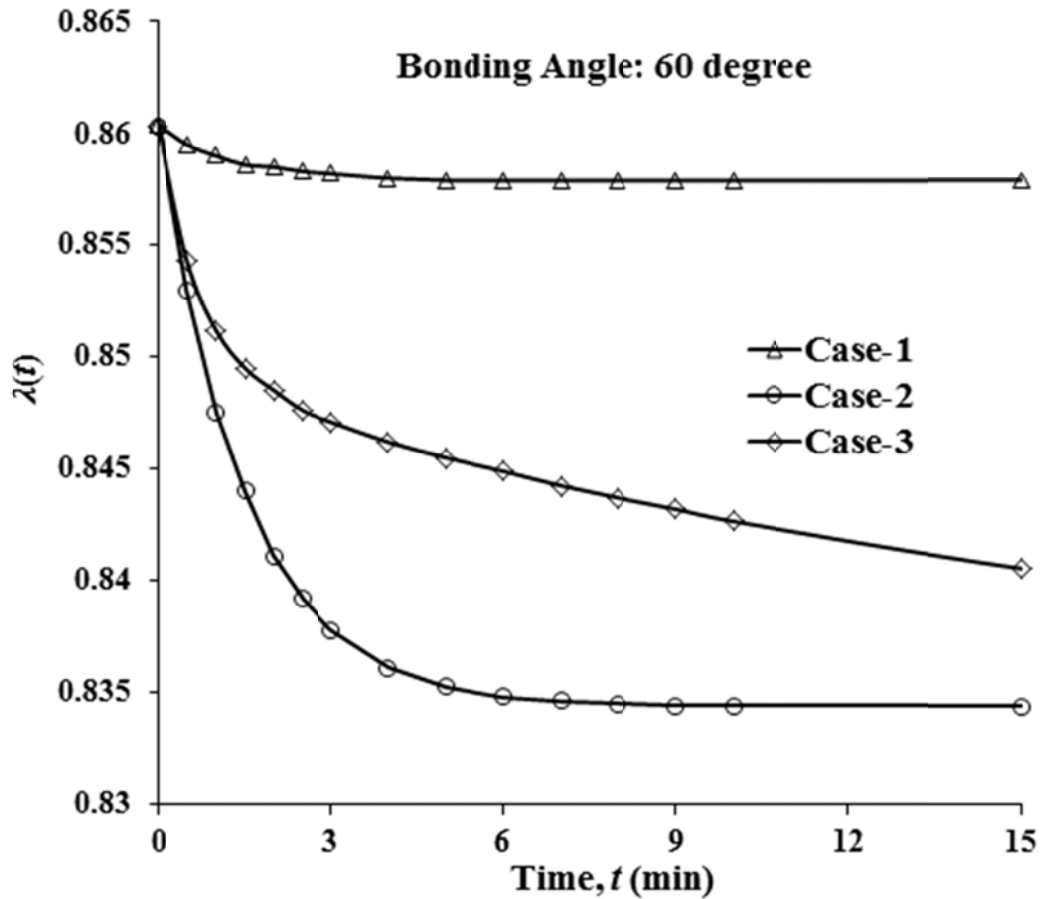


Figure 5.8: Variation of  $\lambda$  with time for a bonding angle of  $60^\circ$

The stress singularity for cases-2 &3 are more pronounced than that for the case-1 (constant Poisson's ratio). These results have a considerable impact on the design of the bi-material interface. Case-1 underestimates the order of the stress singularity, whereas, Case-2 over estimates the order of stress singularity. Therefore, the prediction of case-2 is a more conservative one regarding the order of stress singularity for the bonding angle of 60 degrees. The critical bonding

angle is determined, for which the value of  $\lambda$  changes from less than 1 to greater than 1. From Figures 5.7 and 5.8, it is already known that the critical bonding angle is between 40 and 60 degrees. The eigenvalue  $\lambda$  is determined for other bonding angles between 40 and 60 degrees with increments of 1 degree. In Figure 5.9, the eigenvalue,  $\lambda$ , for Case-1 is shown for bonding angles of 49 and 50 degrees.

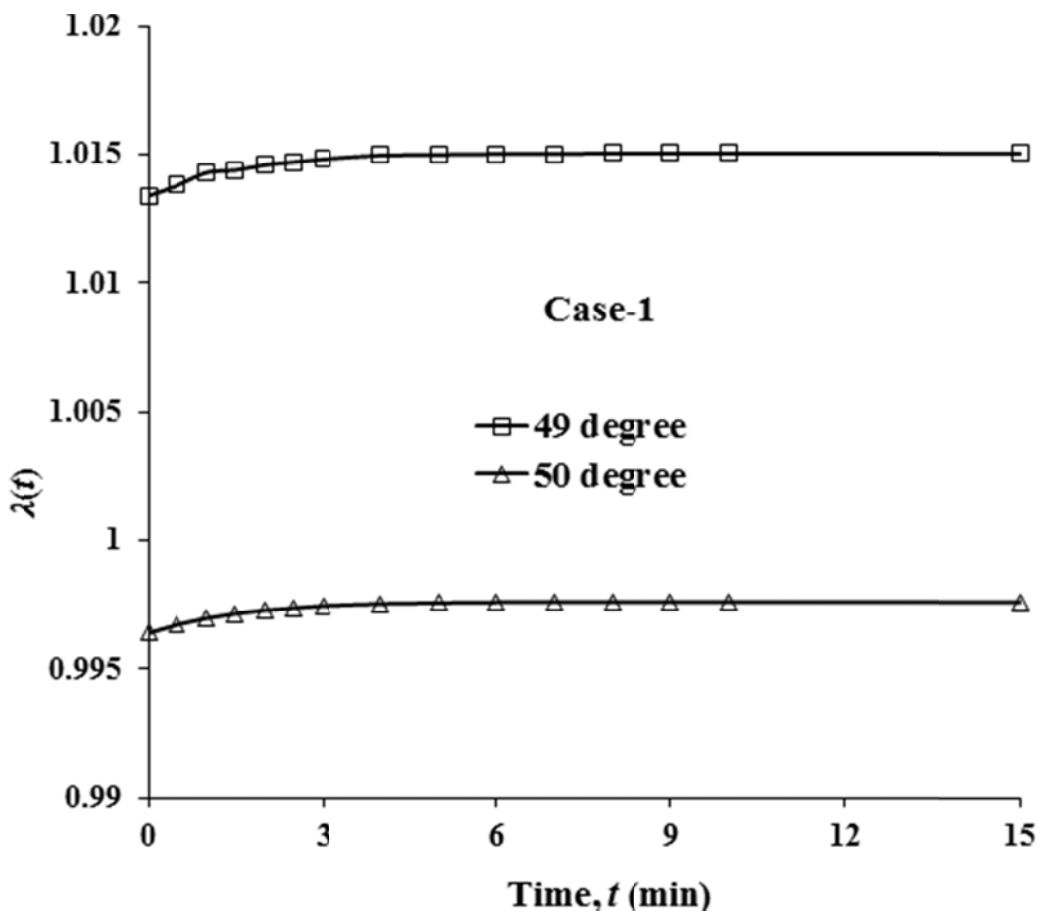


Figure 5.9: Variation of  $\lambda$  with time for bonding angles 49° and 50° for Case-1

It is therefore concluded that the critical bonding angle for the present aluminum/epoxy interface is in between 49 and 50 degrees, when the Poisson's ratio of the viscoelastic material (epoxy) is assumed as constant (Case-1).

Figure 5.10 shows the values of  $\lambda$  for bonding angles of 49 degrees, for the three different cases. It is interesting to see that for a bonding angle of 49 degrees, the eigenvalue  $\lambda$  is greater than 1 at  $t = 0$  but evolves to be less than 1 after a few minutes by using cases-2 & 3. It indicates that initially there is no stress singularity for the bonding angle of 49 degrees, but after few minutes the stress singularity appears at the interface corner.

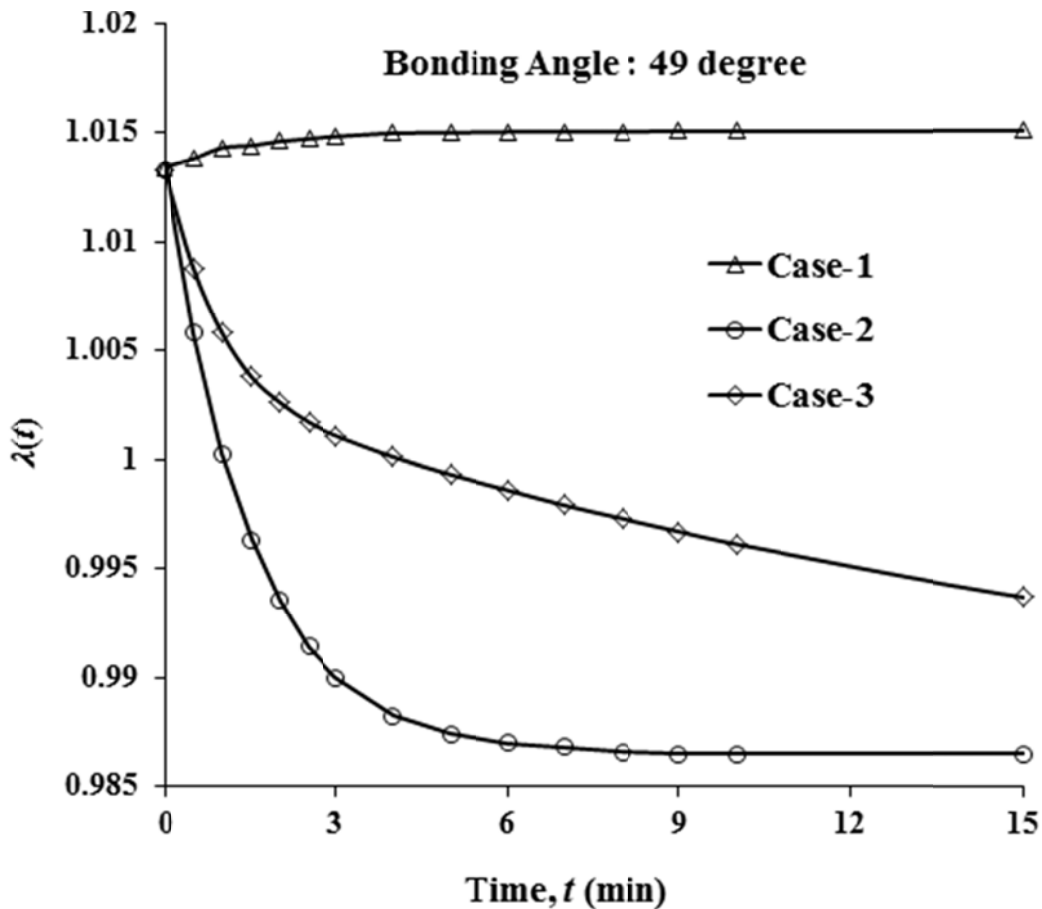


Figure 5.10: Variation of  $\lambda$  with time for a bonding angle of  $49^\circ$

Figure 5.11 shows the variation of eigenvalue  $\lambda$  for a bonding angle of 48 degrees. It is seen that for all three cases, the eigenvalue  $\lambda$  is greater than 1 ( $\lambda > 1$ ); means the singularity disappears for the bonding angle 48°. Thus, considering the time-dependency of Poisson's ratio (cases-2 and 3), the critical bonding angle for the present aluminum/epoxy is determined as being between 48 and 49 degrees.

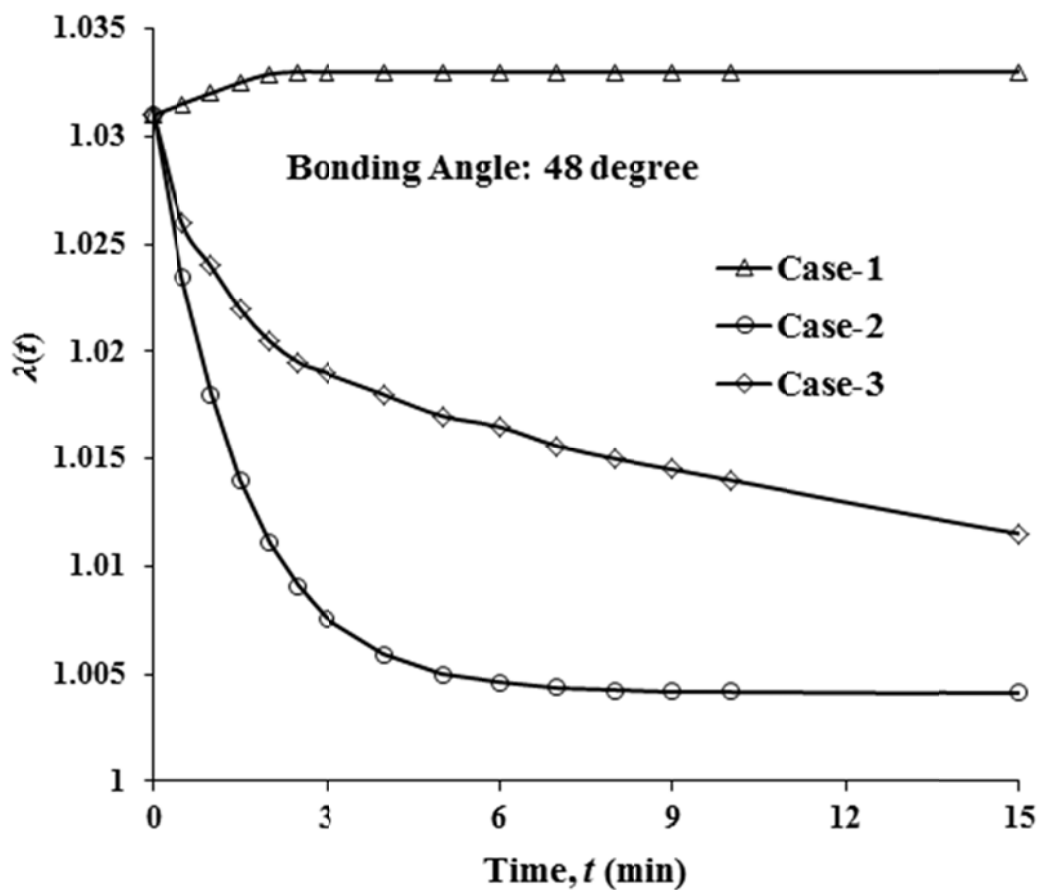


Figure 5.11: Variation of  $\lambda$  with time for a bonding angle of 48°

## 5.7 DETERMINATION OF THE CRITICAL BONDING ANGLE BY FINITE ELEMENT ANALYSIS

Finite element analysis is carried out by using commercial code ANSYS to determine the stress distribution along the interface and to verify the results obtained from the analytical model. The axi-symmetric finite element model of the suggested specimen is shown in Figure 2.2, where aluminum is considered as material-1 and epoxy as the material-2. 8-nodes PLANE 183 element is used as the element type for both materials. This element has viscoelasticity and large strain capabilities. The mesh sizes close to the interface are made very fine and coarse mesh is used for the area away from the interface to reduce the computational time. Linear viscoelastic Prony model (consistent with Case-3) is used for the modeling of epoxy.

The radius of the cylindrical specimen,  $R$ , is 10 mm and a tensile load is applied at the top end while the bottom end is fixed in the longitudinal direction. The maximum axial stress of 10 MPa is applied in 30 equal load steps and the time at the end of the load step is 15 minutes (900 seconds). After solving the nonlinear problem (material nonlinearity), the distribution of stress components along the interface are recorded. From the stress components, using stress transformation, the normal and shear stress components along the interface are determined. An effective interface stress is defined as  $\sigma_{eff} = \sqrt{\sigma_n^2 + 3\tau^2}$  (where,  $\sigma_n$  and  $\tau$  are the normal and shear interface stress components, respectively) and are also calculated. The similar analyses are carried out for specimens with

different bonding angles. If the stress at the interface corner increases with the refinement of mesh size and doesn't converge to a finite value, this indicates the presence of the stress singularity. For a non-singular stress case the stress at the interface corner converges to a finite value. The results obtained from the last step of loading are presented here only.

The distributions of effective interface stress along the interface are shown in Figure 5.12 for two different bonding angles of  $40^\circ$  and  $60^\circ$ . It is seen that excessive stresses exist near the free edge of the interface for the bonding angle of  $60^\circ$ . These stress values increase without convergent limits with increasing the mesh density, indicating that the stress singularity exists at the free edge. However, for the case of the  $40^\circ$  bonding angle, finite values of the interface stresses are exhibited and the stress convergence is confirmed by increasing FEM mesh density. These results are consistent with those obtained from the analytical solution.

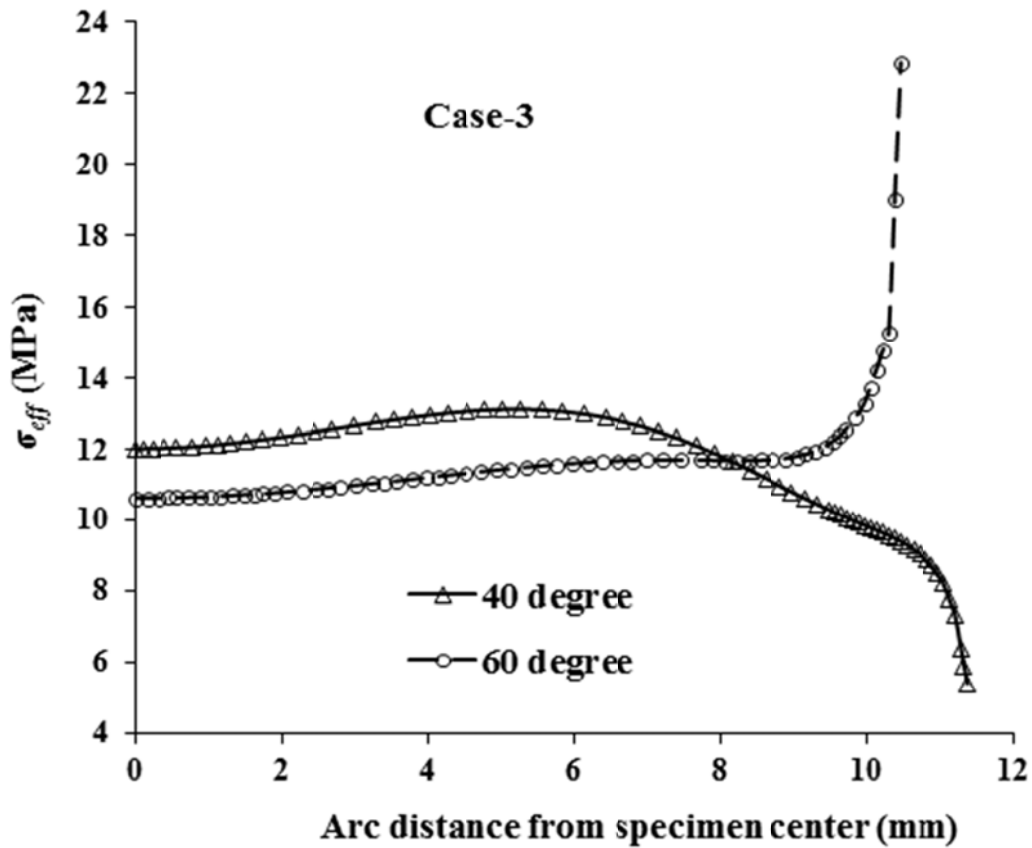


Figure 5.12: Effective stress along the interface for bonding angles of 40° and 60° (Case-3)

Then the same analysis is carried out for other bonding angles from 40° to 60° by the increment of 1° each time. The distributions of the effective interface stress along the interface for the bonding angles of 48° and 49° are shown in Figure 5.13. It is found that the shape of the curve near the free edge starts to change from downward to upward direction, when the bonding angle changes

from  $48^\circ$  to  $49^\circ$ . This confirms that the value of the critical bonding angle for the current aluminum/epoxy (elastic/viscoelastic) bi-material interface is between  $48^\circ$  and  $49^\circ$ . This result is the same as obtained by using the analytical solution in the previous section. Thus, the accuracy of the analytical model is also verified.

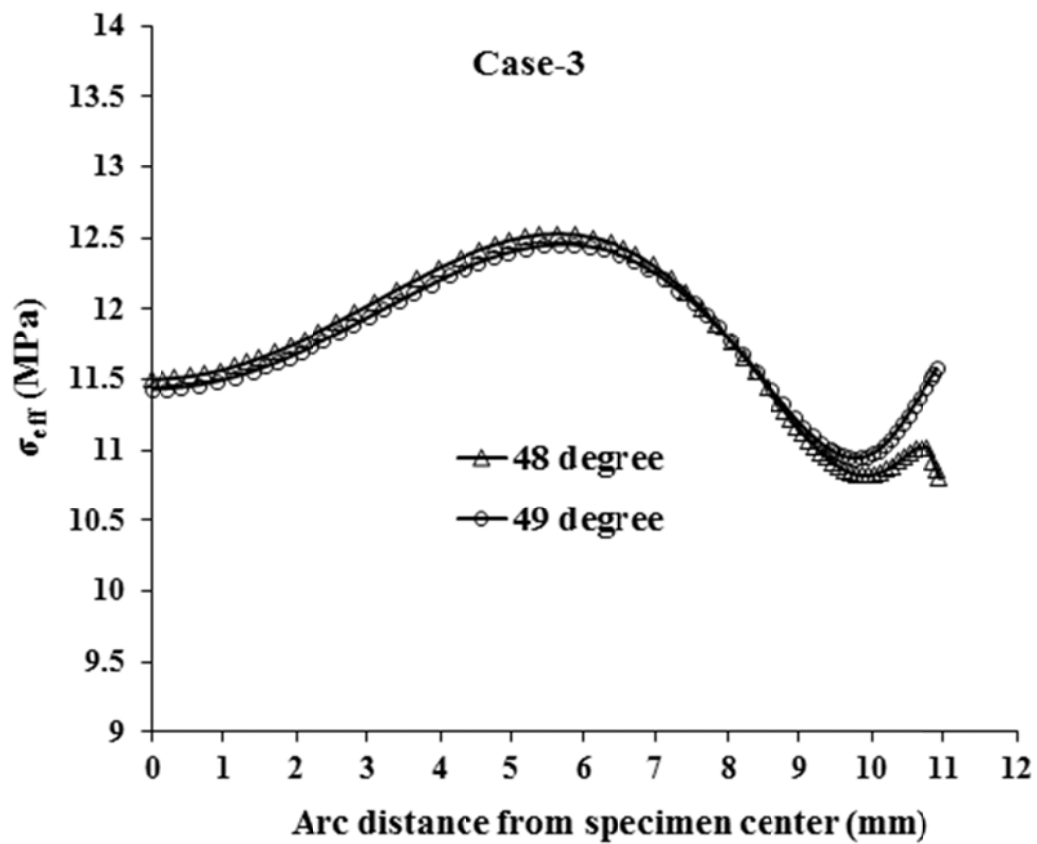


Figure 5.13: Effective stress along the interface for bonding angles of  $48^\circ$  and  $49^\circ$  (Case-3)

## 5.8 DETERMINATION OF THE INTERFACE BONDING STRENGTH BETWEEN ELASTIC/VISCOELASTIC MATERIALS

The critical bonding angle  $\theta_c$  is determined in the previous section as approximately  $48^\circ$ . Therefore, the test specimens are manufactured with a bonding angle of  $40^\circ$ , which satisfies the condition of eliminating the stress singularity ( $\theta_0 < \theta_c$ ). The geometry of the specimen is similar as shown in Figure 4.6 (Chapter 4). The details about the specimen preparation can be found in Section 4.3 of Chapter 4.

A multi-axial testing machine is used to conduct the tests. This machine has the capacity to apply combined loading (torsion and tension). Using the controller of the machine, various combinations of normal and shear load are applied on the specimens. With the help of an accurate data acquisition system, the failure loads and time required to reach the failure loads are recorded for each test and are given in Table 5.2.

Table 5.2: Maximum failure loads and time required to reach failure

No	Tensile load (N)	Torsional Load (N. m)	Time (sec)
1	0	43.6	327.03
2	1646.34	44.1	330.74
3	3368.84	33.79	287.6
4	5473.60	21.96	328.04
5	6441.28	0	580.68

The viscoelastic epoxy material is time and rate dependent. The slower is the loading rate, the more the viscoelastic effect. Figure 5.14 shows the stress-strain relation for the epoxy at different loading rates.

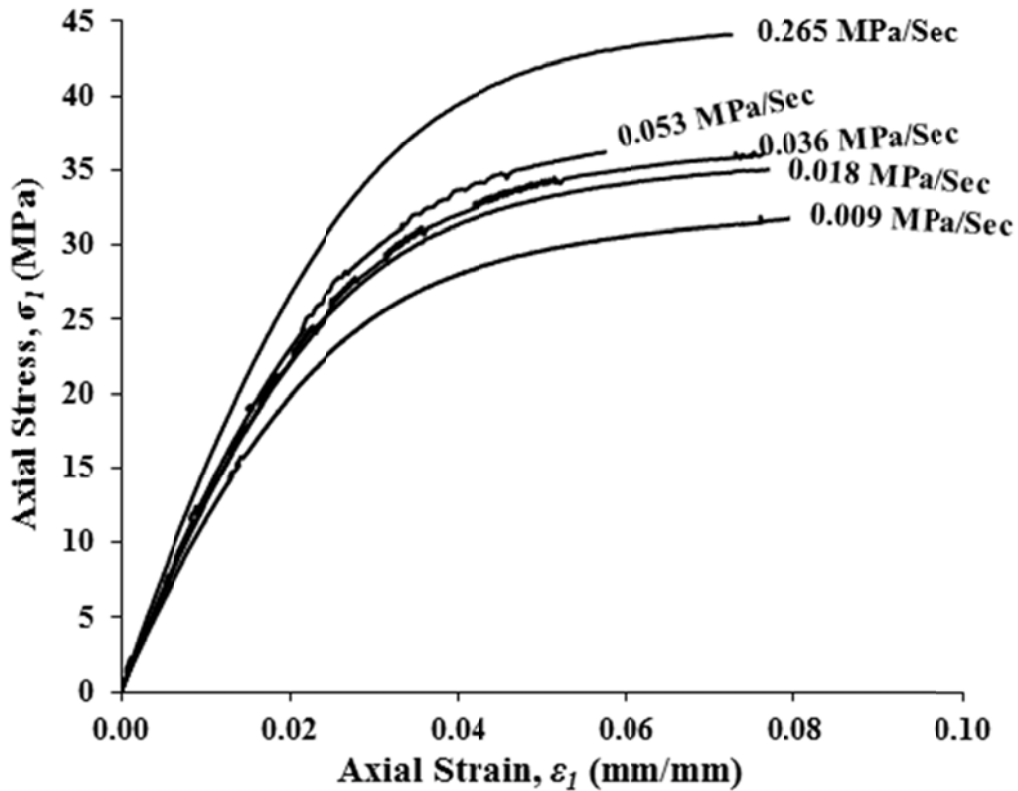


Figure 5.14: Stress-strain curves of epoxy for different loading rates

### 5.8.1 Iterative method for determining the interface bonding strength envelope

In order to find the stress distribution along the interface corresponding to the failure load given in Table 5.2, finite element analyses are carried out. Non-linear (material nonlinearity) finite element analysis is carried out by using the commercial code ANSYS. Though axi-symmetric PLANE 183 element is used

for the determination of the critical bonding angle, it cannot be used for the torsional loading (non-axi-symmetric load) case. In fact, there is no 2-D element is available in ANSYS that can be used for the torsional loading on a viscoelastic material. Therefore a 3D analysis using SOLID 185 element is carried out for combined torsional and normal loadings. Figure 5.15 shows the 3D finite element model of the specimen.

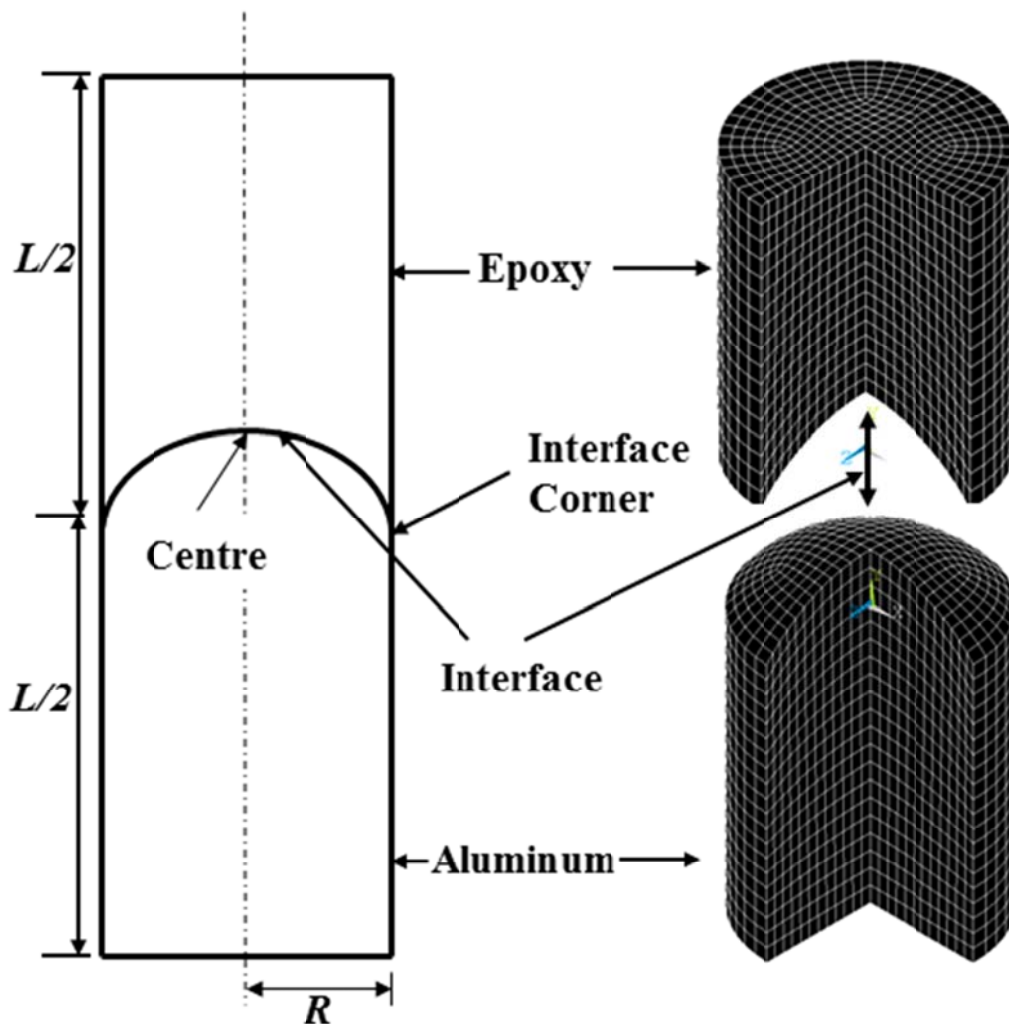


Figure 5.15: 3D finite element model for the bi-material interface bonding strength specimen

It is given earlier (Figure 4.6 in Chapter 4) that the actual length of each part of material in the specimen is  $L/2 = 60$  mm. 3D modeling of the specimen in ANSYS with this dimension requires a large number of elements, which in other word will make the problem time consuming. To determine an optimum length of the FEM model, four models with different lengths,  $L/2 = 15, 20, 25$  and  $30$  mm are analyzed for an arbitrary tensile load of  $10$  MPa applied on the top. The bottom of the model is kept fixed. The effective interface stress at the interface corner for the above four cases are plotted against the ratio of the model length to the specimen diameter ( $D = 20$  mm) and is shown in Figure 5.16.

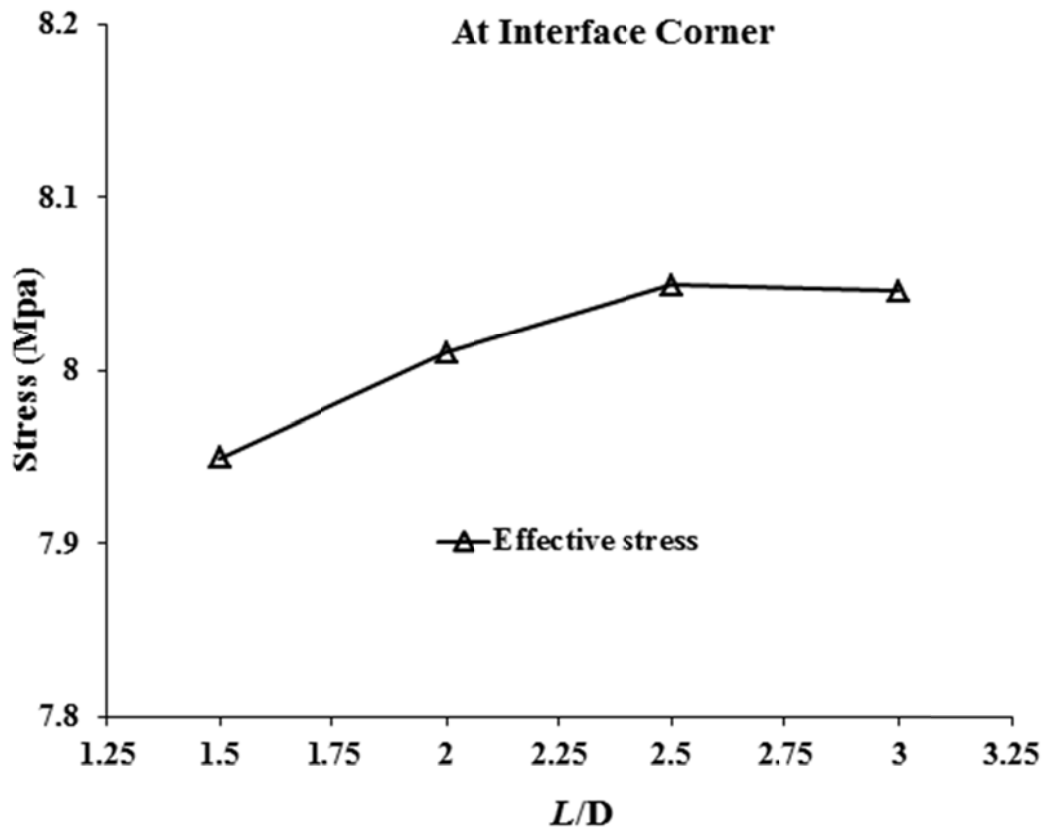


Figure 5.16: Effect of finite element model length on the analysis

It is seen that when,  $L/D = 2.5$ , means,  $L/2 = 25$  mm, the model gives an accurate enough value. Thus, the model with  $L/2 = 25$  mm and  $R = 10$  mm is used for this analysis. This model consists of 15,984 elements and 17,366 nodes.

The failure loads and corresponding times to failure obtained from tests (given in Table 5.2) are applied in the finite element analysis. The interface normal, shear and effective interface stress curves are obtained as described earlier. As an example, the stress curves along the interface of Specimen No. 3 with maximum tensile and torsional loads of 3368.84 N and 33.79 N-m, respectively, are shown in Figure 5.17.

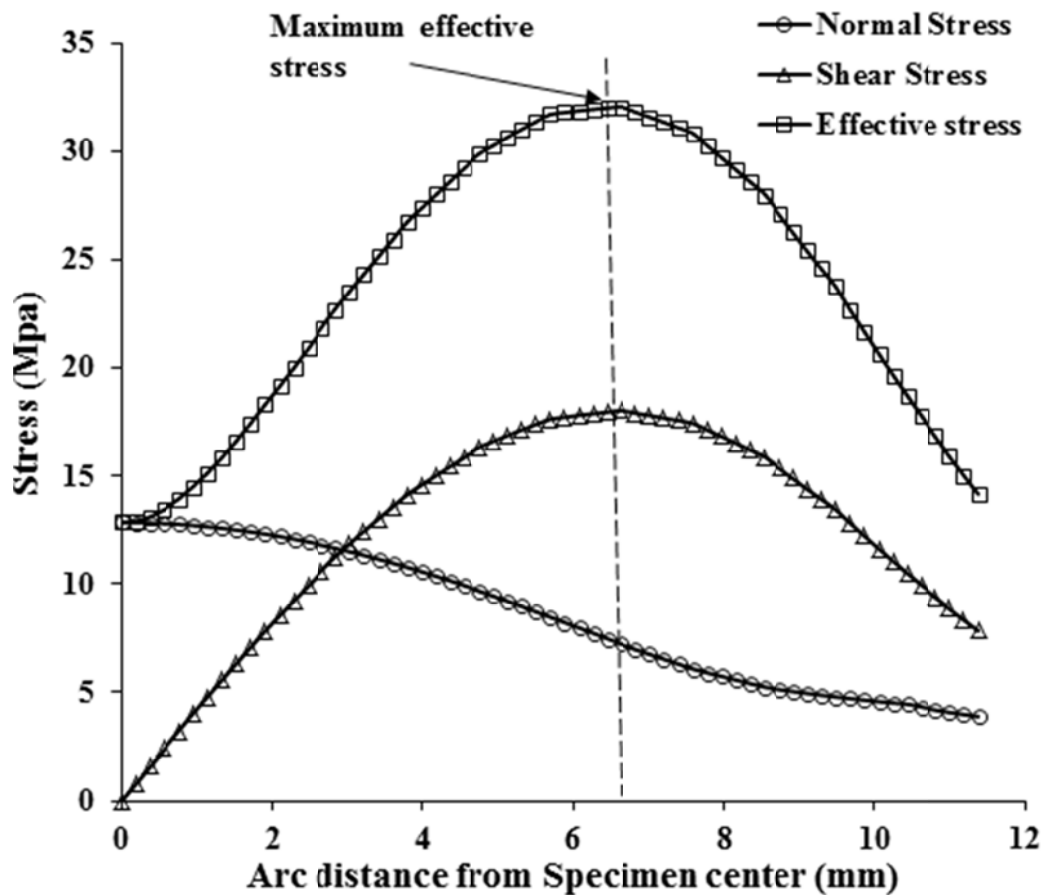


Figure 5.17: Stress distribution along the interface for combined loading

For the pure torsional loading case, there is no normal interface stress component; therefore, the maximum interface shear stress along the interface, denoting as  $\tau_s$ , is directly taken as the shear strength of the bi-material interface. Figure 5.18 shows the shear stress distribution along the interface for the specimen subjected to maximum pure torsional loading. The normal stress along the interface vanishes in this case. The maximum value of the shear stress is  $\tau_s = 21.85$  MPa.

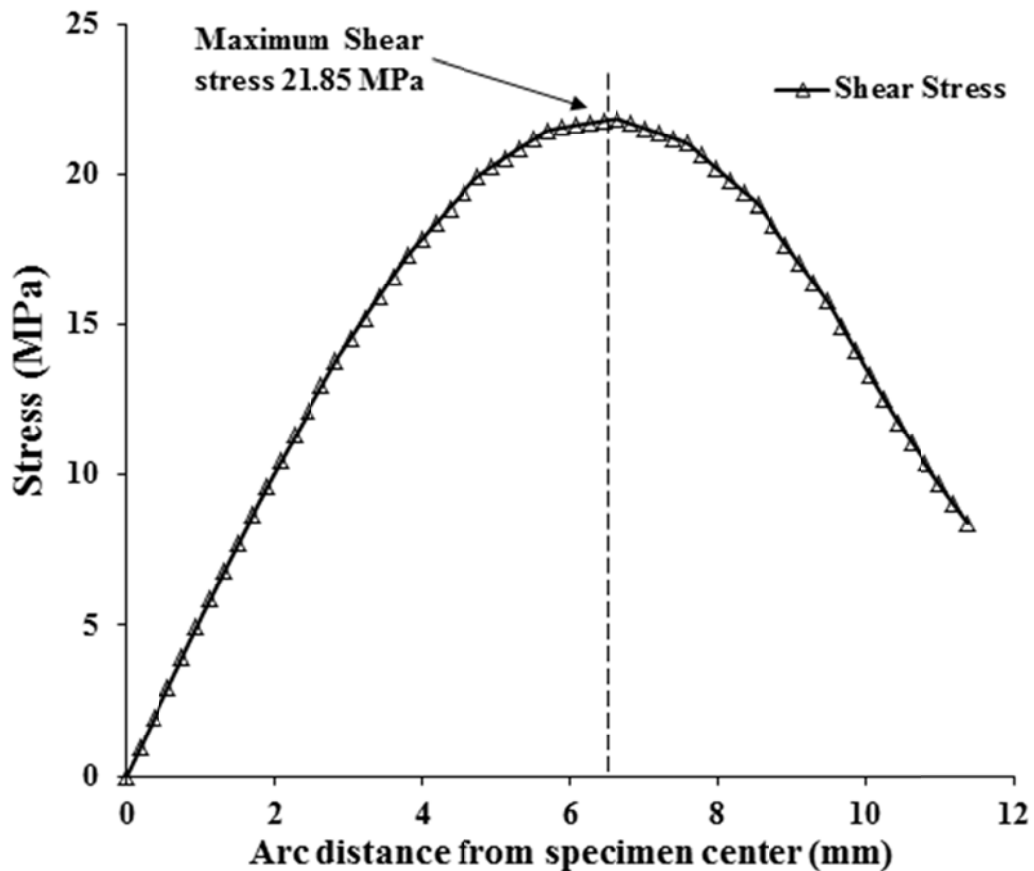


Figure 5.18: Stress distribution along the interface for pure torsional loading case

For the pure global normal loading and other combined normal-shear loading cases, both normal and shear interface stress components exist along the interface. Therefore, a normal-shear bonding strength criterion (envelope) is required to accurately define the interface bonding strength. The criterion is expressed as,

$$f(\sigma_n, \tau) = C \quad (5.21)$$

where  $\sigma_n$  and  $\tau$  are interface normal and shear stress components, respectively, and  $C$  is a constant. The function  $f$  and the constant  $C$  can be determined through the following iteration procedure:

(i) For the first trial condition, the effective interface stress criterion is assumed, so

$$f^{(1)}(\sigma_n, \tau) = \sqrt{\sigma_n^2 + 3\tau^2} = \sqrt{3}\tau_s$$

The constant  $C = \sqrt{3}\tau_s$  is obtained by applying the pure torsional loading case in which  $\sigma_n = 0$ .

Therefore, the first trial criterion (effective stress) is

$$f^{(1)} = \sqrt{\sigma_n^2 + 3\tau^2} = 37.85$$

Or, it can be written as

$$\left(\frac{\sigma_n}{37.85}\right)^2 + \left(\frac{\tau}{21.85}\right)^2 = 1 \quad (5.22)$$

Now, from the interface normal and shear stress curves of each loading test case, the location of the maximum value of  $\sqrt{\sigma_n^2 + 3\tau^2}$  along the interface is

found; the corresponding pair of normal and shear stress values for each test case is recorded. These pairs of stresses are denoted as  $[\sigma_{n,k}, \tau_k]^{(1)}$ ,  $k = 1, \dots, 5$ .

Figure 5.19 shows the points,  $[\sigma_{n,k}, \tau_k]^{(1)}$ ,  $k = 1, \dots, 5$  obtained and the effective interface stress criterion curve (Equation 5.22). Except for the point  $[0, \tau_s]$  obtained from the pure shear test, no other points are on the curve expressed by Equation (5.22).

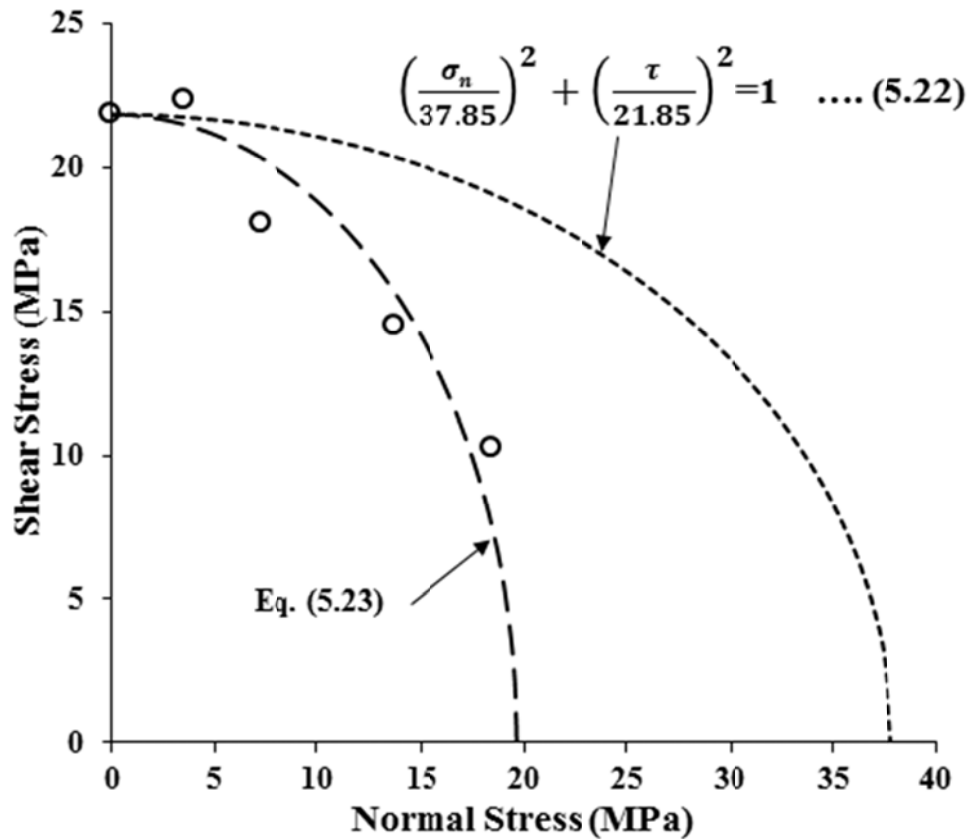


Figure 5.19: Interface bonding strength envelope based on effective stress criterion

Next, the second trial criterion is found by applying the best fit curve technique. By keeping the value  $\tau_s = 20.86$  MPa, it is found that the following equation (Eq. 5.23) fits the previous data points very well (see Figure 5.19)

$$\left(\frac{\sigma_n}{19.67}\right)^2 + \left(\frac{\tau}{21.85}\right)^2 = 1 \quad (5.23)$$

Based on the above second trial criterion, a second set of stress points  $[\sigma_{n,k}, \tau_k]^{(2)}$ ,  $k = 1, \dots, 5$ , is obtained based on the maximum values of the left side of Equation (5.23) for each test case. Figure 5.20 shows both Equation (5.23) and corresponding points  $[\sigma_{n,k}, \tau_k]^{(2)}$ ,  $k = 1, \dots, 5$ .

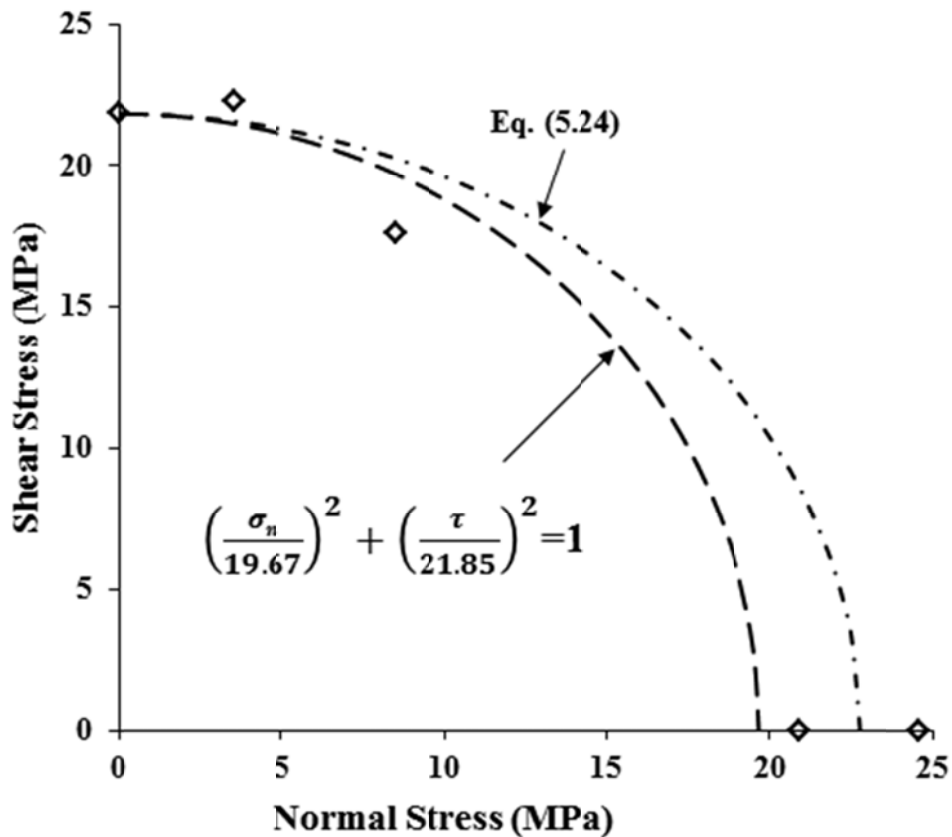


Figure 5.20: Interface bonding strength envelope after 1<sup>st</sup> iteration

It is clear that this criterion doesn't fit the data points very well (Figure 5.20). As previous, the third criterion is obtained by fitting the stress points  $[\sigma_{n,k}, \tau_k]^{(2)}$ ,  $k = 1, \dots, 5$  as follows

$$\left(\frac{\sigma_n}{22.75}\right)^2 + \left(\frac{\tau}{21.85}\right)^2 = 1 \quad (5.24)$$

Following the same procedure, for this trial criterion (Equation 5.24), a third set of stress points  $[\sigma_{n,k}, \tau_k]^{(3)}$ ,  $k = 1, \dots, 5$ , is obtained for each test case. Figure 5.21 shows both Equation (5.24) and corresponding stress points  $[\sigma_{n,k}, \tau_k]^{(3)}$ ,  $k = 1, \dots, 5$ .

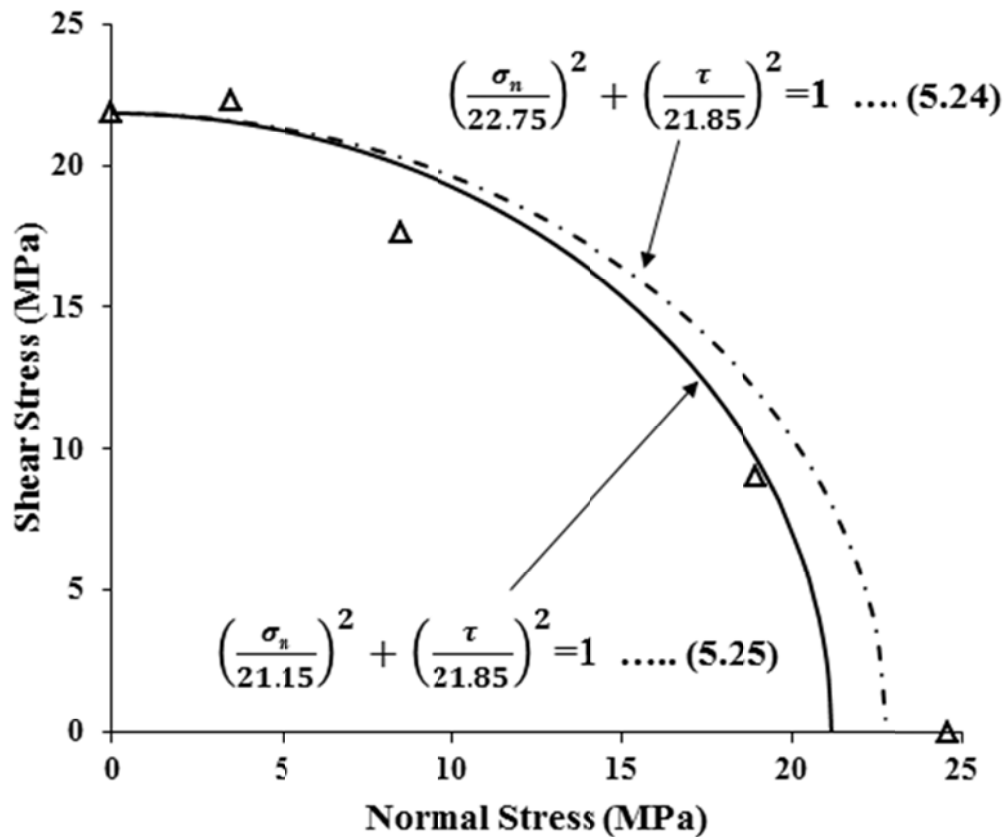


Figure 5.21: Bonding strength envelope for the tested aluminum/epoxy interface

Continuing the iteration procedure, the fourth criterion is obtained as follows (Equation 5.25),

$$\left(\frac{\sigma_n}{21.15}\right)^2 + \left(\frac{\tau}{21.85}\right)^2 = 1 \quad (5.25)$$

This trial condition (Equation 5.25) produces the same data points  $[\sigma_{n,k}, \tau_k]^{(3)}$ , i.e. a converged criterion is obtained. . Therefore, for the tested aluminum/epoxy (elastic/viscoelastic) bi-material interface, Equation (5.25), as shown in Figure 5.21, represents its normal-shear interface bonding strength criterion (envelope) in the range of the first quarter of the normal-shear stress plane.

---

**BIBLIOGRAPHY**

- Brinson, H. F., Brinson, L. C., 2008. *Polymer Engineering Science and Viscoelasticity- An Introduction*, Springer, New York.
- Christensen, R. M., 1982. *Theory of Viscoelasticity - An Introduction*. Second edition, Academic Press, New York.
- Delale, F., Erdogan, F., 1981. Viscoelastic analysis of adhesively bonded joints. *Journal of Applied Mechanics*. 48, 331-338.
- Deng, T. H., Knauss, W. G., 1997. The temperature and frequency dependence of the bulk compliance of poly (vinylacetate): a re-examination”, *Mechanics of Time-Dependent Materials*. 1, 33–49.
- Dundurs, J., 1969. Discussion of edge-bonded dissimilar orthogonal elastic wedges under normal and shear loading. *Journal of Applied Mechanics*. 36, 650-652.
- Fung, Y. C., 1965. *Introductions to Solid Mechanics*. Prentice Hall, New Jersey.
- Lee, E. H., 1954. Stress analysis in viscoelastic bodies. Brown University, TR No. 8, Nord 11446.
- Lee, E. H., 1955. Stress analysis of viscoelastic bodies. *Quarterly of Applied Mathematics*. 13(2), 183-190.

- 
- Lee, S. S., 1997. Free-Edge Stress Singularity in a Two-Dimensional Unidirectional Viscoelastic Laminate Model. *Journal of Applied Mechanics*. 64, 408-414.
- Nagaraja, Y. R., Alwar, R. S, 1980. Viscoelastic Analysis of An Adhesive-Bonded Plane Lap Joint. *Computers and Structures*. 111, 621-627.
- Qian, Z. Q., Akisanya, A. R., 1999. An investigation of the stress singularity near the free edge of scarf joint. *European Journal of mechanics- A/Solids*. 18, 443-463.
- Qian, Z.Q., Akisanya, A.R., Imbabi, M.S., 2000. Edge effects in the failure of elastic/viscoelastic joints subjected to surface tractions. *International Journal of Solids and Structures*. 37, 5973-5994
- Schapary, R. A., 1962. Approximate methods of transform inversion for viscoelastic stress analysis. *Proceedings of 4th U.S. National Congress of Applied Mechanics*. 2, 1075-1085.
- Schiff, J. L., 1999. *The Laplace transform-theory and applications*. Springer-Verlag, New York.
- Tscharnuter, D., Jerabek, M., Major, Z., W. Lang, R.W., 2011. Time-dependent Poisson's ratio of polypropylene compounds for various strain histories. *Mechanics of Time Dependent Materials*. 15 (1), 15-28.

Yadagiri, S., Reddy, C. P., Reddy, T. S., 1987. Viscoelastic analysis of adhesively bonded joints. *Computers and Structures*. 27, 445-454.

## **CHAPTER 6: VISCOELASTIC/VISCOELASTIC BI-MATERIAL INTERFACE**

Part of this chapter has been submitted/ published as

1. **Chowdhuri, M. A. K.,** Xia, Z., 2012. Application of a New Experimental Method to Determine Bi-Material Interface Bonding Strength. *SEM XII International Congress & Exposition on Experimental and Applied Mechanics*, June 11-14, Costa Mesa, California, USA
2. **Chowdhuri, M. A. K.,** Xia, Z., 2012. Stress Singularity Analysis of a Viscoelastic /Viscoelastic Bonded Joint. *ASME 2012 International Mechanical Engineering Congress & Exposition*, Nov 09-15, Houston, Texas, USA (Accepted)

## CHAPTER 6

### VISCOELASTIC/VISCOELASTIC BI-MATERIAL INTERFACE

---

This chapter presents the bi-material interface bonding strength envelope determination of a viscoelastic/viscoelastic bonded joint. For this case, interface between viscoelastic PVC and epoxy materials are considered. Both PVC and epoxy are assumed as linear viscoelastic materials. This chapter is organized as in the following order: scope of the study, material modeling, analytical solution to find the stress singularity and critical bonding angle, and determination of the bonding strength of a PVC/epoxy bi-material interface.

#### 6.1 SCOPE OF THE STUDY

In chapter 5, analyses of the stress singularity and interface bonding strength determination for elastic/viscoelastic bonded joints has been briefly explained. To the best of our knowledge, the analytical solution to determine the stress singularity at the interface corner of a viscoelastic/viscoelastic bonded joint is yet to be further explored. In this study, the analytical solution to determine the stress singularity considering the three different cases of material modeling described in previous chapter (Chapter 5) are developed. Once the stress singularity is eliminated from the interface corner, the interface bonding strength

between two viscoelastic materials is determined based on the proposed method (details about the method have been given in Chapter 2).

## 6.2 VISCOELASTIC PROPERTIES OF PVC

The three different material models described in Chapter 5 for the elastic/viscoelastic interface, are also considered for the material modeling of viscoelastic/viscoelastic interface. It is noted that PVC and epoxy are considered as constituent materials for this study of viscoelastic/viscoelastic interface. Since, the material modeling for epoxy has already briefly described in Chapter 5, the present discussions are kept limited to the material modeling of PVC only.

From the measured data in section 3.2.3 of Chapter 3, the required properties of PVC to express as Equations (5.3), (5.4) and (5.6) in Chapter 5 are given in Table 6.1.

Table 6.1: Experimental viscoelastic properties of PVC

Property	At $t = 0$	At $t = \infty$	Relaxation time
Shear Modulus, $\mu$ (MPa)	$\mu(0) = 1242$	$\mu(\infty) = 830$	$t_0 = 45$ sec
Poisson's ratio, $\nu$	$\nu_0 = \nu(0) = 0.362$	$\nu(\infty) = 0.395$	$t_0 = 45$ sec

Based on the three cases of material models (details in Chapter 5), the viscoelastic properties of PVC are expressed as follows:

Case-1:

$$\text{The viscoelastic shear modulus, } \mu(t) = 830 + 412 e^{-t/45} \quad (6.1)$$

$$\text{and Poisson's ratio, } \nu(t) = 0.362$$

Case-2:

$$\text{The viscoelastic shear modulus, } \mu(t) = 830 + 412 e^{-t/45} \quad (6.2)$$

$$\text{and Poisson's ratio, } \nu(t) = 0.395 - 0.033 e^{-t/45}$$

Case-3:

Figure 6.1 shows the experimental viscoelastic shear modulus curve for PVC and the fitting curve according to the model described in Case-3. Thus, Equation (6.3) represents the viscoelastic properties of PVC obtained from fitting the experimental curve.

$$\mu(t) = 830 + 305 e^{-t/12} + 107 e^{-t/695} \quad (6.3)$$

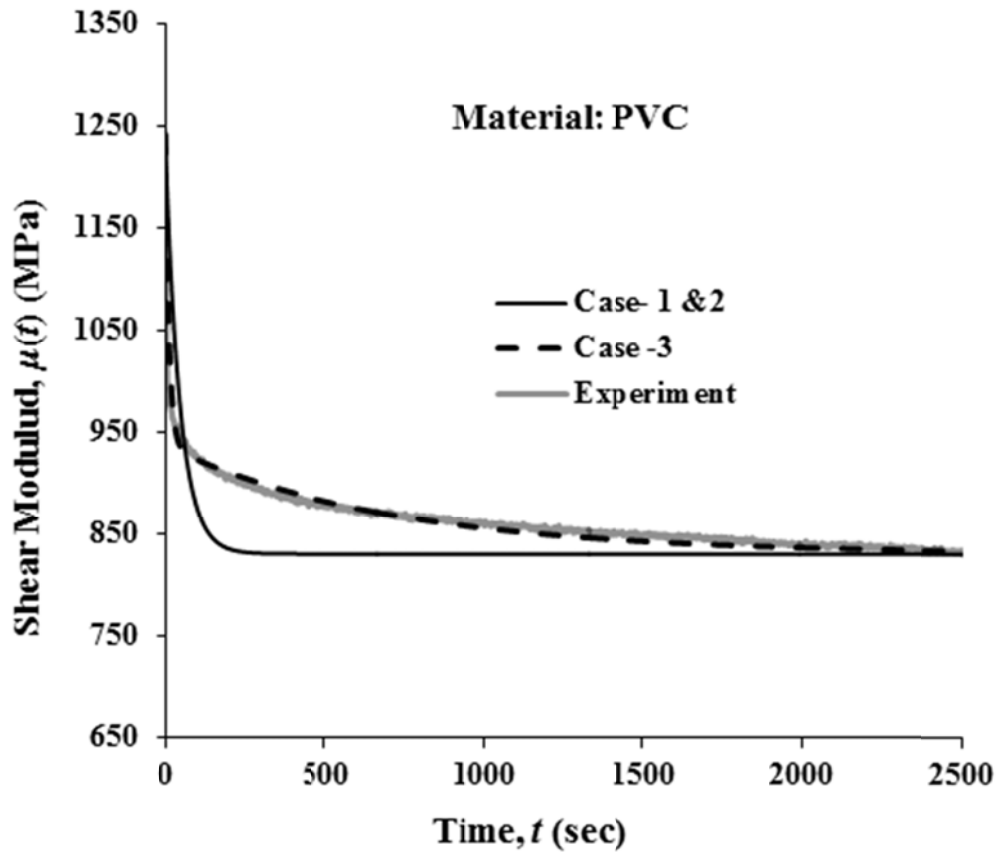


Figure 6.1: Experimental and modeled viscoelastic shear modulus of PVC

Similar to the epoxy, it is seen that to represent the viscoelastic behavior of PVC, case-3 should be considered (Figure 6.1) for material modeling.

Similarly, from Figure 6.2, the Poisson's ratio of PVC considering case-3 is given by Equation (6.4)

$$\nu(t) = 0.395 - 0.012 e^{-t/436} - 0.021 e^{-t/76} \quad (6.4)$$

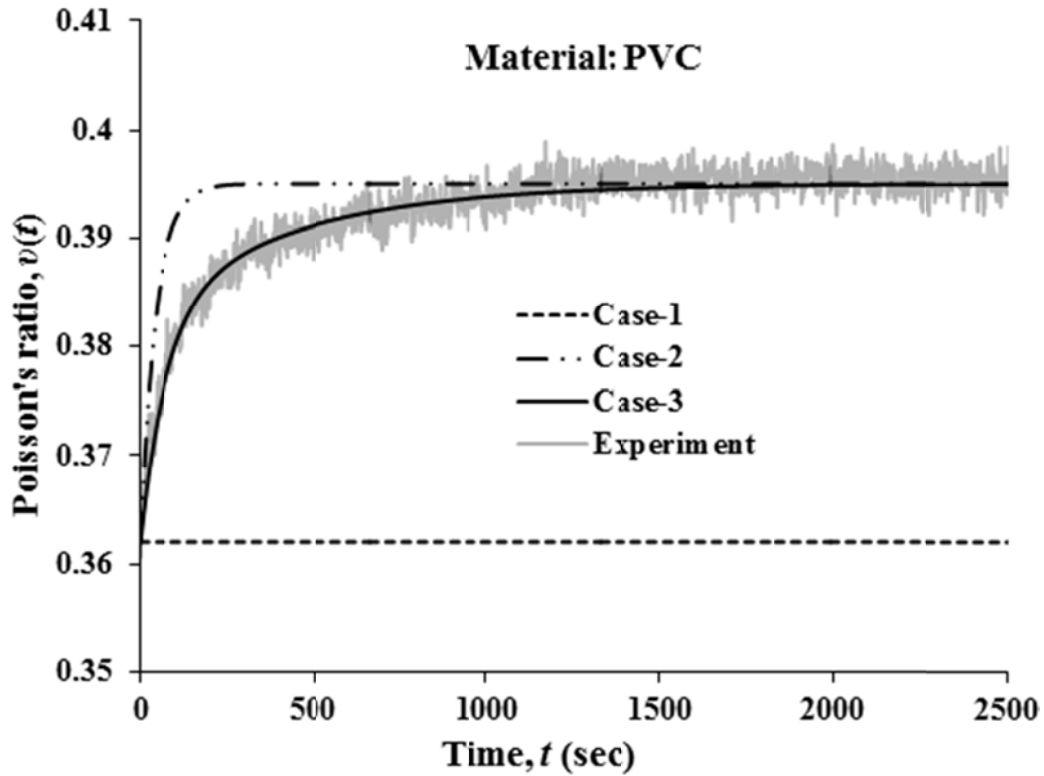


Figure 6.2: Experimental and modeled viscoelastic Poisson's ratio of PVC

### 6.3 ANALYTICAL SOLUTION FOR VISCOELASTIC/VISCOELASTIC BONDED JOINTS

#### 6.3.1 Case-1: The shear modulus is time dependent but Poisson's ratio is time independent

The analytical solution for a viscoelastic/viscoelastic bonded joint is obtained by following a similar methodology used in Chapter 5 for the elastic/viscoelastic bonded joint. The only difference is that here both the materials are viscoelastic, whereas only epoxy was viscoelastic in the previous case in Chapter 5. So it is easily understandable that the calculation or formulation

of analytical solution for a viscoelastic/viscoelastic interface is more tedious than that for an elastic/viscoelastic interface.

For case-1, using the elastic viscoelastic analogy the Dundurs' (1969)

Parameters in the transformed domain are obtained as follows:

$$s\alpha^*(s) = \frac{s\mu_1^*(s)(1-s\nu_2^*(s)) - s\mu_2^*(s)(1-s\nu_1^*(s))}{s\mu_1^*(s)(1-s\nu_2^*(s)) + s\mu_2^*(s)(1-s\nu_1^*(s))}$$

$$\alpha^*(s) = \frac{1}{s} \left[ \frac{s\left(\frac{C_1}{s} + \frac{C_2}{s+\phi_1}\right)(1-\nu_{20}) - s\left(\frac{D_1}{s} + \frac{D_2}{s+\phi_2}\right)(1-\nu_{10})}{s\left(\frac{C_1}{s} + \frac{C_2}{s+\phi_1}\right)(1-\nu_{20}) + s\left(\frac{D_1}{s} + \frac{D_2}{s+\phi_2}\right)(1-\nu_{10})} \right] \quad (6.5a)$$

And,

$$s\beta^*(s) = \frac{s\mu_1^*(s)(1-2s\nu_2^*(s)) - s\mu_2^*(s)(1-2s\nu_1^*(s))}{2[s\mu_1^*(s)(1-s\nu_2^*(s)) + s\mu_2^*(s)(1-s\nu_1^*(s))]}$$

$$\beta^*(s) = \frac{1}{s} \left[ \frac{s\left(\frac{C_1}{s} + \frac{C_2}{s+\phi_1}\right)(1-2\nu_{20}) - s\left(\frac{D_1}{s} + \frac{D_2}{s+\phi_2}\right)(1-2\nu_{10})}{2\left[s\left(\frac{C_1}{s} + \frac{C_2}{s+\phi_1}\right)(1-\nu_{20}) + s\left(\frac{D_1}{s} + \frac{D_2}{s+\phi_2}\right)(1-\nu_{10})\right]} \right] \quad (6.5b)$$

where, the shear modulus of the two linear viscoelastic materials are expressed as follows for case-1,

$$\mu_1(t) = C_1 + C_2 e^{-\phi_1 t} \quad (6.6a)$$

$$\mu_2(t) = D_1 + D_2 e^{-\phi_2 t} \quad (6.6b)$$

where,  $\phi_1 = 1/t_{10}$ ,  $\phi_2 = 1/t_{20}$  and  $t_{10}$  and  $t_{20}$  are the viscoelastic relaxation time for the PVC and Epoxy, respectively.

Using Laplace inverse transformation, the Dundurs' parameters in time domain are given by Equation (6.7)

$$\begin{aligned} \alpha(t) = & \frac{1}{\psi} [ \{ (-\eta D_1 (D_1 + D_2) (\nu_{10} - 1)^2 + (e^\zeta + e^\chi - 1) \eta (C_2 D_1 - C_1 D_2) (\nu_{10} - 1) (\nu_{20} - 1) + \eta C_1 (\nu_{20} - 1)^2 (C_1 + C_2) \} \\ & + (e^\zeta - e^\chi) \{ (\phi_1 - \phi_2) (\nu_{10} - 1) ((D_1 (\nu_{10} - 1) + C_1 (\nu_{20} - 1)) (C_2 D_1 + C_1 D_2)) (\nu_{20} - 1) \\ & + (\nu_{10} - 1) (D_2 (\nu_{10} - 1) (C_1 D_2 \phi_1 + C_2 D_1 (\phi_1 - 2\phi_2)) + (C_2 (\nu_{20} - 1) (C_1 D_2 (2\phi_1 - \phi_2) - C_2 D_1 \phi_2)) (\nu_{20} - 1)) \} ] \end{aligned} \quad (6.7a)$$

And,

$$\begin{aligned} \beta(t) = & \frac{1}{2} [ \frac{((D_1 (1 - 2\nu_{10}) + C_1 (2\nu_{20} - 1))}{(D_1 (\nu_{10} - 1) + C_1 (\nu_{20} - 1))} + \frac{\eta}{2} (D_1 (\nu_{10} - 1) + C_1 (\nu_{20} - 1)) ((D_1 + D_2) (\nu_{10} - 1) + (C_1 + C_2) (\nu_{20} - 1)) \\ & (2 - 3\nu_{20} + \nu_{10} (4\nu_{20} - 3))^2 ((e^\zeta + e^\chi) \eta (C_2 D_1 - C_1 D_2) + (e^\chi - e^\zeta) C_1 D_2^2 \phi_1 (1 + \nu_{10}) \\ & + (e^\zeta - e^\chi) (C_2 D_1 D_2 (\nu_{10} - 1) (\phi_1 - 2\phi_2) + (C_1 D_2 + C_2 D_1) (D_1 (\nu_{10} - 1) + C_1 (\nu_{20} - 1)) (\phi_1 - \phi_2) \\ & + C_2 (\nu_{20} - 1) (C_1 D_2 (2\phi_1 - \phi_2) - C_2 D_1 \phi_2)) ] \end{aligned} \quad (6.7b)$$

where,

$$\psi = \eta (D_1 (\nu_{10} - 1) + C_1 (\nu_{20} - 1)) ((D_1 + D_2) (\nu_{10} - 1) + (C_1 + C_2) (\nu_{20} - 1)) ,$$

$$\eta = \text{Sqrt} [ -4\phi_1 \phi_2 (D_1 (\nu_{10} - 1) + C_1 (\nu_{20} - 1)) ((D_1 + D_2) (\nu_{10} - 1) + (C_1 + C_2) (\nu_{20} - 1)) + (C_1 (\phi_1 + \phi_2) (\nu_{10} + \nu_{20} - 2) + D_2 \phi_1 (\nu_{10} - 1) + C_2 \phi_2 (\nu_{20} - 1))^2 ] ,$$

$$\zeta = \frac{-c - \eta}{b} t ,$$

$$\chi = \frac{-c + \eta}{b} t ,$$

$$c = (D_1 \phi_2 + (D_1 + D_2) \phi_1) (\nu_{10} - 1) + (C_1 \phi_1 + (C_1 + C_2) \phi_2) (\nu_{20} - 1) ,$$

$$b = 2((D_1 + D_2) (\nu_{10} - 1) + (C_1 + C_2) (\nu_{20} - 1))$$

The eigenvalue equation (Equation 4.18) to determine  $\lambda$  in time domain is obtained as Equation (6.8)

$$\begin{aligned} \tau_1 \sin^2 \lambda \pi + \tau_2 \cdot 2(2\lambda^2 \cos^2 \gamma - 1) \sin \lambda \pi \sin 2\lambda \gamma - \tau_3 \cdot 4\lambda^2 \sin \lambda \pi \sin 2\lambda \gamma \cos^2 \gamma \\ + \tau_4 \cdot 4\lambda^2 \cos^2 \gamma (1 - \cos \lambda \pi \cos 2\lambda \gamma - 2\lambda^2 \cos^2 \gamma) + \tau_5 \cdot \{ \sin^2 2\lambda \gamma + 4\lambda^2 (\lambda^2 - 1) \cos^2 \gamma - \lambda^4 \sin^2 2\gamma \} \\ + \tau_6 \cdot \{ 4\lambda^2 \cos^2 \gamma (\lambda^2 \cos^2 \gamma - 1 + \cos \lambda \pi \cos 2\lambda \gamma) + (\cos \lambda \pi - \cos 2\lambda \gamma)^2 \} = 0 \end{aligned} \quad (6.8)$$

Where,

$$\tau_1 = \frac{e^{-t(\phi_1+\phi_2)}}{(\phi_2 - \phi_1)} \left[ \begin{array}{l} e^{-t\phi_1} (\phi_2 - \phi_1) (e^{t\phi_2} D_1^2 + 2D_1 D_2 + D_2^2 (1 - t\phi_2)) (\nu_{10} - 1)^2 + \\ 2C_2 (e^{t\phi_2} D_1 (\phi_2 - \phi_1) + D_2 (\phi_2 e^{t\phi_1} - \phi_1 e^{t\phi_2})) (\nu_{10} - 1) (\nu_{20} - 1) + \\ 2C_1 (\phi_2 - \phi_1) (e^{t\phi_1} (e^{t\phi_2} D_1 + D_2) (\nu_{10} - 1) + e^{t\phi_2} C_2 (\nu_{20} - 1)) (\nu_{20} - 1) - \\ e^{t(\phi_1+\phi_2)} C_1^2 (\phi_1 - \phi_2) (\nu_{20} - 1)^2 - e^{t\phi_2} C_2^2 (t\phi_1 - 1) (\phi_2 - \phi_1) (\nu_{20} - 1)^2 \end{array} \right]$$

$$\tau_2 = e^{-t(\phi_1+\phi_2)} \left[ \begin{array}{l} -e^{-t\phi_1} (e^{t\phi_2} D_1^2 + 2D_1 D_2 + D_2^2 (1 - t\phi_2)) (\nu_{10} - 1)^2 + \\ e^{t(\phi_1+\phi_2)} C_1^2 (\nu_{20} - 1)^2 + 2e^{t\phi_2} C_1 C_2 (\nu_{20} - 1)^2 \\ - e^{t\phi_2} C_2^2 (t\phi_1 - 1) (\phi_2 - \phi_1) (\nu_{20} - 1)^2 \end{array} \right]$$

$$\tau_3 = \frac{1}{2} \left[ \begin{array}{l} C_1^2 - D_1^2 + C_1 D_1 \nu_{10} + 3D_1^2 \nu_{10} - 2D_1^2 \nu_{10}^2 + e^{-t\phi_2} D_2^2 \phi_2 (1 - 3\nu_{10} + 2\nu_{10}^2) \\ + \frac{e^{-t\phi_2} D_2}{(\phi_2 - \phi_1)} \left( (2D_1 + D_2) (\phi_1 - \phi_2) (1 - 3\nu_{10} + 2\nu_{10}^2) \right) - 3C_1^2 \nu_{20} - C_1 D_2 \nu_{20} \\ + 2C_1^2 \nu_{20}^2 - e^{-t\phi_2} t C_2^2 \phi_1 (1 - 3\nu_{20} + 2\nu_{20}^2) \\ + \frac{e^{-t\phi_2} C_2}{(\phi_2 - \phi_1)} \left( \begin{array}{l} (C_2 \phi_1 + C_1 (\phi_1 - \phi_2)) (\nu_{10} - \nu_{20}) \\ + 2C_1 (\phi_1 - \phi_2) (1 - 3\nu_{20} + 2\nu_{20}^2) \\ + C_2 (\phi_1 - \phi_2) (1 - 3\nu_{20} + 2\nu_{20}^2) \end{array} \right) \end{array} \right]$$

$$\tau_4 = \frac{e^{-t(\phi_1+\phi_2)}}{2(\phi_2 - \phi_1)} \left[ \begin{array}{l} e^{-t\phi_1} (\phi_2 - \phi_1) (e^{t\phi_2} D_1^2 + 2D_1 D_2 + D_2^2 (1 - t\phi_2)) + \\ (1 - 3\nu_{10} + 2\nu_{10}^2) - e^{-t(\phi_1+\phi_2)} C_1^2 (\phi_1 - \phi_2) (1 - 3\nu_{10} + 2\nu_{10}^2) \\ - e^{t\phi_2} C_2^2 (t\phi_1 - 1) (\phi_2 - \phi_1) (1 - 3\nu_{20} + 2\nu_{20}^2) \\ - C_2 (e^{t\phi_2} D_1 (\phi_2 - \phi_1) + D_2 (\phi_2 e^{t\phi_1} - \phi_1 e^{t\phi_2})) (2 - 3\nu_{20} + \nu_{10} (4\nu_{20} - 3)) \\ + C_1 (\phi_2 - \phi_1) \left( \begin{array}{l} 2e^{t\phi_1} C_2 (1 - 3\nu_{20} + 2\nu_{20}^2) \\ - e^{t\phi_1} (e^{t\phi_2} D_1 + D_2) (2 - 3\nu_{20} + \nu_{10} (4\nu_{20} - 3)) \end{array} \right) \end{array} \right]$$

$$\tau_5 = \frac{e^{-t(\phi_1 + \phi_2)}}{(\phi_2 - \phi_1)} \left[ \begin{array}{l} e^{-t\phi_1} (\phi_2 - \phi_1) (e^{t\phi_2} D_1^2 + 2D_1 D_2 + D_2^2 (1 - t\phi_2)) (\nu_{10} - 1)^2 \\ - 2C_2 (e^{t\phi_2} D_1 (\phi_2 - \phi_1) + D_2 (\phi_2 e^{t\phi_1} - \phi_1 e^{t\phi_2})) (\nu_{10} - 1) (\nu_{20} - 1) \\ + 2C_1 (\phi_2 - \phi_1) (e^{t\phi_2} C_2 (\nu_{20} - 1) - e^{t\phi_1} (e^{t\phi_2} D_1 + D_2) (\nu_{10} - 1)) (\nu_{20} - 1) \\ - e^{-t(\phi_1 + \phi_2)} C_1^2 (\phi_1 - \phi_2) (\nu_{20} - 1)^2 - e^{t\phi_2} C_2^2 (t\phi_1 - 1) (\phi_2 - \phi_1) (\nu_{20} - 1)^2 \end{array} \right]$$

$$\tau_6 = \frac{e^{-t(\phi_1 + \phi_2)}}{4(\phi_2 - \phi_1)} \left[ \begin{array}{l} e^{-t\phi_1} (\phi_2 - \phi_1) (e^{t\phi_2} D_1^2 + 2D_1 D_2 + D_2^2 (1 - t\phi_2)) (2\nu_{10} - 1)^2 \\ - e^{-t(\phi_1 + \phi_2)} C_1^2 (\phi_1 - \phi_2) (2\nu_{20} - 1)^2 - e^{t\phi_2} C_2^2 (t\phi_1 - 1) (\phi_2 - \phi_1) (2\nu_{20} - 1)^2 \\ - 2C_2 (e^{t\phi_2} D_1 (\phi_2 - \phi_1) + D_2 (\phi_2 e^{t\phi_1} - \phi_1 e^{t\phi_2})) (2\nu_{10} - 1) \\ + 2C_1 (\phi_2 - \phi_1) (e^{t\phi_2} C_2 (2\nu_{20} - 1) - e^{t\phi_1} (e^{t\phi_2} D_1 + D_2) (2\nu_{10} - 1)) (2\nu_{20} - 1) \end{array} \right]$$

### 6.3.2 Case-2: Both the shear modulus and Poisson's ratio are time dependent

According to the description of material properties in case-2, the shear moduli of two materials bonded together along a common interface are expressed as follows,

$$\mu_1(t) = C_1 + C_2 e^{-\phi_1 t} \quad (6.9a)$$

$$\mu_2(t) = D_1 + D_2 e^{-\phi_2 t} \quad (6.9b)$$

and

$$\nu_1(t) = A_1 - A_2 e^{-\phi_1 t} \quad (6.10a)$$

$$\nu_2(t) = B_1 - B_2 e^{-\phi_2 t} \quad (6.10b)$$

Where,  $\mu_1, \nu_1$  are the shear modulus and Poisson's ratio of material-1 and  $\mu_2, \nu_2$  are the shear modulus and Poisson's ratio of material-2;  $\phi_1 = 1/t_{10}$ ,  $\phi_2 = 1/t_{20}$  and  $t_{10}$  and  $t_{20}$  are the viscoelastic relaxation time for the two materials respectively.

Applying the elastic viscoelastic analogy, the transform Dundurs' Parameters for case-2 are given by

$$s\alpha^*(s) = \frac{s\mu_1^*(s)(1-s\nu_2^*(s)) - s\mu_2^*(s)(1-s\nu_1^*(s))}{s\mu_1^*(s)(1-s\nu_2^*(s)) + s\mu_2^*(s)(1-s\nu_1^*(s))}$$

$$\alpha^*(s) = \frac{1}{s} \left[ \frac{\left(\frac{C_1}{s} + \frac{C_2}{s+\phi_1}\right)\left(1 - s\left(\frac{B_1}{s} - \frac{B_2}{s+\phi_2}\right)\right) - \left(\frac{D_1}{s} + \frac{D_2}{s+\phi_2}\right)\left(1 - s\left(\frac{A_1}{s} - \frac{A_2}{s+\phi_1}\right)\right)}{\left(\frac{C_1}{s} + \frac{C_2}{s+\phi_1}\right)\left(1 - s\left(\frac{B_1}{s} - \frac{B_2}{s+\phi_2}\right)\right) + \left(\frac{D_1}{s} + \frac{D_2}{s+\phi_2}\right)\left(1 - s\left(\frac{A_1}{s} - \frac{A_2}{s+\phi_1}\right)\right)} \right]$$

(6.11a)

And,

$$s\beta^*(s) = \frac{s\mu_1^*(s)(1-2s\nu_2^*(s)) - s\mu_2^*(s)(1-2s\nu_1^*(s))}{2[s\mu_1^*(s)(1-s\nu_2^*(s)) + s\mu_2^*(s)(1-s\nu_1^*(s))]}$$

$$\beta^*(s) = \frac{1}{s} \left[ \frac{\left(\frac{C_1}{s} + \frac{C_2}{s+\phi_1}\right)\left(1 - 2s\left(\frac{B_1}{s} - \frac{B_2}{s+\phi_2}\right)\right) - \left(\frac{D_1}{s} + \frac{D_2}{s+\phi_2}\right)\left(1 - 2s\left(\frac{A_1}{s} - \frac{A_2}{s+\phi_1}\right)\right)}{2\left[\left(\frac{C_1}{s} + \frac{C_2}{s+\phi_1}\right)\left(1 - s\left(\frac{B_1}{s} - \frac{B_2}{s+\phi_2}\right)\right) + \left(\frac{D_1}{s} + \frac{D_2}{s+\phi_2}\right)\left(1 - s\left(\frac{A_1}{s} - \frac{A_2}{s+\phi_1}\right)\right)\right]} \right]$$

(6.11b)

Carrying out the inverse Laplace transformation and using the properties mentioned earlier in case-2, the Dundurs' parameter in time domain are given by:

$$\alpha(t) = 699.72 \times 10^{-3} + 157.04 \times 10^{-3} e^{-1.05694t} - 422.31 \times 10^{-3} e^{-0.4516t} \quad (6.12a)$$

$$\beta(t) = 60.91 \times 10^{-3} + 13.01 \times 10^{-3} e^{-1.05694t} - 30.87 \times 10^{-3} e^{-0.4516t} \quad (6.12b)$$

Similarly as previous, for case-2, the eigenvalue equation (Equation 4.18) in time domain is given by

$$\begin{aligned} &\tau_1 \sin^2 \lambda \pi - \tau_2 \cdot 2(2\lambda^2 \cos^2 \gamma - 1) \sin \lambda \pi \sin 2\lambda \gamma + \tau_3 \cdot 4\lambda^2 \sin \lambda \pi \sin 2\lambda \gamma \cos^2 \gamma \\ &+ \tau_4 \cdot 4\lambda^2 \cos^2 \gamma (1 - \cos \lambda \pi \cos 2\lambda \gamma - 2\lambda^2 \cos^2 \gamma) + \tau_5 \cdot \{\sin^2 2\lambda \gamma + 4\lambda^2 (\lambda^2 - 1) \cos^2 \gamma - \lambda^4 \sin^2 2\gamma\} \\ &+ \tau_6 \cdot \{4\lambda^2 \cos^2 \gamma (\lambda^2 \cos^2 \gamma - 1 + \cos \lambda \pi \cos 2\lambda \gamma) + (\cos \lambda \pi - \cos 2\lambda \gamma)^2\} = 0 \end{aligned} \quad (6.13)$$

where,

$$\tau_1 = 295.92 + (591.84 - 102.85t) \times e^{-t/0.75} + (138.47 - 24.40t) \times e^{-t/1.5}$$

$$\tau_2 = 207.06 + (286.29 - 84.20t) \times e^{-t/0.75} - (47.51 - 21.41t) \times e^{-t/1.5}$$

$$\tau_3 = 180.25 + (288.91 - 7.92t) \times e^{-t/0.75} - (2.74 - 1.39t) \times e^{-t/1.5}$$

$$\tau_4 = 126.12 + (8.39 - 6.48t) \times e^{-t/0.75} - (1.81 - 1.22t) \times e^{-t/1.5}$$

$$\tau_5 = 144.88 + (72.09 - 68.93t) \times e^{-t/0.75} - (23.27 - 18.79t) \times e^{-t/1.5}$$

$$\tau_6 = 1.10 + (0.94 - 0.61t) \times e^{-t/0.75} - (0.1 - 0.08t) \times e^{-t/1.5}$$

### 6.3.3 Case -3: Both the shear modulus and Poisson's ratios are time dependent and more accurately represent the behavior of the material

For case-3, using the material properties of PVC (Equations 6.3 and 6.4) and epoxy (Equations 5.10 and 5.11); and following the procedure mentioned above, the Dundurs' parameters in time domain are given by

$$\alpha(t) = (699.72 + 127.17e^{-4.315t} - 293.11e^{-2.213t} + 2.216e^{-1.179t} - 8.19e^{-0.784t} - 7.46e^{-0.137t} - 31.07e^{-0.09t} - 56.27e^{-0.074t} + 1.46e^{-0.055t}) \times 10^{-3} \quad (6.14a)$$

$$\beta(t) = (609.12 + 23.8e^{-4.315t} - 58e^{-2.213t} + 15.65e^{-1.179t} - 5.04e^{-0.784t} - 5.30e^{-0.137t} - 4.76e^{-0.09t} - 10.02e^{-0.074t} + 25.83e^{-0.055t}) \times 10^{-3} \quad (6.14b)$$

And, the eigenvalue equation (Equation 4.18) in time domain for case-3 is given as follows:

$$\begin{aligned} & \tau_1 \sin^2 \lambda \pi - \tau_2 (2\lambda^2 \cos^2 \gamma - 1) \sin \lambda \pi \sin 2\lambda \gamma + \tau_3 4\lambda^2 \sin \lambda \pi \sin 2\lambda \gamma \cos^2 \gamma \\ & + \tau_4 4\lambda^2 \cos^2 \gamma (1 - \cos \lambda \pi \cos 2\lambda \gamma - 2\lambda^2 \cos^2 \gamma) + \tau_5 \{ \sin^2 2\lambda \gamma + 4\lambda^2 (\lambda^2 - 1) \cos^2 \gamma - \lambda^4 \sin^2 2\gamma \} \\ & + \tau_6 \{ 4\lambda^2 \cos^2 \gamma (\lambda^2 \cos^2 \gamma - 1 + \cos \lambda \pi \cos 2\lambda \gamma) + (\cos \lambda \pi - \cos 2\lambda \gamma)^2 \} = 0 \end{aligned} \quad (6.15)$$

where,

$$\tau_1 = e^{-10.18t} \left( \begin{array}{l} 0.296e^{10.18t} + e^{10.1t} (172535 - 554.47t) - e^{10.1t} (173198 + 507.32t) + \dots \\ \dots e^{10.12t} (838.95 - 5.43t) - e^{10.05t} (175.5 + 1.72t) + e^{5.18t} (0.4 - 0.16t) + \dots \\ \dots e^{7.36t} (0.16 - 0.7t) + e^{8.98t} \times 10^{-3} (9.7 - 0.1t) + e^{9.4t} \times 10^{-3} (3.1 - 0.01t) \end{array} \right)$$

$$\tau_2 = e^{-10.18t} \left( \begin{array}{l} 0.207e^{10.18t} + e^{5.18t} (0.23 - 0.16t) + e^{8.98t} \times 10^{-3} (9.17 - 0.1t) - \dots \\ \dots e^{9.4t} \times 10^{-3} (0.4 - 0.001t) - e^{7.36t} (0.06 - 0.07t) + e^{10.05t} (115.7 + 1.13t) - \dots \\ \dots e^{10.12t} (552.9 - 3.58t) + e^{10.1t} (114159 + 334.38t) - e^{10.1t} (113722 - 365.5t) \end{array} \right)$$

$$\tau_3 = e^{-10.18t} \left( \begin{array}{l} 0.018e^{10.18t} + e^{10.1t} (24800.8 - 79.7t) - e^{10.1t} (24896.2 + 72.92t) + \dots \\ \dots e^{10.12t} (120.6 - 0.78t) - e^{10.05t} (25.2 + 0.25t) + e^{5.18t} (0.028 - 0.024t) - \dots \\ \dots e^{7.36t} (0.018 - 0.015t) + e^{8.98t} \times 10^{-3} (5.4 - 0.1t) - e^{9.4t} \times 10^{-3} (1.5 - 0.01t) \end{array} \right)$$

$$\tau_4 = e^{-10.18t} \left( \begin{array}{l} 0.013e^{10.18t} + e^{10.1t} (5608.4 - 18.02t) - e^{10.1t} (5629.9 + 16.5t) + \dots \\ \dots e^{10.12t} (27.3 - 0.18t) - e^{10.05t} (5.71 + 0.06t) + e^{5.18t} (0.002 - 0.024t) - \dots \\ \dots e^{7.36t} (0.005 - 0.015t) + e^{8.98t} \times 10^{-3} (4.87 - 0.1t) - e^{9.4t} \times 10^{-3} (1.23 - 0.01t) \end{array} \right)$$

$$\tau_5 = e^{-10.18t} \left( \begin{array}{l} 0.145e^{10.18t} + e^{5.18t} (0.06 - 0.16t) + e^{8.98t} \times 10^{-3} (8.6 - 0.1t) - \dots \\ \dots e^{9.4t} \times 10^{-3} (2.3 - 0.003t) - e^{7.36t} (0.034 - 0.07t) + e^{10.05t} (73.5 + 0.72t) - \dots \\ \dots e^{10.12t} (351.3 - 2.28t) + e^{10.1t} (72537 + 212.5t) - e^{10.1t} (72259.8 - 232.2t) \end{array} \right)$$

$$\tau_6 = e^{-10.18t} \left( \begin{array}{l} 0.0011e^{10.18t} - e^{5.18t} (0.0007 - 0.004t) + e^{8.98t} \times 10^{-3} (1.1 - 0.1t) - \dots \\ \dots e^{9.4t} \times 10^{-3} (0.1 - 0.005t) - e^{7.36t} (0.0003 - 0.003t) + e^{10.05t} (0.1 + 0.01t) - \dots \\ \dots e^{10.12t} (4.7 - 0.03t) + e^{10.1t} (978.1 + 2.87t) - e^{10.1t} (974.3 - 3.131t) \end{array} \right)$$

#### 6.4 STRESS SINGULARITY AND CRITICAL BONDING ANGLE FOR A PVC/ EPOXY BONDED JOINT

The material properties of PVC are presented briefly earlier in this chapter. The viscoelastic properties of epoxy have been described in previous chapter (Chapter 5). Once the properties of both materials are known, the time dependent Dundurs' parameters are determined for the three material models using the above analytical formulation. Variation in the Dundurs' parameters ( $\alpha$ ,  $\beta$ ) with time is shown in Figures 6.3 and 6.4.

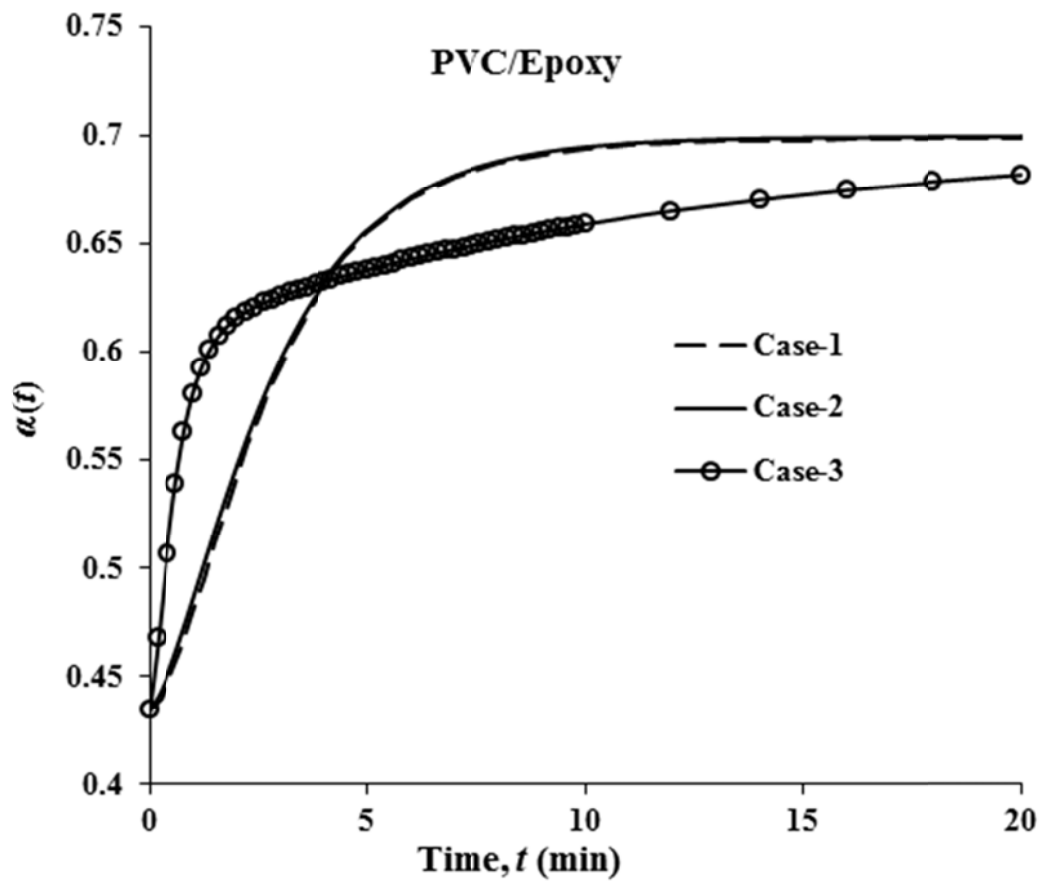


Figure 6.3: Variation of Dundurs' parameter  $\alpha(t)$  with time

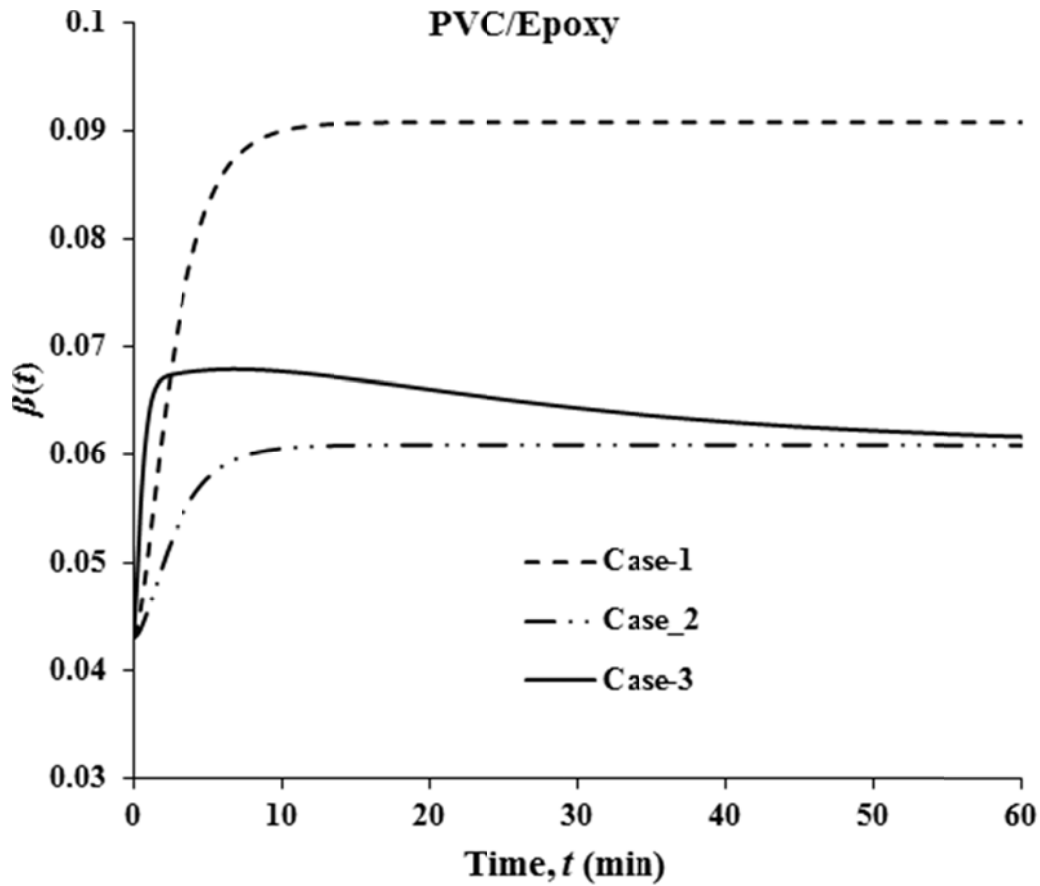


Figure 6.4: Variation of Dundurs' parameter  $\beta(t)$  with time

Figure 6.3 shows that the viscoelastic Poisson's ratio has an insignificant influence on  $\alpha$ . For the same viscoelastic shear modulus, value of  $\alpha$  is the same for both constant and time-dependent Poisson's ratio (Case-1 and Case 2). However,  $\alpha$  is influenced by the viscoelastic shear modulus. Thus, there exists a difference in  $\alpha$  for the case-3 with that for cases -1 & 2. Figure 6.4 illustrates the

effect of Poisson's ratio on  $\beta$ . It is observed that the difference between the response of  $\beta$  for constant and time dependent Poisson's ratio is noticeable. For case -3, initially, the Dundurs' parameter  $\beta$  shows the similar trend as case-1, however, after a while it follows the similar trend as case-2 but at a slower rate. It can be concluded that the case-1 cannot predict the behavior of the stress singularity over a long time period and case-2 can only predict the stress singularity after sufficient amount of time.

Next, the eigenvalue  $\lambda$  is determined for different bonding angles for the above mentioned three different cases. It can be reviewed again that the order of the stress singularity is  $(\lambda-1)$  and the condition for the elimination of the stress singularity is  $\lambda > 1$ . Higher the value of  $\lambda$  (when  $\lambda < 1$ ) indicates lower the order of the stress singularity at the interface corner. Figure 6.5 shows the variation of  $\lambda$  with time for a bonding angle of 40 degrees.

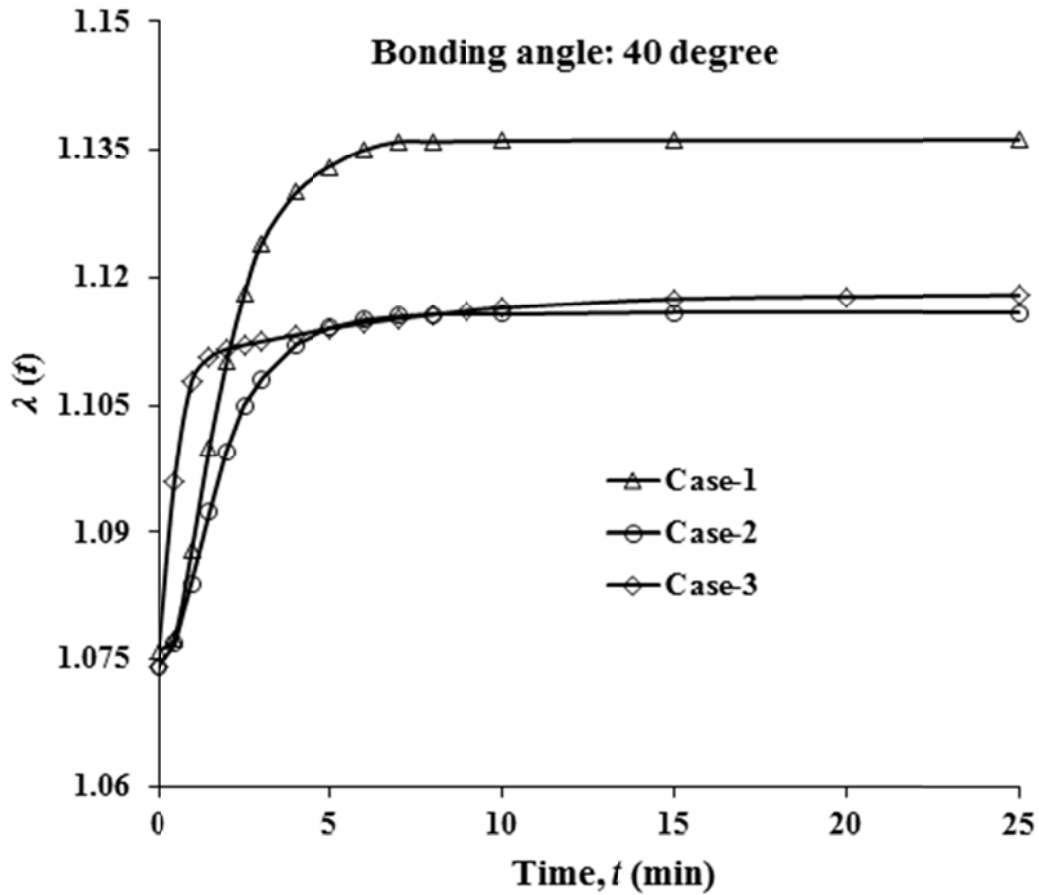


Figure 6.5: Variation of  $\lambda$  with time for the bonding angle  $40^\circ$

For bonding angle  $40^\circ$ , the value of  $\lambda$  is always greater than 1 in all three cases. This indicates that there is no stress singularity existing at the interface corner. The value of  $\lambda$  increases with time in all cases. Case-1 determines higher value of  $\lambda$  than cases- 2 & 3; predicts less singularity in any structure containing viscoelastic/viscoelastic interface than actually it has. In Figure 6.6, results are shown for a bonding angle of  $60$  degrees. It is clear that for the bonding angle  $60$  degree, the stress singularity always exists ( $\lambda < 1$ ) at the interface corner for all three cases.

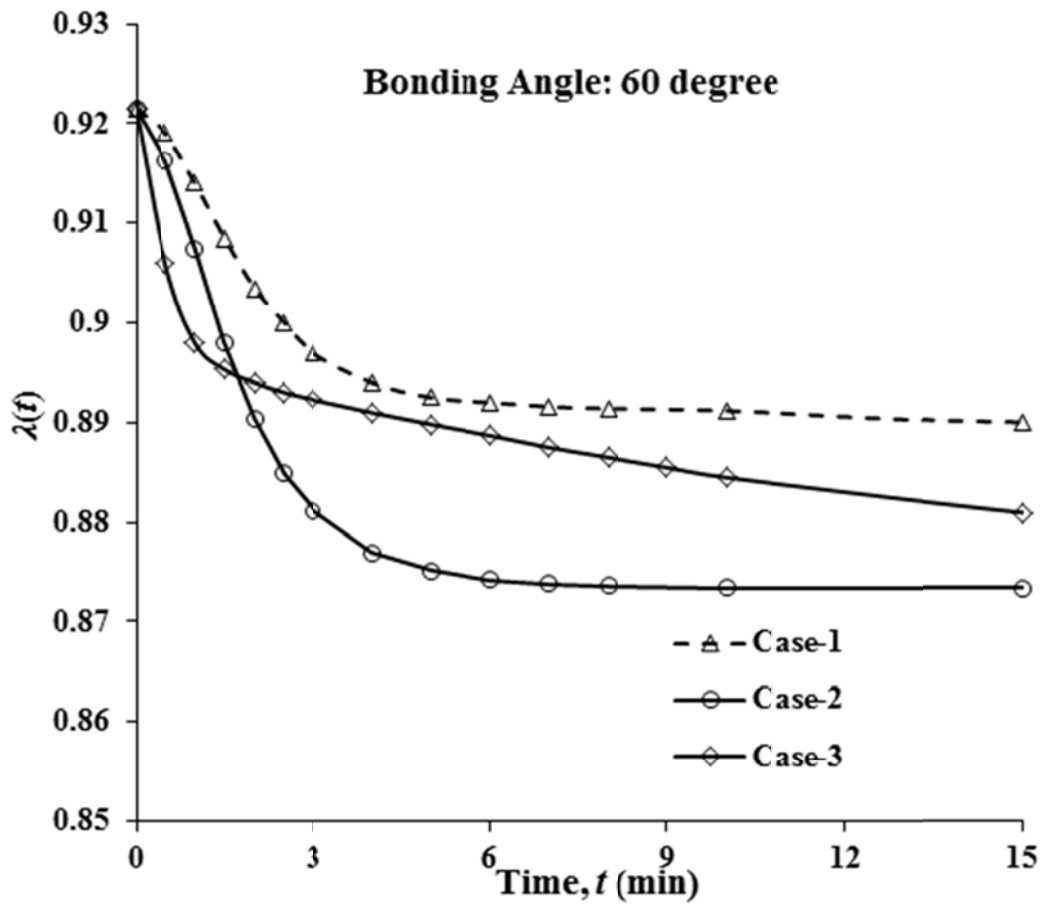


Figure 6.6: Variation of  $\lambda$  with time for the bonding angle  $60^\circ$

It is seen from Figure 6.6 that the stress singularity increases with time for all the three cases.

As described in earlier chapter that the critical bonding angle is determined for which the value of  $\lambda$  changes from less than 1 to greater than 1. Figure 6.7 shows the variation of eigenvalue  $\lambda$  with time for a bonding angle of  $49^\circ$ .

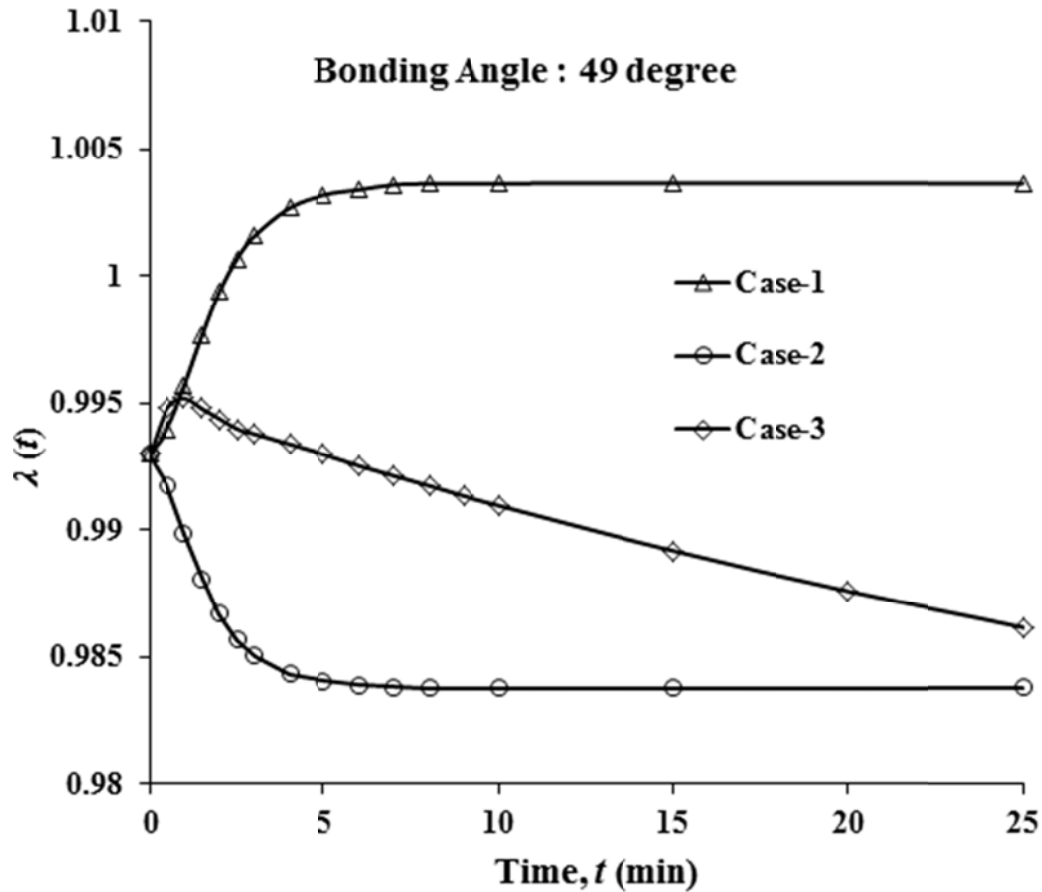


Figure 6.7: Variation of  $\lambda$  with time for the bonding angle  $49^\circ$

In the Figure 6.7, the importance of accurate material modeling is clearly visible. For the bonding angle  $49^\circ$ , case-1 predicts that, initially there exist stress singularity at the interface corner but it disappears with time. However, this result is completely misleading. Case-2 and case-3 ensures that for this bonding angle, the singularity increases with time rather than decreases. It is known that the singularity increases with time. For the case of a finite stress or non-singular stress at the interface corner, the order of the stress singularity may increase or decrease with time.

Next, in Figure 6.8 the variation of eigenvalue  $\lambda$  with time for a bonding angle of  $48^\circ$  is shown. Considering the case-1 and the definition of critical bonding angle, the critical bonding angle for the tested PVC/Epoxy interface is determined in between  $48^\circ$  and  $49^\circ$ . However, cases -2 and 3 prove that this result is not accurate as there exist stress singularity for the bonding angle of  $48^\circ$ .

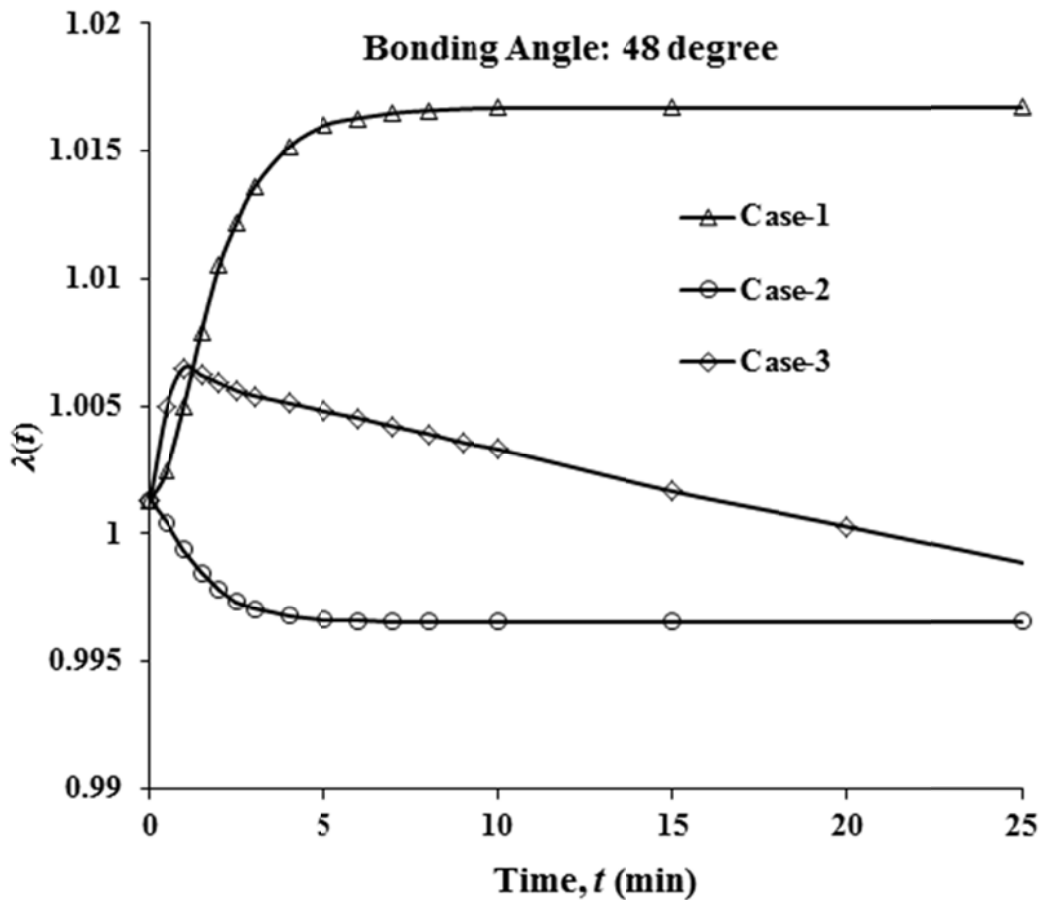


Figure 6.8: Variation of  $\lambda$  with time for the bonding angle  $48^\circ$

Figure 6.9 shows the variation of eigenvalue  $\lambda$  for a bonding angle of  $47^\circ$ . It is seen that for all three cases the value of  $\lambda$  is greater than 1 ( $\lambda > 1$ ); means the singularity disappears for the bonding angle  $47^\circ$ . Thus, the critical bonding angle for the tested PVC/Epoxy is determined as in between  $47^\circ$  and  $48^\circ$  ( $47^\circ \leq \theta_c < 48^\circ$ ).

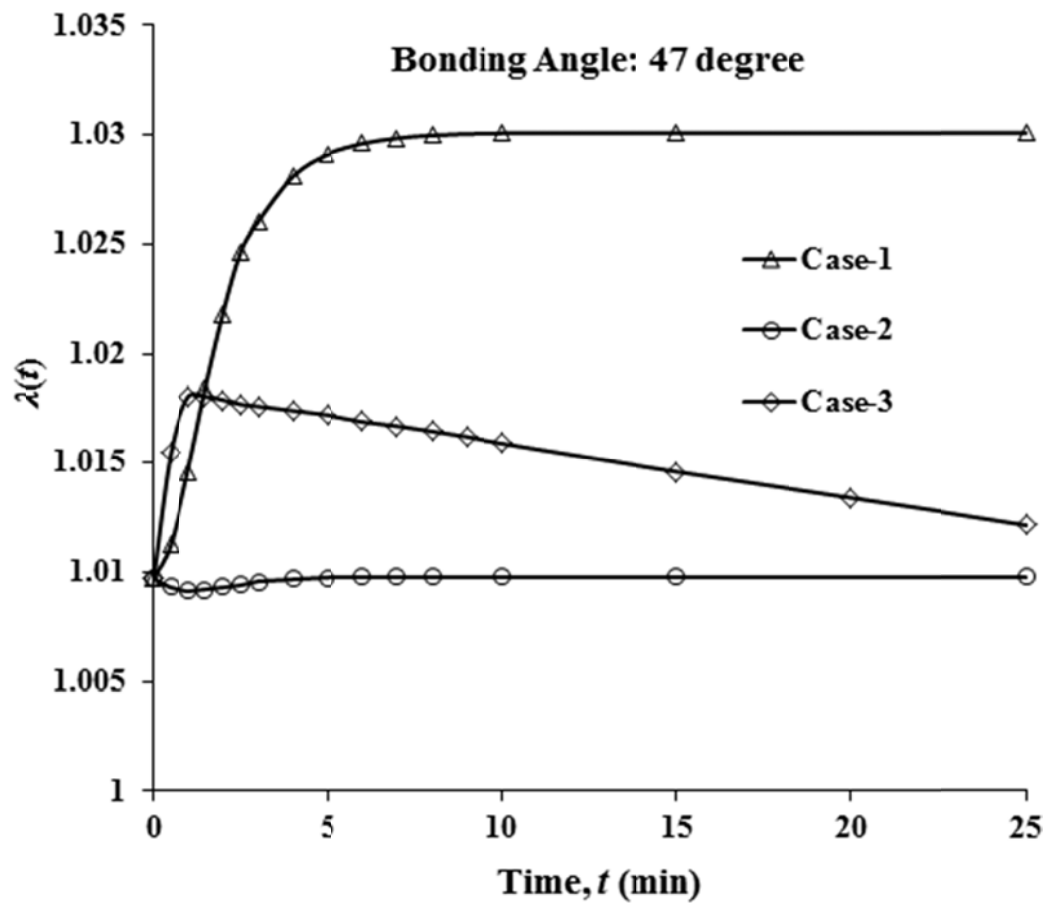


Figure 6.9: Variation of  $\lambda$  with time for the bonding angle  $47^\circ$

## 6.5 DETERMINATION OF CRITICAL BONDING ANGLE BY FINITE ELEMENT ANALYSIS

The results obtained from the analytical solution are verified by the finite element analysis. The axi-symmetric finite element model shown in Figure 2.2 (Chapter 2) is also used in this analysis. It is clear enough that PVC is modeled as material -1 and Epoxy is as material-2. Similar to the elastic/viscoelastic analysis, 8-noded PLANE 183 element is used for both materials in this analysis. A uniform tensile stress of 10 MPa is applied at top end while the bottom end is fixed in longitudinal direction. The axi-symmetric problem is solved in 30 equal load steps and the time at the end of load step is 15 minutes (900 seconds).

Figure 6.10 shows the distributions of interface effective stress along the interface for two different bonding angles of  $40^\circ$  and  $60^\circ$ . From the definition of the stress singularity it is found that for the bonding angle of  $60^\circ$ , there exists stress singularity at the free edge of the interface. However, for the case of  $40^\circ$  bonding angle, finite values of the interface stresses are exhibited and the stress convergence is confirmed by increasing FEM mesh density.

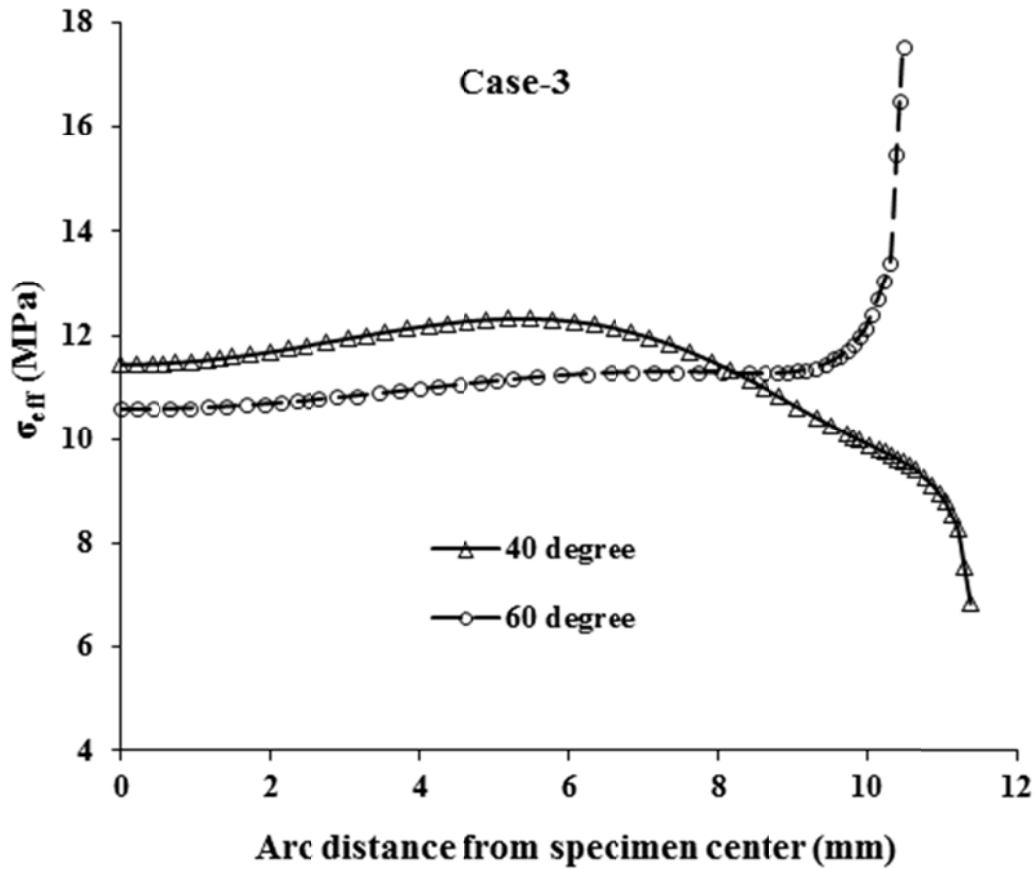


Figure 6.10: Effective stress along the interface for bonding angles of 40° and 60° (Case-3).

The same analysis is carried out for other bonding angles from 40° to 60° by the increment of 1° each time and the distributions of interface effective stress along the interface for bonding angles 47°, 48° and 49° are shown in Figure 6.11. It is seen that for the 47° bonding angle, the shape of the effective stress curve near the free edge is clearly going to the downward direction but for 49° bonding

angle, it is going to the upward direction. For the  $48^\circ$  bonding angle, the effective stress curve near the free edge shows the similar trend to that of for the  $49^\circ$  bonding angle. This confirms that the value of the critical bonding angle for the viscoelastic PVC/Epoxy bi-material interface is in between  $47^\circ$  and  $48^\circ$ . This result verifies the results obtained from the analytical model.

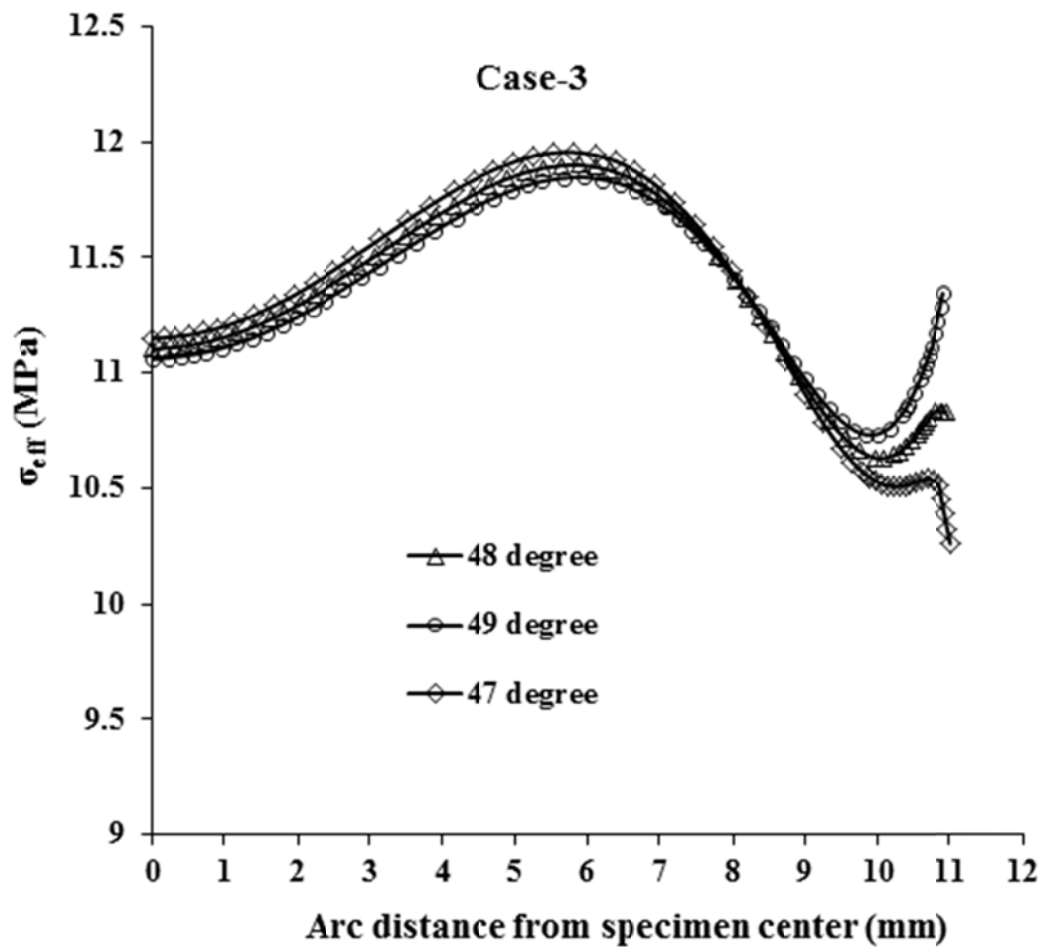


Figure 6.11: Effective stress along the interface for the bonding angles of  $47^\circ$ ,  $48^\circ$  and  $49^\circ$  (Case-3).

## 6.6 DETERMINATION OF INTERFACE BONDING STRENGTH BETWEEN VISCOELASTIC/VISCOELASTIC MATERIALS

The test specimens are manufactured with a bonding angle of  $40^\circ$ . The specimens are tested under various combinations of normal and shear stress. The failure loads and time required to reach the failure load are recorded for each test from the multi-axial testing machine and is given in Table 6.2.

Table 6.2: Maximum failure loads and time required to reach failure

No	Tensile load (N)	Torsional Load (N. m)	Time (sec)
1	0	33.98	676.67
2	766.80	34.06	358.14
3	1620.21	28.10	265.95
4	2552.72	18.82	367.03
5	3112.75	0	368.92

Finite element analysis is carried out for each test case with the maximum failure loads given in Table 6.2. As mentioned in the earlier chapter that 3D analysis is needed to analyze the viscoelastic interface for the torsional and combined loading. The 3D finite element model of the specimen and details of this analysis can be found in Chapter 5 (Figure 5.15).

After solving the problem, the stress components along the interface in the last step of loading are recorded. Using the stress transformation, the interface normal, shear and effective stress distributions along the interface are determined. Figure 6.12 shows the stress curves along the interface of specimen under pure tensile loading. It is now clear that both normal and shear stress components are present in the tensile/combined loading case.

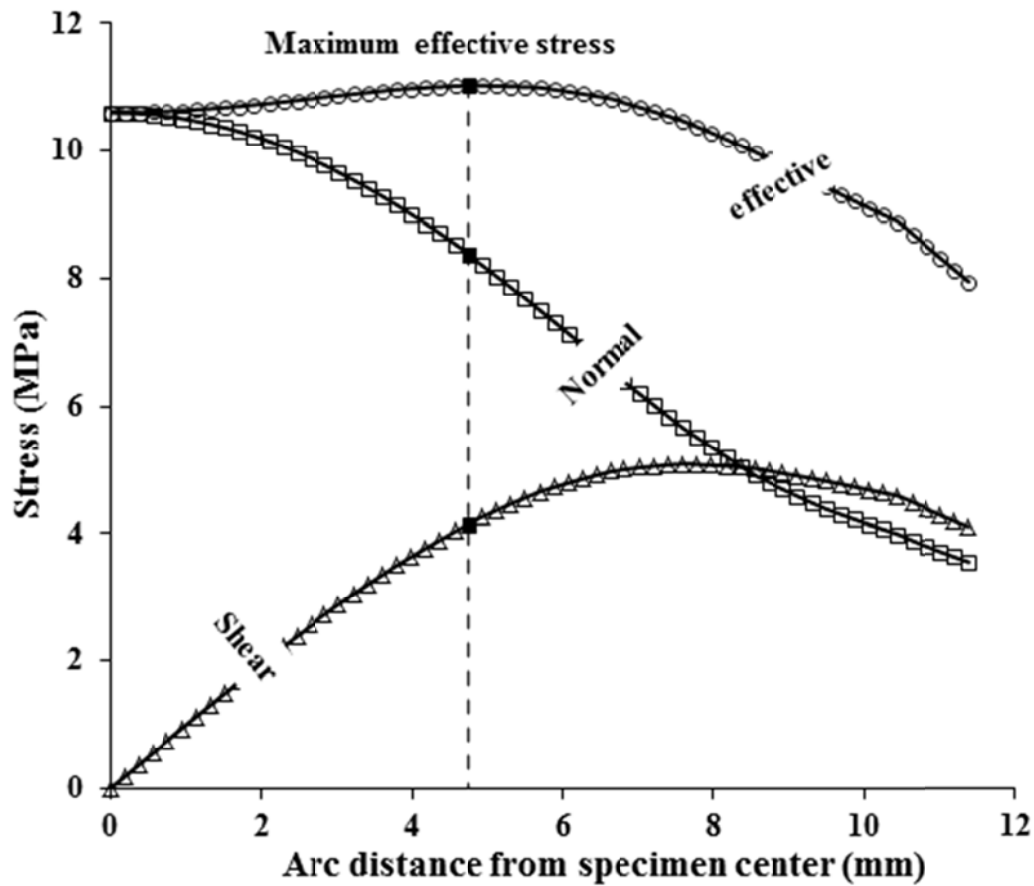


Figure 6.12: Stress distribution along the interface for pure tensile loading

Figure 6.13 shows the stress distribution along the interface of the specimen under pure torsional loading. There is no normal interface stress

component for the application of pure torsional loading. Therefore, the maximum interface shear stress along the interface, denoted by  $\tau_s$ , is directly taken as the shear strength of the bi-material interface. Thus the interface shear bonding strength for the viscoelastic PVC/Epoxy is determined as  $\tau_s = 15.14$  MPa.

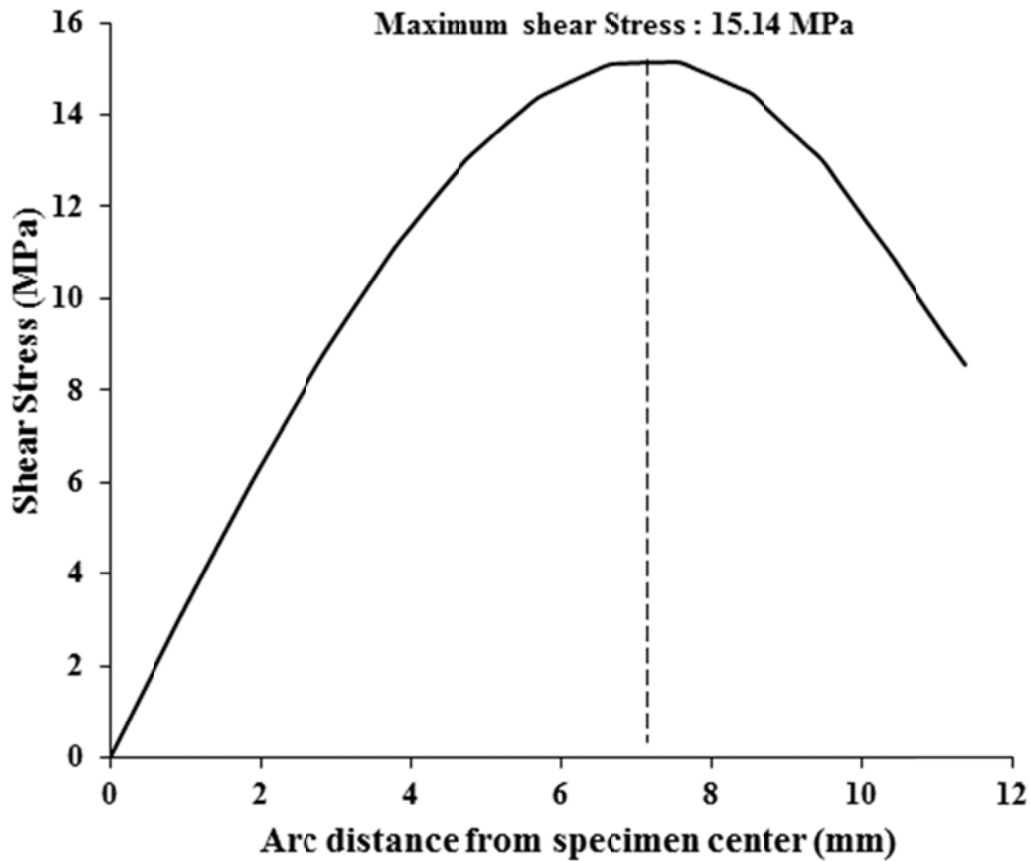


Figure 6.13: Stress distribution along the interface for pure torsional loading case

For the pure global normal loading and other combined normal-shear loading cases, both normal and shear interface stress components exist. So, a normal-shear bonding strength criterion (envelope) is required to define the interface bonding strength. As mentioned earlier that the criterion is expressed as,

$$f(\sigma_n, \tau) = C$$

where  $\sigma_n$  and  $\tau$  are interface normal and shear stress components, respectively, and  $C$  is a constant. The function  $f$  and the constant  $C$  can be determined through the following iteration procedure:

(i) The effective stress criterion is assumed as first trial condition, so

$$f^{(1)}(\sigma_n, \tau) = \sqrt{\sigma_n^2 + 3\tau^2} = \sqrt{3}\tau_s$$

The constant  $C = \sqrt{3}\tau_s$  is obtained by applying the pure torsional loading case in which  $\sigma_n = 0$ .

Therefore, the first trial criterion (effective stress) is

$$\left(\frac{\sigma_n}{26.22}\right)^2 + \left(\frac{\tau}{15.14}\right)^2 = 1 \quad (6.15)$$

Next, from the interface normal and shear stress curves of each loading test case, the location of the maximum value of  $\sqrt{\sigma_n^2 + 3\tau^2}$  along the interface is identified and the corresponding pair of normal and shear stress values for each test case is recorded. These pairs of stresses are considered as the 1<sup>st</sup> stress data points and denoted as “1<sup>st</sup> data set”.

Figure 6.14 shows the points obtained considering the effective stress criterion and the effective stress curve expressed by Equation 6.15.

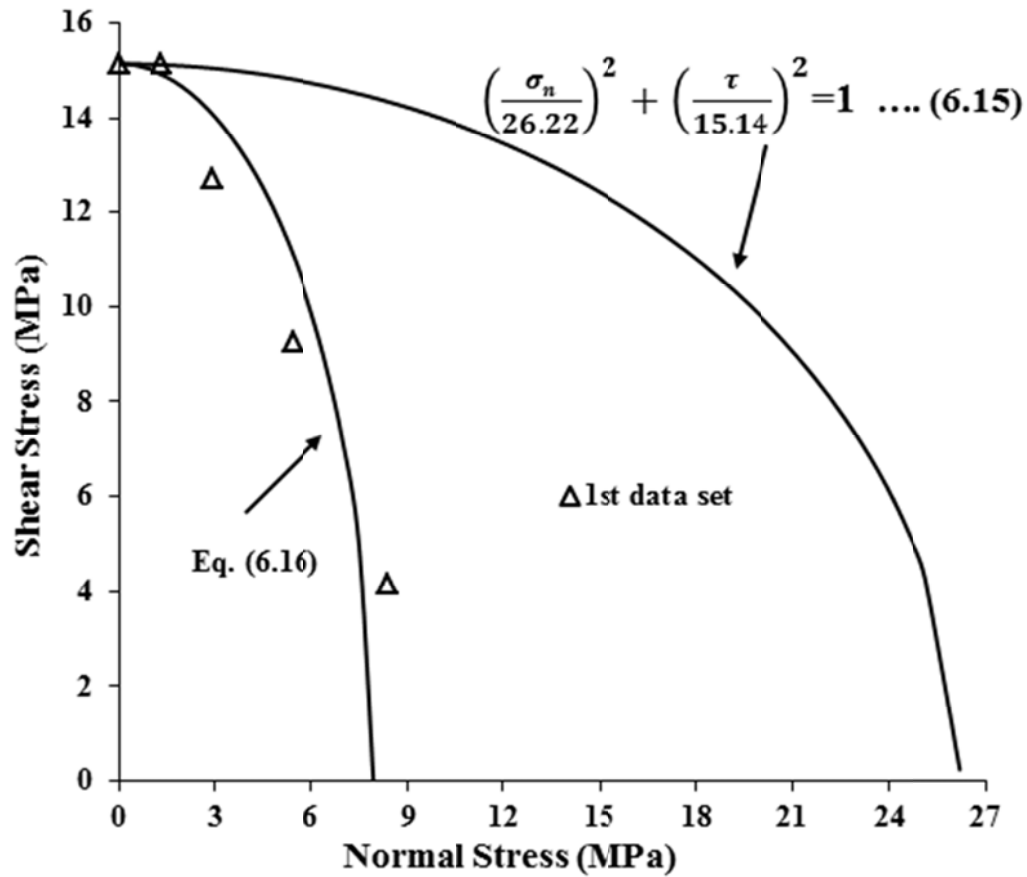


Figure 6.14: Interface bonding strength envelope based on effective stress criterion

It is noted that the stress data points are not fitted by the effective stress criterion. Next, the second trial criterion is found by applying the best fit curve technique on the 1<sup>st</sup> stress data points. By keeping the value  $\tau_s = 15.84$  MPa, the second trial criterion is obtained as Equation 6.16 (see Figure 6.14).

$$\left(\frac{\sigma_n}{7.95}\right)^2 + \left(\frac{\tau}{15.14}\right)^2 = 1 \quad (6.16)$$

Based on the above second trial criterion, a second set of stress data points is obtained based on the maximum values of the left side of Equation (6.16) for each test case and denoted as “2<sup>nd</sup> data set”. Figure 6.15 shows both Equation (6.16) and corresponding stress data points.

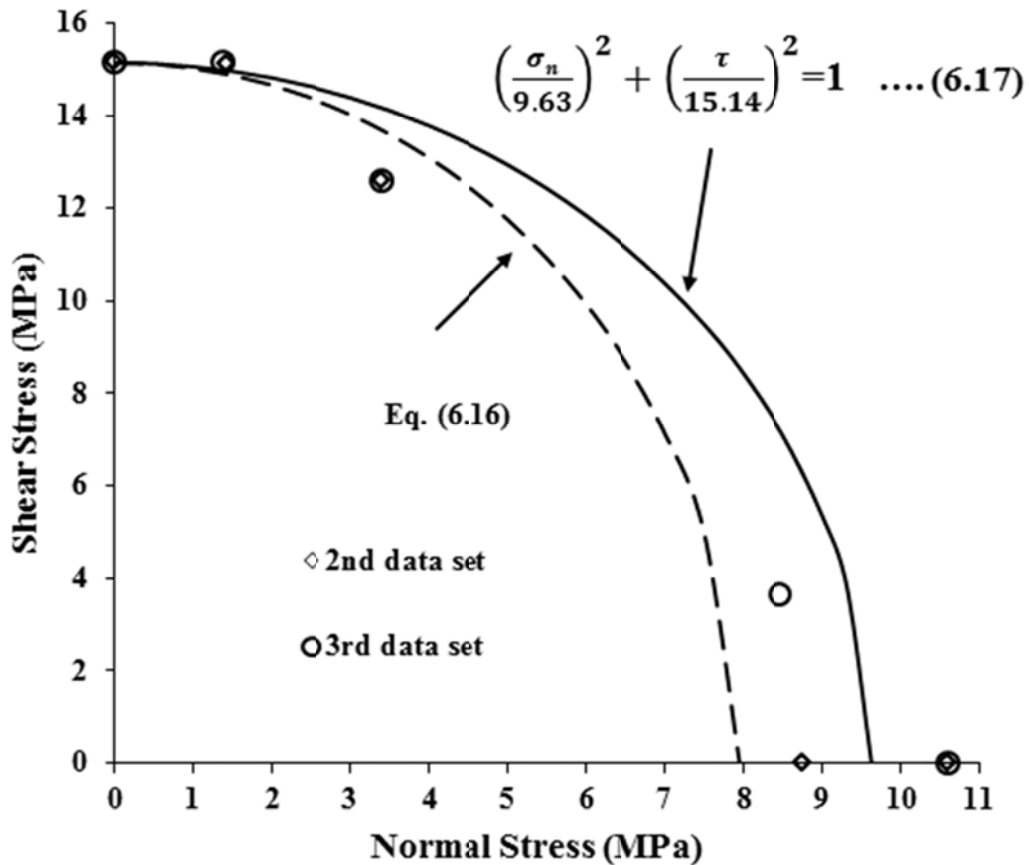


Figure 6.15: Interface bonding strength envelope in different iterations

It is also clear that this criterion doesn't fit the “2<sup>nd</sup> data set” well. The third criterion is obtained by fitting the 2<sup>nd</sup> set of stress data points as follows

$$\left(\frac{\sigma_n}{9.63}\right)^2 + \left(\frac{\tau}{15.14}\right)^2 = 1 \quad (6.17)$$

---

Following the same procedure, for this trial criterion (Equation 6.17), a third set of stress points is obtained for each test case. Figure 6.15 also includes the third set of stress data points. It is observed that Equation (6.17) also fits the third set of stress data points. Further iteration produces the same stress data points, i.e. a converged strength criterion is obtained. Therefore, for the tested viscoelastic/viscoelastic (PVC/Epoxy) bi-material interface, Equation (6.17), as shown in Figure 6.15, represents its normal-shear interface bonding strength criterion (envelope) in the range of the first quarter of the normal-shear stress plane.

**BIBLIOGRAPHY**

Dundurs, J., 1969. Discussion of edge-bonded dissimilar orthogonal elastic wedges under normal and shear loading. *Journal of Applied Mechanics*. 36, 650-652.

## **CHAPTER 7: APPLICATION IN DENTAL RESTORATIONS**

Part of this chapter has been published as

**Chowdhuri , M. A. K.,** Xia, Z., Yu, D., 2011. A Study on Optimal Bonding Angles of Bi-material Interfaces in Dental Crowns with Porcelain Fused to Metal. Proc. IMechE Part H: *Journal of Engineering in Medicine*, 225(7), 657-668.

## CHAPTER 7

### APPLICATION IN DENTAL RESTORATIONS

---

Structures consisting of two dissimilar materials bonded together along a common interface are increasingly used in various bio-medical disciplines. One of the important examples of such applications is in the dental crowns which are used to replace the damaged tooth structures. Porcelain fused to metal (PFM) and all ceramic crowns are widely used in dental restorations. Optimal design for Porcelain fused to metal crown based on the developed method is presented in this chapter.

#### 7.1 BACKGROUND STUDY

Structures consisting of two dissimilar materials bonded together along a common interface are often found in various engineering and biomedical applications, for example, in dental crowns which are used to repair damaged teeth. Porcelain fused to metal (PFM) restorations are popular because low fusing porcelain enamels have coefficients of thermal expansion that are similar to those of the supporting metals (Craig et al., 1971). Clinical aspects of PFM restorations have been extensively studied and reported in the literature; see references

(Masterton and Davis, 1964; Mumford, 1965; Straussberg et al., 1966), among others.

Although it is uncertain if the PFM bond is a van der Waals bond or a chemical bond, the bond strength developed between porcelain enamels and gold alloys has received considerable attention in studies that have attempted to understand the failure of PFM crowns (Shell and Nielsen, 1962; Ryge, 1965, Knap and Ryge, 1966). Stashevich and Guzman (1984) reported that inadequate adhesion between the ceramic and metal layers is one of the main reasons for fracture in ceramic–metal items such as integral prostheses formed by alloys with porcelain shells. DeHoff and Anusavice (1984) reported that porcelain– metal incompatibility may cause localized marginal distortion of metal–ceramic crowns.

Craig et al. (1971) examined stress distribution in restorations and the supporting structure in considering different designs, loading sites, and magnitudes of load using a two-dimensional (2D) photoelastic technique. They recommended that the porcelain–gold joint at the shoulder should be at an angle of 30° to the horizontal for better stress distribution.

Various factors can affect the long-term viability of crowns, such as geometry of preparation, type of composite cement and adhesive system, marginal adaptation, periodontal response, tooth morphology functional and parafunctional activities, etc. The most common failure modes associated with dental restorations are fracture, micro-leakage, and debonding (Clark, 2008; Whitworth et al., 2002; Lu et al., 2008). The failure at the interface is primarily caused by a stress concentration/singularity in the dental ceramic at the corner of the interface

(Soboyejo et al., 2001; Lawn et al., 2002). Li et al. (2004), on the basis of finite element analyses, suggested that a high stress concentration exists at the crown–cement interface of dental bridges. For resin-bonded bridge structures, clinical observations and experimental investigations have shown that debonding at the interface is a major mode of failure (Knight, 1993; Culy and Tyas, 1998). Also, for all ceramic crowns, the major clinical failure is observed at the interface between the crown (dental ceramic) and cement (Kelly, 1997). In dental crown restorations, the Young's modulus of the crown material is different to that of the cement. Hence, there is a stress concentration in the crown at the interface between the crown and the cement (Soboyejo et al., 2001).

From the above review, it is clear that failures are usually initiated from the corners of the interfaces in dental crowns or bridges, where either a high stress concentration or a stress singularity can be created. In this study, the principles of continuum mechanics (interface mechanics is a branch of this area) are used to study the characteristics of interface stress distribution along the interface between two materials and the dependence of the stress distribution on the geometry of the interface, especially the conditions with or without stress concentration/singularity at the free edge corners of the interface. The analysis is based on the materials' bulk mechanical properties (Young's modulus and Poisson's ratio for elastic interfaces between two materials). The work presented here suggests that there are two possible routes to reduce/avoid a stress singularity at the corner of an interface: one is to change the material combination thereby

minimizing the difference in the mechanical properties of the two materials; the other is to optimally design the interface geometry. The focus of this research is in fact on the latter method. Only PFM crowns containing precious or non-precious metals are considered in this study; however, the proposed method can be applied to other types of crown. From a micro- or nano-scale point of view the surface structures of most materials differ from their bulk (substrate) properties; for example, the surface structures of most metals can include an oxide layer, a strain-hardening layer, etc. The study of micro-/nano-structural characteristics at the interface between two materials (more accurately, the word ‘interphase’ should be used) is important in order to understand the chemical/physical bonding mechanisms between the two materials. However, this is beyond the scope of this study.

## 7.2 MATERIALS

The materials considered in this study are porcelain, cement, and metal. Two types of metal are included: the precious-metal-based alloy, Olympia and the non-precious-metal-based alloy, Wirobond-280. These materials are currently used in many dental laboratories.

All of the materials used in this research are considered to be linear elastic and isotropic. Only two elastic properties, Young’s modulus of elasticity ( $E$ ) and Poisson’s ratio ( $\nu$ ) are therefore required to characterize these materials. The

modulus of elasticity of porcelain has been reported several times in the literature (Anusavice et al., 1980; Lawn et al., 2001; Li et al., 2004) as being between 68 and 68.9 GPa and the Poisson's ratio as being between 0.25 and 0.28 (Anusavice et al., 1980; Li et al., 2004). The modulus of elasticity of Olympia and Wirobond-280 are specified by their respective manufacturers as approximately 124 GPa and 220 GPa respectively. The Poisson's ratio for gold alloys varies from 0.383 to 0.397 (Suansuwan and swain, 2001). The data for the Poisson's ratio of Wirobond-280 is not available. Thus, the Poisson's ratio,  $\nu$  of Wirobond-280 is estimated from its constituent properties by the commonly used rule of mixing

$$\nu = \sum_{i=1}^7 \nu_i V_i \quad (7.1)$$

where  $\nu_i$  and  $V_i$  are the Poisson's ratio and volume fraction of each constituent, respectively, The Volume fraction of each constituent is calculated by

$$V_i = \frac{\rho}{\rho_i} W_i \quad (7.2)$$

where  $W_i$  is the weight fraction,  $\rho_i$  is density of constituent  $i$ , and  $\rho$  is the density of the WIROBOND-280 alloy. Thus the obtained Poisson's ratio,  $\nu$  of WIROBOND-280 is 0.275. Details of this calculation can be found Table 7.1.

Table 7.1: Poisson's ratio calculation for Wirobond-280

Components	Weight fraction (%)	Poisson's ratio, $\nu$	Density, $\rho$ (gm/cm <sup>3</sup> )	Volume fraction, $V$ (%)	$\nu \times V/100$
Co	60.2	0.31	8.9	57.49	.1782
Cr	25	0.21	7.14	29.76	.0625
W	6.2	0.28	19.2	2.74	0.008
Mo	4.8	0.31	10.28	3.97	.012
Ga	2.9	0.35	5.9	4.18	.015
Si	0.45 (let)	-	-	-	-
Mn	0.45 (let)	-	-	-	-
Total	100				0.275

Manufacturer: BEGO; Elastic modulus: 220 GPa, Density: 8.5 gm/cm<sup>3</sup>

There are numerous cements currently in use in dental practice. Zinc phosphate, zinc silico-phosphate, and silicate cement are among the most widely used compounds. van Noort (2002) reported that zinc phosphate cement is extensively used in clinical practice because of its long history of success and favorable handling properties. The elastic properties for zinc phosphate are taken from Nakayama et al. (1974). The properties of porcelain, Olympia, Wirobond-280, and the zinc phosphate dental cement are summarized in Table 7.2.

Table 7.2: Elastic properties of dental materials

Material	Modulus of Elasticity, E (GPa)	Poisson's Ratio, $\nu$
Porcelain	68	0.25
OLYMPIA	124	0.38
WIROBOND 280	220	0.275
Dental Cement	60	0.32

Manufacturer of OLYMPIA: JELENKO

### 7.3 DEVELOPMENT OF THE MODEL

Figure 7.1 shows a sectional view of a PFM crown. One can see that the three materials are joined together along two different interfaces: the interface between porcelain and metal and the interface between metal and dental cement. Of course, there exists another interface between cement and dentine (not shown on Figure 7.1), but the properties of the cement can be considered to be similar to dental cement according to Zarone et al. (2005). From the point of view of interface mechanics, the closer the mechanical properties of the two materials, the less severity of the stress concentration/singularity at their interface. Thus, the cement/dentine interface is not included in the model. Of course, if the difference in properties between the dental cement and dentine is large, this interface should also be included in the analysis. In principal, there is no difficulty in applying the proposed method to that case.

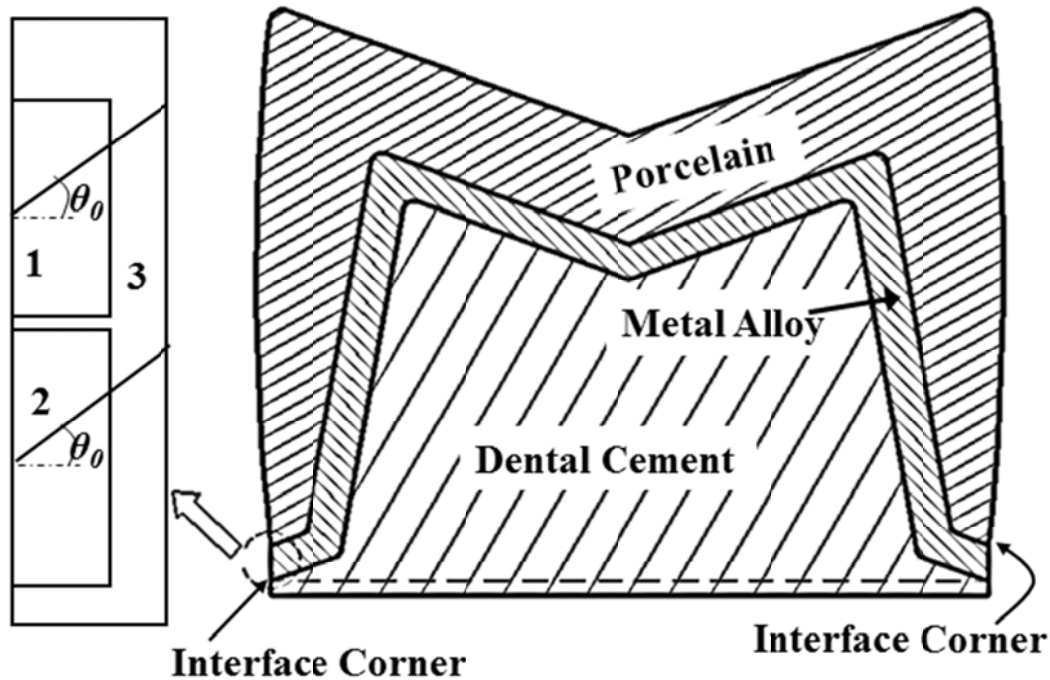


Figure 7.1: Sectional view of a PFM crown and local model near the free edge corner of the interface

As described in the Introduction, the main reason for the failure of a PFM crown is debonding, which is most likely to start from the free edge corners of the interfaces as shown in Figure 7.1. This is due to the existence of a high stress concentration or even a stress singularity at these corners of the interface. A stress singularity means that theoretically the stress value goes to infinity when a load is applied on the crown. To focus the stress analysis on the area near the free edge corners, three types of local models are obtained from the global crown model as shown to the left of Figure 1: model 1 contains the interface between porcelain and metal; model 2 represents the interface between metal and cement, and model

3 contains both interfaces. The bonding angle,  $\theta_0$ , is defined as the angle between the interface and the horizontal plane near the corner as shown in Figure 1. This bonding angle is not equal to the bonding angle defined in Chapter 2 (this bonding angle is equal to  $\gamma = 90 - \theta_0$  in Chapter 2). The bonding angle is defined here this way to match with the current dental specifications. For a given combination of materials, the stress field near the corner of the interface depends on the bonding angle  $\theta_0$ . The objective of this work is to find an appropriate range of bonding angles at which the stress singularity at the free edge corners of the interface can be eliminated.

#### **7.4 STRESS SINGULARITY ANALYSIS USING FINITE ELEMENT MODELING**

Figure 7.2 shows the finite element models of the three considered local models. Figure 7.2(a) is used for models 1 and 2, since both models contain a single interface, whereas for model 3, Figure 2(b) is required. For each case a larger mesh size is used for areas away from the interface. In the area close to the interface, especially near the free edge interface corner, very small meshes are used. The commercial finite element analysis code ANSYS with the 2D axisymmetric element Plane 42 is used for the analysis. The boundary conditions for the left-hand side and the top of the local model (these two sides are connected by the body of the crown) are obtained from the global axisymmetric analysis

results of the full crown. It is found in the global analysis that the displacement  $U_x$  of the left-hand side is almost constant and the pressure applied on the top of the local model is almost the same as the applied global pressure on the full crown. Therefore, the boundary conditions applied on the four sides of the local model were:  $U_x = \text{constant}$  (obtained from the global analysis) at the left-hand side,  $U_y = 0$  at the bottom side,  $P = \text{constant}$  (obtained from the global analysis) at the top side, and free traction condition at the left hand side.

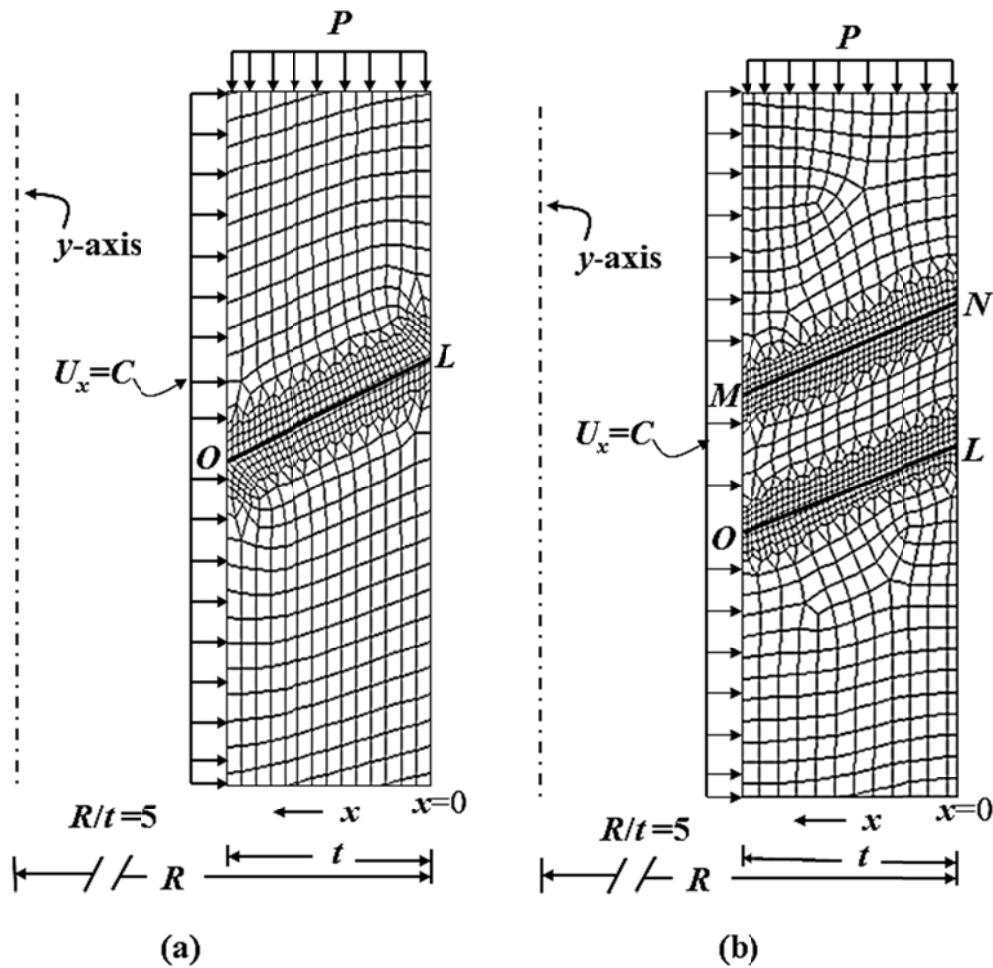


Figure 7.2: Finite element models: (a) single interface and (b) two interfaces

After solving the problem, the normal and shear stress components,  $\sigma_n$  and  $\tau$ , along the interface are determined by stress transformation, and the effective stress,  $\sigma_{eff} = \sqrt{\sigma_n^2 + 3\tau^2}$  is also calculated. If the stress at the corner of an interface for a particular bonding angle increases with the refinement of the mesh and does not converge to a finite value, then this is taken to indicate the presence of a stress singularity. In contrast, for a non-singular case, the stress at the corner of an interface converges to a finite value with the refinement of the mesh. The same analysis is carried out for different bonding angles and the results are shown in Figures 7.3 to 7.6.

The variation of the effective stress along the porcelain–metal interface for precious-metal-based and non-precious-metal based alloy crowns are plotted against the horizontal distance from the free edge corner in Figure 7.3. From Figure 7.3(a), it can be seen that for a bonding angle between 20 and 50° the effective stress converges to finite values at the corner of the interface,  $x = 0$ . However, for the case of a 5° bonding angle, at  $x = 0$ , the stress value does not converge to a finite value in fact it increases with further refinement of the mesh size (see the enlarged figure to the left of Figure 7.3(a)). This indicates that a stress singularity exists at the porcelain–metal interface corner of precious-metal-based crowns for a bonding angle of 5°. Similarly, Figure 7.3(b) shows that for the porcelain–metal interface with non-precious-metal based alloy a stress singularity exists for a bonding angle of 5° but there are no stress singularities for bonding angles of 32 and 50°.

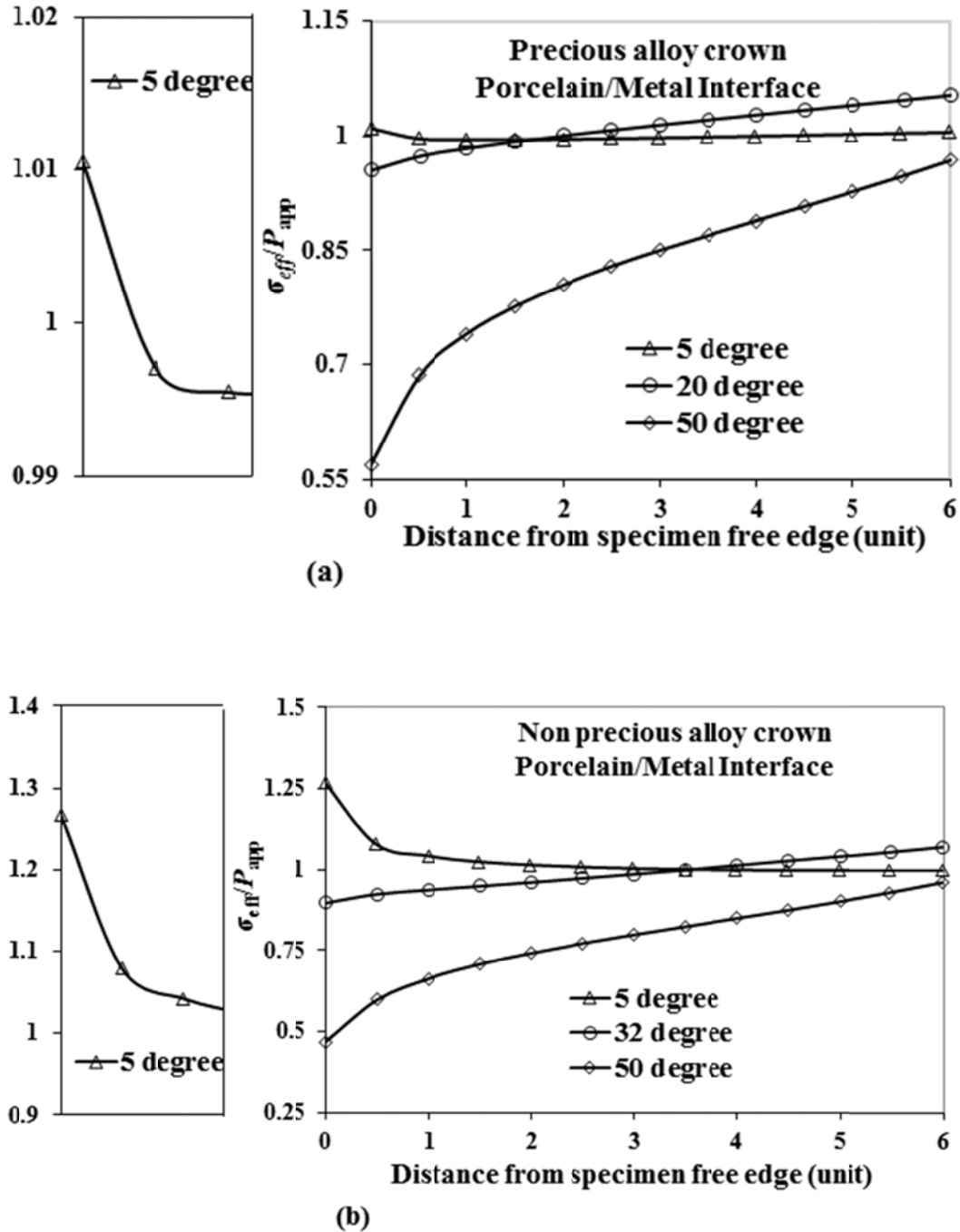
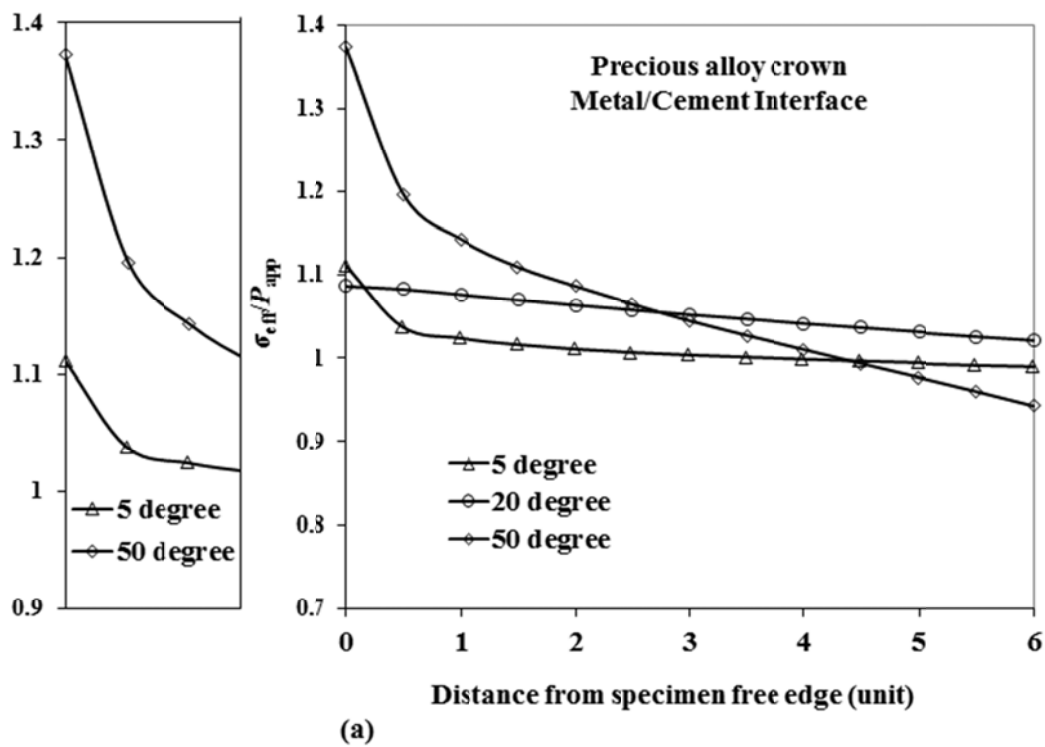


Figure 7.3: Effective stress distribution along porcelain-metal interface for different bonding angles: (a) precious-metal-based crown and (b) non-precious-metal based crown

The results obtained for the metal–cement interface are presented in Figure 7.4. It is interesting to note that for the metal–cement interface stress singularities exist for cases with smaller or larger bonding angles (5 and 50°) but at certain bonding angles between them the stress singularity can be eliminated (20° in Figure 7.4(a) and 32° in Figure 7.4(b)).



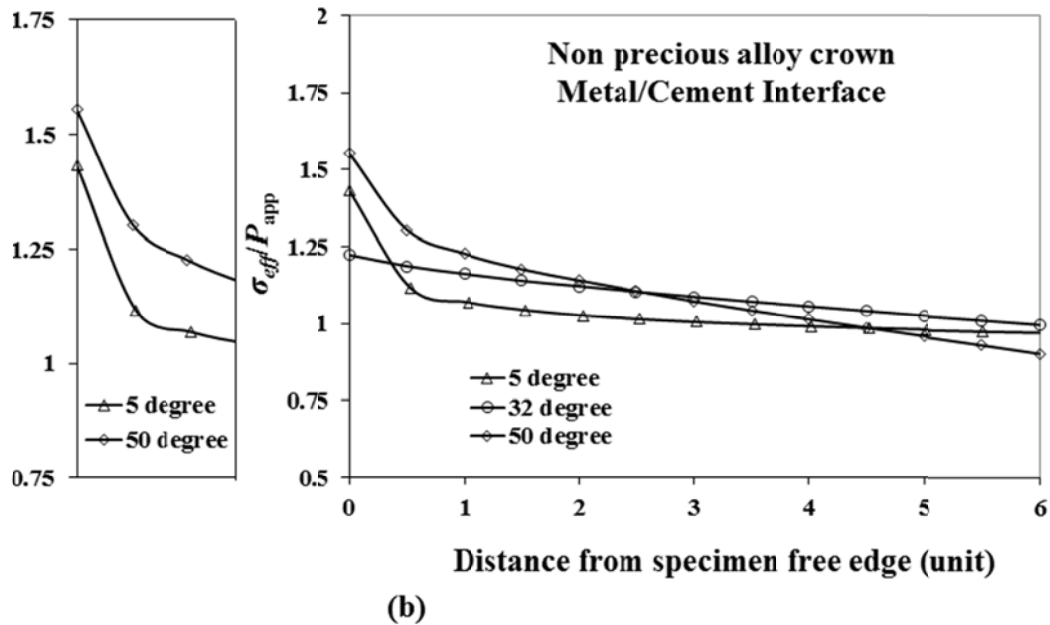


Figure 7.4: Effective stress distribution along metal-cement interface for different bonding angles: (a) precious-metal-based crown and (b) non-precious-metal based crown

Furthermore, model 3 with two interfaces is analyzed to see if there is any effect of the coexistence of the interfaces. Comparing the results in Figure 7.5 with the results in Figures 7.3(a) and 7.4(a) and the results in Figure 7.6 with those in Figures 3(b) and 7.4(b) one can find that there is no difference in terms of the existence/elimination of stress singularities. Thus, the results obtained from the FEM of model 3 are consistent with those obtained from FEM model 1 and model 2. This is expected since a stress singularity is a phenomenon that only occurs very close to the interface free edge corner.

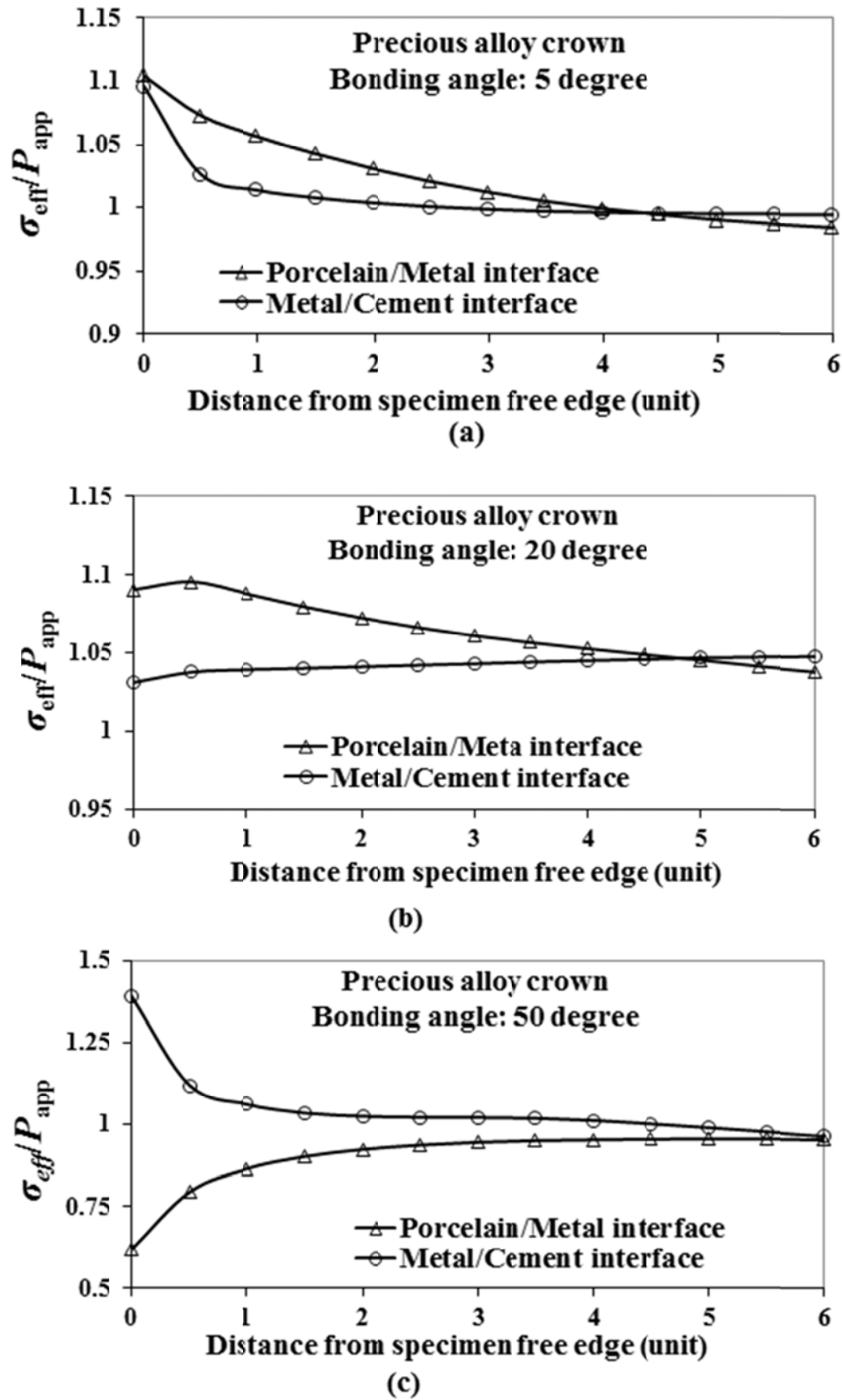


Figure 7.5: Variation of effective stress of precious-metal-based crown along both interfaces for bonding angles of: (a) 5°; (b) 20°; and (c) 50°

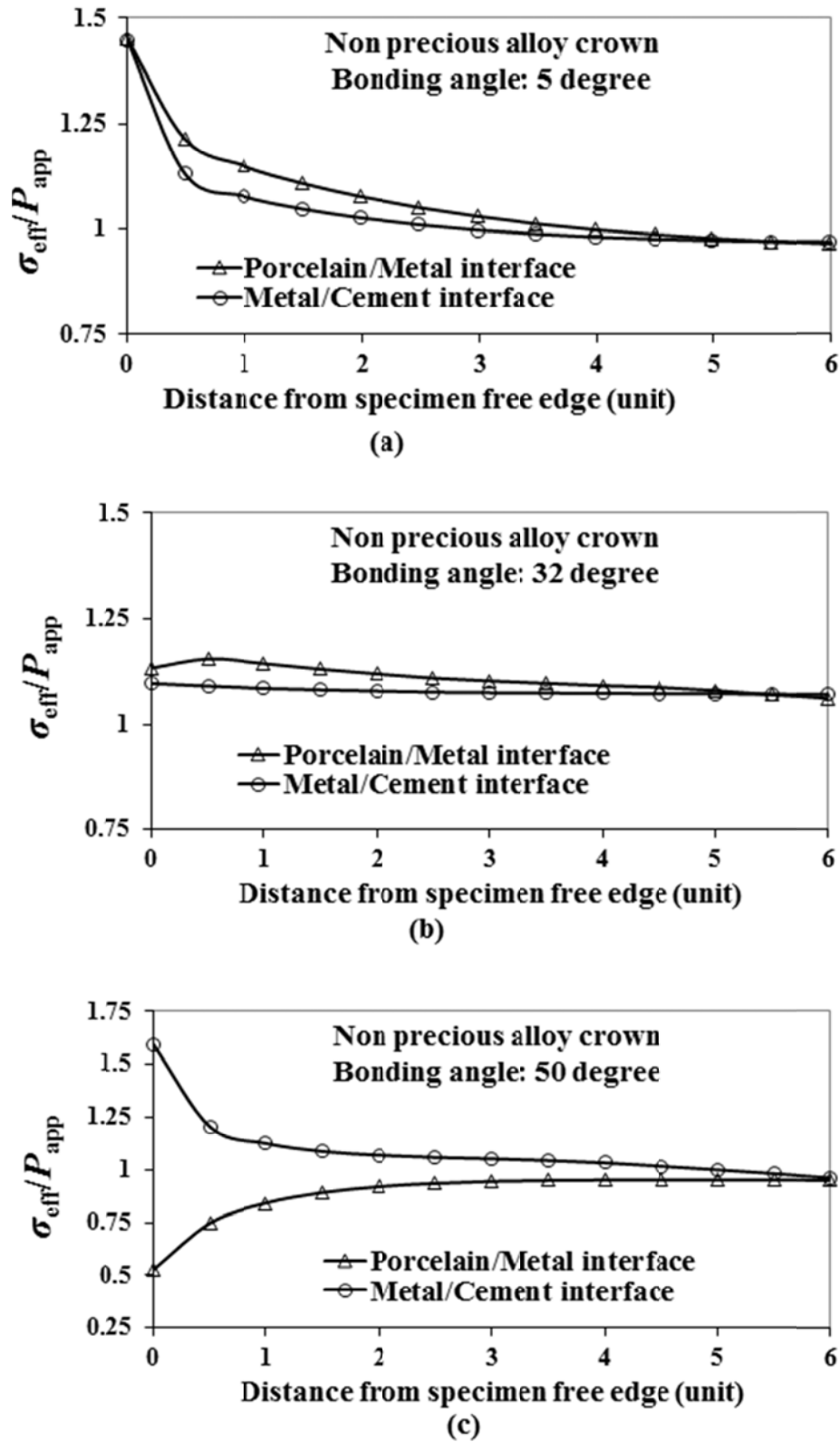


Figure 7.6: Variation of effective stress of non-precious-metal-based crown along both interfaces for bonding angles of: (a) 5°; (b) 32°; and (c) 50°

## 7.5 STRESS SINGULARITY ANALYSIS BY AN ANALYTICAL METHOD

To more accurately determine the range of bonding angles with or without a stress singularity, the use of an analytical solution could be more convenient. There is an extensive literature on efforts to obtain analytical solutions of the singular stress field near the free edge of an interface between two materials, see references (Bogy, 1971; Munaz and Yang, 1992; Qian and Akisanya, 1999; Liu et al., 1999), among others. Details about analytical solution can be found in Chapter 2 and 3. No matter what mathematical methods are used, the stress field near the free edge tends to be cast into the following asymptotic form

$$\sigma_{ij} = Hr^{\lambda-1} f_{ij}(\theta, \alpha, \beta, \lambda) \quad (i, j = 1, 2) \quad (7.3)$$

In the above expression,  $r, \theta$  are the polar coordinate,  $H$  is the stress intensity factor,  $\alpha, \beta$  are Dundurs' (1969) parameters which depend on combinations of the elastic constants of the two materials,

$$\alpha = \frac{\mu_1(k_2 + 1) - (k_1 + 1)\mu_2}{\mu_1(k_2 + 1) + (k_1 + 1)\mu_2}; \quad \beta = \frac{\mu_1(k_2 - 1) - (k_1 - 1)\mu_2}{\mu_1(k_2 + 1) + (k_1 + 1)\mu_2}; \quad (7.4)$$

where,  $\mu_j = \frac{E_j}{2(\nu_j + 1)}$ ,  $k_j = 3 - 4\nu_j$ ,  $\mu$  is shear modulus,  $E$  is elastic

modulus,  $\nu$  is Poisson's ratio and subscript  $j$  is material index. The  $\lambda$  is eigenvalue obtained from the following eigenvalue equation (see section 4.2.1 in chapter 4 for detail derivations)

$$\begin{aligned} & \sin^2 \lambda \pi + 2(2\lambda^2 \cos^2 \theta_0 - 1)\alpha \sin \lambda \pi \sin 2\lambda \theta_0 - 4\lambda^2 \beta \sin \lambda \pi \sin 2\lambda \theta_0 \cos^2 \theta_0 + 4\lambda^2 \cos^2 \theta_0 \\ & (1 - \cos \lambda \pi \cos 2\lambda \theta_0 - 2\lambda^2 \cos^2 \theta_0) \alpha \beta + [\sin^2 2\lambda \theta_0 + 4\lambda^2 (\lambda^2 - 1) \cos^2 \theta_0 - \lambda^4 \sin^2 2\theta_0] \alpha^2 + \\ & [4\lambda^2 \cos^2 \theta_0 (\lambda^2 \cos^2 \theta_0 - 1 + \cos \lambda \pi \cos 2\lambda \theta_0) + (\cos \lambda \pi - \cos 2\lambda \theta_0)^2] \beta^2 = 0 \end{aligned} \quad (7.5)$$

In the above equation,  $\theta_0$  is the bonding angle defined in Figure 7.1

From the Equation (7.3), if  $0 < \lambda < 1$ , the stress component goes to infinite when  $r \rightarrow 0$ , i.e. there exists stress singularity. For  $\lambda > 1$ , the stress singularity is eliminated.

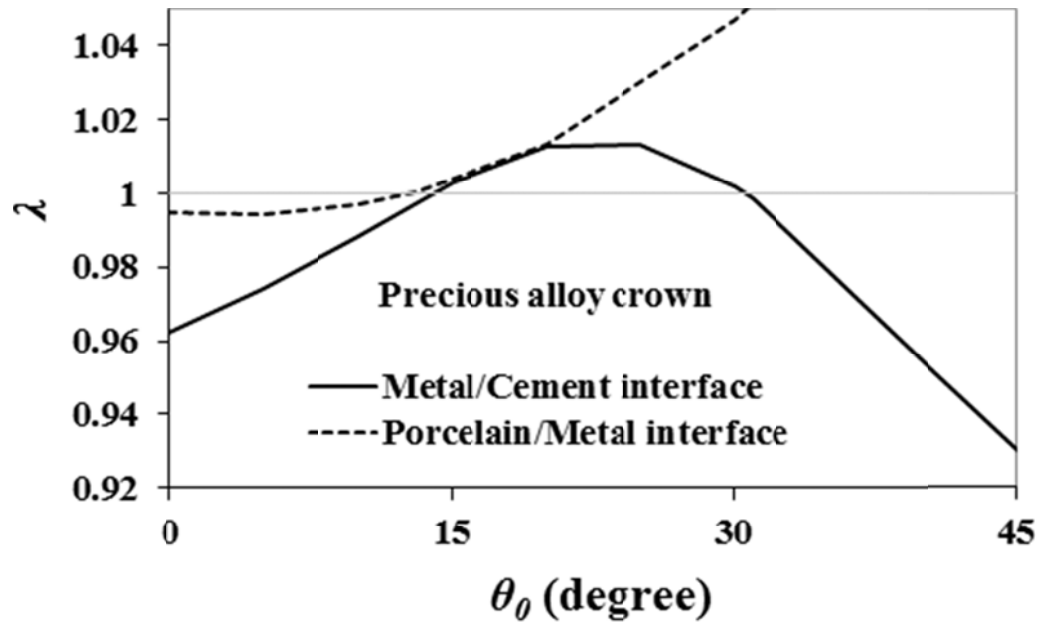
Based on the properties of materials given in Table 2, the eigenvalue of  $\lambda$  is calculated by using Equation (7.5). The results obtained for both the porcelain–metal and metal–cement interfaces of the precious-metal-based and non-precious-metal-based alloy crowns are listed in Tables 7.3 and 7.4, respectively. Figure 7.7 clearly shows the variation of the eigenvalue  $\lambda$  as a function of the bonding angle. To summarize the presented analysis results, one can see that for PFM crowns made with the precious metal- based alloy Olympia and in the range of bonding angles  $15^\circ \leq \theta_0 \leq 30^\circ$ , the stress singularity can be eliminated: however, for PFM crowns made with the non-precious-metal-based alloy Wirobond-280 the bonding angle range that is stress singularity free is  $30^\circ \leq \theta_0 \leq 35^\circ$ .

Table 7.3: Value of  $\lambda$  corresponding to different bonding angles for precious alloy crown

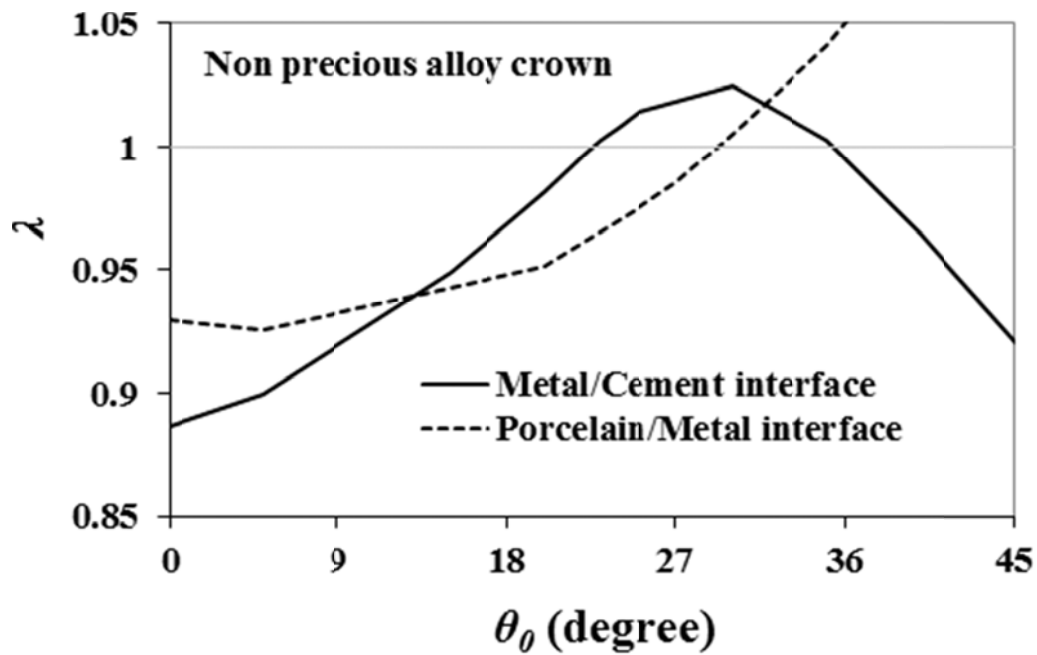
Porcelain/Metal (OLYMPIA) interface		Metal (OLYMPIA) /Cement interface	
Bonding angle, $\theta_0$	$\lambda$	Bonding angle, $\theta_0$	$\lambda$
0	0.995	0	0.9622
5	0.9945	5	0.974
10	0.997	10	0.9884
12	0.9989	15	1.0028
13	1.0001	20	1.0126
20	1.0135	25	1.013
30	1.047	30	1.0019
45	1.12	31	0.9984
60	1.149	45	0.93
75	1.086	60	0.875
90	1	75	0.866
		80	0.902
		85	0.942
		90	1

Table 7.4: Value of  $\lambda$  corresponding to different bonding angles for non-precious alloy crown

Porcelain/Metal (WIROBOND-280) interface		Metal (WIROBOND-280)/Cement interface	
Bonding angle, $\theta_0$	$\lambda$	Bonding angle, $\theta_0$	$\lambda$
0	0.93	0	0.887
5	0.926	5	0.9
20	0.952	15	0.949
25	0.975	20	0.982
27	0.986	22	0.996
28	0.992	23	1.0024
29	0.9985	24	1.0085
30	1.0052	25	1.014
35	1.041	30	1.025
40	1.087	35	1.003
45	1.137	40	0.965
60	1.228	45	0.921
65	1.207	55	0.85
70	1.17	60	0.825
75	1.128	75	0.803
90	1	90	1



(a)



(b)

Figure 7.7: Variation of  $\lambda$  with the bonding angle  $\theta_0$  for (a) precious-metal-based crown and (b) non-precious-metal-based crown

## 7.6 OPTIMAL OFF-VERTICAL ANGLE OF THE METAL LAYER

Based on the recommendations for the bonding angles at the free edge corners of an interface made in the previous section, FEM analyses are further carried out on the global crown model to determine the optimal off-vertical position of the metal layer. Figure 7.8 shows the 2D axisymmetric model and corresponding FEM model used in the analyses.

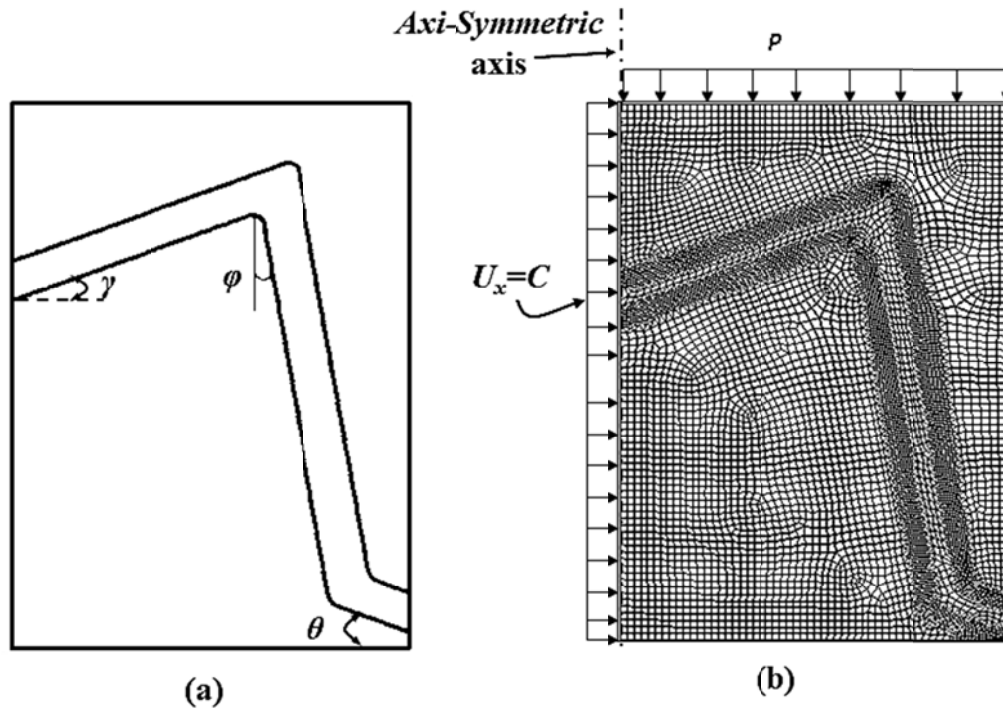


Figure 7.8: (a) Global axisymmetric model of PFM crown and (b) FEM mesh and applied boundary

The bonding angle at the interface free edge corner is taken as  $\theta_0 = 20^\circ$  for the precious-metal-based crown and  $\theta_0 = 32^\circ$  for the non-precious-metal-based crown. Thus, a stress singularity does not exist at the free edge corner of the interface. The angle  $\varphi$  in Figure 7.8 is the defined off-vertical angle. The stress distributions as a function of  $\varphi$  are obtained at a constant value of the applied pressure at the top surface. Note that in the analyses a constant angle  $\gamma = 20^\circ$  is assumed, see Figure 7.8.

The contour plots of the effective stress at  $\varphi = 5^\circ, 10^\circ$  and  $20^\circ$  for the precious-metal-based crown are shown in Figure 7.9(a) and at  $\varphi = 5^\circ, 10^\circ$  and  $12^\circ$  for the non-precious-metal-based crown are shown in Figure 7.9(b), respectively. The high stress zone in each figure is marked with a circle. From Figure 7.9(a) (precious-metal-based crown) it can be seen that at  $\varphi = 5^\circ$ , there are two high stress concentration zones in the metal layer, and at  $\varphi = 20^\circ$  there is a very small high stress concentration zone at the lower part of the metal–cement interface. However, no such stress concentration with a lower maximum stress level exists at  $\varphi = 10^\circ$ . Similarly, from Figure 9(b) (nonprecious- metal-based crown) the optimal off-vertical angle of the metal layer is  $\varphi = 12^\circ$ .

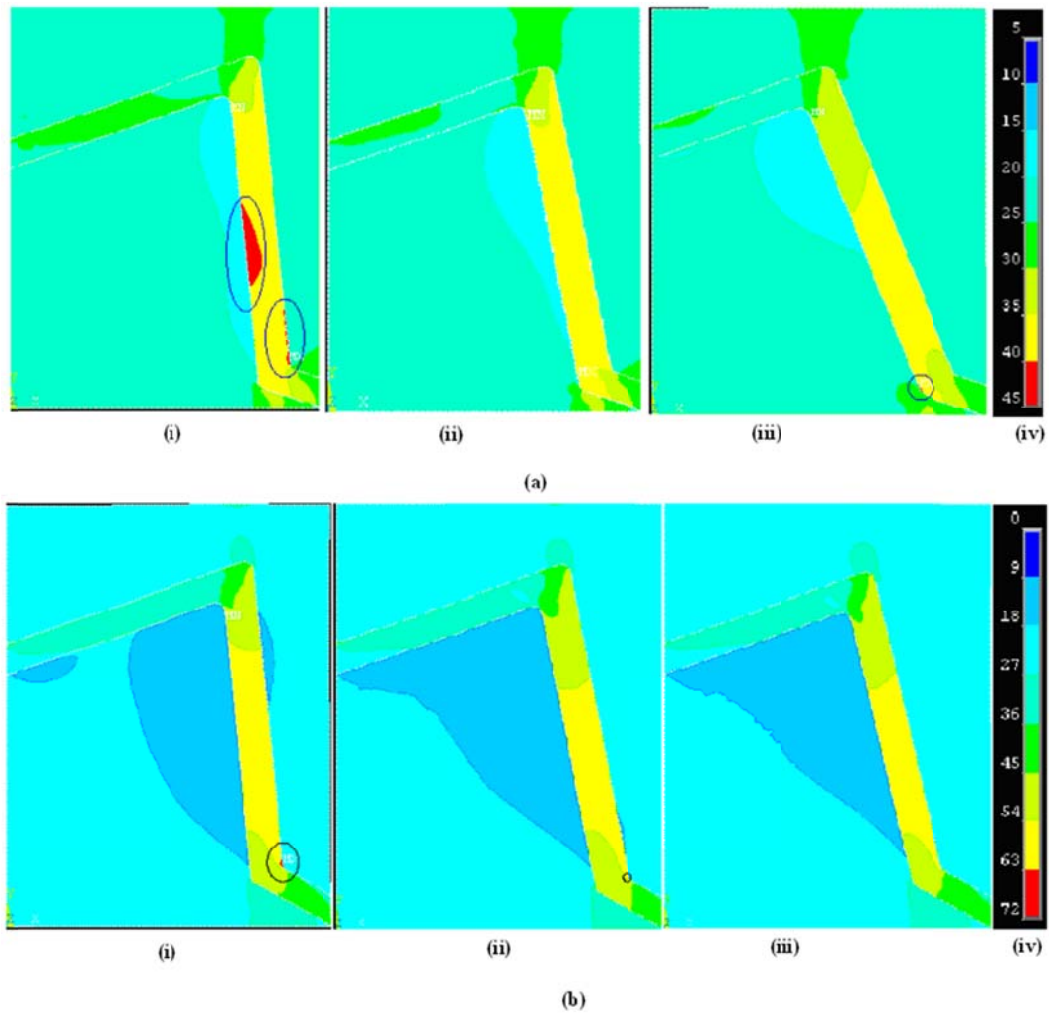


Figure 7.9: Contour plot of nodal effective stresses of (a) precious-metal based crown for (i)  $\phi=5^\circ$ , (ii)  $\phi=10^\circ$ , (iii)  $\phi=20^\circ$ ; and (b) non-precious-metal based crown for (i)  $\phi=5^\circ$ , (ii)  $\phi=10^\circ$ , (iii)  $\phi=12^\circ$

## 7.7 FURTHER OBSERVATION AND REMARKS

Figure 7.10 shows some alternative interface edge designs currently adopted in dental restoration technology. Based on the presented results, the feather edge design does not appear to be a good choice for both precious-metal-based and non-precious-metal-based crowns. This is because if a PFM crown is made with a feather edge with a bonding angle between  $15$  and  $30^\circ$  using a precious-metal based alloy or between  $30$  and  $35^\circ$  for nonprecious metal-based alloy, it will need a large amount of porcelain, which is undesirable and unrealistic. At the same time, if the bonding angle is not in the above ranges, the crown may be prone to failure at the free edge corners of the interface due to the existence of stress singularities.

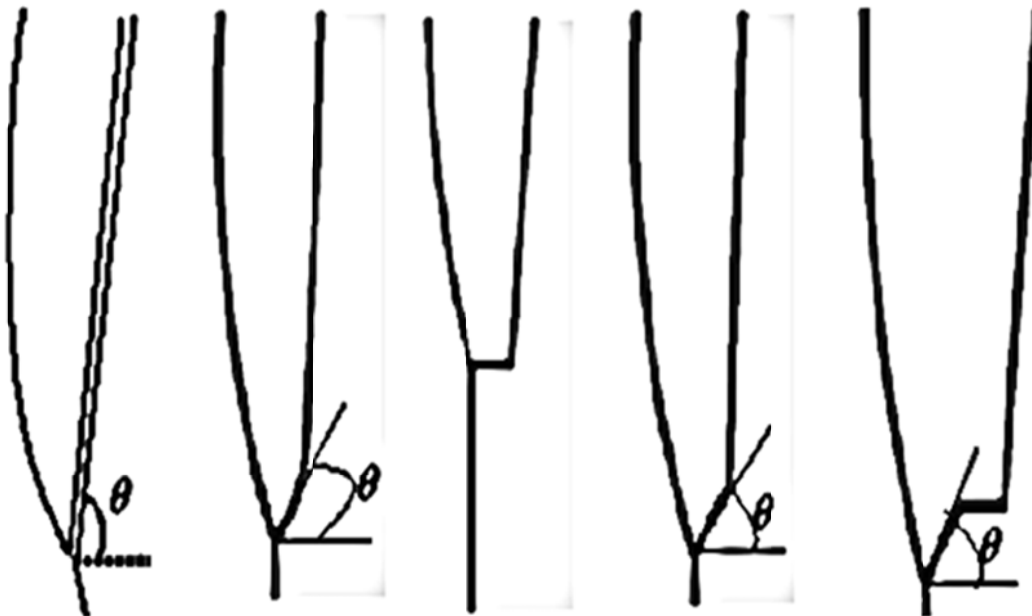


Figure 7.10: Different types of margin for tooth crown: (a) feather; (b) chamfer; (c) shoulder; (d) bevel; and (e) bevel-shoulder

Usually for shoulder edge crowns, the bonding angle is maintained between 0 and 5°. Such a design should also be avoided because a stress singularity could exist at both of the free edges of the interface.

It seems that chamfer, bevel, and bevel shoulder edges might be suitable if the bonding angle at the interface is within the safe range between 15 and 30° for crowns made from precious-metal-based alloys and from 30 to 35° for crowns with from nonprecious- metal-based alloys. It is interesting to note that the bonding angle of 30° suggested in Craig et al. (1971), which is based on a 2D photoelastic experimental method, is just within the current suggested bonding angle ranges for either precious-metal based or non-precious-metal-based crowns.

**BIBLIOGRAPHY**

- Anusavice, K. J., Dehoff, P. H., Fairhurst, C. W., 1980. Comparative evaluation of ceramic-metal bond tests using finite element stress analysis. *Journal of Dental Research*. 59(3), 608–613.
- Bogy, D. B., 1971. Two edge-bonded elastic wedges of different materials and wedge angles under surface tractions. *Journal of Applied Mechanics*. 38, 377-386.
- Clark, S., 2008. Optimum life-time management of coronal fractures in anterior teeth: a review of crowns, veneers, composite resin restorations and intra-coronal bleaching. Evidence-based Healthcare Advisory Group, Research and Development, Accident Compensation Corporation.
- Craig, R. G., El-Ebrashi, M. K., Peyton, F. A., 1971. Stress distribution in porcelain-fused-to-gold crowns and preparations constructed with photoelastic plastics. *Journal of Dental Research*. 50(5), 1278–1283.
- Culy, G., Tyas, M. J., 1998. Direct resin-bonded, fibre-reinforced anterior bridges: a clinical report. *Australian Dental Journal*. 43(1), 1–4.
- DeHoff, P. H., Anusavice, K. J., 1984. Effect of metal design on marginal distortion of metal-ceramic crowns. *Journal of Dental Research*. 63(11), 1327–1331.

- 
- Dundurs, J., 1969. Discussion of edge-bonded dissimilar orthogonal elastic wedges under normal and shear loading. *Journal of Applied Mechanics*. 36, 650-652.
- Kelly, J. R., 1997. Ceramics in restorative and prosthetic dentistry. *Annual Review of Materials Science*. 27, 443–468.
- Knap, F. J., Ryge, G. 1966. Study of bond strength of dental porcelain fused to metal. *Journal of Dental Research*. 45(4), 1047–1051.
- Knight, G. M., 1993. The immediate cantilever resin bridge. *Australian Dental Association News Bulletin*. 206, 26–29.
- Lawn, B. R., Deng, Y., Lloyd, I. K., Janal, M. N., Rekow, E. D., Thompson, V. P., 2002. Materials design of ceramic-based layer structures for crowns. *Journal of Dental Research*. 81(6), 433–438.
- Lawn, B. R., Deng, Y., Thompson, V. P., 2001. Use of contact testing in the characterization and design of all-ceramic crownlike layer structures: a review. *Journal of Prosthetic Dentistry*. 86(5), 495–510.
- Li, W., Swain, M. V., Li, Q., Ironside, J., Steven, G. P., 2004. Fibre reinforced composite dental bridge. Part II: numerical investigation. *Biomaterials*. 25(20), 4995–5001.

- 
- Liu, Y. H., Xu, J. Q., Ding, H. J., 1999. Order of singularity and singular stress field about an aximetric interface corner in three dimensional isotropic elasticity. *International Journal of Solids and Structures*. 36, 4425-4445.
- Lu, C., Zhang, D., Zhang, X., Han, D., 2008. Experimental investigation for fracture modes of manmade dental crown under contact loads. *Chinese Journal of Applied Mechanics*. 25(2), 308–311.
- Masterton, J. B., Davis, V. M., 1964. Complete veneer gold-porcelain bonded crowns, an evaluation of aesthetics, design, and applications in the light of clinical experience. *Dental Practice*. 14, 449–463.
- Mumford, G., 1965. The porcelain fused to metal restoration. *Dental Clinics of North America*. 23, 241–249.
- Munz, D., Yang, Y. Y., 1992. Stress singularities at the interface in bonded dissimilar materials under mechanical and thermal loading. *Journal of Applied Mechanics*. 59(4), 857–861.
- Nakayama, W. T., Hall, D. R., Grenoble, D. E., Katz, J. L., 1974. Elastic properties of dental resin restorative materials. *Journal of Dental Research*. 53(5), 1121–1126.
- Qian, Z. Q., Akisanya, A. R., 1999. An investigation of the stress singularity near the free edge of scarf joints. *European Journal of Mechanics A-Solids*. 18, 443-463.

- 
- Ryge, G., 1965. Current American research on porcelainfused- to-metal restorations. *International Dental Journal*. 15(3), 385–392.
- Shell, J. S., Nielsen, J. P., 1962. Study of the bond between gold alloys and porcelain. *Journal of Dental Research*. 41, 1424–1437.
- Soboyejo, W. O., Wang, R., Katsube, N., Seghi, R., Pagedas, C., Skraba, P., Mumm, D. R., Evans, A. G., 2001. Contact damage of model dental multilayers: experiments and finite element simulations. *Key Engineering Materials*. 198/199, 135–178.
- Stashevich, E. E., Guzman, I. Y., 1984. Methods of determining the bond strength between dental porcelain and alloy. *Steklo I Keramika*. 3, 30–31.
- Straussberg, G., Katz, G., Kuwata, M., 1966. Design of gold supporting structures for fused porcelain restorations. *Journal of Prosthetic Dentistry*. 16(5), 928–936.
- Suansuwan, N., Swain, M. V., 2001. Determination of elastic properties of metal alloys and dental porcelains. *Journal of Oral Rehabilitation*. 28(2), 133–139.
- van Noort, R., 2002. *Introduction to dental materials*. second edition. Mosby, Philadelphia.

Whitworth, J. M., Walls, A. W. G., Wassell, R. W., 2002. Crowns and extra-coronal restorations: endodontic considerations: the pulp, the root-treated tooth and the crown. *British Dental Journal*. 192, 315–327.

Zarone, F., Apicella, D., Sorrentino, R., Ferro, V., Aversa, R., Apicella, A., 2005. Influence of tooth preparation design on the stress distribution in maxillary central incisors restored by means of alumina porcelain veneers: a 3D-finite element analysis. *Dental Materials*. 21(12), 1178–1188.

## **CHAPTER 8**

### **CONCLUSIONS**

---

The objective of this research was to develop a new test method for the determination of biaxial normal-shear bonding strength envelope for bi-material interfaces. A new method, which includes the design of a special interface geometry, test procedure and calculation algorithm has been developed to accomplish the objective of this study.

#### **8.1 SUMMARY OF THE RESEARCH**

The present research can be summarized as below.

- A brief review on the papers available in open literature related to the bi-material interface strength is presented. The current practices including the ASTM standard methods encounter difficulties to accurately determine the value of the interface bonding strength. They have certain major disadvantages such as the non-uniform multi-axial stress distribution over the interface area and/or the presence of singularities of the interfacial stress components.

- 
- A new test method to determine the bi-axial normal-shear bonding strength at bi-material interface has been developed. This method includes the design of special interface geometry to eliminate the stress singularity at the free edge of the interface and the corresponding test and calculation procedures to obtain the interface bonding strength envelope.
  - A cylindrical specimen of two bulk materials with a spherical interface is developed to measure the interface bonding strength of two materials by eliminating the stress singularity. In this design, the soft material is at the convex side of the interface, while the hard material is at the concave side of the interface. The bonding angle, which is defined as the angle between the tangent of the spherical interface to the generator of the cylindrical surface, must be less than the critical bonding angle for the elimination of the stress singularity.
  - The 810-Material Testing System is used to conduct all the tensile and relaxation tests. The multi-axial testing machine is used to conduct the interface strength tests. It has the capacity to apply combined loading on the specimen (torsion and tension).
  - Three different materials are used in this research. These materials are selected based on their applicability, availability, machinability and low cost. The selected materials are aluminum, epoxy and polyvinylchloride (PVC).

- 
- Aluminum and epoxy are used for the determination of the interface bonding strength between elastic and elastic materials. It is found from experiment that at a very fast loading rate, the viscoelastic epoxy can be approximately treated as an elastic material.
  - To see the viscoelastic effect on the interface bonding strength, the same materials combination (Aluminum/Epoxy) is used for the bonding strength determination of elastic/viscoelastic interface. However, for this case the loading rate is kept much slower than the elastic/elastic case.
  - PVC and epoxy are used for the viscoelastic/viscoelastic interface bonding strength measurement.
  - Analytical solution to determine the order of the stress singularity and the critical bonding angle for the elastic/elastic interface is developed based on an axi-symmetric asymptotic stress analysis.
  - The analytical solutions for the elastic/viscoelastic and viscoelastic/viscoelastic interfaces are derived from the analytical solution for elastic/elastic interface using the elastic-viscoelastic corresponding analogy.
  - To determine the analytical solution for the interface containing any viscoelastic material, accurate modeling of the material properties is very important. Three different cases of material modeling are considered in

this study; (i) Viscoelastic shear modulus is modeled as a standard linear solid model and Poisson's ratio is assumed to be constant, (ii) Both the viscoelastic shear modulus and Poisson's ratio are modeled as the standard linear solid model, (iii) Both the viscoelastic shear modulus and Poisson's ratio are modeled as a Wiechert Model consisting of two Maxwell elements with a spring in parallel. This model can more accurately simulate the viscoelastic behavior of studied materials: epoxy and PVC.

- From the analytical solution of elastic/elastic interface, the critical bonding angle for the tested aluminum/epoxy interface is determined as in between  $49^\circ$  and  $50^\circ$ . However, considering the viscoelasticity of epoxy, from the analytical solution for the elastic/viscoelastic interface, the critical bonding angle for the aluminum/epoxy interface is determined as in between  $48^\circ$  and  $49^\circ$ . The critical bonding angle for PVC/epoxy interface is determined as in between  $47^\circ$  and  $48^\circ$  from the analytical solution for the viscoelastic/viscoelastic interface.
- All the results obtained from the analytical solutions are verified by the finite element numerical analysis method.
- A detrimental time effect may have on the viscoelastic interface design with the stress singularity because the order of the singularity may increase with time.

- There is no interface stress singularity for the application of pure torsional loading on the specimen if they are designed according to the developed method.
- Since the stress distributions are not uniform along the interface, an iterative calculation method integrated with FEM stress analysis is developed to determine the bi-axial normal-shear interface bonding strength envelope.
- The normal-shear interface bonding strength envelope for the tested aluminum/epoxy (Elastic/Elastic) in the range of the first quarter of the normal-shear stress plane is determined as

$$\left(\frac{\sigma_n}{19.76}\right)^2 + \left(\frac{\tau}{20.86}\right)^2 = 1$$

- The normal-shear interface bonding strength envelope for the tested aluminum/epoxy (Elastic/Viscoelastic) in the range of the first quarter of the normal-shear stress plane is determined as

$$\left(\frac{\sigma_n}{21.15}\right)^2 + \left(\frac{\tau}{21.85}\right)^2 = 1$$

- The normal-shear interface bonding strength envelope for the PVC/epoxy (Viscoelastic/Viscoelastic) in the range of the first quarter of the normal-shear stress plane is determined as

$$\left(\frac{\sigma_n}{9.63}\right)^2 + \left(\frac{\tau}{15.14}\right)^2 = 1$$

- For the elastic/elastic (Aluminum/Epoxy) interface, the average maximum failure (debonding) load with the ASTM butt joint specimens is obtained as 2161 N with a data scatter band of 13%, while with the present designed specimens, this value is obtained as 5727 N with a scatter band of 12%. The large difference in the load carrying capability of these two groups of specimen shows the great potential in the optimal design of bi-material interface for advanced materials and structures.
- For the developed specimen design, the interface debonding started near the central area of the interface, not from the edge of the interface as in the case of the ASTM butt joint specimens.
- The developed method is a more accurate and practical approach to characterize this important mechanical property of bi-material interface. The new test method provides a biaxial normal-shear bonding strength criterion (envelope) for the bi-material interface. Such criterion and data base are critical for an accurate and realistic theoretical/numerical modeling of the damage and failure of the interfaces.
- As an application of the research in the dental restorations, an optimal geometry design for a PFM dental crown has been carried out. It is found

that to eliminate the stress singularity at the interface free edge corner, the appropriate margin angle range is 15-30 degrees for the precious alloy PFM crown and 30-35 degrees for the non-precious alloy PFM crown, respectively.

- The optimal off-vertical angle of the metal layer in the PFM crown is  $10^\circ$  for a precious-metal-based crown and  $12^\circ$  for the nonprecious- metal-based crown, respectively.
- The results may serve as a general guide for the design and manufacture of the dental crowns.
- The optimal range of the bonding angles may be different if the materials or their properties are changed; however, the proposed numerical and analytical methods can also be used to determine the optimal geometric parameters in those cases.
- The interface bonding strength is an inherent physical property for a given bi-material interface and should not be changed with the change of the interface geometry. With the different designs of interface geometry, the interface stress distributions are different, thus resulting in different load carrying capabilities of the specimens. Although it is possible to design the proper interface geometries to avoid the stress singularity, it is very difficult (if it is not impossible) to design a specimen that could produce a

pure uniform normal stress distribution at the bi-material interface without any stress singularity.

- For the proposed specimen design, failure will always happen at the interface under the tensile or shear loading if there is no defect in the two bulk materials. This is because of the maximum stress in the specimen is prominently at the interface due to the incompatibility of mechanical properties of the two materials.
- The developed test method will be ineffective if the bi-material interface bonding strength is greater than the ultimate strength of one of the materials. Even in that case the failure of the weaker material will be most likely initiated near the interface due to the stress concentration.

## **8.2 FURTHER RECOMMENDATIONS**

Since, the mechanics of interface is a new developing branch of solid mechanics, continuing research on this area will make this new branch richer. In addition to the current research, future researches can be carried on the following topics.

- **Orthotropic Materials Structures:** In the present research, all the materials are considered as isotropic. In future, the similar research can be carried on the

- interface between orthotropic materials or between orthotropic and isotropic materials.
- **Interface Fatigue:** It is well known that the corner geometry at the end of the bonded area have a significant influence on the fatigue strength of composites bonded joints. Determination of the accurate interface fatigue strength can be an interesting topic for future research.
  - **Failure Mechanism of Structures with Interface:** Further research can be carried on to study the damage mechanism of structures with bi-material interface.
  - **Smart Materials and Structures:** Nowadays, composite materials are reinforced with shape memory alloy (SMA) wires in many applications. The interface between the SMA wire and the composite matrix plays an important role to the overall performances of the structure. The design of such a smart composite may be a future potential research area.
  - **Other Applications:** In addition to the dental industry, electronic packaging might be another prospective area for this branch of study. There are multi interfaces between the solder and the parts in electronic packaging. This research can be extended to make a better design of the connections to increase resistance to damage. The interface characterization also has a great potential in the aerospace industry.